IUTAM Bookseries

Stefanie Gutschmidt
James N. Hewett
Mathieu Sellier *Editors*

IUTAM Symposium on Recent Advances in Moving Boundary Problems in Mechanics

Proceedings of the IUTAM Symposium on Moving Boundary Problems, Christchurch, New Zealand, February 12–15, 2018

Springer

IUTAM Bookseries

Volume 34

The IUTAM Bookseries publishes the refereed proceedings of symposia organized by the International Union of Theoretical and Applied Mechanics (IUTAM).

Every two years the IUTAM General Assembly decides on the list of IUTAM Symposia. The Assembly calls upon the advice of the Symposia panels. Proposals for Symposia are made through the Assembly members, the Adhering Organizations, and the Affiliated Organizations, and are submitted online when a call is launched on the IUTAM website.

The IUTAM Symposia are reserved to invited participants. Those wishing to participate in an IUTAM Symposium are therefore advised to contact the Chairman of the Scientific Committee in due time in advance of the meeting. From 1996 to 2010, Kluwer Academic Publishers, now Springer, was the preferred publisher of the refereed proceedings of the IUTAM Symposia. Proceedings have also been published as special issues of appropriate journals. From 2018, this bookseries is again recommended by IUTAM for publication of Symposia proceedings.

Indexed in Ei Compendex and Scopus.

More information about this series at http://www.springer.com/series/7695

Stefanie Gutschmidt · James N. Hewett ·
Mathieu Sellier
Editors

IUTAM Symposium on Recent Advances in Moving Boundary Problems in Mechanics

Proceedings of the IUTAM Symposium on Moving Boundary Problems, Christchurch, New Zealand, February 12–15, 2018

Springer

Editors
Stefanie Gutschmidt
Department of Mechanical Engineering
University of Canterbury
Christchurch, New Zealand

James N. Hewett
Department of Mechanical Engineering
University of Canterbury
Christchurch, New Zealand

Mathieu Sellier
Department of Mechanical Engineering
University of Canterbury
Christchurch, New Zealand

ISSN 1875-3507 ISSN 1875-3493 (electronic)
IUTAM Bookseries
ISBN 978-3-030-13719-9 ISBN 978-3-030-13720-5 (eBook)
https://doi.org/10.1007/978-3-030-13720-5

Library of Congress Control Number: 2019931856

This Springer imprint is published by the registered company Springer Nature Switzerland AG
The registered company address is: Gewerbestrasse 11, 6330 Cham, Switzerland

Preface

Background

Many problems in mechanics involve a deformable domain with moving boundaries. Examples include two-way fluid–structure interaction, free surface flows, flows over soft tissues and textiles, flows involving accretion/erosion, flows through deformable porous media, material forming, to name but a few. The interaction of the moving boundary with the participating medium leads to fascinating phenomena in a very broad range of contexts such as flutter, wave breaking, dune formation, ripple formation on the ocean floor, flow instabilities, structure resonance and failure, atherosclerosis, ice formation on aircraft wings, etc.

The presence of a moving boundary also presents considerable challenges when it comes to modeling and understanding the underlying system dynamics. The moving boundary often introduces nonlinearities, which call for special analytical or numerical treatment. Many techniques have been developed over the years to handle the moving boundary and the corresponding deformable medium. Examples include front tracking methods, front fixing methods, the volume of fluid method, the arbitrary Lagrangian–Eulerian method, etc. These methods have allowed the community to tackle forever more complex problems of engineering and physics, but challenges still remain and the range of applications for which these techniques can be applied is vast.

Symposium

The IUTAM symposium on "Recent Advances in Moving Boundary Problems in Mechanics" occurred from February 12 to February 15, 2018 in Christchurch, New Zealand. The aims of the symposium were to

1. gather the international community of engineers and scientists involved in moving boundary problems in mechanics,
2. attract a broad spectrum of researchers from various backgrounds (theoreticians, numerical analysts, experimentalists, applied mathematicians, engineers, physicists, etc.), and
3. unify a fragmented community to cross-fertilize ideas.

It was a pleasure to host about 50 participants from 17 different countries, a truly international cross section of the field. The single stream format of the symposium over 4 days afforded many opportunities for all participants to interact and get to know one another. Talks were broadly organized in themes: fluid–structure interaction, bioengineering applications, multiphase flows, analytical and numerical methods, Stefan problems, structures with a moving boundary, and optimization. The symposium had a good mix of participants (65% Engineering, 31% Applied Mathematics, 4% Physics). Presentations also spanned the whole spectrum from theory to applications. Most of the talks were oriented toward fluid mechanics (approximately 40% fluid, 40% fluid–structure interaction, 20% solid).

We were delighted to have had four engaging and inspiring plenary talks:

1. Prof. Yvonne Stokes (University of Adelaide): "Can we fabricate that fibre?"
2. Prof. Scott McCue (Queensland University of Technology): "Three dimensional linear and nonlinear surface wave patterns"
3. Prof. Jun Zhang (NYU): "Symmetry breaking bifurcations arising from fluid-structure interaction"
4. Prof. Frederic Dias (University College Dublin): "Recent advances in slamming"

We gratefully acknowledge their contribution to the success of the symposium.

Beyond the stimulating environment of the symposium, we will also keep fond memories of the social events including the symposium banquet and the Akaroa Harbour cruise.

Finally, we would like to acknowledge the professional and financial support of IUTAM, the College of Engineering at the University of Canterbury, the scientific committee, and local organizing team. Our special and personal thanks go to the symposium secretary James N. Hewett, who ran this symposium in such a way that everyone will keep this symposium in mind with very pleasant memories.

In summary, this symposium not only "moved boundaries" but also broke boundaries between researchers and pushed them to enhance knowledge in the field.

Christchurch, New Zealand

Stefanie Gutschmidt
James N. Hewett
Mathieu Sellier

Contents

Chapter 1
Can We Fabricate That Fibre?

Yvonne M. Stokes, Darren G. Crowdy, Heike Ebendorff-Heidepriem, Peter Buchak and Michael J. Chen

Abstract This paper reviews the development of an efficient mathematical model for the drawing of optical fibres using extensional flow theory which is applicable for fibres of arbitrary geometry. The model is comprised of a 1D axial stretching problem describing the change in area of the cross-section from preform to fibre coupled with a 2D cross-plane problem describing the evolution of a cross-section. The solution of the axial stretching problem may be written in an exact form while the cross-plane problem must, in general, be solved numerically. The model may be used to solve forward and inverse problems and gives results that compare well with experiments.

Keywords Extensional flow · Free-boundary problem · Optical fibres

1.1 Introduction

Modelling of fibre drawing has been a topic of interest for around five decades, motivated initially by the 'spinning' of textile fibres [13] and film-blowing [14], and, more recently, by optical fibre technologies [1, 2, 5–8, 15–18] and the fabrication

Y. M. Stokes (✉) · M. J. Chen
School of Mathematical Sciences, The University of Adelaide,
Adelaide, SA 5005, Australia
e-mail: yvonne.stokes@adelaide.edu.au
URL: http://www.maths.adelaide.edu.au/yvonne.stokes/

D. G. Crowdy
Department of Mathematics, Imperial College London,
London SW7 2AZ, UK

H. Ebendorff-Heidepriem
Institute for Photonics and Advanced Sensing, School of Chemistry and Physics,
The University of Adelaide, Adelaide, SA 5005, Australia

P. Buchak
LowReTech LLC, 3401 Market St, Suite 200, Philadelphia, PA 19104, USA

S. Gutschmidt et al. (eds.), *IUTAM Symposium on Recent Advances in Moving Boundary Problems in Mechanics*, IUTAM Bookseries 34,
https://doi.org/10.1007/978-3-030-13720-5_1

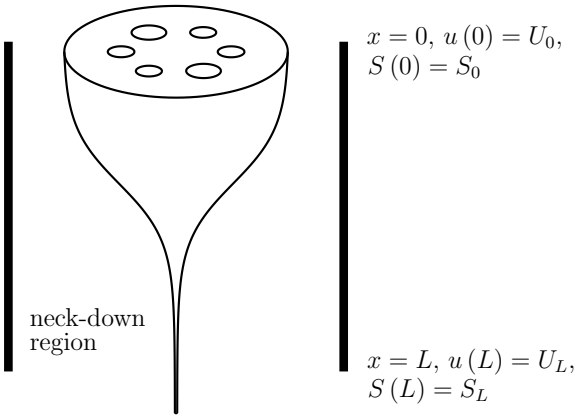

Fig. 1.1 Schematic diagram of the neck-down region, $0 \leq x \leq L$, over which the cross-sectional area of the preform S_0 reduces to that of the fibre S_L due to the large draw speed U_L relative to the feed speed U_0.

of capillary tubes [9]. The aim of this paper is to review key research in the context of drawing of microstructured optical fibres.

Microstructured optical fibres, containing patterns of air channels running along their length, have revolutionised optical fibre technology, promising a virtually limitless range of fibre designs for a wide range of applications, including communication networks, medical devices and sensing [10, 11]. These are fabricated as depicted in Fig. 1.1; a preform (1–3 cm diameter and with a length of around 10 cm or so), with a cross-section of appropriate geometry and having area S_0, is fed into a heated region at a feed speed U_0 and pulled at a higher draw speed U_L by winding onto a spool some distance downstream beyond the neck-down region of length comparable to, but not necessarily identical with, the heated region. Internal channels may be pressurised. In the laboratory reference frame this drawing process over the neck-down region $0 \leq x \leq L$ may be considered a steady-state problem. The resulting fibre will, typically, have a diameter of $100-200\,\mu$m, a cross-sectional area $S_L \ll S_0$, and a length of a kilometre or more, while the internal air channels have diameters comparable to the wavelength of light. Even when the channels are not pressurised, the fibre drawing process modifies the shape of the cross-sectional geometry from that of the preform (see Fig. 1.2), as well as its scale, so that fabrication of a fibre with a desired structure presents a major challenge. What initial preform is suitable and what draw parameters should be used? Can it even be made? This is an inverse problem and mathematics is essential to its solution.

While full 3D numerical simulation has been used to investigate deformation of the cross-sectional geometry during fibre drawing [16, 17], this is still not practical for fibres with complex cross-sectional geometries because of the fine mesh resolution and large computational resources required. However, the slenderness of the geometry enables extensional flow theory to be used to develop accurate and efficient models and we here focus on these.

The first such model of steady-state fibre drawing seems to be due to Matovich and Pearson [13] who examined the drawing of solid axisymmetric fibres having no

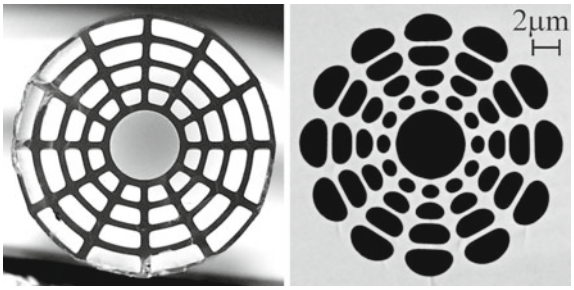

Fig. 1.2 Cross-sectional geometry of (left) a fibre preform with total pattern diameter 3 cm, and (right) the resulting fibre with total pattern diameter 20 μm. These show the deformation due to the fibre drawing process. Photographs reproduced with the permission of the Institute for Photonics and Advanced Sensing, The University of Adelaide

internal structure. They obtained the form of the solution assuming a Newtonian fluid and neglecting surface tension and/or inertial forces; they also considered some non-Newtonian fluid models. Dewynne, Howell and Wilmott [7] showed that, assuming a Newtonian fluid and with neglect of surface tension, fibre drawing results only in a change in the cross-sectional scale, but not its shape, so that the steady-state model, for any given preform geometry, may be written as a boundary-value problem in one spatial dimension for the cross-sectional area as a function of axial position, which is readily solved. In an appendix they also noted that, for the case of non-negligible surface tension, the first-order model for the cross-sectional area is the same as for the zero surface tension case, but that the cross-section no longer maintains its shape which must be determined by solving a second-order 2D cross-flow problem. Modelling of fibre drawing including surface tension was considered in detail by Cummings and Howell [5] for fibres with no internal cross-sectional geometry and for a fluid of constant temperature (viscosity). They showed that the 2D cross-flow problem may be written as a classical 2D free-boundary Stokes-flow problem.

Motivated specifically by the drawing of microstructured optical fibres, Fitt et al. [8] used extensional-flow theory to derive coupled flow and temperature models for the steady drawing of axisymmetric capillary tubes. A Newtonian viscous fluid with temperature-dependent viscosity was assumed and inertia, gravity, surface tension and pressurisation of internal channels were included in the model. Various cases neglecting one or more of these were considered but the complete exact solution for isothermal fibre drawing with non-negligible surface tension, and neglecting inertia, gravity and pressurisation, was not found. Griffiths and Howell [9] obtained the solution for thin-walled annular tubes in their work extending the model of Cummings and Howell [5] to the non-isothermal drawing of (not necessarily axisymmetric) thin-walled tubes.

Solution of the extensional flow model with non-negligible surface tension for the drawing of microstructred optical fibres of arbitrary cross-sectional geometry and, indeed, also the drawing of an annular tube with arbitrary wall thickness, proved elusive but was finally solved by Stokes et al. [15]. The breakthrough that led to

this model is described in Sect. 1.2. Importantly, both forward and inverse problems may be solved as described in Sect. 1.3. Pressurisation of internal channels is not considered in this paper but was added by Chen et al. [2]. Section 1.4 contains concluding remarks and also shows some stunningly accurate comparisons of the model and experiments.

1.2 Mathematical Model

Let the x-axis lie on the central axis of the fibre and be directed downwards in the direction of stretching (Fig. 1.1); y and z are then the transverse coordinates. At $x = 0$ the cross-sectional geometry is that of the preform, which has cross-sectional area S_0, and at $x = L$ the cross-sectional geometry is that of the fibre, which has cross-sectional area S_L, so that the neck-down region over which we model is $0 \leq x \leq L$. In this Eulerian reference frame fibre-drawing is a steady-state problem. Further, the effect of gravity is negligible. Then, for a preform of arbitrary geometry, we start with the full (3D) steady Navier–Stokes equations,

$$\begin{aligned} \nabla \cdot \boldsymbol{u} &= 0, \\ \rho\,(\boldsymbol{u} \cdot \nabla \boldsymbol{u}) &= -\nabla p + \nabla \cdot \boldsymbol{\sigma}, \end{aligned}$$

where $\boldsymbol{u} = (u, v, w)$ is the velocity vector, p is pressure, $\boldsymbol{\sigma} = \mu(\nabla \boldsymbol{u} + (\nabla \boldsymbol{u})^T)$ is the usual viscous-stress tensor, and ρ and μ are the constant density and temperature-dependent viscosity of the fluid. The fibre has a number of free-surface boundaries, the external free surface and the surfaces of each of the interior air channels. In this paper we denote the collection of free-surface boundaries by $G(x, y, z, t) = 0$ on which we have the dynamic and kinematic boundary conditions

$$\boldsymbol{\sigma} \cdot \boldsymbol{n} = -\gamma \kappa \boldsymbol{n}, \quad \boldsymbol{u} \cdot \boldsymbol{n} = 0.$$

Here γ is the coefficient of surface tension, assumed to be constant, κ is the curvature of the boundary and $\boldsymbol{n}$ is an outward normal to the boundary. In addition we have the boundary conditions

$$u(0, y, z) = U_0, \quad u(L, y, z) = U_L.$$

1.2.1 The Axial Stretching Problem

As discussed previously the geometry through the neck-down region from preform to fibre is slender so that we may, as is common [5, 7–9, 13, 15], use extensional flow theory. Thus we set $\epsilon = \sqrt{S_0}/L \ll 1$ and then scale variables and parameters as follows:

$$\mu = \bar{\mu}\mu^*, \quad \gamma = \frac{\bar{\mu}U_0\sqrt{S_0}}{L}\gamma^*,$$
$$(x, y, z) = L(x', \epsilon y', \epsilon z'), \quad p = \frac{\bar{\mu}U_0}{L}p',$$
$$\boldsymbol{u} = (u, v, w) = U_0(u', \epsilon v', \epsilon w'), \quad S = S_0 S',$$

where primes denote dimensionless variables, asterisks denote dimensionless parameters, and $\bar{\mu}$ is a typical viscosity. Because the resulting scaled equations involve only $O(1)$ and $O(\epsilon^2)$ terms, but no $O(\epsilon)$ terms, we also expand scaled dependent variables in powers of ϵ^2 [7]:

$$u' = u_0 + \epsilon^2 u_1 + \epsilon^4 u_2 + \ldots,$$
$$v' = v_0 + \epsilon^2 v_1 + \epsilon^4 v_2 + \ldots,$$

and so on. From this we find that, to leading order the axial velocity and pressure are independent of the transverse coordinates, i.e. $u_0 = u_0(x, t)$ and $p_0 = p_0(x, t)$. As shown in [8], a similar process can be used to show that, at leading order, the temperature is independent of the transverse coordinates, so that this is also true of the temperature-dependent viscosity μ and its scaled form μ^*. In this paper we assume $\mu(x)$ to be a known function and take $\bar{\mu}$ to be its harmonic mean over the neck-down region,

$$\bar{\mu} = \frac{L}{\int_0^L 1/\mu(x)dx} \quad \Rightarrow \quad \int_0^1 \frac{1}{\mu^*(x')}dx' = 1.$$

Finally we note that the Reynolds number $\mathrm{Re} = \rho U_0 L/\bar{\mu}$ is much less than unity (typically $\mathrm{Re} \sim 10^{-8}$) so that inertia may be neglected.

With these scalings, and after considerable work [5, 7, 15], the leading-order model for $S_0(x')$ and $u_0(x')$ is obtained. Dropping primes on dimensionless variables and subscripts on the leading order components of the dependent variables, this is

$$u(x)S(x) = 1, \tag{1.1}$$
$$3\mu^*(x)Su_x + \frac{\gamma^*}{2}\sqrt{S}\Gamma = 6\sigma^*, \tag{1.2}$$
$$S(0) = 1, \; u(0) = 1, \; u(1) = D = 1/S(1), \tag{1.3}$$

where $\Gamma(x)$ is the total length of all internal and external boundaries at position x, σ^* is the scaled tension in the fibre, and $D = U_L/U_0$ is the draw ratio. We refer to this as the axial stretching problem. Clearly, we may use (1.1) to substitute for u or S in (1.2), and so reduce this model to a single first-order ODE for S or u, with associated boundary conditions. We note that a given draw ratio D will dictate the fibre tension σ^* or vice versa. In general, we must determine $\Gamma(x)$ from a model for the cross-plane flow but we first consider the case of zero surface tension $\gamma^* = 0$

which removes the term involving Γ and enables straight-forward solution of the axial stretching problem.

1.2.2 The Case of Zero Surface Tension

This case was considered in detail by Dewynne and others [6, 7] who showed that, at leading order, the cross-plane flow solution may be written entirely in terms of the leading order axial flow component u,

$$p = -\mu^* \frac{\partial u}{\partial x},\ v = -\frac{y}{2}\frac{\partial u}{\partial x},\ w = -\frac{z}{2}\frac{\partial u}{\partial x}.$$

From this solution we have that the cross section changes in *scale* but not in *shape*. Therefore, we need only solve for the cross-sectional area $S(x)$ which has solution

$$S(x) = \exp\left(-2\sigma^* \int_0^x \frac{1}{\mu^*(x')} dx'\right),$$
$$S(1) = \frac{1}{D} = \exp\left(-2\sigma^*\right),$$

where we have made use of the fact that the harmonic mean of μ^* over $0 \leq x \leq 1$ is unity and found that the draw ratio D determines the fibre tension σ^*.

1.2.3 The Cross-Plane Flow Problem for Non-negligible Surface Tension

We now come to the leading order cross-plane flow problem for $\gamma^* > 0$. As shown by Cummings and Howell [5], the zero surface tension solution may be considered an eigensolution of this problem and the flow solution written as the sum of the eigensolution and a part due to surface tension. We also move to the reference frame moving with a cross-section from $x = 0$ to $x = 1$, in which reference frame the problem is unsteady and the variable x is replaced by the time variable t. We rescale variables using the cross-sectional area $S(x)$ as follows:

$$(y, z) = \sqrt{S}\,(\tilde{y}, \tilde{z}),\ t = \tilde{t},\ \Gamma = \sqrt{S}\tilde{\Gamma},\ \kappa = \frac{\tilde{\kappa}}{\sqrt{S}}$$
$$p = p_{ZST} + \frac{\gamma^*}{\sqrt{S}}\tilde{p},\ (v, w) = (v_{ZST}, w_{ZST}) + \frac{\gamma^*}{\mu^*}(\tilde{v}, \tilde{w}),$$

where p_{ZST}, v_{ZST}, w_{ZST} is the leading order cross-plane flow solution for $\gamma^* = 0$ and tildes denote the new dimensionless variables. In addition we use the 'reduced time' transformation introduced for constant viscosity in [5] and for temperature-dependent viscosity in [9],

$$\tau = \gamma^* \int_0^{\tilde{t}} \frac{dt}{\mu^* \sqrt{S}}.$$

The cross-plane problem so obtained is a classical 2D free-boundary Stokes-flow problem driven by unit surface tension in a domain of unit area:

$$\tilde{v}_{\tilde{y}} + \tilde{w}_{\tilde{z}} = 0, \ \tilde{v}_{\tilde{y}\tilde{y}} + \tilde{v}_{\tilde{z}\tilde{z}} = \tilde{p}_{\tilde{y}}, \ \tilde{w}_{\tilde{y}\tilde{y}} + \tilde{w}_{\tilde{z}\tilde{z}} = \tilde{p}_{\tilde{z}}, \tag{1.4}$$

$$G_\tau + \tilde{v} G_{\tilde{y}} + \tilde{w} G_{\tilde{z}} = 0, \ \text{on } G = 0, \tag{1.5}$$

$$G_{\tilde{y}}(-\tilde{p} + 2\tilde{v}_{\tilde{y}}) + G_{\tilde{z}}(\tilde{v}_{\tilde{z}} + \tilde{w}_{\tilde{y}}) = -\tilde{\kappa} G_{\tilde{y}}, \ \text{on } G = 0, \tag{1.6}$$

$$G_{\tilde{y}}(\tilde{v}_{\tilde{z}} + \tilde{w}_{\tilde{y}}) + G_{\tilde{z}}(-\tilde{p} + 2\tilde{w}_{\tilde{z}}) = -\tilde{\kappa} G_{\tilde{z}}, \ \text{on } G = 0, \tag{1.7}$$

Here subscripts denote differentiation with respect to the subscript variable. Solution of the cross-plane problem gives the re-scaled cross-flow and cross-sectional geometry, including the boundary length $\tilde{\Gamma}$, as functions of reduced time τ.

1.2.4 *Coupling of Axial Stretching and Cross-Plane Flow Problems*

The cross-plane problem (1.4)–(1.7) in terms of τ is coupled with the Eulerian axial stretching problem (1.1)–(1.3) in terms of x via

$$\frac{dx}{d\tilde{t}} = u \quad \Rightarrow \quad \frac{\gamma^*}{\mu^* \sqrt{S}} \frac{dx}{d\tau} = u, \quad x(0) = 0. \tag{1.8}$$

While a solution has been obtained for a thin-walled tube with μ^* an exponential function of temperature [9], obtaining a solution more generally is difficult. However, as shown by Stokes et al. [15] the two coupled problems are readily solved for general geometries and viscosity functions if the 1D axial stretching model is written in terms of the variable τ,

$$-\frac{3\gamma^*}{\sqrt{S}} \frac{dS}{d\tau} + \frac{\gamma^*}{2} \Gamma(\tau) = 6\sigma^*,$$

and putting $\chi = \sqrt{S}$ and $\Gamma = \sqrt{S}\tilde{\Gamma}$ reduces this to the first-order ODE

$$\frac{d\chi}{d\tau} - \frac{\chi}{12} \tilde{\Gamma} = -\frac{\sigma^*}{\gamma^*},$$

where $\tilde{\Gamma}(\tau)$ is obtained from the cross-plane problem which is independent of the axial stretching problem and may be solved first. Defining the integrating factor

$$H(\tau) = \exp\left(-\frac{1}{12}\int_0^\tau \tilde{\Gamma}(\tau')d\tau'\right), \tag{1.9}$$

the solution may be written as

$$\chi(\tau) = \frac{1}{H(\tau)}\left(1 - \frac{\sigma^*}{\gamma^*}\int_0^\tau H(\tau')d\tau'\right). \tag{1.10}$$

Thus, in summary, the cross-plane model gives the total boundary length $\tilde{\Gamma}(\tau)$, $0 \le \tau \le \tau_1$ where τ_1 determines the fibre shape but not its size. Any appropriate analytical or numerical method may be used to solve for the cross-plane shape and boundary length and, hence for the integrating factor (1.9). The stretching flow problem has the exact solution (1.10) in terms of the integrating factor. The draw ratio $D = U_L/U_0 = 1/\chi^2(\tau_1) = 1/S(\tau_1)$ determines the size of the final fibre cross-section and, from (1.10), we have the relation between the fibre shape (τ_1) and the ratio of fibre and surface tension (σ^*/γ^*),

$$\frac{1}{\sqrt{D}} = \frac{1}{H(\tau_1)}\left(1 - \frac{\sigma^*}{\gamma^*}\int_0^{\tau_1} H(\tau')d\tau'\right).$$

From (1.8) we obtain the separable ODE relating τ and x,

$$\frac{dx}{d\tau} = \frac{\mu^*}{\gamma^*\chi}, \quad x(0) = 0,$$

integration of which gives the fibre tension σ^*,

$$\int_0^1 \frac{1}{\mu^*(x')}dx' = 1 = -\frac{1}{\sigma^*}\log\left(\frac{H(\tau_1)}{\sqrt{D}}\right).$$

The model involves the four parameters σ^* (fibre tension), γ^* (surface tension), $D = U_L/U_0 = S_0/S_L$ (draw ratio, equivalently fibre size), and τ_1 (fibre geometry). These are not all independent; two must be specified and the remaining two determined as part of the solution.

An important result from this solution is that for drawing a desired fibre from a given preform we can use the model to determine the required physical fibre tension without knowing the temperature profile. As discussed in detail in [15], for a given preform geometry and a given fibre geometry (i.e. D and τ_1), the model gives the required ratio σ^*/γ^* which is related to the ratio of the physical parameters σ and γ by

$$\frac{\sigma^*}{\gamma^*} = \frac{1}{6\sqrt{S_0}}\frac{\sigma}{\gamma}. \tag{1.11}$$

Since the surface tension γ is a known fluid property and the cross-sectional area S_0 of the preform is also known, we may use (1.11) to compute the physical fibre tension σ. Provided the draw tower allows for measurement of fibre tension during a draw, the furnace temperature can be adjusted to achieve the desired fibre tension without the need to know anything about the fluid temperature itself. In fact, since the model also gives σ^* and assuming the (approximate) neck-down length is known, the (approximate) harmonic mean of the fluid temperature through the neck-down region may be computed from

$$\sigma = \frac{\bar{\mu}U_0S_0}{L}6\sigma^* \quad \Rightarrow \quad \bar{\mu} = \frac{\sigma L}{6U_0S_0\sigma^*}.$$

1.3 Forward and Inverse Solutions

Solution of the forward problem is done by solving the cross-plane problem for a given preform geometry over reduced time $0 \leq \tau \leq \tau_1$, for some chosen value τ_1, and then solving the axial stretching problem. Solution of the inverse problem is achieved by solving the cross-plane problem backwards from a given fibre geometry. When the cross-plane problem may be solved analytically, both forward and inverse problems are easily solved; see, for example, the solutions given in [15] for the drawing of (i) an annular tube and (ii) the tube made by arranging a number of circular rods of appropriate radius in a circle. These two examples were also used to show that the inverse problem is inherently unstable; small imperfections in the description of the fibre are amplified as the model is run backwards, leading to different preform geometries, some of which may not be practical.

To overcome this instability in numerical solution of the inverse cross-plane problem, some form of regularisation must be used. An example of this is [1] where a modified form of Crowdy's [4] elliptical-pore model, which constrains elliptical holes in the 2D cross-section to remain elliptical as they evolve, is obtained and used to solve both forward and inverse problems. Figure 1.3, reproduced from [1], shows some different preform cross-sectional geometries each of which will yield the same fibre geometry when drawn using the correct value of the draw ratio and fibre tension.

1.4 Conclusions

In this paper we have reviewed the development of an efficient mathematical model for fibre drawing using extensional flow theory. The model is comprised of a 2D free-boundary Stokes-flow problem describing the flow and geometry evolution in the

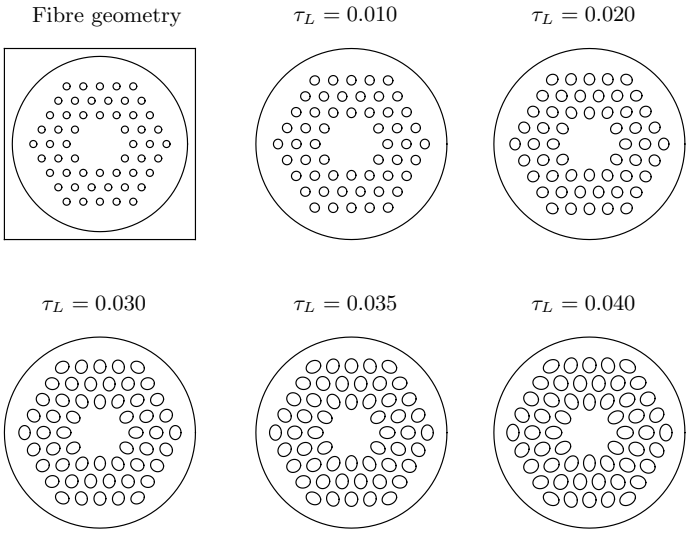

Fig. 1.3 Options for preform geometries yielding the fibre geometry shown, calculated by running the elliptical-pore model backwards. To obtain a fibre with the geometry shown and a given cross-sectional area the preform of chosen geometry must be drawn with the correct draw ratio and the correct fibre tension which may be determined from the model solution.

cross-section, and a 1D axial stretching problem which describes the change in cross-sectional area from preform to fibre. By writing and solving both of these problems in a reference frame moving with a cross-section, and in terms of an appropriately transformed time variable, an analytic solution of the axial stretching problem for the evolution of the cross-sectional area has been obtained in terms of a function involving the total boundary length of the cross-section. This boundary length must be obtained by solving the 2D cross-plane problem; for some geometries analytical solutions are available but, in general, the 2D cross-plane problem must be solved numerically. This model is applicable to fibres of arbitrary cross-sectional geometry and it enables solution of both forward and inverse problems. When solving the inverse problem the cross-plane problem is run in reverse and some form of regularisation may be needed to overcome instability and ensure practically realisable preform geometries.

It is noteworthy that the model enables determination of the tension in the fibre required to draw a given fibre from a given preform, without the need to know anything about the temperature of the fibre material. Then, when using a draw tower fitted with a tension-measuring device, the furnace temperature can be adjusted to yield the required fibre tension. This is of great practical value since determining the temperature and, therefore, the viscosity, through the neck-down region is extremely difficult, if not impossible. We also here note that the model indicates that all temperature profiles which yield viscosity profiles with the same harmonic mean through the neck-down region give the same fibre from a given preform. The temperature

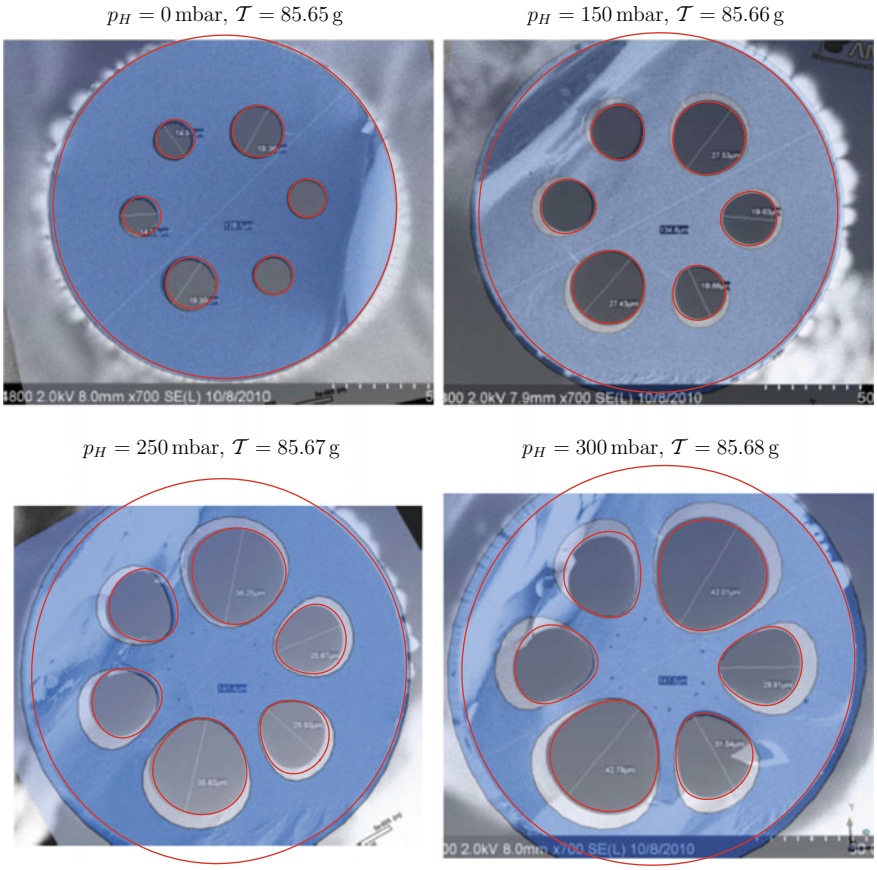

Fig. 1.4 Experimental microscope images of the fibre cross-section, overlaid with the finite element simulation of [12] (pale blue transparency) and the results of the new asymptotic simulation (thin red lines). Shown are the four values of pressurisation from [12, Fig. 3]. For each example the pressurisation applied is shown in the caption above the image, along with the fibre tension as calculated by the iterative scheme.

profile affects the evolution of the geometry along the neck-down region but not the end result.

Although not discussed in this paper, it is possible to include active pressurisation of the air channels during fibre drawing, which modifies the balance between fibre tension and surface tension. In this case there is two-way coupling between the cross-plane flow and axial stretching problems which must be solved simultaneously. Importantly, measurement of fibre tension still circumvents the need to know the temperature profile. For further detail on this model see [2].

Figure 1.4, taken from [3], compares the extensional-flow model including active pressurisation with experimental results and a 3D finite-element simulation for a 6-hole preform with an external diameter of 4 mm. The extensional-flow model captures the cross-sectional fibre geometry extremely well and better than the finite-element simulation. This provides excellent validation of the extensional-flow modelling approach. For further details see [3].

In closing we note that the model accuracy decreases as the preform diameter and the draw ratio increase. Good comparison is seen between model and experiment for preforms with external diameters up to around 10 mm and the model is a useful predictive tool for determining how to fabricate a desired fibre. For quite large preform diameter, around 3 cm, there is reasonable qualitative agreement between model and experiment for some choices of parameters but significant discrepancy for others, in particular large draw ratio and large tension. This is the subject of ongoing research.

References

1. Buchak, P., Crowdy, D.G., Stokes, Y.M., Ebendorff-Heidepriem, H.: Elliptical pore regularisation of the inverse problem for microstructured optical fibre fabrication. J. Fluid Mech. **778**, 5–38 (2015). https://doi.org/10.1017/jfm.2015.337
2. Chen, M.J., Stokes, Y.M., Buchak, P., Crowdy, D.G., Ebendorff-Heidepriem, H.: Microstructured optical fibre drawing with active channel pressurisation. J. Fluid Mech. **783**, 137–165 (2015). https://doi.org/10.1017/jfm.2015.570
3. Chen, M.J., Stokes, Y.M., Buchak, P., Crowdy, D.G., Ebendorff-Heidepriem, H.: Asymptotic modelling of a six-hole MOF. J. Lightwave Tech. **34**, 5651–5656 (2016). https://doi.org/10.1109/JLT.2016.2628438
4. Crowdy, D.G.: An elliptical-pore model of late-stage planar viscous sintering. J. Fluid Mech. **501**, 251–277 (2004). https://doi.org/10.1017/S0022112003007559
5. Cummings, L.J., Howell, P.D.: On the evolution of non-axisymmetric viscous fibres with surface tension, inertia and gravity. J. Fluid Mech. **389**, 361–389 (1999). https://doi.org/10.1017/S0022112099005030
6. Dewynne, J.N., Ockendon, J.R., Wilmott, P.: A systematic derivation of the leading-order equations for extensional flows in slender geometries. J. Fluid Mech. **244**, 323–338 (1992). https://doi.org/10.1017/S0022112092003094
7. Dewynne, J.N., Howell, P.D., Wilmott, P.: Slender viscous fibres with inertia and gravity. Q. J. Mech. Appl. Math. **47**, 541–555 (1994). https://doi.org/10.1093/qjmam/47.4.541
8. Fitt, A.D., Furusawa, K., Monro, T.M., Please, C.P., Richardson, D.A.: The mathematical modelling of capillary drawing for holey fibre manufacture. J. Eng. Maths **43**, 201–227 (2002). https://doi.org/10.1023/A:1020328606157
9. Griffiths, I.M., Howell, P.D.: Mathematical modelling of non-axisymmetric capillary tube drawing. J. Fluid Mech. **605**, 181–206 (2008). https://doi.org/10.1017/S002211200800147X
10. Institute for Photonics and Advanced Sensing: Research themes (2017). https://www.adelaide.edu.au/ipas/research/, viewed 19 November 2017
11. Knight, J.C.: Photonic crystal fibres. Nature **424**, 847–851 (2003). https://doi.org/10.1038/nature01940
12. Luzi, G., Epple, P., Scharrer, M., Fujimoto, K., Rauh, C., Delgado, A.: Numerical solution and experimental validation of the drawing process of six-hole optical fibers including the effects of inner pressure and surface tension. J. Lightwave Technol. **30**, 1306–1311 (2012). https://doi.org/10.1109/JLT.2012.2185486

13. Matovich, M.A., Pearson, J.R.A.: Spinning a molten threadline; steady-state isothermal viscous flows. Ind. Eng. Chem. Fund. **8**, 512–520 (1969). https://doi.org/10.1021/i160031a023
14. Pearson, J.R.A., Petrie, C.J.S.: The flow of a tubular film. Part 2 Interpretation of the model and discussion of solutions. J. Fluid Mech. **42**, 609–625 (1970). https://doi.org/10.1017/S0022112070001507
15. Stokes, Y.M., Buchak, P., Crowdy, D.G., Ebendorff-Heidepriem, H.: Drawing of microstructured fibres: circular and noncircular tubes. J. Fluid Mech. **755**, 176–203 (2014). https://doi.org/10.1017/jfm.2014.408
16. Xue, S.C., Tanner, R.I., Barton, G.W., Lwin, R., Large, M.C.J., Poladian, L.: Fabrication of microstructured optical fibres - part I: problem formulation and numerical modelling of transient draw process. J. Lightwave Technol. **23**, 2245–2254 (2015). https://doi.org/10.1109/JLT.2005.850055
17. Xue, S.C., Tanner, R.I., Barton, G.W., Lwin, R., Large, M.C.J., Poladian, L.: Fabrication of microstructured optical fibres - part II: numerical modelling of steady-state draw process. J. Lightwave Technol. **23**, 2255–2266 (2015). https://doi.org/10.1109/JLT.2005.850058
18. Yarin, A.L.: Surface-tension-driven flows at low Reynolds number arising in optoelectronic technology. J. Fluid Mech. **286**, 173–200 (1995). https://doi.org/10.1017/S0022112095000693

Chapter 2
A Numerical Study on Free Hovering Fruit-Fly with Flexible Wings

Y. Yao, K. S. Yeo and T. T. Nguyen

Abstract Insect flyers have drawn the attention of many biologists, mechanists and engineers due to their unparalleled manoeuvrability. In this article, we introduce a comprehensive FSI model to investigate a model fruit-fly with flexible wings. We then apply the model in the numerical study of the interaction between aerodynamic and structural processes in free hovering flight. The model fruit-fly is allowed to fly with six-degrees of freedom (6-DoF) and hovers steadily with active wing kinematic control. The present study provides a convenient approach to track the dynamic deformation of flexible wings and the instantaneous aerodynamic forces and power in free flight. The results of hovering flight simulations show that the flexibility of insect wing allows the wing to bend and passively adapt to the detaching direction of leading-edge vortices (LEVs), which helps to enhance lift force and reduce the aerodynamic power consumption in free flight.

Keywords Insect flight · Flexible wing · Free flight · Computational fluid dynamics · Fluid-structure interaction

2.1 Introduction

Winged insects are amazingly agile flapping wing flyers which can hover, fly upside down, and execute rapid manoeuvres [1]. The flapping wing flights are more efficient in low Reynolds number regime, which outperforms conventional fixed and rotary wing aircrafts [2]. Due to their unparalleled manoeuvrability and efficiency, winged insects have long captured the interest of zoologists and aerodynamicists. The advance of computational fluid dynamics (CFD) enabled researchers to explore the unsteady aerodynamics of flapping wings and behaviours of free insect flight via numerical approaches. The aerodynamic performance of insect flight in different scenarios has been investigated in the literature [2–4]. Moreover, there have been also

Y. Yao (✉) · K. S. Yeo · T. T. Nguyen
National University of Singapore, 9 Engineering Drive 1, Singapore 117575, Singapore
e-mail: yaoyang@u.nus.edu

S. Gutschmidt et al. (eds.), *IUTAM Symposium on Recent Advances in Moving Boundary Problems in Mechanics*, IUTAM Bookseries 34,
https://doi.org/10.1007/978-3-030-13720-5_2

several attempts to model natural flexible insect wings via fluid-structural interaction (FSI) analysis [5, 6]. The recent work of Nguyen et al. [6] enabled the modelling of flexible wings with large deformation and revealed that wing flexibility plays an important role in allowing insect wings to undergo aerodynamically favourable deformation. However, few studies integrated the deformation of wing in free insect flight study. Thus, the effects of wing flexibility on natural free flight remain untouched.

In this article, we present a comprehensive FSI model for insect flight with flexible wings and set out to seek for a better understanding of the interaction between aerodynamic and structural processes in free flights. The model insect is allowed to fly with six-degrees of freedom (6-DoF) and comprises a pair of flexible wings. The present numerical method allows the interaction between meshfree node cloud surrounding moving bodies and background Cartesian grid, and will be described in Sect. 2. In Sect. 3, the flight performances of model insects with rigid and flexible wings are presented and analysed respectively. Some qualitative aspects of the fluid dynamics are discussed to provide insights in the effect of flexibility on aerodynamic loads on the flapping wings. The key conclusions arising from the present work are summarized in Sect. 4.

2.2 Methods

2.2.1 Modelling of Free Flying Insect

To correctly simulate insect motion in free flight, flow field surrounding flying insect needs to be solved to evaluate unsteady aerodynamic forces generated by flapping wings. The complex geometry and dynamics of the flyer make simulation of such flows highly challenging for conventional computational fluid dynamics (CFD) methods. In this study, we solve moving boundary problem involved in flapping wing flight with a singular value decomposition (SVD) based generalized finite difference (GFD) scheme on a hybrid coupled Cartesian-meshfree grid system. The SVD-GFD method was first proposed by Ang et al. [7], then was further extended to solve complex moving boundary problems like insect flapping flight, fish swimming, and others. The present methodology has been validated by comparing results obtained in standard cases with numerical and experimental data published in the literature.

The computational setup used for ground effect study is presented in Fig. 2.1. The flow field between the wing stroke plane and the ground was discretized by uniform Cartesian mesh (grid interval $0.025R$, and R is the wing length of the flyer) to obtain satisfactory resolution. Highly refined meshfree grid was used near the surfaces as shown in Fig. 2.1b.

The motion of the flyer is driven by the reaction force of the fluid obtained in the numerical simulation. Once the flow field is solved by the aforementioned numerical methods, aerodynamic forces can be computed to obtain the solution of the kinematic and dynamics equations in accordance with Newton's laws.

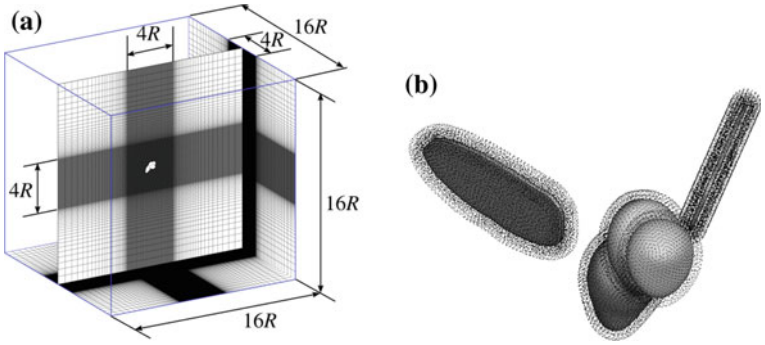

Fig. 2.1 Configuration of computational grid for free hovering fruit-fly study. **a** Background Cartesian mesh; **b** Meshfree cloud around the model insect

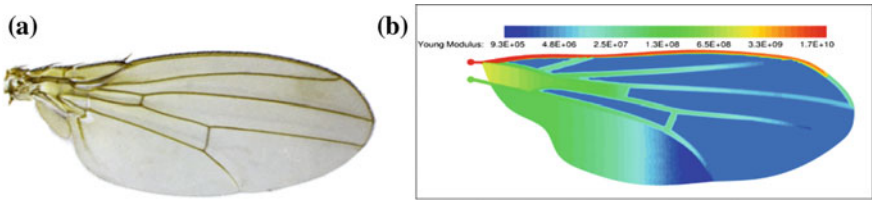

Fig. 2.2 Insect wing model adapted from Nguyen et al. [6]. **a** Natural fruit-fly wing; **b** LER wing model

2.2.2 Modelling of Flexible Wing

The non-linear dynamics of the flexible wings under coupled inertia-aerodynamic loadings is then modelled through a finite element method-based loose fluid-structural coupling process described in [6]. The open-source FEA library, Vega [8], which offers a wide choice of numerical schemes and material models, was adopted this study to solve the non-linear structural dynamic problems related to flexible wings.

The discretized second order system of differential equations that describes the motion of a deformable solid can be constructed using the principle of virtual work and finite element discretization [9]. The co-rotational linear elasticity model is chosen thanks to its relative simplicity, inexpensive computational cost and good behaviour in problems involving large deformation [8]. The implicit Newmark integrator is selected to advance the solution in time due to its reliability [10].

A leading-edge reinforced (LER) wing shown in Fig. 2.2 is adopted in this work to better represent the thin shell structures of natural flexible wings. The LER wing features a distribution of stiffening veins and connecting soft membrane that is abstracted from that of the natural wing. The construction and properties of the LER wing may be found in [6] with details.

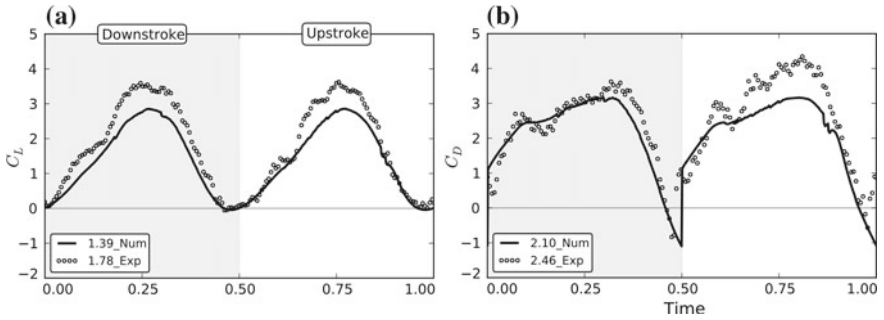

Fig. 2.3 Instantaneous lift and drag histories of a fruit-fly wing executing simple harmonic motion at Re = 200

2.2.3 Validation

We adopted the experimental results in Lua et al. [11] to validate the CFD scheme presented in this paper. In the experiments of Lua et al., the forces on the insect wings were estimated from a scaled robot wing and normalized to the insect scale. As shown in Fig. 2.3, our numerical results closely tracked the build-up and decrease of the experimental data, and correctly captured major force peaks and troughs in the whole wingbeat. This relative error between experimental and numerical results also agreed with the previous numerical studies [4, 12], and it may be caused by the oscillation/flutter of the robotic wing due to its imperfect rigidity and slips within the actuator mechanisms. The general agreement indicates that the present FSI solver can predict the force generation of insect wings with sufficient accuracy for our purpose. More comprehensive validations for the FSI solver, including analyses of non-deformable, stationary and moving objects, can be found in the authors' previous paper [6].

2.3 Results and Discussions

Many insects have been observed to hover with approximately horizontal stroke plane [13]. This flight status is named normal hovering, and has been considered as the most basic mode of flapping wing flight by researchers [4, 14]. In the present work, we implement the proposed FSI model to investigate the effects of wing flexibility on the normal hovering flight of a model fruit-fly.

The morphological model of the fruit-fly was extracted from the images photographed by Fry et al. [14] and Holtzman and Kaufman [15]. The model flyer has a wing length of $R = 2.39$ mm and a body length of $L = 2.78$ mm. The basic wing kinematics was assumed to be simple harmonic motion with an initial flapping fre-

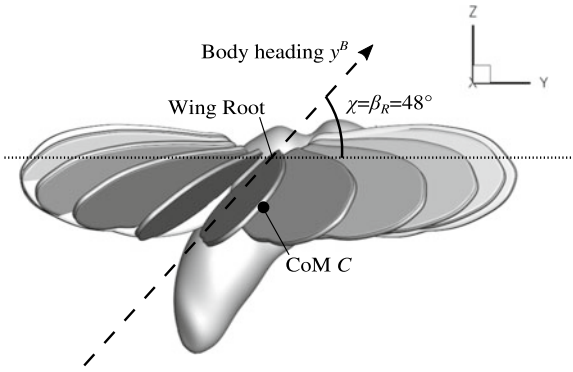

Fig. 2.4 Designated body posture in normal hovering flight

quency of $f = 260$ Hz. Then the Reynolds number of the flapping wing flight, which represent the ratio of inertial to viscous aerodynamic forces, could be determined:

$$\mathrm{Re}_{flap} = \frac{\Phi f R^2}{\nu}$$

where Φ is the stroke amplitude and ν is viscosity. A nominal Re of 148 may be worked out for Fry et al.'s sample of six free hovering fruit flies [14], which had an average wing-beat frequency f = 218 Hz (range 211–227 Hz).

The flyer was controlled to maintain a designated posture shown in Fig. 2.4. In normal hovering flight, the mean body angle $\bar{\chi}$ was set to 48°, while the stroke-plane was set to be horizontal at the non-dimensional time $t^* = 0$. In the simulations, the model flyer is regulated by a stroke-plane based kinematic control algorithm to maintain long-term steady hovering status. The basic wing kinematics was assumed to be simple harmonic motion with an initial flapping frequency of 260 Hz. The stroke-plane was adjusted forward or backward within a set range of $\beta_R = \beta_{R,0} \pm 6°$, where β_R is the angle between stroke-plane and body heading, to keep the flyer stay at the designated position. A small stroke bias was then set and adjusted actively in the flight to keep the net pitch moment in balance.

2.3.1 Flight Performance

Figures 2.5 and 2.6 show the details of the flyer's motion in normal hovering over a period of 100 wingbeats with rigid and flexible wings respectively. The body displacement was normalized by the wing length R. The time histories of body displacement and rotation presented in Figs. 2.5 and 2.6 indicate that the lateral motion (yawing, rolling and lateral displacement (x-direction)) is negligible in hovering flight. There was a significant body oscillation appearing in the first ten wingbeats of the hovering flight ($t^* < 10$). The flyer then gradually stabilized to steady cyclical motion in the

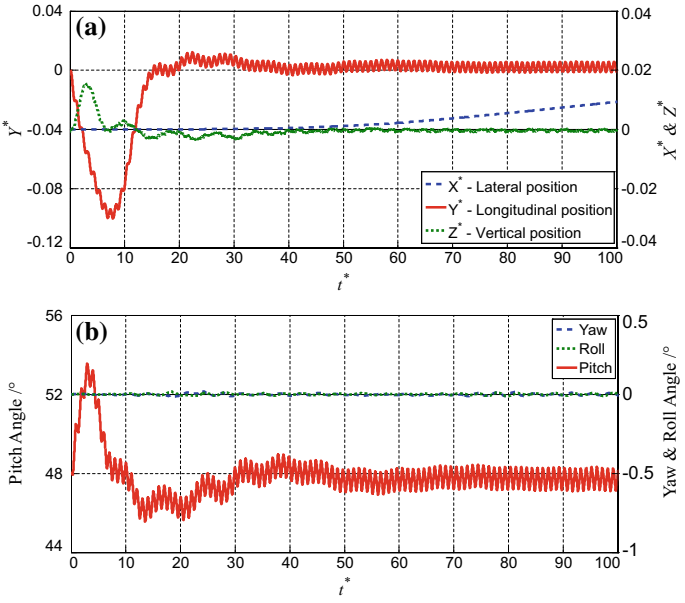

Fig. 2.5 Time histories of motion and kinematic parameters in normal hovering flight with rigid wings. **a** Displacement of centre of mass; **b** Yaw, roll and pitch angles of the flyer

course of simulation. The rigid wing flyer deviated about 0.1R backward, 0.015R upward from the designated hovering position in the early stage of flight (Fig. 2.5a), while the body pitched up about 5.5° (Fig. 2.5b). For the flexible wing flyer, the maximum deviation of the body displacement was about 0.052R backward, 0.018R upward (Fig. 2.6a), and it was about 2.7° for body pitch (Fig. 2.6b).

The large body oscillation at the beginning of flight is due to the unbalanced forces and moments produced in the first wingbeat as the flyer accelerate its flapping wings from rest. The decreased deviation in the flexible wing flight indicates the deformation of the LER wings would reduce the unbalanced pitch moment and longitudinal force in the 1st wingbeat compared with the rigid wing. The smaller pitch angle further alleviated the burden of the horizontal motion control. This alleviated initial body oscillation leads to a 20% cut-down of the settling time in the flight with flexible LER wings (see Table 2.1).

Moreover, comparing the results shown in Table 2.1, it is noted that the steady-state body fluctuations associated with wing flapping slightly decreased on the flight with flexible wings. The 10-wingbeat mean flapping frequency also reduced in the flexible wing case. We further computed the peak and 10-wingbeat mean power consumption in steady hovering flight. The results provided in Table 2.1 agree well with experimental data in [14]. The different power consumptions indicate that the flexible wing flight is more efficient than the rigid wing one. The mean power consumption of the flexible wing flight was about 20% less than that of the rigid wing flight. The

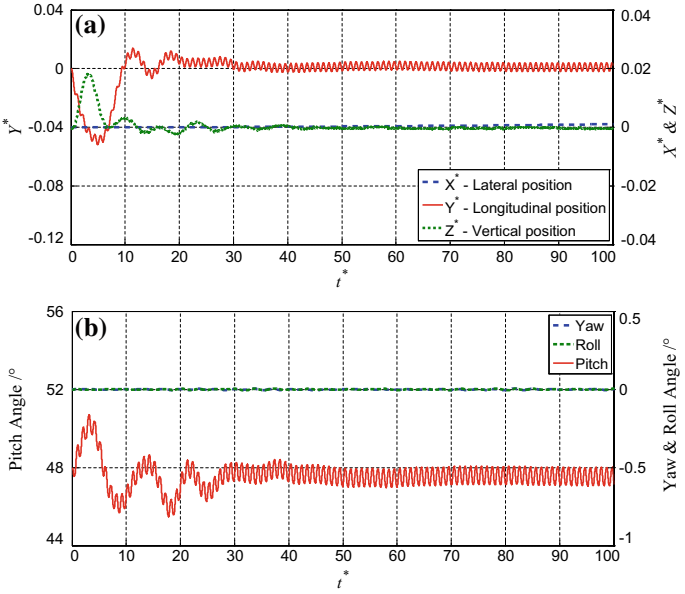

Fig. 2.6 Time histories of motion and kinematic parameters in normal hovering flight with flexible wings (LER wings). **a** Displacement of centre of mass; **b** Yaw, roll and pitch angles of the flyer

Table 2.1 Flight performance of model flyer over 10 wingbeats in quasi-steady flight

	Rigid wing	LER wing
Horizontal deviation $Y^* - \bar{Y}_D^* \big/ 10^{-3}$	(−1.44, +5.88)	(−3.78, +2.44)
Vertical deviation $Z^* - \bar{Z}_D^* \big/ 10^{-3}$	(−0.86, +0.06)	(−3.87, −0.04)
Pitch deviation $\chi^* - \bar{\chi}_D^* \big/ ^\circ$	(−0.80, +0.34)	(−0.93, +0.25)
Mean flapping frequency $\bar{f} \big/ \mathrm{Hz}$	262.8	258.5
Peak power $P_{peak}^* \big/ \mathrm{W\,kg^{-1}}$	272.9	202.9
Mean power $\bar{P}^* \big/ \mathrm{W\,kg^{-1}}$	136.9	110.2

present results indicate that natural flexible wings will help damp flight oscillations and reduce power consumption of the flyer for natural insect flyers.

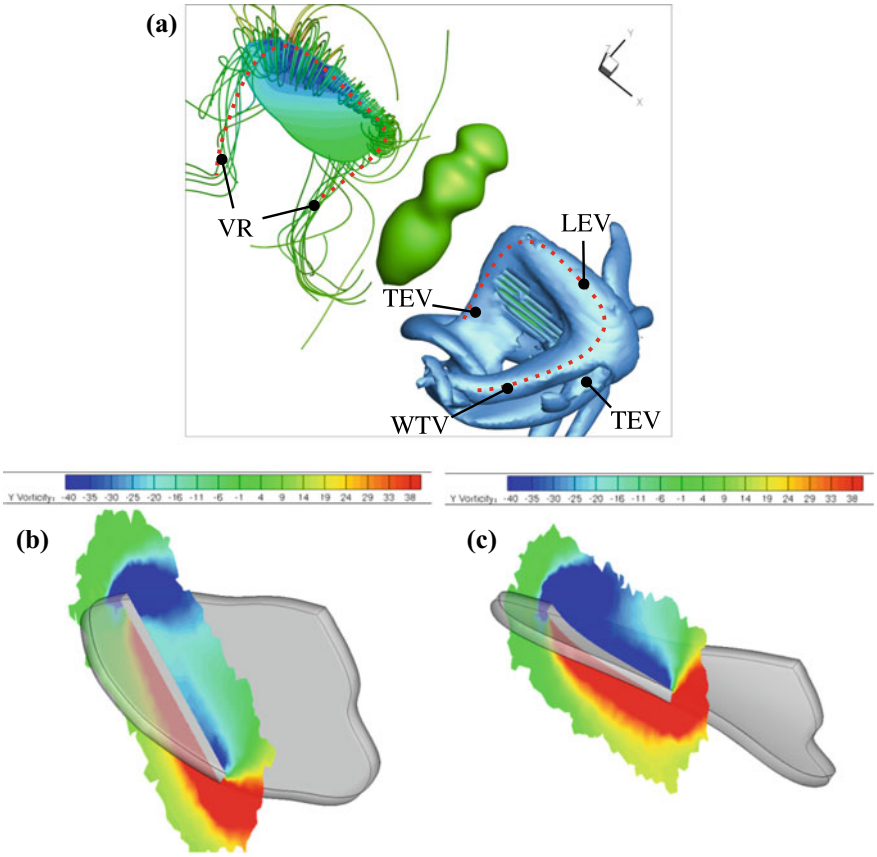

Fig. 2.7 Vortices on the flapping wing in mid down-stroke of hovering flight. **a** Near field vortex structure showing by iso-surfaces of $\lambda_2 = -80$; **b** Spanwise vorticity contours on slice at 0.8 span on rigid wing; **c** Spanwise vorticity contours on slice at 0.8 span on flexible LER wing

2.3.2 Vortex Structures

More details of the flow structures around the free flying model insect have been extracted from the CFD results. The present numerical method resolves the full details of temporal dynamics of the flow field. It provides us a convenient way to visualize and quantify the 3D vortices produced by the rigid and flexible wings. Since the evolution of the vortex wake in hovering flapping flight was well documented and discussed in previous works [4, 12, 16], this paper will focus on the flow field obtained at the mid-downstroke of a wingbeat (in quasi-steady hovering) to analyse the near-field vortex dynamics generated by both rigid and flexible wings.

In hovering flight, the wings shed a copious amount of vorticity into the surrounding air. These take the forms of a leading-edge vortex (LEV), a wing-tip vortex

(WTV) and a trailing-edge vortex (TEV)—identified by the regions on the wing where they are generated as shown Fig. 2.7a. The vortices connected with each other to form a vortex ring (VR) on the wing. The LEV was formed at the sharp leading of the wing, and engulfed the wing from wing root to tip. The WTV extended contiguously from the LEV, and detaches from the wing surface at the distal end of the wing. The WTV stretched from the beginning to the end of the stroke during flapping motion due to the continuous shedding from the LEV. The TEV grew in size and strength as the mid angle-of-attack of the wing increases. It then detached from the wing and moved downstream from the trailing edge. The shedding TEV near the wing tip, which entangled with the WTV, decayed in the course of flapping motion, whereas it forms a sheet-like vortex near the wing root stretching from the wing base to the middle of the wing plane. The bulk of vortical flow was shed into wake via the VR, especially the WTV due to centrifugal effect.

Further details of vortices near the leading edge could be found in Fig. 2.7b, c. Between the rigid and LER wings, the LEV is comparable in magnitude, but quite different in its location on the wing's upper surface. The flexibility of LER wing allow the wing to deflect upwards and the deflection delayed the separation of LEV. The deformation of LER wing clearly presents a reduced frontal area to translational drag. The closely attached LEV on the LER wing also induces lower pressure over upper wing surfaces, which enhances the suction effect and leads to lift enhancement. Similar to the results given in [6], the above flow condition persists and continues to benefit lift production beyond the mid-stroke.

The VRs, comprising the LEV, TEV and WTV, was shed into the vortex wake during wing supination at the start of each stroke. Figure 2.8 shows that stacked VRs dominated the vortex wake. The VRs formed in the previous downstroke (VR-D) and

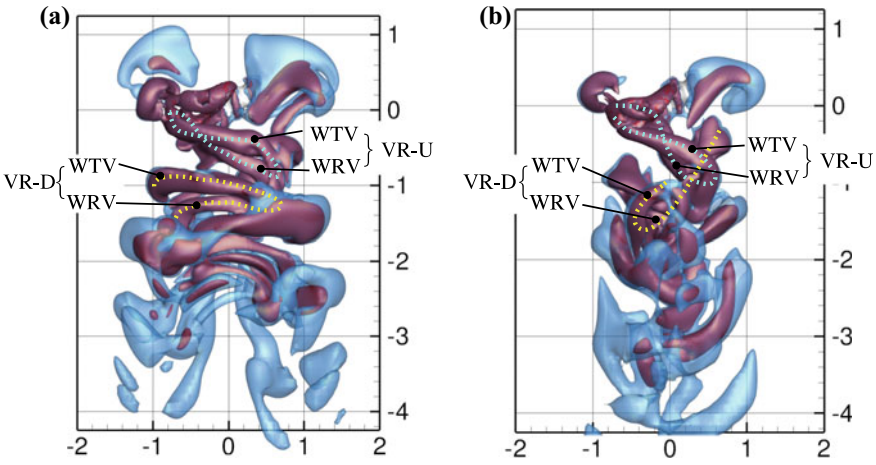

Fig. 2.8 Side views of shedding vortex wake in hovering flights showing by iso-surfaces of $\lambda_2 = -1.8$ (dark red) and $\lambda_2 = -0.18$ (light blue). **a** Flight with rigid wings; **b** Flight with flexible LER wings

upstroke (VR-U) can be identified in the vortex wake. The shedding VRs consisted two branches, a WTV and a wing root vortex (WRV). The WRV was developed from the sheet-like TEV and shed from the inner edge of the wings. Strong downwash flow jet passing through the VRs was observed in the velocity field. The significant deformation of the LER wing caused the downwash to turn more vertical (comparing Fig. 2.8a, b).

2.4 Concluding Remarks

In this paper, we implemented a comprehensive computational framework to accomplish the numerical simulation of free hovering insect flight with flexible wings. The model fruit-fly was allowed to hover with 6-DoF in the study through the regulation of the stroke-plane based kinematic controller. A quantitatively analysis of aerodynamic performance is first carried out for flights with flexible and rigid wings. The results indicate that the hovering flight with flexible wing is more efficient in terms of lift generation and power consumption. The flexibility also helps to reduce the body oscillation in steady flight. Flow visualization further demonstrates that the flexible wing can passively adapt to detaching leading edge vortex (LEV). Thus, the deformation of wing delays the detachment of LEV and contributes to high lift generation.

The present numerical study on fruit-fly model may imply that the flexibility of wing could also enhance the performance of other kinds of insects. The present results encourage us to investigate larger insects with softer wings, such as butterflies, moths and dragonflies. Moreover, the capability of the present computational framework could be extended to analyse the behaviour of insect and wing deformation in rapid and complex manoeuvring flight.

References

1. Wang, Z.J.: Dissecting insect flight. Annu. Rev. Fluid Mech. **37**(1), 183–210 (2005)
2. Wu, T.Y.: Fish swimming and bird/insect flight. Annu. Rev. Fluid Mech. **43**(1), 25–58 (2011)
3. Sun, M.: Insect flight dynamics stability and control. Rev. Mod. Phys. **86**(2), 615–646 (2014)
4. Wu, D., Yeo, K.S., Lim, T.T.: A numerical study on the free hovering flight of a model insect at low Reynolds number. Comput. Fluids **103**, 234–261 (2014)
5. Nakata, T., Liu, H.: A fluid-structure interaction model of insect flight with flexible wings. J. Comput. Phys. **231**(4), 1822–1847 (2012)
6. Nguyen, T.T., Shyam Sundar, D., Yeo, K.S., Lim, T.T.: Modeling and analysis of insect-like flexible wings at low Reynolds number. J. Fluids Struct. **62**, 294–317 (2016)
7. Ang, S.J., Yeo, K.S., Chew, C.S., Shu, C.: A singular-value decomposition (SVD)-based generalized finite difference (GFD) method for close-interaction moving boundary flow problems. Int. J. Numer. Methods Eng. **76**(12), 1892–1929 (2008)
8. Barbič, J., Sin, F.S., Schroeder, D.: Vega FEM Library. http://www.jernejbarbic.com/vega (2012)

9. Sin, F.S., Schroeder, D., Barbič, J.: Vega: non-linear FEM deformable object simulator. In: Computer Graphics Forum. Wiley Online Library (2012)
10. Wood, W.L.: Practical Time-Stepping Schemes. Oxford Applied Mathematics and Computing Science Series. Clarendon Press, Oxford (1990)
11. Lua, K.B., Lai, K.C., Lim, T.T., Yeo, K.S.: On the aerodynamic characteristics of hovering rigid and flexible hawkmoth-like wings. Exp. Fluids **49**(6), 1263–1291 (2010)
12. Liu, H.: Integrated modelling of insect flight: from morphology, kinematics to aerodynamics. J. Comput. Phys. **228**(2), 439–459 (2009)
13. Dudley, R.: The Biomechanics of Insect Flight: Form, Function, Evolution. Princeton University Press, Princeton, USA (2000)
14. Fry, S.N., Sayaman, R., Dickinson, M.H.: The aerodynamics of hovering flight in Drosophila. J. Exp. Biol. **208**, 2303–2318 (2005)
15. Holtzman S., Kaufman T.: Large-scale imaging of Drosophila melanogaster mutations. http://flybase.org/reports/FBrf0220532.html (2013)
16. Jardin, T., Farcy, A., David, L.: Three-dimensional effects in hovering flapping flight. J. Fluid Mech. **702**, 102–125 (2012)

Chapter 3
Three-Dimensional Flight Simulation with Transient Moving-Aerofoil Models

Arion Pons and Fehmi Cirak

Abstract The simulation of highly transient three-dimensional flight has relevance to several areas of current aerospace research, including the design of biomimetic micro-air vehicles. Modelling transient aerofoil motion in such systems is difficult due to the competing demands of model fidelity and computation time. In this work we present a fully three-dimensional flight simulator for biomimetic moving-wing aircraft, using a Goman-Khrabrov type model to capture transient aerodynamic effects. Parameters for this model are identified from quasistatic data and transient computational fluid dynamics, with a quantitative assessment of the model's limitations. Flight simulation results are presented for a Pugachev cobra manoeuvre, and the significance of transient aerodynamic modelling is demonstrated.

Keywords Biomimetic · Flight simulation · Aerodynamics · Goman-Khrabrov

3.1 Flight Simulator Framework

3.1.1 Biomimetic Systems

Biomimetic flapping aircraft have seen significant study over a wide range of scales: biomimetic insects [1, 2], pigeons [3], bats [4, 5], and pterosaurs [6, 7] have been considered, among many others. A key impediment to their practical implementation—particularly in high-performance applications—is the difficulty of flight modelling and analysis, arising from the complexity of flapping-wing aerodynamics. High-fidelity computational models are often required [8, 9], which limits the scope of analysis that may be carried out.

In this work we devise reduced-order models for the transient post-stall aerodynamic analysis of a flapping wing system, with a target scale of c. 1 m (e.g. larger biomimetic vertebrates), and a characteristic wing Reynolds number of c. 3×10^5.

A. Pons (✉) · F. Cirak
University of Cambridge, Cambridge CB2 1PZ, UK
e-mail: adp53@cam.ac.uk

S. Gutschmidt et al. (eds.), *IUTAM Symposium on Recent Advances in Moving Boundary Problems in Mechanics*, IUTAM Bookseries 34,
https://doi.org/10.1007/978-3-030-13720-5_3

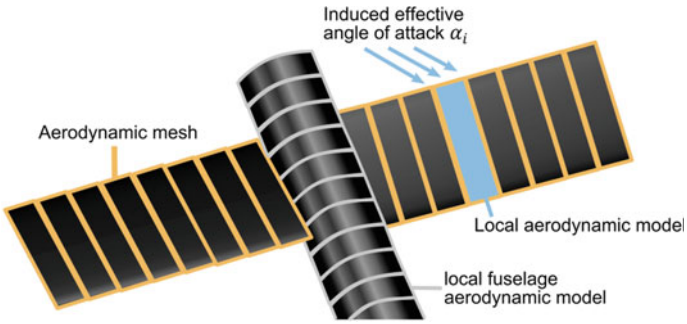

Fig. 3.1 Schematic of aerodynamic mesh framework

This is implemented in a flight simulator for a hybrid biomimetic aircraft; consisting of a conventional propulsion system (e.g. propeller) coupled with three degree-of-freedom wing rotation to enable biomimetic supermanoeuvrability—highly transient, post-stall manoeuvres. The inclusion of transient post-stall aerodynamic effects is self-evidently a key factor in accurately simulating such manoeuvres.

3.1.2 Structural Dynamics and Integration

Multibody dynamics are used to describe the structural behaviour of the modelled aircraft. All system internal degrees of freedom (e.g. wing motion) are assumed to be actuated, leading to a six degree-of-freedom system model which nevertheless includes the inertial effects of wing motion exactly. The system orientation is parameterized with an orientation quaternion, and the system model is integrated with a quaternion variational integrator, similar to that of Manchester and Peck [10].

3.1.3 Aerodynamic Framework

The system aerodynamics are formulated in a strip theory/blade element momentum framework. Each component of the airframe, lifting surface or otherwise, is discretized along its major axis into a series of two-dimensional section models. Local aerodynamic quantities at each section model are computed from the body kinematics (including the effect of wing motion-induced flow) and resolved into polar coordinates, leading to local values of the effective angle of attack α_i, its rate $\dot{\alpha}_i$, and the airspeed U. Figure 3.1 shows a schematic of this discretization process.

This framework neglects the effects of spanwise flow and of flow shadowing or other interactions within the airframe. While the aerodynamic mesh framework does

not preclude the modelling of spanwise flow or inter-section coupling effects, no models to this end have yet been suggested in the literature.

The aerofoil considered in this paper is the wing aerofoil (ST50W) from the ShowTime 50, an existing highly-manoeuvrable remote-control aircraft. This aerofoil is used for the wings of the case study biomimetic system. Quasistatic data for this aerofoil is available from Selig [11]. The stabilisers use other aerofoils, which contain control surfaces. The modelling approach for these aerofoils is not covered in this paper.

3.2 Goman-Khrabrov (GK) Modelling

3.2.1 Transient Aerodynamic Models

In situations where computational models of transient aerodynamic effects are unfeasible, some form of lower-order dynamic stall and lift hysteresis model is required. Phenomenological models of this form include the ONERA [12] and Goman-Khrabrov (GK) [13] models, among others [14]. Model reduction techniques are also available [15–17], though these still require higher-fidelity data to work on. At a simpler level, Theodorsen's aerodynamic theory provides a method by which the dynamic effects of low-amplitude pitching and dihedral motion may be modelled [18, 19]; though the method does not extend to large amplitudes [20]. Wagner's indicial response function [20] and the finite-state theory of Peters et al. [21] perform similar roles. Few of these methods, however, have been applied to morphing-wing systems.

In this work we apply a GK model to our biomimetic system. The application of such a model to fully three-dimensional flight simulation requires some significant extensions and generalisations. Here the phenomenological nature of this model is a significant advantage, as physical reasoning can be utilised to diagnose the causes of model breakdown, and to guide the model identification process.

3.2.2 GK Model Formulation

The Goman-Khrabrov dynamic stall model may be expressed as follows. For any section model, the aerodynamic coefficients (lift, drag and moment) are decomposed into attached-flow $\left(C_{i,\mathrm{att}}\right)$ and separated-flow $\left(C_{i,\mathrm{sep}}\right)$ components, each as a function of angle of attack α. These components are then recomposed with a mixing parameter p, describing the degree of local flow separation:

$$C_i(\alpha) = pC_{i,\mathrm{att}}(\alpha) + (1-p)C_{i,\mathrm{sep}}(\alpha). \tag{3.1}$$

In a fully attached flow regime $p = 0$, and in a fully separated flow regime $p = 1$; and thus the behaviour of p only governs the system aerodynamic behaviour in the transition zone. In Goman and Khrabrov's original model [13], p was related directly to the location of the flow separation point along the airfoil chord; $p = 1$ representing separation at the leading edge and $p = 0$ at the trailing edge, i.e. not at all. However, more modern approaches [22–24] have loosened this direct relation in favour of a parameter-identification approach.

In the case of aerofoil quasistatic motion, the behaviour of p is governed solely by a quasistatic mixing function, $p = p_0(\alpha)$, representing the flow separation progression through the transition region. Note that it is possible to account for static lift hysteresis here, by defining separate p_0^+ and p_0^- functions representing quasistatic pitch-up and pitch-down motion [22]; but we do not consider this here. In the case of transient motion, p is modelled by a first-order ordinary differential equation:

$$\tau_1 \dot{p} = p_0(\alpha - \tau_2 \dot{\alpha}), \tag{3.2}$$

where $\{\tau_1, \tau_2\}$ are delay times, corresponding respectively to the system time constant (i.e. the system delay in responding to a change in state) and the separation-delaying effect of pitch rate ($\dot{\alpha}$). With an accurate identification of the delays $\{\tau_1, \tau_2\}$, quasistatic mixing function $p_0(\alpha)$ and separated and attached flow models $C_{i,\text{att}}$ and $C_{i,\text{sep}}$, accurate models of transient airfoil pitching model may be obtained [22].

3.2.3 *Identification of Quasistatic Model Parameters*

A key distinction may be made in the GK model between quasistatic and dynamic model parameters. The former, $p_0(\alpha)$, $C_{i,\text{att}}(\alpha)$ and $C_{i,\text{sep}}(\alpha)$, are features of the decomposition of aerodynamic coefficients into separated and attached components, and are thus not directly associated with any dynamic effects. They may be identified directly from quasistatic data. The attached flow regime is modelled well by linear relations, as per potential flow theory, whereas the separated flow regime is modelled well by sinusoids, as per separated-flow thin-aerofoil theory [23]. We in fact propose a split sinusoid model, as this yields a significantly better fit; particularly for the drag and moment coefficients:

$$\begin{aligned} C_{i,\text{sep}}(\alpha) &= A_i \sin(B_i|\alpha - C_i| + D_i), \\ C_{i,\text{att}}(\alpha) &= \begin{cases} E_i\alpha + F_i & -90^\circ \leq \alpha \leq 90^\circ \\ G_i(\alpha - 180^\circ) + H_i & 90^\circ < \alpha \leq 180^\circ \\ G_i(\alpha + 180^\circ) + H_i & -180^\circ \leq \alpha < -90^\circ, \end{cases} \end{aligned} \tag{3.3}$$

with coefficients $A_i - H_i$. It should be noted that, in a fully three-dimensional flight simulator, cases of lifting surface reverse flow ($\alpha \cong 180^\circ$) may occur. An identification of trailing edge $p_0(\alpha)$ and $C_{i,\text{att}}(\alpha)$ are thus also required: hence the

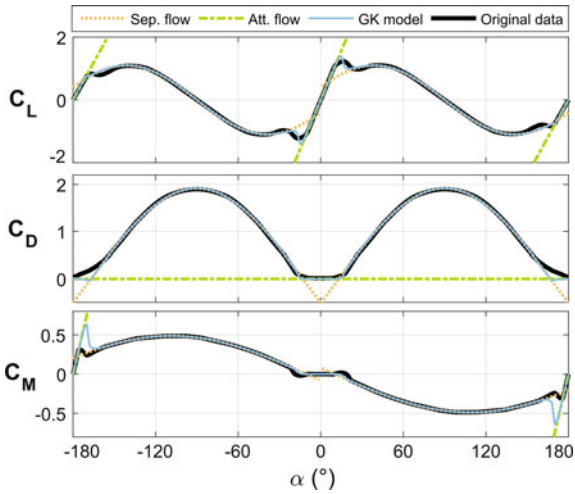

Fig. 3.2 Aerodynamic coefficients for the ST50W: attached and separated flow models, original data, and reconstructed model

formulation $C_{i,\mathrm{att}}(\alpha)$, which additionally accounts for the discontinuity (between $\pm 180°$) at this location. Phenomenologically the leading and trailing edge models are unlikely to be identical on account of the sharp tip on the trailing edge—leading to more rapid flow separation and a change in the attached flow gradients. The identification and implementation of a full leading and trailing edge GK model has not been attempted before.

A direct identification of p_0 is more difficult, and typically requires a large number of data points within the transitional flow regime (c.f. [22]). When this is not available, and particularly when considering multiple aerodynamic coefficients (lift, drag and moment) direct identification is not possible. To overcome this, Reich et al. [23] proposed a general empirical result, an inverse tangent sigmoid. Applied to the leading and trailing edge the model may be expressed:

$$p_0(\alpha) = \begin{cases} -0.0058\,\tan^{-1}(w_+|\alpha| + 16) + 0.5 & -90^\circ \le \alpha \le 90^\circ \\ -0.0058\,\tan^{-1}(w_-(|\alpha| - 180) + 16) + 0.5 & 90^\circ < |\alpha| \le 180^\circ. \end{cases} \tag{3.4}$$

As an addition, we include a width parameter $w_\pm$ ($= 1$ in Reich et al. [23]) for the purpose of modelling the aerofoil trailing edge.

The quasistatic model specification is now complete. Figure 3.2 shows the attached and separated flow models identified from the quasistatic ST50W data of Selig [11]. Figure 3.3 shows the empirical p_0 model from Reich et al. [23], compared with the results of results generated by a direct identification, which may be obtained simply by solving Eq. 3.1 for p at each quasistatic data point. The trailing edge results are presented around $\alpha = 0$ for convenience. Figure 3.2 shows additionally the GK reconstruction of the quasistatic data, computed with $p = p_0(\alpha)$ in Eq. 3.1.

As can be seen, the identification of the separated and attached flow models is very good: the split sinusoid model performs significantly better than a plain sinusoid

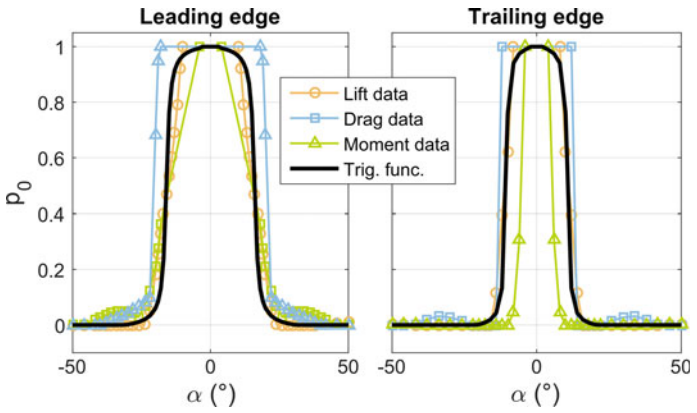

Fig. 3.3 Identified $p_0(\alpha)$ functions for the ST50W, compared with the arctangent sigmoid

would, as can be noted by the significant non-zero values of the separated flow models at $\alpha = 0$. The empirical result for p_0 also represents a good fit: for the leading edge we have $w_+ = 1$ as per Reich et al. [23]; for the trailing edge $w_- = 1.6$ to match the profile observed in the lift and drag coefficient data. There is a degree of spread in the directly identified p_0 profiles, notably in the trailing edge moment coefficient, and this leads to a degree of error in the reconstructed quasistatic profiles (again, notably in the trailing edge moment coefficient). However, attempting to extend the model to a unique $p_0(\alpha)$ function in each coefficient breaks the physical relevance of p and yields a model which ceases to have any phenomenological basis. Overall, a single $p_0(\alpha)$ is adequate. This completes the identification of the quasistatic parameters.

3.2.4 Identification of Transient Model Parameters

To identify the dynamic delay times $\{\tau_1, \tau_2\}$ we turn to computational fluid dynamics (CFD). A two-dimensional transient flow simulation of the aerofoil at Reynolds number 3×10^5 is created in OpenFoam, equipped with a moving-mesh solver to allow arbitrary specified in-plane wing motion. Figure 3.4 shows the simulation geometry, along with the standard simulation mesh and the velocity and pressure boundary conditions. Turbulence in the flow domain is modelled using the Menter shear-stress-transport model [25] with wall functions to resolve the boundary layer. The turbulent kinetic energy and specific rate of dissipation boundary conditions are all switching conditions which take a fixed freestream value on cells with flow into the domain, and constrained to zero gradient on cells with outward flow.

The flow initial conditions are supplied via a steady state solution to system at the initial aerofoil orientation, obtained via the SIMPLE algorithm [26]. The transient flow equations are solved using the PIMPLE algorithm, an OpenFoam-

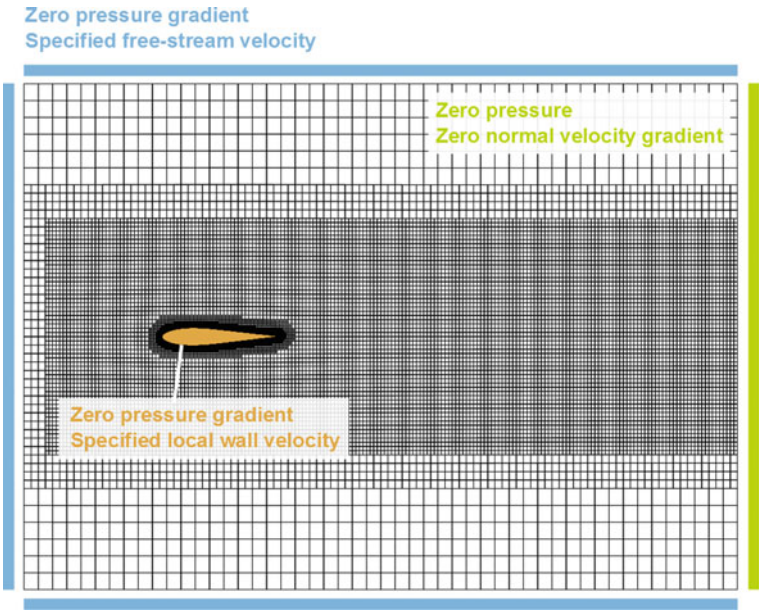

Fig. 3.4 Schematic of CFD model geometry and mesh, with boundary conditions

specific combination of the SIMPLE and PISO algorithms [27]. A mesh convergence analysis is carried out. Aerodynamic coefficient results for simulations at fixed angle-of-attack are notably larger than those reported in Selig [11], as a result of closed-jet tunnel conditions (c.f. [28]) generated by the moderately-sized domain size. However, as the identification of $\{\tau_1, \tau_2\}$ is independent of the magnitude of the aerodynamic components, this is not a fundamental difficulty: the quasistatic model parameters can be re-identified for the closed-jet tunnel results. Then, under the assumption that the closed-jet conditions do not fundamentally alter the nature or timescale of the dynamic stall event, the identified $\{\tau_1, \tau_2\}$ may be applied to the original model. While a larger domain size could remove this need for re-identification, the smaller closed-jet tunnel domain allows a larger number of simulations to be carried out for an equivalent computational effort.

Results from the simulation of sinusoidal pitching motion at several reduced frequencies are used to identify $\{\tau_1, \tau_2\}$. These reduced frequencies are defined as $k = b\omega/U$, where b is the aerofoil semichord, U the airspeed and ω the dimensional oscillatory frequency. A reasonable match for reduced frequencies below $k = 0.70$ is found to be $\tau_1 = 1b/U$, $\tau_2 = 3b/U$. Figures 3.5, 3.6 and 3.7 shows the GK model predictions compared with the CFD data for results at $k = 0.175, 0.35, 0.70$ (0.5, 1.0 and 2.0 Hz). The quasistatic coefficient curve, in the absence of GK modelling, is also noted. As can be seen, a reasonable quantitative match is obtained. The observed noise effects (e.g. Fig. 3.6) are related to the transition between attached and separated flow regimes. A notable result is that of $k = 0.70$: the CFD dynamic

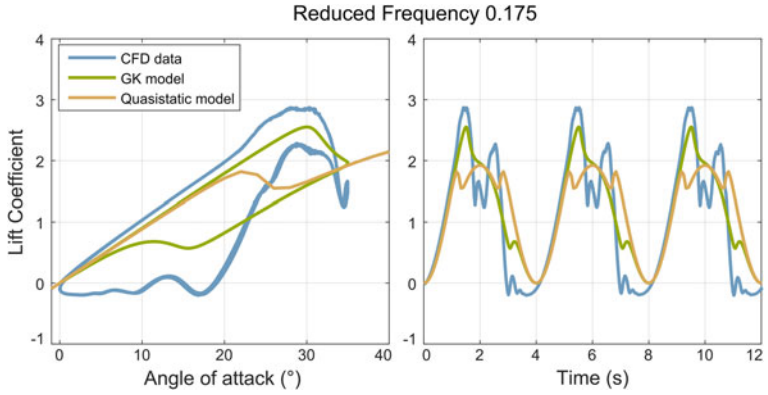

Fig. 3.5 GK model and CFD lift coefficient results for $k = 0.175$

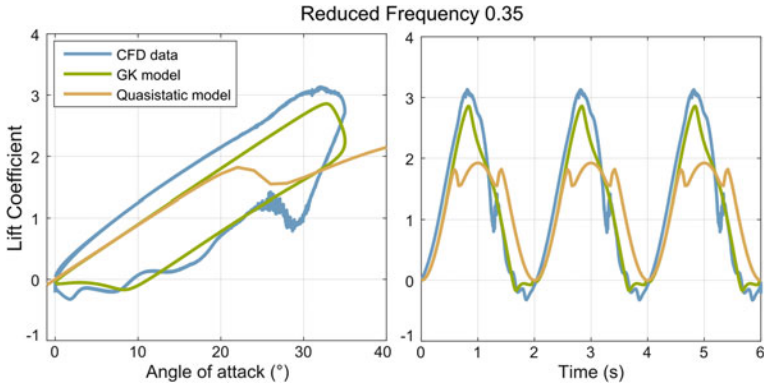

Fig. 3.6 GK model and CFD lift coefficient results for $k = 0.35$

stall loop in angle-of-attack space is of similar size and shape, but at significantly higher coefficient values. This difference is attributable to added mass effects, and indicates the beginning of model breakdown.

3.2.5 Limitations on the Identification of Transient Parameters

Severe model breakdown is observed above $k = 1.40$ (2 Hz): Fig. 3.8 demonstrates this effect. The broad elliptical coefficient curves are characteristic of added mass effects, as in Theodorsen's aerodynamic theory [29]. However, it is not clear how such models of added mass effects can be synthesised with the GK model, especially as the former are typically expressed in the frequency domain [29]. Until such synthesis

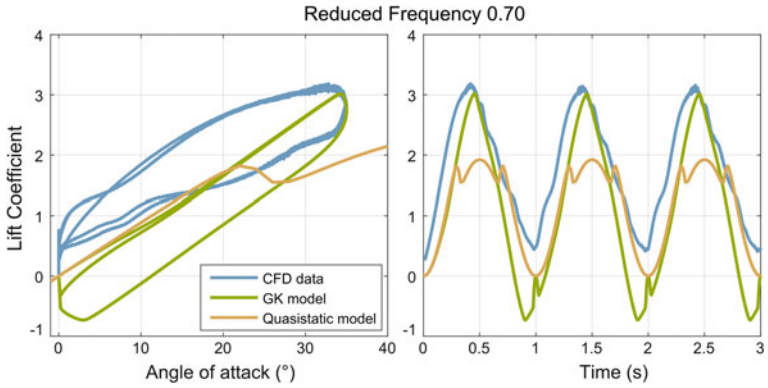

Fig. 3.7 GK model and CFD lift coefficient results for $k = 0.70$

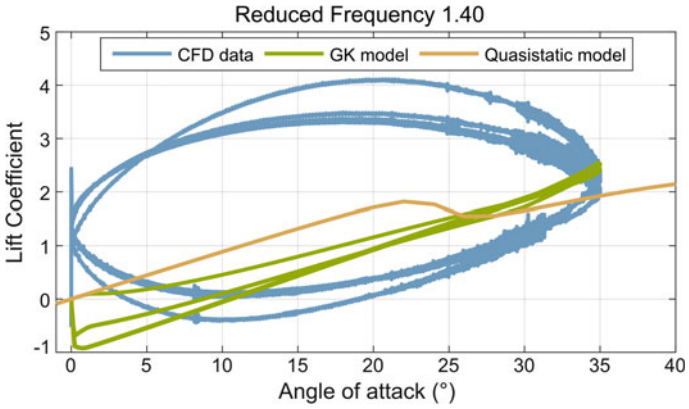

Fig. 3.8 GK model and CFD lift coefficient results for $k = 1.40$

models are developed, this aerodynamic model must be regarded as valid only up to $k = 0.70$.

3.3 Flight Simulation

3.3.1 Cobra Manoeuvre

As a test case, we simulate a Pugachev cobra manoeuvre [30] carried out by a biomimetic morphing-wing system. The manoeuvre is designed via longitudinal stability analysis: this process is not presented here. Figure 3.9 however shows the manoeuvre, simulated with GK and quasistatic aerodynamic models. As can be seen,

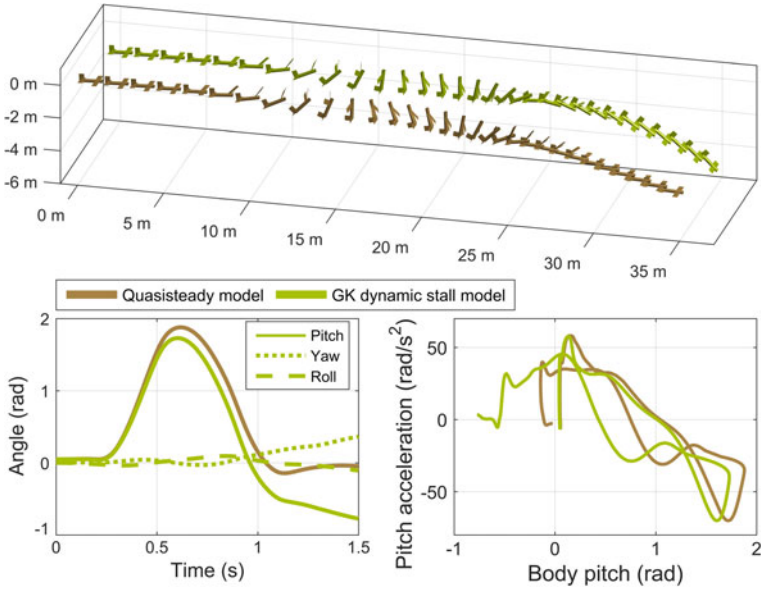

Fig. 3.9 Flight simulation results for the Pugachev cobra manoeuvre, for GK and quasistatic aerodynamic models

the implementation of GK modelling has a significant effect on the manoeuvre: delayed reattachment in the later phases of the manoeuvre leads to a much longer duration of pitch-down moment, drawing the aircraft into a dive. Changes of control design are thus required to avoid this effect—demonstrating the relevance of GK modelling to this system.

3.3.2 Spectral Analysis

To check whether the Pugachev cobra manoeuvre breaches the validity conditions of the GK model, we perform a spectral analysis of the angle-of-attack history of the GK simulation. Under the Fourier transform, $\alpha(t) = \hat{\alpha}\exp(i\omega t)$, the system spectrum in ω may be used to estimate the spectrum in reduced frequency; $k = b\omega/U$. We base this estimate on the (left) wingtip angle of attack: the location showing the greatest induced flow from wing motion. However, as U is a time-domain quantity, we compute $\max(k)$ and $\min(k)$ over the manoeuvre history based on the maximum and minimum U. Figure 3.10 shows the time-domain history of the wingtip α and its corresponding reduced-frequency spectrum, with the GK model validity boundary at $k = 0.70$ noted. As can be seen, even under the most conservative estimate, the manoeuvre contains negligible frequency components above the model validity boundary. This analysis demonstrates the validity of this Pugachev cobra

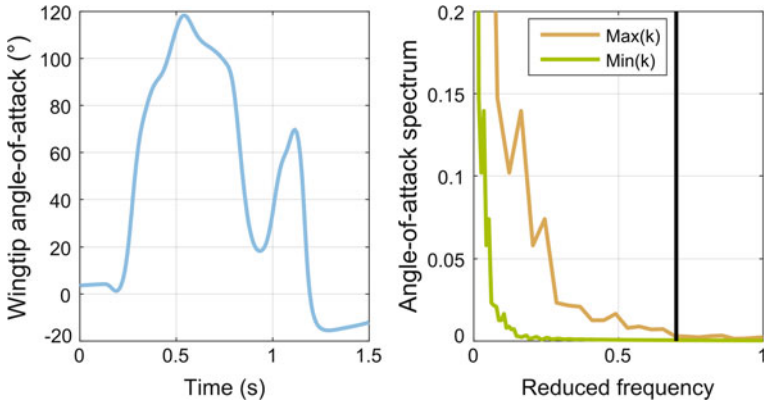

Fig. 3.10 Time-domain history and reduced frequency spectrum of the left wingtip angle-of-attack during the Pugachev cobra manoeuvre (GK model simulation)

simulation with the GK model, and provides a method of assessing the validity of these frequency-dependent aerodynamic models applied to other strongly transient flight simulations. This confirms the noted significance of the GK model to the control and guidance of this supermanoeuvre, as carried out by the biomimetic morphing-wing system considered in this work.

3.4 Conclusion

In this work we have presented a fully three-dimensional flight simulator for biomimetic moving-wing aircraft, including a Goman-Khrabrov (GK) type model to capture transient aerodynamic effects. We identify parameters for the GK model from quasistatic data and simulations of the transient aerodynamics via computational fluid dynamics, and we give a quantitative assessment of the model's limitations. Flight simulation results are presented for a Pugachev cobra manoeuvre, demonstrating both the potential of biomimetic systems for complex post-stall manoeuvring, and the significance of transient aerodynamic modelling for such manoeuvres. For future work, there is scope for the development of more accurate models based on larger computational fluid dynamic data sets, and including added mass and Reynolds number effects. There is also the potential for the design and simulation of more complex post-stall manoeuvres in biomimetic systems; and for applications in high-performance biomimetic unmanned aerial vehicles.

References

1. Graule, M.A., Chirarattananon, P., Fuller, S.B., Jafferis, N.T., Ma, K.Y., Spenko, M., Kornbluh, R., Wood, R.J.: Perching and takeoff of a robotic insect on overhangs using switchable electrostatic adhesion. Science **352**(6288), 978–982 (2016)
2. Ma, K.Y., Chirarattananon, P., Fuller, S.B., Wood, R.J.: Controlled flight of a biologically inspired, insect-scale robot. Science **340**(6132), 603–607 (2013)
3. Mahardika, N., Nguyen, Q.V., Park, H.C.: A pigeon-inspired design for a biomimetic flapping wing. In: Ghasemi-Nejhad, M.N. (ed.) Active and Passive Smart Structures and Integrated Systems 2010, SPIE, pp. 76431Q-76431Q–11. SPIE, Bellingham, WA (2010)
4. Furst, S.J., Bunget, G., Seelecke, S.: Design and fabrication of a bat-inspired flapping-flight platform using shape memory alloy muscles and joints. Smart Mater. Struct. **22**(1), 014011 (2013)
5. Recchiuto, C.T., Molfino, R., Hedenströem, A., Peremans, H., Cipolla, V., Frediani, A., Rizzo, E., Muscolo, G.G.: Bioinspired mechanisms and sensorimotor schemes for flying: a preliminary study for a robotic bat. In: Mistry, M., Leonardis, A., Witkowski, M., Melhuish, C. (eds.) Advances in Autonomous Robotics Systems, pp. 37–47. Springer, Cham, Switzerland (2014)
6. Zakaria, M.Y., Taha, H.E., Hajj, M.R.: Design optimization of flapping ornithopters: the pterosaur replica in forward flight. J. Aircr. **53**(1), 48–59 (2015)
7. Roberts, B., Lind, R., Chatterjee, S.: Flight dynamics of a pterosaur-inspired aircraft utilizing a variable-placement vertical tail. Bioinspiration Biomim. **6**(2), 026010 (2011)
8. Culbreth, M., Allaneau, Y., Jameson, A.: High-fidelity optimization of flapping airfoils and wings. In: 29th AIAA Applied Aerodynamics Conference, AIAA, Honolulu, HI (2011)
9. Tuncer, I.H., Platzer, M.F.: Computational study of flapping airfoil aerodynamics. J. Aircr. **37**(3), 514–520 (2000)
10. Manchester, Z.R., Peck, M.A.: Quaternion variational integrators for spacecraft dynamics. J. Guid. Control Dyn. **39**(1), 69–76 (2016)
11. Selig, M.: Modeling Full-envelope aerodynamics of small UAVs in realtime. In: AIAA Atmospheric Flight Mechanics Conference, AIAA, Toronto, ON (2010)
12. McAlister, K.W., Lambert, O., Petot, D.: Application of the ONERA Model of Dynamic Stall. Technical Paper 2399, NASA, Washington, D.C. (1984)
13. Goman, M., Khrabrov, A.: State-space representation of aerodynamic characteristics of an aircraft at high angles of attack. J. Aircr. **31**(5), 1109–1115 (1994)
14. Holierhoek, J.G., de Vaal, J.B., van Zuijlen, A.H., Bijl, H.: Comparing different dynamic stall models: comparing different dynamic stall models. Wind Energy **16**(1), 139–158 (2013)
15. Brunton, S., Rowley, C.: Unsteady aerodynamic models for agile flight at low Reynolds number. In: 48th AIAA Aerospace Sciences Meeting, AIAA, Orlando, FL (2010)
16. Balajewicz, M., Nitzsche, F., Feszty, D.: Application of multi-input Volterra theory to nonlinear multi-degree-of-freedom aerodynamic systems. AIAA J. **48**(1), 56–62 (2010)
17. Wang, Q., Qian, W., He, K.: Unsteady aerodynamic modeling at high angles of attack using support vector machines. Chin. J. Aeronaut. **28**(3), 659–668 (2015)
18. Liska, S., Dowell, E.H.: Continuum aeroelastic model for a folding-wing configuration. AIAA J. **47**(10), 2350–2358 (2009)
19. Wang, I.: Aeroelastic and Flight Dynamics Analysis of Folding Wing Systems. Doctoral Dissertation, Duke University (2013)
20. Brunton, S., Rowley, C.: Modeling the unsteady aerodynamic forces on small-scale wings. In: 47th AIAA Aerospace Sciences Meeting, AIAA, Orlando, FL (2009)
21. Peters, D.A., Karunamoorthy, S., Cao, W.-M.: Finite state induced flow models. I—two-dimensional thin airfoil. J. Aircr. **32**(2), 313–322 (1995)
22. Williams, D.R., Reißner, F., Greenblatt, D., Müller-Vahl, H., Strangfeld, C.: Modeling lift hysteresis on pitching airfoils with a modified Goman-Khrabrov model. AIAA J. **55**(2), 403–409 (2017)
23. Reich, G.W., Eastep, F.E., Altman, A., Albertani, R.: Transient poststall aerodynamic modeling for extreme maneuvers in micro air vehicles. J. Aircr. **48**(2), 403–411 (2011)

24. Williams, D.R., An, X., Iliev, S., King, R., Reißner, F.: Dynamic hysteresis control of lift on a pitching wing. Exp. Fluids **56**(112) (2015)
25. Menter, F.R.: Two-equation Eddy-viscosity turbulence models for engineering applications. AIAA J. **32**(8), 1598–1605 (1994)
26. Ferziger, J.H., Perić, M.: Computational Methods for Fluid Dynamics. Springer, New York (2002)
27. Robertson, E., Choudhury, V., Bhushan, S., Walters, D.K.: Validation of OpenFOAM numerical methods and turbulence models for incompressible bluff body flows. Comput. Fluids **123**, 122–145 (2015)
28. Du, L., Berson, A., Dominy, R.G.: Aerofoil behaviour at high angles of attack and at Reynolds numbers appropriate for small wind turbines. Proc. Inst. Mech. Eng. Part C: J. Mech. Eng. Sci. **229**(11), 2007–2022 (2015)
29. Bisplinghoff, R.L., Ashley, H., Halfman, R.L.: Aeroelasticity. Addison-Wesley, Reading, MA (1957)
30. Ericsson, L.E.: Cobra maneuver unsteady aerodynamic considerations. J. Aircr. **32**(1), 214–216 (1995)

Chapter 4
Vortex Shedding and Flow-Induced Vibration of Two Cylinders in Tandem

Negar Hosseini, Martin D. Griffith and Justin S. Leontini

Abstract This paper presents a study of the interaction between a fluid flow and two cylinders in a tandem arrangement. The cylinders are identical in size and either rigidly mounted, or elastically mounted but restricted to one degree of freedom in the cross-flow direction. The Reynolds number is $Re = UD/\nu = 200$ where U is the freestream velocity, D is the cylinder diameter and ν is the kinematic viscosity. The sharp interface immersed boundary method is used to conduct two-dimensional simulations of the interaction between fluid and the two structures as a function of elasticity level quantified by the reduced velocity ($U^* = U/f_N \cdot D$) where f_N is the natural structural frequency of each cylinder *in vacuo*, and pitch p which is the streamwise distance between the centres of the two cylinders. In the first stage, aerodynamic forces, frequency spectrum and amplitude of oscillation have been measured as a function of p for rigid cylinder system. The results showed that in the rigid two-cylinder system, there are four distinct regimes. In the second stage, a similar study with varying pitch but also with varying reduced velocity, U^*, has been conducted for elastically mounted cylinders. It is found that for systems with very small p, the behaviour is highly nonlinear and the oscillation of both bodies exceeds that of a single isolated cylinder. Over a critical value of p the oscillation of the front cylinder is very similar to a single cylinder system and is therefore essentially independent of pitch. However, the rear cylinder behaviour is strongly dependent on the pitch. The rear cylinder can oscillate with an amplitude which is higher or lower than the amplitude of oscillation for a single cylinder depending on the U^* value.

Keywords Fluid-structure interactions · Vortex shedding

N. Hosseini (✉) · M. D. Griffith · J. S. Leontini
Swinburne University of Technology, John St, Hawthorn, VIC 3122, Australia
e-mail: negar.mhoseini@gmail.com

S. Gutschmidt et al. (eds.), *IUTAM Symposium on Recent Advances in Moving Boundary Problems in Mechanics*, IUTAM Bookseries 34,
https://doi.org/10.1007/978-3-030-13720-5_4

4.1 Introduction

The vortex shedding in the wake of bluff bodies can cause motion of structures in situations ranging from off-shore structures, to electricity wires, to wind turbines. This phenomenon can be destructive or useful based on the application. Interaction of fluid and a single cylinder system has been studied for many years, including rigidly mounted immovable cylinders [1], cylinders where motion is imposed externally [2] and elastically mounted cylinders free to respond to the flow [3]. If the cylinder is elastically mounted and the frequency of the Kármán vortex shedding is close to the natural frequency of the structure, a high-amplitude resonance-type of oscillation occurs. This vortex-induced vibration occurs for a range of natural frequencies of the structure [4].

Although studying the interaction of fluid and a single isolated structure is of fundamental importance, investigating this concept for multi-structure systems is highly important in a practical sense as groups of closely spaced structures are ubiquitous in both engineering and nature. The flow interference which is the effect of the presence of other bodies in the flow has a significant importance in aerodynamics and hydrodynamics. This interference can lead to phenomena such as wake-induced galloping and wake-induced vibration [5, 6].

The simplest system in which flow interference can be studied is a system of two cylinders that are rigidly mounted. The arrangement of structures is classified to three different groups including tandem, side-by-side and staggered arrangements. In tandem arrangement, the line connecting the centre of all the bodies is parallel to the free stream direction, while in the side-by-side arrangement, this line is in the cross-flow direction. The staggered arrangement can be considered as combination of these two previous arrangements as the connecting line makes an angle to the free stream direction which is not zero or 90°. Systems in these arrangements have been studied investigating the impact of cylinder spacing [7–10], showing a range of flow regimes that appear to be essentially independent of Re. Extending further are a series of studies of two elastically mounted cylinders in a tandem arrangements [11] and in a staggered arrangement [12].

Here, the flow behaviour of two cylinders in a tandem arrangement is studied primarily as a function of the distance between the cylinders, or pitch p. First, the cylinders are rigidly mounted. The results confirm the major flow regimes found in previous studies, showing four distinct regimes as a function of the pitch. Second, the cylinders are elastically mounted and the pitch p and the elasticity (quantified by the reduced velocity U^*) is varied. The most important finding is that over a critical value of p, the front cylinder behaviour is essentially the same as that of an isolated cylinder, and further increases in pitch have little impact. However, the behaviour of the rear cylinder is found to be strongly dependent on the pitch p and this is quantified in terms of the cylinder oscillations amplitude.

4.2 Methodology

The sharp interface immersed boundary method has been implemented to simulate the fluid and cylindrical structures in two dimensions. The implementation used is described in detail and shown to be accurate in simulating fluid-structure interaction problems in [13] and the basic method closely follows that presented in [14], therefore only a brief overview is provided here. In this method the stationary and vibrating cylinders are modeled by a Lagrangian set of finite immersed elements in an underlying Cartesian grid.

The incompressible Navier–Stokes equations govern the motion of the fluid

$$\begin{gathered} \frac{\partial \mathbf{u}}{\partial \tau} = -(\mathbf{u} \cdot \nabla)\mathbf{u} - \nabla P + \frac{1}{Re}\nabla^2 \mathbf{u} + \mathbf{A}_b, \\ \nabla \cdot \mathbf{u} = 0, \end{gathered} \tag{4.1}$$

where $\tau = tU/D$ is the time non-dimensionalised by the advective time scale, $\mathbf{u}$ is the velocity field non-dimensionalised by the free-stream velocity U, P is the pressure field non-dimensionalised by ρU^2, and $\mathbf{A}_b$ is a generic acceleration term that models the presence of an immersed boundary. A second-order central finite-difference scheme is used to spatially discretise these equations. Time integration is implemented using a second-order accurate two-way time-splitting scheme which first takes a "velocity sub-step" by integrating the advection, diffusion and immersed boundary acceleration terms to an intermediate time. The pressure is then integrated in a "pressure sub-step" from this intermediate time to the end of the timestep, using a pressure field found by solving a Poisson equation that is formed by enforcing continuity at the end of the pressure sub-step.

When the bodies are elastically mounted, the equation of motion of each of the structures (Eq. 4.2) which will be coupled to Navier–Stokes equations via the immersed boundary acceleration term (Eq. 4.1) is given by

$$m\ddot{y} + ky = F(t) \tag{4.2}$$

where m, k and $F(t)$ are mass, stiffness and the time dependent force caused by fluid stresses. y, $\dot{y}$ and $\ddot{y}$ are respectively the displacement, velocity and acceleration of the cylinder. The stiffness is expressed in this study via the reduced velocity $U^* = U/(f_N \cdot D)$, where $f_N = \sqrt{k/m}/(2\pi)$ is the natural structural frequency of the cylinder structure. The acceleration term in the Navier–Stokes equations (Eq. 4.1) is affected by the body motion, and the fluid forces in Eq. (4.2) come from the fluid stresses, proving a two-way coupling between the fluid and structural equations.

At the immersed boundary, a no-slip boundary condition is applied such that

$$\mathbf{u}_i = \dot{\mathbf{X}}_\mathbf{i} \tag{4.3}$$

where the $\mathbf{u}_i$ represents the velocity component of fluid and $\dot{\mathbf{X}}_\mathbf{i}$ is the velocity of the boundary. A Neumann condition ($\partial P/\partial \mathbf{n} = 0$) where $\mathbf{n}$ is the normal vector

enforces a zero pressure gradient at the surface. The presence of the boundary is enforced by identifying ghost points—points in the Cartesian mesh which are inside the boundary but have neighbours in the fluid. A stencil is formed for these points that involves the boundary condition at the closest point on the boundary to the ghost node. This modified stencil is what provides the immersed boundary acceleration term in Eq. (4.1), and the ghost point values then make it possible to simply interpolate fluid field values such as pressure and traction to the immersed surface to calculate forces. Body motion is therefore relatively simply implemented as the only requirement is to identify the ghost points at each timestep and construct the interpolation stencil.

The outer domain boundary conditions are standard for an open flow. For the velocity, a freestream condition is applied upstream and laterally, and a Neumann condition ($\partial \mathbf{u}/\partial \mathbf{n} = 0$) is applied at the outflow. For the pressure, a Neumann condition ($\partial P/\partial \mathbf{n} = 0$) is applied at the upstream and lateral boundaries, and a Dirichlet condition $P = 0$ applied at the outflow.

The justification and validation of this set of boundary conditions for tandem two-cylinder system was provided in [12, 13, 15].

The initial condition for all the simulations is assumed to start from rest. Since all the simulations started from rest, the presence of any hysteresis was not assessed.

The two cylinders are symmetrically spaced on sides of the origin point. A box with a regular grid spacing and dimensions of $(p+4)D \times 4D$ is placed with origin in its centre. The inlet and outlet distance from the closest sides of the box is $13D$ and $35D$ in x-direction. In y-direction $13D$ is the lateral distance and is considered from the top and bottom edges of the box. Total number of nodes is 2048 and 1024 in x-direction and y-direction, respectively. The smallest mesh size is $\Delta x = D/128$ in the box around the bodies. A schematic description of this defined mesh domain is shown in Fig. 4.1.

A mesh convergence study was investigated for the same code and similar set-up in [12]. The convergence data was reproduced and shown in Table 1 of [12].

This code has previously being compared to the published results for similar fluid-structure interaction problems from multiple different codes and has been shown faithfully to reproduce the results [12, 13].

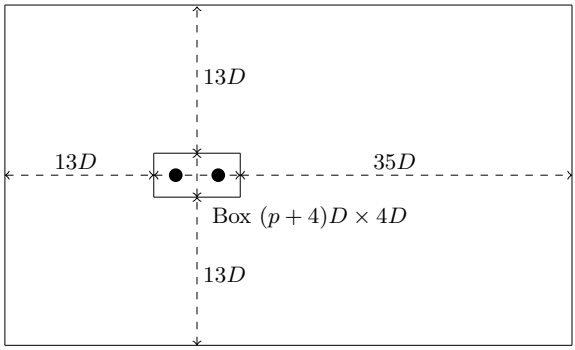

Fig. 4.1 Schematic description of the defined domain which controls the mesh resolution for the present study. The small box around the cylinders has the dimensions of $(p+4)D \times 4D$

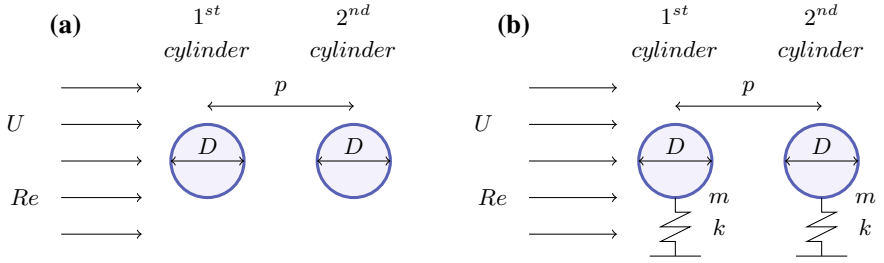

Fig. 4.2 Schematic description of the present study for **a** rigid-cylinder system and **b** elastically mounted system, where D is diameter, p is pitch, U is free stream velocity, Re is Reynolds number of free stream, k is spring stiffness and m is mass of the cylinder

4.3 Results

The base investigation starts with two rigidly mounted cylinders in a tandem arrangement as a limiting case for examining the elastically-mounted cylinders. The schematic description of the system is provided in Fig. 4.2.

4.3.1 Rigidly-Mounted Cylinders

The data for maximum lift coefficient, mean drag coefficient and frequency spectrum for the rigid two-cylinder system as a function of p are presented in Fig. 4.3.

There are four distinct regimes as a function of p. Example images of each regime showing contours of vorticity are provided in Fig. 4.4.

In the first regime which is for closely placed cylinders ($p \leq 1.8$), they behave as a single streamlined structure. The separated flow from the front cylinder reattaches to the rear cylinder and stable recirculation appears in the gap between the two rigid cylinders.

By increasing p in the range of $1.8 < p \leq 3.6$, in regime 2, the flow in the gap experiences some fluctuations. However, the separated flow from the front cylinder still reattaches to the rear cylinder, and there is no distinct vortex formation and shedding in the gap.

Further increase in p results in the commencement of regime 3. This regime is marked by the onset of full vortex formation and shedding in the gap ($3.6 < p \leq 4.6$) from the front cylinder. Effectively a single vortex occupies the entire gap between the cylinders.

With increasing p, with the formation of a second vortex in the gap, the flow conditions switch to regime 4. The frequency of vortex shedding for both of the cylinders is almost identical and converges to the single cylinder vortex shedding frequency for large values of p.

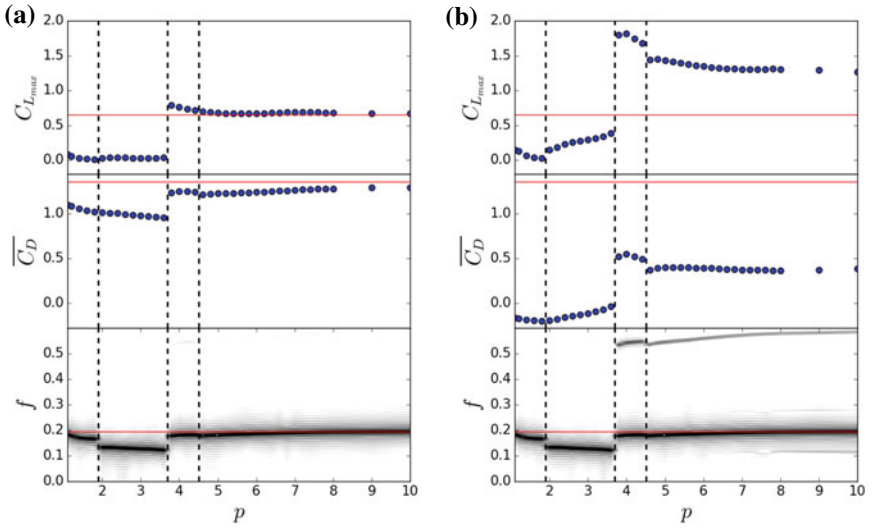

Fig. 4.3 The plots of maximum lift coefficient, mean drag coefficient and frequency spectrum for **a** first cylinder, **b** second cylinder. The horizontal red lines are representative of the corresponding parameter value for a single cylinder system. The vertical dashed lines are used to separate the regimes

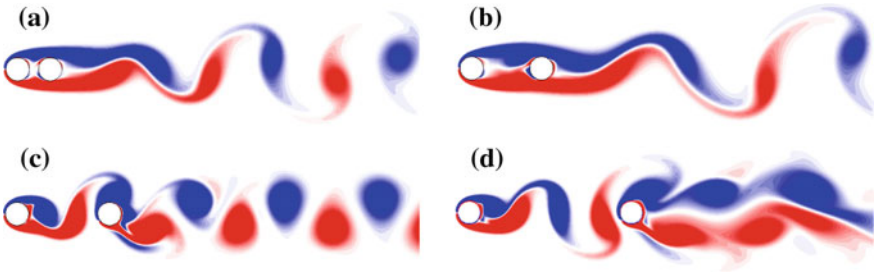

Fig. 4.4 Flow visualizations of two-rigid cylinder system with **a** $p = 1.5$ (regime 1), **b** $p = 3.0$ (regime 2), **c** $p = 4.0$ (regime 3), **d** $p = 7.0$ (regime 4). All the flow visualizations are in the same phase (maximum lift coefficient of rear cylinder). Vorticity fields are shown by red and blue colors for positive and negative signs, respectively

For a very high p, the parameters for the front cylinder converges to those of a single cylinder system. Interestingly, when the cylinders are far enough apart, even for very large values of p, the rear cylinder parameters, including $C_{L_{max}}$ and $\overline{C_D}$ converges to a different value due to the flow interference effect of the front cylinder.

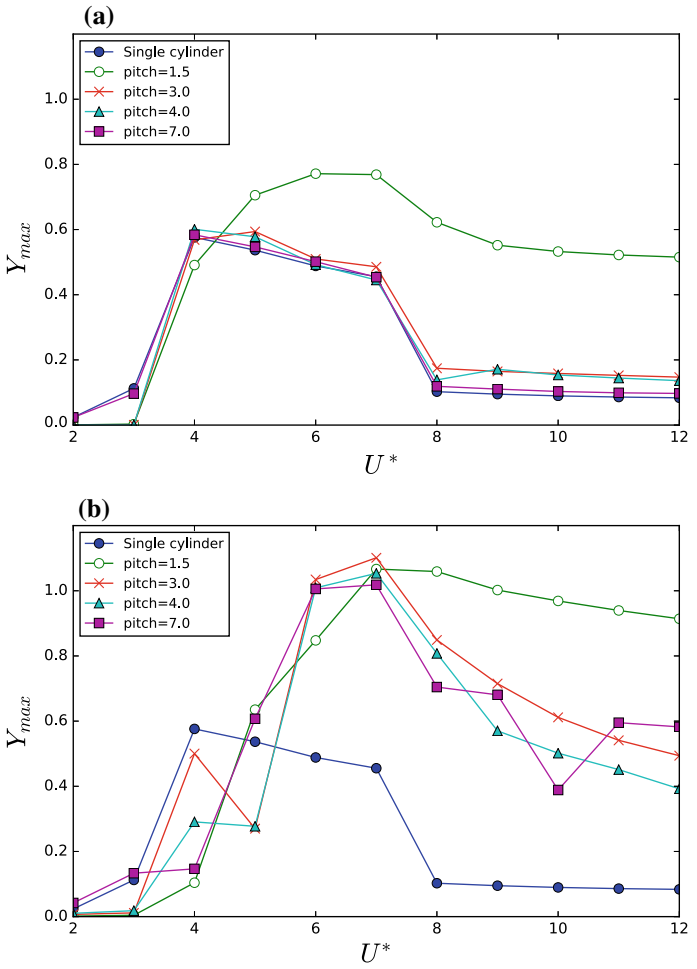

Fig. 4.5 Amplitude of oscillation for **a** front cylinder and **b** rear cylinder as a function of U^* for systems with different pitch. The lines are used to provide a better visual guide

4.3.2 Elastically-Mounted Cylinders

In the next stage, elastically-mounted cylinders with one degree of freedom oscillation in cross-flow direction have been studied.

One representative pitch from each regime of rigid cylinder system has been selected—$p = 1.5, 3, 4, 7$—and the study extended to elastically-mounted systems as a function of U^* for these pitches. The maximum cross-flow displacement for each representative pitch with different values of U^* for front and rear cylinders in comparison to the single cylinder oscillation are presented in Fig. 4.5.

As can be seen, the effect of adding an additional cylinder on the front cylinder is subtle, while the rear cylinder presents completely different behaviour. When $p = 1.5$, the behaviour of two cylinders are different from the systems with larger value of p and both of the cylinders oscillate with higher amplitude of oscillation when U^* is high enough. Once the distance between two cylinders increases, there is a loss of feedback from the rear to the front cylinder, and the amplitude of oscillation for the elastically mounted front cylinder converges to that of the single cylinder system. This critical pitch which is in the range of $1.5 < P_{cr} < 3.0$ is considerably shorter than critical value of p in the rigidly mounted two-cylinder system for the onset of vortex shedding form the front cylinder.

Figure 4.6 presents the response of the single cylinder and the front cylinder in two-cylinder system in terms of the maximum lift coefficient $C_{L_{max}}$, maximum amplitude of oscillation A_{max}, frequency of oscillation f and phase lag between the lift force and oscillation as a function of reduced velocity U^*.

As can be seen in this figure, by increasing pitch to $p > 1.5$ the oscillation and lift force properties get closer to the single cylinder properties.

The oscillation of the rear cylinder is different from the single cylinder. For low values of U^*, the front cylinder has higher amplitude of oscillation while higher U^* values, rear cylinder oscillates with higher amplitude for all the values of p that were tested.

By comparing the data for all values of pitch, the highest amplitude of oscillation of the system can be seen for the rear cylinder when $U^* = 7.0$ for all values of p.

The frequency of oscillation for the rear cylinder is shown in Fig. 4.7. The highest amplitude, when $U^* = 7.0$, is concurrent with a frequency of oscillation close to the natural frequency. This indicates the synchronization in the system. Since this is a non-linear phenomenon and resonance is a linear phenomenon, it would be an over simplification to consider this non-linear high amplitude oscillation as resonance.

The flow visualization of the elastically-mounted system for $U^* = 7.0$ for all values of p is presented in Fig. 4.8. In all the images, the rear cylinder is at its maximum displacement.

When $p = 1.5$, although the separated flow reattaches the rear cylinder in rigid cylinder, there are strong fluctuations in the gap of the elastically-mounted system, driving an oscillation of both cylinders that is much larger than that for a single isolated cylinder. A previous study [12] has shown this mode is driven by a complicated interaction where vortices are forced between the gap between the bodies, such that the negative vortex from the top of the front cylinder interacts with the positive vortex formed at the bottom of the rear cylinder. For this to occur the two cylinders need to oscillate essentially out of phase, as is evident in Fig. 4.8a.

For the larger pitches $p \geqslant 3$, the images in Figs. 4.8b–d show that the vortex formation process from the front cylinder is basically unaffected by the presence of the rear cylinder. It is also clear that there is some similarity of the vortex formation process from the rear cylinder and its interaction with the vortices impinging on the rear cylinder from the front cylinder. The wake behind the two bodies for $p = 3, 4, 7$

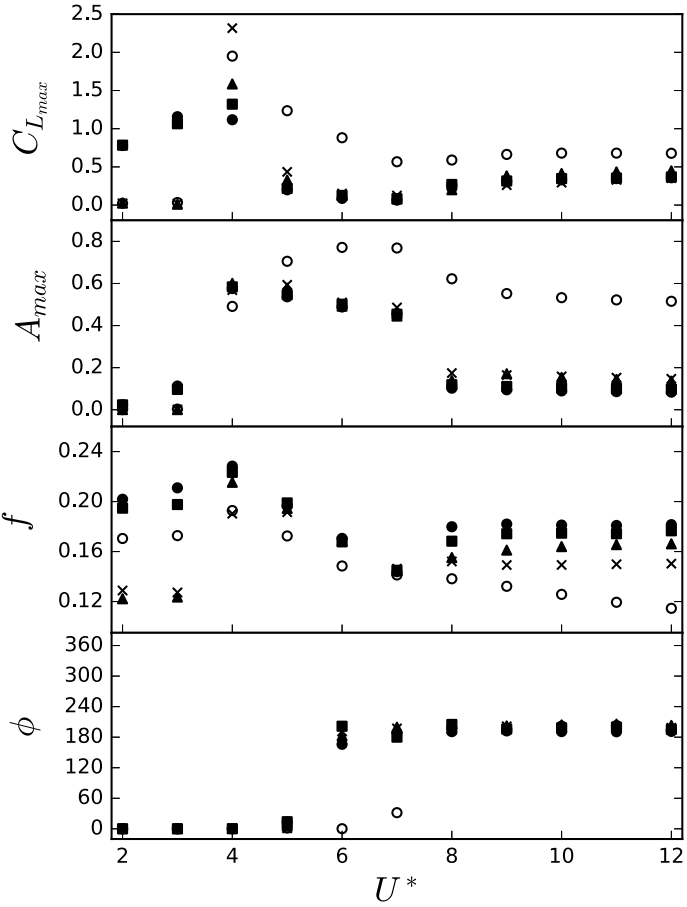

Fig. 4.6 From top to bottom, the $C_{L_{max}}$, A_{max}, frequency of oscillation and phase lag between displacement and lift force data is shown for the single cylinder and the front cylinder of two-cylinder system as a function of U^*. The corresponding data for single cylinder is shown with •, and the front cylinder data is shown with ○, ×, ▲ and ■ when p = 1.5, 3.0, 4.0 and 7.0

all display a variant of a 2P wake [2], with two pairs of oppositely signed vortices formed per cycle of oscillation. However, it appears that the phase of the oscillation between the front and rear cylinders adjusts so that the positive vortex (shown in red) formed from the front cylinder passes under the rear cylinder when the rear cylinder is at the peak of its motion.

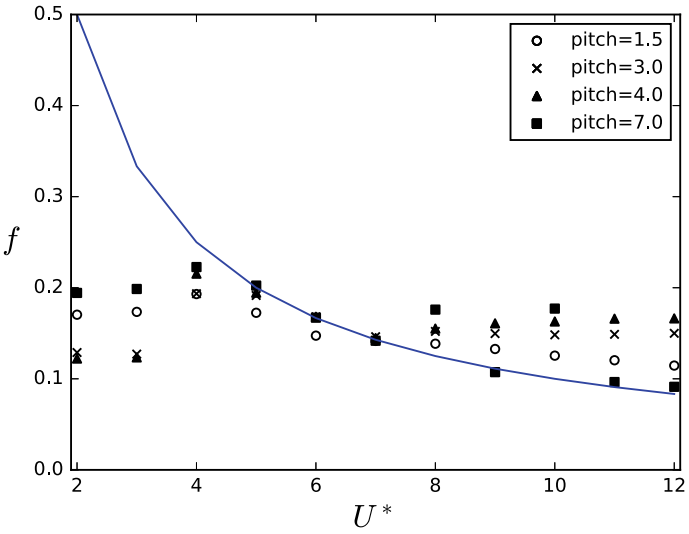

Fig. 4.7 The primary frequency of oscillation for the rear cylinder in two-cylinder system with different p. The natural frequency of oscillation is shown by the solid line

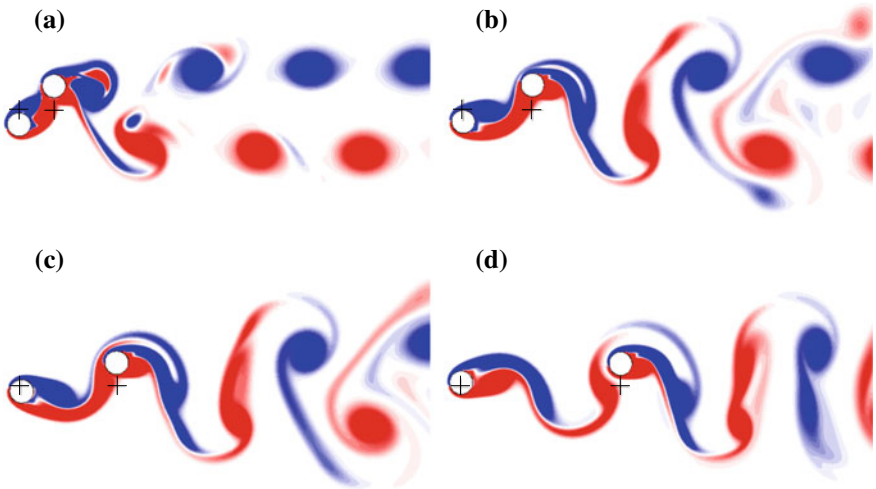

Fig. 4.8 Flow visualizations for elastically-mounted systems when the rear cylinder is in the maximum cross-flow displacement from the starting point and $U^* = 7.0$ with **a** $p = 1.5$, **b** $p = 3.0$, **c** $p = 4.0$ and **d** $p = 7.0$. Vorticity fields are shown by red and blue colors for positive and negative signs, respectively. The initial position of each cylinder is shown by +

4.4 Conclusion

The rigid cylinder system simulation results with different pitch confirm the experimental and high Re results by Zdravkovich [7]. There are four distinct regimes for aerodynamic forces and frequency spectrum of two rigid cylinders as a function of p. By increasing the p to high values, the studied parameters converge to specific values. Although these converged values are very close to single-cylinder values for the front cylinder, there is a considerable difference for the rear cylinder. This conclusion indicates the importance of studying systems with multiple structures.

In elastically-mounted cylinder systems, the cylinders are free to oscillate in the transverse direction to the free stream. It is found that the elasticity (the reduced velocity) has a significant impact on the behaviour of the flow. For two cylinders with short pitch of $p = 1.5$ (which is much less than the critical value of p for the onset of vortex shedding in the gap between cylinders in the equivalent rigid system) large amplitude oscillations and associated vortex shedding can be observed for both cylinders once U^* is large enough. For cylinders with longer pitch, the vortex shedding from, and the motion of, the front cylinder is basically independent of pitch, and the rear cylinder motion adjusts to maintain a consistent motion with respect to the arrival of a vortex shed from the front cylinder.

Acknowledgements This work has been financially supported by the Australian Research Council Discovery Projects scheme via grant DP150103177 and Swinburne University Postgraduate Research Award. The computational work has been supported by the National Computational Infrastructure Merit Allocation Scheme via grant IZ4, and the Swinburne Centre for Astrophysics and Supercomputing.

References

1. Thompson, M.C., Hourigan, K., Sheridan, J.: Three-dimensional instabilities in the wake of a circular cylinder. Exp. Therm. Fluid Sci. **12**, 190–196 (1996)
2. Williamson, C.H.K., Roshko, A.: Vortex formation in the wake of an oscillating cylinder. J. Fluids Struct. **2**, 355–381 (1988)
3. Leontini, J.S., Thompson, M.C., Hourigan, K.: The beginning of branching behaviour of vortex-induced vibration during two-dimensional flow. J. Fluids Struct. **22**, 857–864 (2006)
4. Williamson, C.H.K., Govardhan, R.: Vortex-induced vibrations. Annu. Rev. Fluid Mech. **36**, 413–455 (2004)
5. Tsui, Y.T.: On wake-induced vibration of a conductor in the wake of another via a 3-D finite element method. J. Sound Vib. **107**(1), 39–58 (1986)
6. Assi, G.R.S., Bearman, P.W., Meneghini, J.R.: On the wake-induced vibration of tandem circular cylinders: the vortex interaction excitation mechanism. J. Fluid Mech. **661**, 365–401 (2010)
7. Zdravkovich, M.M.: The effects of interference between circular cylinders in cross flow. J. Fluids Struct. **1**(2), 239–261 (1987)
8. Sumner, D., Price, S., Paidoussis, M.: Flow-pattern identification for two staggered circular cylinders in cross-flow. J. Fluid Mech. **411**, 263–303 (2000)
9. Hu, J.C., Zhou, Y.: Flow structure behind two staggered circular cylinders. Part 1. downstream evolution and classification. J. Fluid Mech. **607**, 51–80 (2008)

10. Wang, S., Tian, F., Jia, L., Lu, X., Yin, X.: Secondary vortex street in the wake of two tandem circular cylinders at low reynolds number. Phys. Rev. E **81**, 036305 (2010)
11. Borazjani, I., Sotiropoulos, F.: Vortex-induced vibrations of two cylinders in tandem arrangement in the proximity-wake interference region. J. Fluid Mech. **621**, 321–364 (2009)
12. Griffith, M.D., Lo Jacono, D., Sheridan, J., Leontini, J.S.: Flow-induced vibration of two cylinders in tandem and staggered arrangements. J. Fluid Mech. **833**, 98–130 (2017)
13. Griffith, M.D., Leontini, J.S.: Sharp interface immersed boundary methods and their application to vortex-induced vibration of a cylinder. J. Fluids Struct. **72**, 38–58 (2017)
14. Mittal, R., Dong, H., Bozkurttas, M., Najjar, F.M., Vargas, A., von Loebbecke, A.: A versatile sharp interface immersed boundary method for incompressible flows with complex boundaries. J. Comp. Phys. **227**, 4825–4852 (2008)
15. Seo, J.H., Mittal, R.: A sharp-interface immersed boundary method with improved mass conservation and reduced spurious pressure oscillations. J. Comput. Phys. **230**(19), 7347–7363 (2011)

Chapter 5
Flow-Induced Vibration and Energy Harvesting Using Fully-Passive Flapping Foils

Justin S. Leontini, Martin D. Griffith, David Lo Jacono and John Sheridan

Abstract When a fluid flows past an elastic body, the ensuing fluid-structure interaction can cause the body to vibrate as energy is transferred from the fluid to the elastic structure. This transfer is via work, and therefore this energy transfer is maximized when large oscillations of the structure occur with fluid forces in phase with the motion. A suitable structure is a plate or foil that can oscillate across the flow in heave, as well as rotate about an axis perpendicular to the flow in pitch. Here, we model the foil as an ellipse of aspect ratio 6, and the Reynolds number is fixed at 200. We consider the efficacy of this system to extract energy from a flowing fluid. Both the pitching and heaving motion are free so the motion is fully passive, but energy is only extracted from the heaving degree of freedom. We present results showing that the energy extracted is of similar magnitude to the net power of semi-active set-ups when the cost of the activation is accounted for. We also show that at this relatively low Reynolds number, the flow undergoes a spontaneous symmetry breaking, and the oscillating foil generates a mean lift force while still extracting energy. The optimal case for energy extraction is also compared to that from Veilleux and Dumas (J. Fluids Struct. 70:102–130, 2017) at a much higher Reynolds number and using a NACA0015 aerofoil. Interestingly it is found that the optimal heave parameters are reasonably similar, indicating that Reynolds number and the details of the body shape only play a minor role in the energy harvesting dynamics.

Keywords Fluid-structure interaction · Energy harvesting

J. S. Leontini (✉) · M. D. Griffith
Swinburne University of Technology, Hawthorn, VIC 3122, Australia
e-mail: justin.leontini@gmail.com

D. L. Jacono
Institut de Mecanique des Fluides de Toulouse (IMFT), Université de Toulouse, CNRS, 31400 Toulouse, France

J. Sheridan
Monash University, Clayton, VIC 3800, Australia

S. Gutschmidt et al. (eds.), *IUTAM Symposium on Recent Advances in Moving Boundary Problems in Mechanics*, IUTAM Bookseries 34,
https://doi.org/10.1007/978-3-030-13720-5_5

5.1 Introduction

Extracting usable energy from a flowing fluid occurs via the fluid doing work on a structure. In the classic case of a turbine, the flow impinging on the turbine blades imparts a stress and therefore force, resulting in subsequent rotation of the turbine and therefore a transfer of energy from the fluid to the structure. The same process can be used to exploit fluid-structure interaction phenomena. The main difference between the utilization of these phenomena compared to regular turbines is that fluid-structure interactions are usually inherently dynamic. The features associated with this dynamism, such as large and strong vortices, can be used to generate relatively large forces and therefore extract energy from the flow in situations where traditional turbines are not suitable. Such situations are in unpredictable flows, flows that are restricted such as in a shallow yet wide channel, or simply at small scale as the friction losses associated with rotary turbines see their efficiencies decrease markedly [11]. Notable examples of fluid-structure interactions being used for energy harvesting include vortex-induced vibrations of cylindrical structures [2, 3, 10], various configurations of small, bending piezoelectric elements (see [6, 7] and the review of energy harvesting from [1]), and flapping or oscillating foils (see the review of [13]).

Out of many potential designs, a simple plate or aerofoil exposed to the flow and allowed to flap with some mechanism to extract energy (effectively dissipating it and therefore acting as a damping) has been shown to be very effective. A recent study [12] performed an in-depth optimization of such a device using a NACA0015 aerofoil at the reasonably high Reynolds number of $Re = 500000$, varying all of the structural parameters.

Here, we also investigate a "flapping foil" set-up, where the foil is free to rotate or pitch around some axis, and to oscillate across the flow and perpendicular to this pitching axis. However, the foil is modelled as a simple elliptical cross section, the Reynolds number is lower at 200 (suitable for centimetre-scale devices) and we focus on the impact of extracting energy only from the heaving motion. We find the dynamics can be complicated, with oscillations occurring around a non-zero mean position, but the values for optimal energy transfer are still similar to those found in [12].

5.2 Methodology

Two-dimensional direct numerical simulations were conducted using a sharp-interface immersed boundary method. The method closely follows that outlined in [9], and a detailed description and validation for fluid-structure interaction problems of the implementation used here are provided in [5]. Therefore only a brief overview is provided here.

The code solves the incompressible Navier–Stokes equations for the fluid motion, which in non-dimensional form are

$$\begin{aligned} \frac{\partial \mathbf{u}}{\partial \tau} &= -\left(\mathbf{u}\cdot\nabla\right)\mathbf{u} - \nabla P + \frac{1}{Re}\nabla^2\mathbf{u} + \mathbf{A}_b \\ \nabla\cdot\mathbf{u} &= 0 \end{aligned} \tag{5.1}$$

where $\mathbf{u}$ is the velocity field normalized by the free stream velocity U, τ is time normalized by the advection time scale D/U where D is the chord length of the foil, P is pressure normalized by the free stream dynamic pressure $\rho U^2/2$ where ρ is the fluid density, $Re = UD/\nu$ is the Reynolds number where ν is the kinematic viscosity, and $\mathbf{A}_b$ is a general acceleration term that accounts for the presence of the immersed boundary.

The body motion in the fully passive case is governed by a simple harmonic oscillator equation in both the heave and pitch degrees of freedom (undamped in the pitch direction) that are coupled when the pitching axis does not coincide with the body centre of mass, such that in non-dimensional form these equations become

$$\begin{aligned} \ddot{y} + c^*\dot{y} + k^* y + x_\theta^*(\dot{\theta}^2\sin\theta - \ddot{\theta}\cos\theta) &= \frac{1}{2\pi m^* \Gamma} C_L \\ \ddot{\theta} + k_\theta^*\theta - x_\theta^*(\ddot{y}\cos\theta) &= \frac{\Gamma}{2\pi I_\theta^*} M_\theta \end{aligned} \tag{5.2}$$

where y is the transverse displacement of the foil pitching axis normalized by D, $c^* = cD/(mU)$ is the normalized heave damping coefficient where m is the mass of the foil structure, $k^* = kD^2/(mU^2)$ is the normalized heave spring stiffness, x_θ^* is the distance from the body centre of mass to the pitching axis, θ is the body angular displacement about its pitching axis, $m^* = m/(\rho V)$ is the ratio of the body mass to the mass of displaced fluid where V is the body volume, Γ is the ellipse aspect ratio, $C_L = F_L/((1/2)\rho U^2 D)$ is the lift coefficient where F_L is the force per unit spanwise length, $k_\theta^* = k_\theta D^2/(IU^2)$ is the normalized torsional spring stiffness where I is the moment of inertia about the pitching axis, $I_\theta^* = I/(\rho V D^2)$ is the normalized moment of inertia, and $M_\theta = T/((1/2)\rho U^2 D^2)$ is the normalized fluid moment on the foil where T is the torque applied per unit spanwise length.

The Navier–Stokes equations (5.1) are coupled to the body motion via the boundary acceleration term, and the body motion Eqs. (5.2) are coupled to the fluid flow field via the lift force and fluid moments which are calculated by integrating the fluid stresses on the immersed boundary. Details of the numerical discretization and solution of these equations is provided in [5].

Boundary conditions on the foil are a no-slip condition for the velocity, and a zero-normal pressure gradient. On the outer domain, for the velocity a Dirichlet condition specifying the free stream velocity is applied on the upstream and transverse boundaries, and a zero-normal gradient applied at the outflow. For the pressure, a zero-normal gradient is applied at the upstream and transverse boundaries, and a Dirichlet condition of zero pressure at the outflow.

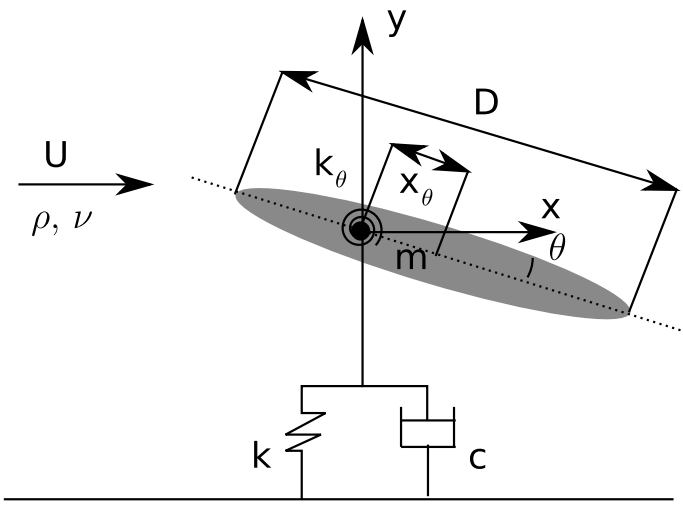

Fig. 5.1 A schematic of the problem studied. The geometric parameters x, y the Cartesian coordinates with the origin at the unperturbed position of the centre of rotation, θ is the the angle of the body with respect to its unperturbed position, D is the chord length of the body, and x_θ is the distance from the centre of rotation to the centre of mass of the body. The structural parameters are the body mass m, the linear spring stiffness k, the linear damping c, and the rotational spring stiffness k_θ. Note the linear spring and damping act through the centre of rotation and the rotational spring acts on rotation about this same point. The flow parameters are the freestream velocity U, the fluid density ρ and the fluid kinematic viscosity ν

The initial conditions for all simulations were the same, with the flow started from rest with the body in a position of zero vertical and rotational displacement.

A schematic of the basic set-up is shown in Fig. 5.1. For the simulations of this study, $Re = 200$, $m^* = 10$, the torsional spring stiffness is nominal at $k_\theta^* = 0.01$, and the normalized mass moment of inertia is $I_\theta^* = 0.1205$. The body geometry is an elliptical cross section with aspect ratio of major to minor axis length 6, and the pitching axis is located at a distance of $D/3$ from the leading edge giving a value $x_\theta^* = -1/6$. Two values of heave damping are studied, one undamped $c^* = 0$, and a second with $c^* = 0.5$, close to the optimal value found in a related study of a semi-passive foil (where the pitch was externally controlled) [4]. The heave stiffness is varied and typically presented as the reduced velocity $U^* = 2\pi/\sqrt{k^*} = U/(f_N D)$ where f_N is the natural structural frequency.

Note also that the fluid mesh, and the mesh describing the elliptical cross section were identical to those used in [4] where a detailed mesh resolution and timestep study was undertaken - these studies are directly applicable to the study here and show the independence from numerical parameters of the results acquired.

5.3 Results and Discussion

5.3.1 The Fully Passive Case—No Energy Extraction

The first case studied is that of a system that is completely undamped. In this configuration, all the terms in Eq. (5.2) are conservative, and so any energy transferred to the structure in one part of the oscillation cycle must be returned to the flow at a later time. While this configuration is of no value from an energy harvesting perspective, it does provide a limiting case and give some indication of the range of responses that may be experienced in terms of amplitudes of motion.

Figure 5.2 shows the response of the body for this case in terms of the range of displacement, and the mean displacement, for both the heaving and pitching degrees of freedom. Note the mean values were obtained by averaging over the last 100τ of the simulation (somewhere around 15–20 cycles). Therefore some small margin of error is likely still present.

The response can be split into three regimes. In the first regime for $U^* \leqslant 6$, the heave displacement shown in Fig. 5.2a shows that as the value of U^* is initially increased (or equivalently k^* is decreased) the amplitude of oscillation increases almost linearly about a zero-mean position. Figure 5.2b shows that the angular displacement also oscillates around a zero-mean position, however, the angular displacement is almost constant. This combination is what would be expected if there was effectively no coupling between the fluid flow and the body motion. The fluid forces and moments are essentially independent of U^* in the range. The constant-amplitude moment results in a constant-amplitude angular displacement, and the constant-amplitude forces result in a constant-amplitude spring force, which means a linear increase in amplitude is required as the stiffness is lowered.

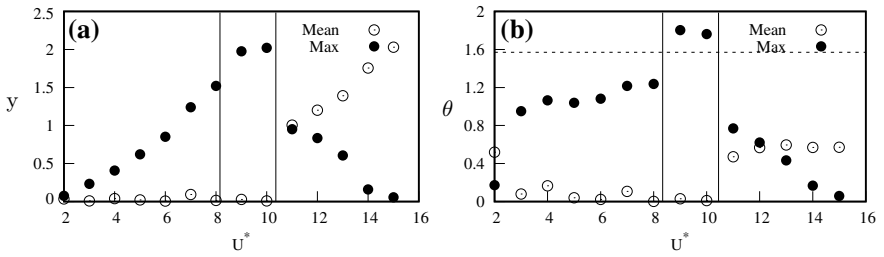

Fig. 5.2 **a** Maximum deviation of displacement from the mean displacement (•) and the mean displacement (○) and **b** maximum deviation of rotation from the mean rotation (•) and the mean rotation (○). The horizontal dashed line in **b** marks a value of $\pi/2$, or the point beyond which the foil has exceeded a vertical orientation. All are plotted as a function of reduced velocity U^* for the completely undamped case. The vertical lines delineate three flow regimes: a disordered motion regime for $U^* \leqslant 8$; a periodic, zero-mean regime for $8 < U^* < 10$; and a periodic, but non-zero mean regime for $U^* \geqslant 10$

In the second regime for $8 < U^* < 10$, the foil motion and vortex formation synchronize. The heaving motion amplitude is almost constant at a very large value of $y \simeq 2$, and the pitching motion has an amplitude of $\theta \simeq 1.8$, indicating that the foil rotates past the vertical orientation. In this regime, both the heaving and pitching motion oscillate around a zero-mean value.

Figure 5.3 shows the time histories of heave and pitch and instantaneous vorticity contours for an example case of this second regime at $U^* = 9$. The synchronization between the two degrees of freedom and the vortex production and shedding is clear. The vortex formation process is reasonably complex, producing a pair of oppositely-signed vortices per half cycle.

In the third regime for $U^* > 10$, a spontaneous symmetry breaking occurs producing a mean lift and therefore a non-zero-mean heave and pitch displacement. The mean heave displacement increases linearly with U^*, and the mean angular or pitch displacement is effectively constant. For both the heave and the pitch, the oscillatory motion about this mean position decreases with increasing U^*. Note that the flow could break symmetry to either side - the side selected by a particular simulation is a function of the small perturbations (round-off, solver tolerance, etc.) present.

Figure 5.4 shows time histories of the heave and angular displacement and instantaneous vorticity contours for an example case in this regime at $U^* = 12$. It is clear from the images that the motion of the body in both degrees of freedom and the vortex formation are synchronized and periodic, even though the flow is asymmetric. Similar symmetry breaking bifurcations have been observed in other wake flows with bodies undergoing large amplitude oscillations [8].

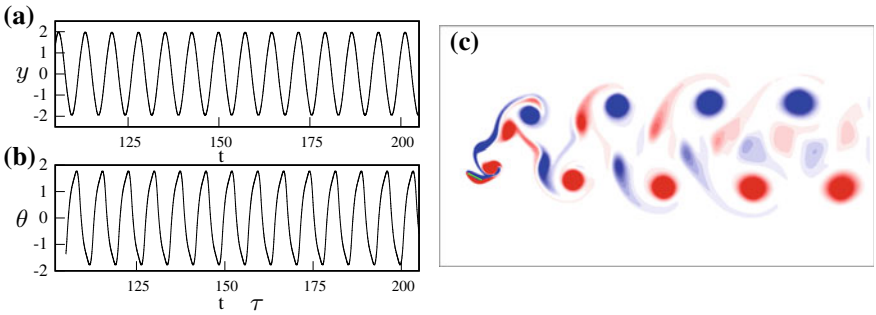

Fig. 5.3 Regime 2 for the undamped case. **a** Time history of heave displacement, **b** time history of angular displacement, and **c** instantaneous image of vorticity contours of the undamped case for $U^* = 9$. Blue/red contours mark negative/positive vorticity at levels $\omega D/U = \pm 1$

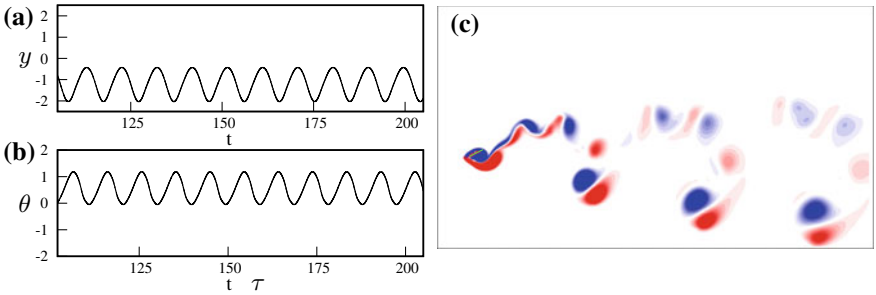

Fig. 5.4 Regime 3 for the undamped case. **a** Time history of heave displacement, **b** time history of angular displacement, and **c** instantaneous image of vorticity contours of the undamped case for $U^* = 12$. Blue/red contours mark negative/positive vorticity at levels $\omega D/U = \pm 1$

5.3.2 *The Fully Passive Case—Energy Extraction via Damping of the Heaving Motion*

The undamped motions of the previous section give some indication of the range of motions that can be expected. Interestingly, they show a wide range of large-amplitude motions that are synchronized and periodic, which could be exploited for energy harvesting. Here, we directly assess the energy that can be extracted from the flow, modelling the power take-off as a linear damping on the heave motion only. This is equivalent to equipping such a device with a linear generator. Of course, the damping applied would be a function of the electrical load on the generator. There will be an optimal value for this damping. Too little damping and close to no power is extracted; too much and the motion is completely quenched. A recent study [12] performed a thorough optimization of a fully passive NACA0015 aerofoil at $Re = 500000$, allowing all structural parameters to vary, and found a value of $c^* = 0.495$ to be optimal. Similarly, a study of a semi-passive pitching and heaving ellipse (where the pitch was externally controlled) [4] found an optimum value of $c^* = 0.503$. We therefore select a value of $c^* = 0.5$ for investigation here.

Figure 5.5 shows the heave amplitude and mean position, and the pitch amplitude and mean position for this example damped case as a function of U^*. Like the undamped case, there are three regimes, however they differ somewhat in character and are further described below.

In the first regime for $U^* \leqslant 6$, the foil again oscillates around a zero-mean position, and like the undamped case this motion is relatively disordered with no synchronization between the flow and the body motion. Similar to the undamped case, there is a linear increase in the heaving oscillatory amplitude and the pitching amplitude is almost constant, however this amplitude is less in the damped case.

In the second regime for $6 < U^* < 9$, the flow is significantly different to the second regime in the undamped case. Here, the flow synchronizes to the body motion, however the symmetry is broken from the beginning, with the body oscillating about

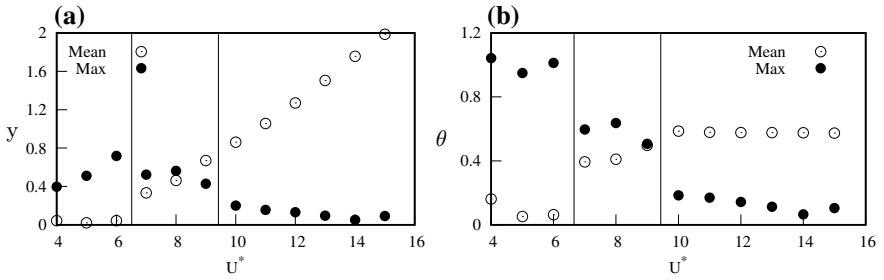

Fig. 5.5 **a** Maximum deviation of displacement from the mean displacement (•) and the mean displacement (○) and **b** maximum deviation of rotation from the mean rotation (•) and the mean rotation (○). All are plotted as a function of reduced velocity U^* for the damped case with $c^* = 0.5$. Three flow regimes are identified: a disordered motion regime for $U^* \leqslant 6$; a periodic, but non-zero-mean regime for $6 < U^* < 9$; and a periodic, but non-zero mean regime for $U^* \geqslant 9$

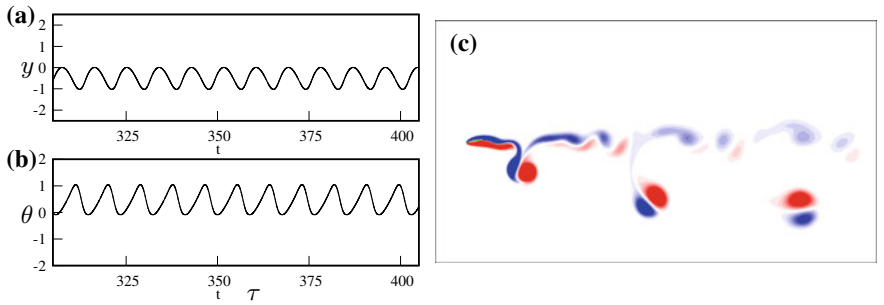

Fig. 5.6 Regime 2 for the damped case. **a** Time history of heave displacement, **b** time history of angular displacement, and **c** instantaneous image of vorticity contours of the undamped case for $U^* = 8$. This is also the optimal case for energy harvesting. Blue/red contours mark negative/positive vorticity at levels $\omega D/U = \pm 1$

a non-zero-mean position as soon as this regime begins. In this way, it is more similar to regime 3 in the undamped case.

Figure 5.6 shows the time history of the heave and pitching motion and instantaneous vorticity contours for an example case in this regime at $U^* = 8$. This case is also the optimal for energy harvesting as will be further explained below. The figure clearly shows the synchronization and periodic motion. It also shows that the asymmetry in the motion is driven by the forming of vortex dipoles in the wake that self convect to one side.

The third regime occurs for $U^* \geqslant 9$. In this regime, the oscillation of the body in both the pitch and heave directions reduces towards zero with increasing U^*, effectively presenting a static aerofoil to the flow. The aerofoil therefore experiences a constant lift force and moment. The constant moment results in a constant angular displacement, while the constant force results in a constant force from elasticity which results in a linearly increasing mean position with decreasing stiffness (or

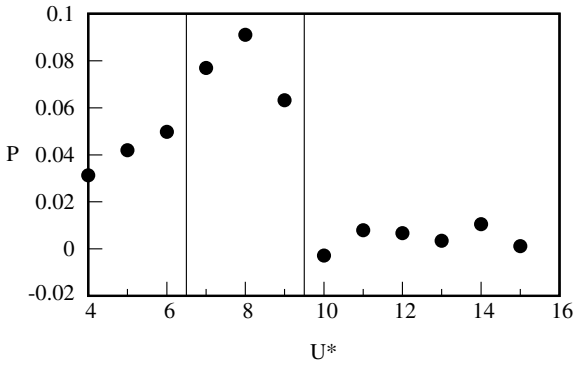

Fig. 5.7 Normalized power as a function of U^* for the damped case. Vertical lines mark the approximate boundaries of the flow regimes. The asymmetric but periodic oscillations of regime 2 of the damped case return the largest power

increasing U^*). As the oscillation in this case is small, this regime is not conducive to energy harvesting.

The average power extracted over a cycle of oscillation can be calculated by integrating the work done on the body in the heaving degree of freedom. In non-dimensional form this can be stated as

$$P = \frac{1}{T}\int_{\tau}^{\tau+T} C_L \cdot \dot{y} d\tau \tag{5.3}$$

where P is the power normalized by the energy flux through an area equivalent to the chord length D multiplied by the span and T is the normalized period of oscillation.

This power is plotted in Fig. 5.7, where the period of integration in Eq. (5.3) has been chosen to coincide with the primary frequency of oscillation. The figure shows that the largest power output is returned by damped regime 2 at a value of $U^* = 8$, which exhibits periodic and large-amplitude oscillations about a non-zero mean. Interestingly the aerofoil study of [12] returned an optimal value of $U^* \simeq 10$; a reasonably similar value considering the change of geometry and the vast difference in Re (200 here versus 500000 in [12]).

It is also clear from the figure that the amount of power returned is reasonably low. P can be thought of as a type of efficiency; it compares the power returned to the energy flux in the flow over a fixed area equal to the plan area of the foil. The optimal case at $U^* = 8$ only returns $P \simeq 0.1$. The semi-passive simulations with active pitching in [4] returned values over three times as large as this. However, it should be pointed out that a semi-active case bears an energy cost associated with controlling the motion of the pitch. The work in [4] showed that a worst-case scenario for this control was a cost of around two-thirds of the energy returned, bringing the net power out down to something similar to the fully passive case investigated here. Also, a fully passive design is somewhat simpler to implement as it requires only a single generator rather than a generator and a motor. Increasing the efficiency of this fully passive design remains a future goal.

5.4 Conclusions

This study has shown that the motion of a fully passive flapping foil can be reasonably complex, with large-amplitude oscillations possible, some around an asymmetric non-zero mean. In fact, these non-zero-mean oscillations return the largest power output when a generator is modelled as a linear damper on the heaving motion. This limited study has shown the potential of a fully passive foil, even at the low Reynolds number of 200 to extract power from a flow, and a goal of future work will be to increase the efficiency of this extraction. We have also shown that even though our geometry is different to previous studies (using an ellipse instead of an aerofoil section) and our Reynolds number is lower, the optimum values for energy extraction are reasonably similar.

References

1. Abdelkefi, A.: Aeroelastic energy harvesting: a review. Int. J. Eng. Sci. **100**, 112–135 (2016)
2. Bernitsas, M.M., Raghavan, K., Ben-Simon, Y., Garcia, E.M.H.: VIVACE (vortex induced vibration aquatic clean energy): a new concept in generation of clean and renewable energy from fluid flow. J. Offshore Mech. Arct. **130**, 041101 (2008)
3. Bernitsas, M.M., Ben-Simon, Y., Raghavan, K., Garcia, E.M.H.: The VIVACE converter: model tests and high damping and Reynolds number around 10^5. J. Offshore Mech. Arct. **131**, 011102 (2009)
4. Griffith, M.D., LoJacono, D., Sheridan, J., Leontini, J.S.: Passive heaving of elliptical cylinders with active pitching - from cylinders towards flapping foils. J. Fluids Struct. **67**, 124–141 (2016)
5. Griffith, M.D., Leontini, J.S.: Sharp interface immersed boundary methods and their application to vortex-induced vibration of a cylinder. J. Fluids Struct. **72**, 38–58 (2017)
6. Hobbs, W.B., Hu, D.L.: Tree-inspired piezoelectric energy harvesting. J. Fluids Struct. **28**, 103–114 (2012)
7. Hobeck, J.D., Inman, D.J.: Artificial piezoelectric grass for energy harvesting from turbulence-induced vibration. Smart Mater. Struct. **21**, 105024 (2012)
8. Leontini, J.S., Griffith, M.D., Lo Jacono, D., Sheridan, J.: The flow-induced vibration of an elliptical cross-section at varying angles of attack. J. Fluids Struct. **78**, 356–373 (2018)
9. Mittal, R., Dong, H., Bozkurttas, M., Najjar, F.M., Vargas, A., von Loebbekke, A.: A versatile sharp interface immersed boundary method for incompressible flows with complex boundaries. J. Comput. Phys. **227**(10), 4825–4852 (2008)
10. Raghavan, K., Bernitsas, M.M.: Experimental investigation of Reynolds number effect of vortex induced vibration of rigid circular cylinder on elastic supports. Ocean Eng. **38**, 719–731 (2011)
11. Rancourt, D., Landry, C., Fréchette, L., Mavris, D.N.: Design space exploration of centimeter-scale wind turbines using a physics-modified optimization formulation. J. Mech. **30**(5), 537–548 (2014)
12. Veilleux, J.-C., Dumas, G.: Numerical optimization of a fully-passive flapping-airfoil turbine. J. Fluids Struct. **70**, 102–130 (2017)
13. Young, J., Lai, J.C.S., Platzer, M.F.: A review of progress and challenges in flapping foil power generation. Prog. Aerosp. Sci. **67**, 2–28 (2014)

Chapter 6
Passive Cavitation Detection During Skin Sonoporation

Jeremy Robertson, Marie Squire and Sid Becker

Abstract Passive cavitation detectors (PCDs) have been effectively employed in high-intensity focused ultrasound (HIFU) and cell sonoporation studies to monitor variations in inertial cavitation activity during the course of ultrasound application. As inertial cavitation is the mechanism responsible for many ultrasound induced bioeffects, this monitoring can provide valuable information in real time about the effectiveness of the ultrasound treatment. Despite the well-established benefits of employing PCD techniques in HIFU and cell sonoporation applications, little attempt has been made to utilize such techniques in the field of low-frequency skin sonoporation. This study presents an attempt to employ a confocal PCD system to monitor inertial cavitation activity during sonoporation in a Franz diffusion cell setup. To determine whether inertial cavitation activity was effectively monitored, the output of the PCD system was compared to the cavitation enhanced transport of caffeine through porcine skin. The correlation between caffeine transport enhancement and PCD response was poor relative to similar correlations presented in the literature. This result should not be seen as an indictment on the concept as the present study was only a first attempt at employing a confocal PCD in a skin sonoporation setup. The authors intend to refine their methodology and repeat the study.

Keywords Cavitation · Sonoporation · Franz diffusion cell

6.1 Introduction

The transdermal route is advantageous for drug delivery as it avoids the first pass metabolism effects which occur with oral delivery and the pain associated with intravenous injection. However, the skin acts as a natural barrier against most topical permeants. In skin sonoporation, a transducer produces a vibrating solid-fluid interface which creates an ultrasound field. This ultrasound field is used to tem-

J. Robertson (✉) · M. Squire · S. Becker
University of Canterbury, Christchurch, New Zealand
e-mail: jeremy.robertson@pg.canterbury.ac.nz

S. Gutschmidt et al. (eds.), *IUTAM Symposium on Recent Advances in Moving Boundary Problems in Mechanics*, IUTAM Bookseries 34,
https://doi.org/10.1007/978-3-030-13720-5_6

porarily enhance the skin's permeability so that topical permeants may more easily diffuse. Five experimental parameters have been shown to influence skin permeability enhancement in skin sonoporation studies: the transducer frequency [1, 2], the ultrasound application time [3, 4], the distance from the transducer to the skin [3, 5], the chemical composition of the coupling fluid [6], and the ultrasound intensity [1, 7]. Each of these parameters can be independently controlled and maintained throughout ultrasound application and their influences on enhancement are well understood. Investigating the influences of these parameters has been, in part, motivated by the desire to optimize ultrasound enhancement [1, 3, 5]. However, such optimization cannot be achieved without first controlling the behavior of the mechanism that actually drives skin permeability increase: inertial cavitation [1, 2, 7].

Inertial cavitation activity can vary over the course of ultrasound application, even if all of the experimental parameters are held constant [8]. This is due to its dependence on coupling fluid temperature and the presence of cavitation nuclei in the coupling fluid, which can both vary during ultrasound application. In order to circumvent this variation and maintain a consistent amount of inertial cavitation activity in their high-intensity focused ultrasound (HIFU) tumor ablation setup, Hockham et al. [8] employed a novel technique. This involved a feedback loop that non-invasively monitored the inertial cavitation activity and then altered the transducer amplitude to mitigate any changes. Before attempting to apply the technique of Hockham et al. [8] to skin sonoporation, it is necessary to first address the question that motivated the present study: can the inertial cavitation activity in a skin sonoporation setup be effectively monitored during sonoporation?

A system for monitoring inertial cavitation activity has already been effectively employed in several different ultrasound biophysics studies, including that of Hockham et al. [8]. This system is known as a passive cavitation detector (PCD). A PCD involves a hydrophone that is positioned in the coupling fluid and aligned with the ultrasound transducer beam in a confocal manner. The signal from this hydrophone is filtered to isolate a band of noise independent of the harmonic and sub-harmonic peaks in the frequency spectrum. The RMS value of this broadband noise emission has been shown to be indicative of the prevalence of inertial cavitation activity in the ultrasound beam [9]. In their study of HIFU induced blood-brain barrier opening, Tung et al. [10] used a PCD to investigate the pressure threshold for inertial cavitation in a blood vessel phantom. In the planar high-frequency cell sonoporation study by Hallow et al. [9], a confocal PCD system was used to monitor variations in inertial cavitation activity during ultrasound application. In that study, broadband noise was found to correlate with cellular bioeffects over a broad range of experimental conditions which lead the authors to advocate for a feedback system similar to the one employed by Hockham et al. [8].

Despite the effective use of PCDs in other ultrasound biophysics applications, there appear to be only three published studies in the field of skin sonoporation that have attempted to include a cavitation monitoring system. Tezel, Sens et al. [2] employed PCD techniques in their skin sonoporation study. However, the PCD data was captured prior to sonoporation instead of during, and although the hydrophone was confocally aligned with the transducer, no skin was present. A similar setup

was used in the study by Tezel and Mitragotri [11]. This study also employed PCD techniques, but not during skin sonoporation. In the study by Tang, Wang et al. [7] a transducer device was epoxied to the bottom of the apparatus. This was used as a PCD device despite the fact that it was not confocally aligned with the transducer in the coupling fluid. All three of these published studies reported encouraging results from their PCD systems, however, none of these systems captured noise emission data with a confocal hydrophone during skin sonoporation. A possible explanation for the limited use of PCDs in skin sonoporation setups can be found in the established geometry and materials used for Franz diffusion cells which are an integral part of most transdermal transport experiments [1, 3, 4, 12, 13]. Due to the small diameters of the donor chambers in these cells, usually around 15 mm [2], confocal positioning of a transducer and hydrophone in the coupling fluid is impractical. In order to facilitate a confocally aligned hydrophone, necessary for the correct implementation of a PCD, a partial redesign of the Franz diffusion cell is necessary.

The purpose of this study was to assess the effectiveness with which a confocally aligned PCD was able to monitor inertial cavitation activity during skin sonoporation in a modified Franz diffusion cell. This was achieved by measuring the broadband noise emission over 10 min of ultrasound application at three different intensity levels. This noise emission was then compared with the transport of caffeine through the sonoporated skin to determine the correlation between transport enhancement and PCD response.

6.2 Materials and Methods

6.2.1 Modified Diffusion Cell

Each of the 10 identical vertical Franz diffusion cells used in this study was made up of a donor and receiver chamber. The donor chamber had an inner diameter of 61 mm, an outer diameter of 65 mm, an aperture diameter of 9 mm, and a total volume of 96 mL. The receiver chamber had a volume of 3.2 mL and an aperture diameter of 9 mm. The donor, receiver and clamp geometries are shown in Fig. 6.1.

The donor and receiver chambers were turned from solid polypropylene rods (Polystone, Dotmar EPP Pty Ltd, Christchurch, New Zealand) on a CNC lathe (Top-Turn CNC 406, Jashco Machine Manufacture Co. LTD, Taichung, Taiwan). Franz diffusion cells are usually made of glass, however, polypropylene was used in the present study due to its low cost and machinability. To form the sampling arm (Fig. 6.1), a section of carbon fiber tube (inner diameter 3.5 mm, outer diameter 6 mm) (Carbon Fiber Tube Pultruded, MAKERshop, Auckland, New Zealand) was glued to the polypropylene receiver with Loctite 401. Two pieces of carbon fiber tubing (inner diameter 2 mm, outer diameter 4 mm) were glued to the donor chamber in order to form the ports (Fig. 6.1) that enabled circulation of the coupling fluid for

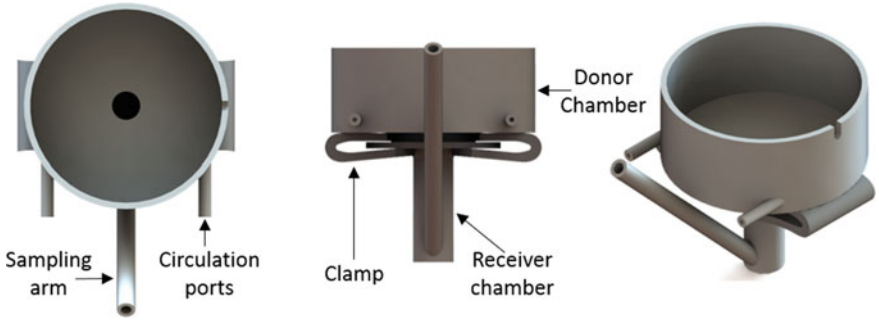

Fig. 6.1 Diffusion cell geometry (left) plan view, (middle) front view, and (right) isometric view

temperature control (described in Sect. 2.4). The donor and receiver chambers were held together by a 3D printed clamp described in [14].

6.2.2 Chemicals and Porcine Skin

Caffeine powder (ReagantPlus) was purchased from Sigma-Aldrich (St Louis, MO). Phosphate buffered saline (PBS) (pH 7.4) was purchased from Thermofisher (Waltham, MA). The caffeine solution was prepared by dissolving the caffeine powder in room temperature PBS at a concentration of 0.5% w/v (5 g/L), as in the study by Sarheed and Abdul Rasool [15].

Porcine ears were obtained from Ashburton Meat Processors Ltd (Ashburton, New Zealand) immediately after slaughter. The ears were cleaned with cold tap water. The top 1 mm of the skin was removed from each ear using a dermatome (Dermatome 50 mm, Nouvag AG, Goldach, Switzerland). The dermatomed pieces of skin were flash frozen in liquid nitrogen using the technique described by Han and Das [16] then immediately transferred to a −20 °C freezer for storage. Prior to each set of experiments, the skin was removed from the freezer and thawed in a container of deionized water at room temperature. Each piece of skin was then visually assessed for uniform thickness and integrity before being mounted in a diffusion cell.

6.2.3 Ultrasound Generation and Intensity

A low-frequency (20 kHz) ultrasound field was generated using a VC 505 ultrasound processor (Sonics and Materials Inc., Connecticut, USA). This unit was operated with a 13 mm diameter replaceable tip (Fig. 6.2). An application time of 10 min was used for all of the skin insonation experiments in this study. The transducer face was positioned 5 mm from the surface of the skin as this was the smallest distance

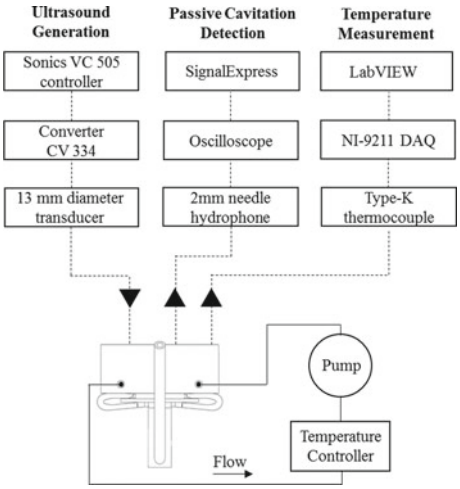

Fig. 6.2 System schematic. The solid lines represent the coupling fluid circuit. The dashed lines represent the signal inputs and outputs to and from the instruments in the coupling fluid

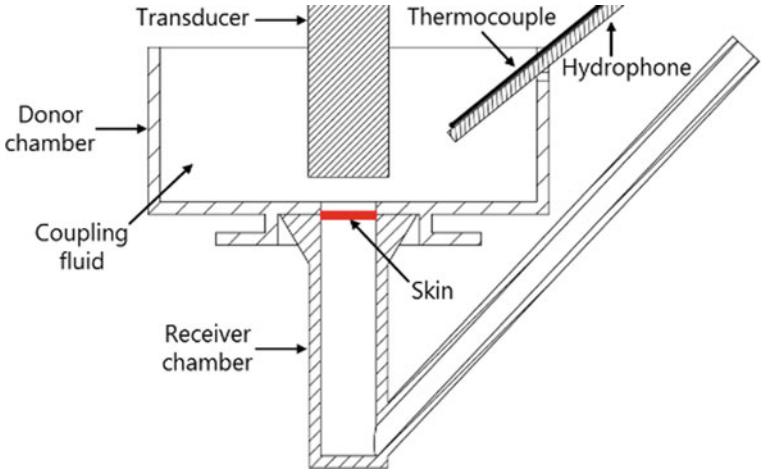

Fig. 6.3 Cross section of the diffusion cell showing the positioning of the transducer, hydrophone, and thermocouple

that allowed for a confocal hydrophone (shown in Fig. 6.3). The intensity of the ultrasound field was determined with the commonly used calorimetric method [3, 4, 13, 17–19]. This method is described in [14].

6.2.4 Temperature Measurement and Control

Continuous application of ultrasound at the intensities used in this study results in significant increases in coupling fluid temperature. A circulating method, described in [14], was used to mitigate this temperature increase during skin sonoporation. The temperature of the coupling fluid was measured with a thermocouple (Wire Type K thermocouple, Jaycar Electronics Pty Ltd, Auckland, New Zealand). The thermocouple was not positioned within the beam of the transducer, where it would have best represented the temperature of the coupling fluid near the skin surface, as this would have partially obscured the skin surface, and resulted in cavitation damage to the thermocouple tip. Instead the thermocouple was positioned outside of the transducer beam (Fig. 6.2). The difference in the temperatures recorded in these two positions was found to be less than 1.5 °C during sonoporation at 39.4 W/cm^2.

6.2.5 Passive Cavitation Detection

The PCD hydrophone was positioned in the coupling fluid so that it was confocal with the ultrasound transducer (Fig. 6.2). This needle hydrophone (2.0 mm Needle Hydrophone, Precision Acoustics Ltd, Dorchester, Dorset, UK) had a sensitivity of −236.4 dBre1 V/μPa at the transducer driving frequency. The position of the hydrophone was kept consistent over all of the experimental repetitions by using an aluminum sleeve that was fixed relative to the transducer and diffusion cell. Between experimental repetitions, the hydrophone was taken out of this sleeve so that the diffusion cell could be switched out and the next one inserted.

The method used to process the raw hydrophone data was described in [14]. Briefly, the hydrophone voltage data was filtered to isolate the broadband noise emission between 92.5 and 97.5 kHz. An RMS value of this filtered data was calculated every 1–2 s. All of the RMS values were then integrated over the 10 min of ultrasound application in order to calculate a single inertial cavitation dose value for each ultrasound application. Therefore, each inertial cavitation dose value represents the time-averaged broadband noise emission for a specific ultrasound application.

6.2.6 Chromatography

Transdermal transport of caffeine was measured with a HPLC system (Ultimate 3000, Thermo Fisher Scientific, MA, USA). The solid phase consisted of a Poroshell 120 column (EC-C18, DKSH NZ Ltd, Palmerston North, New Zealand). This column was maintained at 40 °C during operation. The mobile phase consisted of 10% acetonitrile in water. The flow rate was 0.8 mL/min. The injection volume was 1 μL.

The retention time was 3.5 min and the reproducibility relative standard deviation was 1%.

6.2.7 Transdermal Transport Experiments

Prior to the ultrasound application, a piece of skin was mounted onto each of the ten diffusion cells. The receiver fluid consisted of PBS while the donor chamber fluid was deionized water. One at a time, each diffusion cell was positioned along with the transducer, hydrophone and thermocouple. The temperature control system was then switched on to lower the coupling fluid (deionized water) to 10 °C. Continuous ultrasound was then applied for 10 min. Following sonoporation of each skin sample, fresh room temperature deionized water was added to the donor chamber to keep the skin hydrated while the other skin samples were sonoporated. After all ten of the skin samples had been individually sonoporated, the deionized water was removed from each of the donor chambers so that the caffeine solution could be applied. This solution was allowed to diffuse for a period of 20 h. During this time the donor chambers were covered with Parafilm (Bemis, WI, USA) to prevent evaporation of the fluid. This process was repeated for three different ultrasound intensities (23.8, 34.2, and 39.4 W/cm^2). In addition to these experiments, two control cases were also investigated. For the first control case, the 10 diffusion cells were set up in the same manner described above, however, no ultrasound was applied. The coupling fluid was simply maintained at 10 °C for 10 min. For the second control case, no ultrasound was applied and the coupling fluid was maintained at 25 °C for 10 min. During each of the 30 ultrasound experiments, the temperature was kept between these two control temperatures by varying the voltage input to the temperature controller.

6.2.8 Physical Dosimeter Experiments

The pitting of aluminum foil under insonation has previously been used to determine the influence of ultrasound parameters on inertial cavitation activity [4]. In the present study, aluminum foil was used as a physical dosimeter in order to demonstrate the influence of the temperature control method on the inertial cavitation activity at the skin aperture. Ten pieces of aluminum foil (Homebrand, Manukau, New Zealand) were insonated (at an intensity of 23.8 W/cm^2) for 5 s with and without coupling fluid circulation. The number of pits in each of the 20 pieces of foil were then counted in order to demonstrate the influence of circulation. In these experiments, the coupling fluid in the donor chamber was deionized water at 10 ± 2 °C.

6.3 Results and Discussion

The results presented in this study were collected in order to assess whether the inertial cavitation activity in a skin sonoporation setup can be effectively monitored during skin sonoporation. However, the present study represents the first time the temperature control system (described in Sect. 2.4) has been used during transdermal transport experiments. Therefore, it was necessary to first ensure that the coupling fluid circulation did not negatively impact the inertial cavitation activity at the skin aperture. This was achieved with physical dosimeter experiments. The mean number of pits after ultrasound application without coupling fluid circulation was 28.8. With coupling fluid circulation, the mean value was 26.3. These values (shown by the crosses in Fig. 6.4) indicate that coupling fluid circulation resulted in only a 9% decrease in inertial cavitation activity at the skin aperture ($p = 0.4$). This small decrease in inertial cavitation is acceptable.

In order to quantify the effects of ultrasound enhancement in this skin sonoporation study, it was necessary to measure the transdermal transport of caffeine through skin samples not exposed to ultrasound. Two such control cases were investigated (as described in Sect. 2.7). Following diffusion for 20 h, the mean and median receiver caffeine concentrations for the control at 10 °C were 31.6 mg/L and 27.6 mg/L respectively (Fig. 6.5). For the control at 25 °C, the mean and median receiver caffeine concentrations were 42.5 mg/L and 34.9 mg/L respectively. These values indicate that the coupling fluid temperature did have a small effect on skin permeability within this range. However, this effect is minor when compared to the effect of ultrasound exposure (Fig. 6.6).

Ultrasound was applied to skin samples at three different intensities (as described in Sect. 2.7). Application at 23.8 W/cm^2 resulted in mean and median receiver caffeine concentrations of 45.9 mg/L and 15.6 mg/L respectively (shown in Fig. 6.6). Application at 34.2 W/cm^2 resulted in mean and median receiver caffeine concentrations of 111.4 mg/L and 95.2 mg/L respectively. Application at 39.4 W/cm^2 resulted in mean and median receiver caffeine concentrations of 116.6 mg/L and 108.7 mg/L

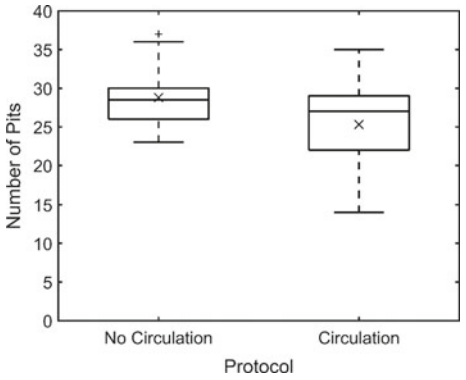

Fig. 6.4 The influence of coupling fluid circulation on the pitting of aluminum foil. The crosses within the boxes represent the mean values ($n = 10$)

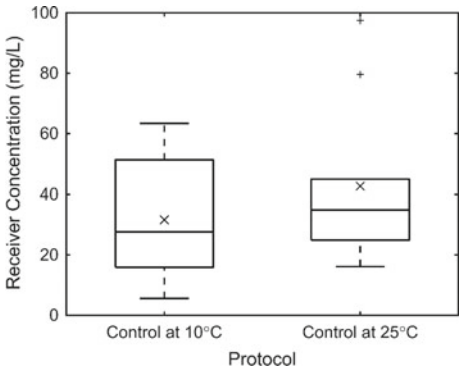

Fig. 6.5 Receiver chamber caffeine concentration after 10 min of exposure to 10 °C or 25 °C deionized water and 20 h of passive caffeine diffusion (n = 10)

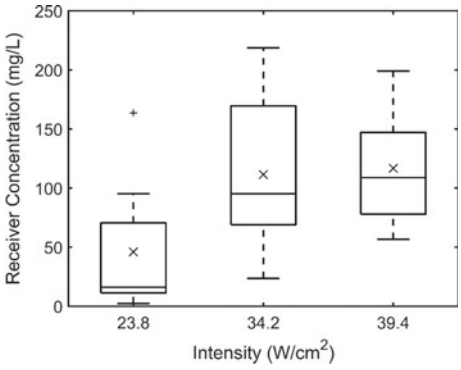

Fig. 6.6 Receiver chamber concentration after 10 min of ultrasound exposure to various intensities. The coupling fluid temperature was maintained between 10 and 20 °C (n = 10)

respectively. When these values are compared to those from the two control cases, it is apparent that no enhancement was achieved at an intensity of 23.8 W/cm^2 while ultrasound at 34.2 W/cm^2 and 39.4 W/cm^2 resulted in mean values that were, respectively, 2.6 ($p < 0.05$) and 2.7 ($p < 0.05$) times the mean of the 25 °C control case.

This greater transport at the two higher intensities can be attributed to the higher degree of inertial cavitation achieved when the intensity is increased. Therefore, if the PCD setup worked as expected, the mean inertial cavitation dose should also have increased with increasing intensity. This trend is indeed apparent when inertial cavitation dose is plotted as a function of ultrasound intensity (Fig. 6.7). However, the analysis of the correlation between transdermal transport enhancement and PCD response must go further than this simple comparison of trends. In order to assess whether the PCD effectively monitored inertial cavitation activity during skin sonoporation, a direct comparison must be made between the inertial cavitation dose and the receiver caffeine concentration for all of the data across the three intensities. This comparison is shown in Fig. 6.8.

The direct correlation between the inertial cavitation dose and receiver caffeine concentration values was poor. There is no clear separation between the intensity groups which was expected considering the clear intensity-concentration and

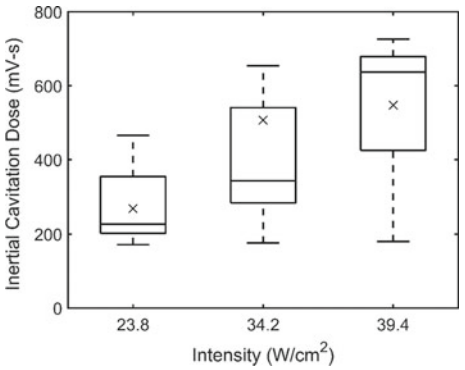

Fig. 6.7 Inertial cavitation dose as a function of ultrasound intensity (n = 9–10)

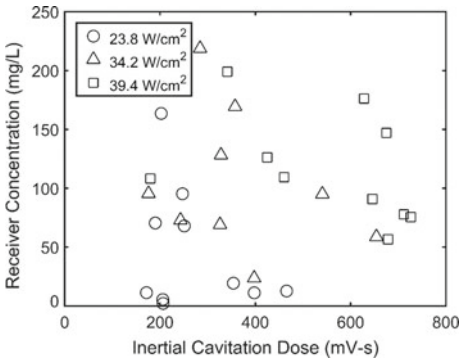

Fig. 6.8 Receiver chamber caffeine concentration as a function of inertial cavitation dose

intensity-dose trends shown in Figs. 6.6 and 6.7. There is also no clear trend within each intensity group.

The poor correlation shown in Fig. 6.8 suggests that the PCD system used in this study did not represent the inertial cavitation behavior that occurred during skin sonoporation. However, this may be misleading. There are several features of the methodology that may have contributed to the poor correlation between caffeine transport and inertial cavitation dose. It is possible that the long caffeine residence time (20 h) caused the effects of the inertial cavitation activity on the skin permeability to be diminished by the effects of hydration which also acts to increase permeability over long periods of time. This issue could have been circumvented if periodic concentration samples had been taken during diffusion. Furthermore, the small molecular weight of caffeine (194 g/mol) may have limited the potential for permeability enhancement as only a small enhancement is possible with such a small drug. These points must be addressed, and the study repeated, if a definitive statement about the effectiveness of the PCD system is to be made. With these caveats in mind, the results of the present study should not be seen as an indictment on PCD systems in skin sonoporation. Nor should the results detract from the potential benefits of employing a functional cavitation feedback loop in a skin sonoporation setup.

6.4 Conclusions

The purpose of this study was to assess the effectiveness with which a confocal PCD monitored the inertial cavitation activity within a Franz diffusion cell during skin sonoporation. If a PCD could be shown to perform in this context, that would enable the implementation of a feedback loop to control inertial cavitation activity. In order to facilitate an assessment of PCD performance, three different intensities were employed to create three distinctly different degrees of inertial cavitation activity. As expected, both receiver caffeine concentration and inertial cavitation dose increased with increasing intensity. However, a clear correlation between inertial cavitation dose and receiver caffeine concentration, which would have been indicative of an effective PCD, could not be obtained. The correlation was poor both between intensity groups and within intensity groups. The authors propose that using a larger permeant, and a shorter residence time will result in an improvement in the correlation.

References

1. Tezel, A., et al.: Frequency dependence of sonophoresis. Pharm. Res. **18**(12), 1694–1700 (2001)
2. Tezel, A., Sens, A., Mitragotri, S.: Investigations of the role of cavitation in low-frequency sonophoresis using acoustic spectroscopy. J. Pharm. Sci. **91**(2), 444–453 (2002)
3. Terahara, T., et al.: Dependence of low-frequency sonophoresis on ultrasound parameters; distance of the horn and intensity. Int. J. Pharm. **235**(1–2), 35–42 (2002)
4. Mitragotri, S., et al.: Determination of threshold energy dose for ultrasound-induced transdermal drug transport. J. Control. Release **63**(1–2), 41–52 (2000)
5. Herwadkar, A., et al.: Low frequency sonophoresis mediated transdermal and intradermal delivery of ketoprofen. Int. J. Pharm. **423**(2), 289–296 (2012)
6. Lavon, I., Grossman, N., Kost, J.: The nature of ultrasound–SLS synergism during enhanced transdermal transport. J. Control. Release **107**(3), 484–494 (2005)
7. Tang, H., et al.: An investigation of the role of cavitation in low-frequency ultrasound-mediated transdermal drug transport. Pharm. Res. **19**(8), 1160–1169 (2002)
8. Hockham, N., Coussios, C.C., Arora, M.: A real-time controller for sustaining thermally relevant acoustic cavitation during ultrasound therapy. IEEE Trans. Ultrason. Ferroelectr. Freq. Control **57**(12), 2685–2694 (2010)
9. Hallow, D.M., et al.: Measurement and correlation of acoustic cavitation with cellular bioeffects. Ultrasound Med. Biol. **32**(7), 1111–1122 (2006)
10. Yao-Sheng, T., Choi, J.J., Konofagou, E.E.: Identifying the inertial cavitation pressure threshold and skull effects in a vessel phantom using focused ultrasound and microbubbles. AIP Conf. Proc. **1215**(1), 186–189 (2010)
11. Tezel, A., Mitragotri, S.: Interactions of inertial cavitation bubbles with stratum corneum lipid bilayers during low-frequency sonophoresis. Biophys. J. **85**(6), 3502–3512 (2003)
12. Smith, N., et al.: Ultrasound-mediated transdermal transport of insulin in vitro through human skin using novel transducer designs. Ultrasound Med. Biol. **29**(2), 311–317 (2003)
13. Merino, G., et al.: Frequency and thermal effects on the enhancement of transdermal transport by sonophoresis. J. Control. Release **88**(1), 85–94 (2003)
14. Robertson, J., Becker, S.: Influence of acoustic reflection on the inertial cavitation dose in a franz diffusion cell. Ultrasound Med. Biol. **44**(5), 1100–1109 (2018)
15. Sarheed, O., Abdul Rasool, B.K.: Development of an optimised application protocol for sonophoretic transdermal delivery of a model hydrophilic drug. Open Biomed. Eng. J. **5**, 14–24 (2011)

16. Han, T., Das, D.B.: Permeability enhancement for transdermal delivery of large molecule using low-frequency sonophoresis combined with microneedles. J. Pharm. Sci. **102**(10), 3614–3622 (2013)
17. Mitragotri, S., et al.: Synergistic effect of low-frequency ultrasound and sodium lauryl sulfate on transdermal transport. J. Pharm. Sci. **89**(7), 892–900 (2000)
18. Morimoto, Y., et al.: Elucidation of the transport pathway in hairless rat skin enhanced by low-frequency sonophoresis based on the solute–water transport relationship and confocal microscopy. J. Control. Release **103**(3), 587–597 (2005)
19. Mutoh, M., et al.: Characterization of transdermal solute transport induced by low-frequency ultrasound in the hairless rat skin. J. Control. Release **92**(1–2), 137–146 (2003)

Chapter 7
CFD Reconstruction of Blood Hemodynamic Based on a Self-made Algorithm in Patients with Acute Type IIIb Aortic Dissection Treated with TEVAR Procedure

A. Polanczyk, A. Piechota-Polanczyk, Ch. Neumayer and I. Huk

Abstract Background: Combination of computational fluid dynamic (CFD) technique and medical data (AngioCT and USG-Doppler data) allowed preparation of a non-invasive method for blood hemodynamic analysis in type B aortic dissection (TBAD). Materials and methods: Three-dimensional digital models of the aorta were reconstructed using pre- and post-operative data from a 39-year-old patient treated for acute TBAD with thoracic endovascular aortic repair (TEVAR). Moreover, the left renal artery and the right common iliac artery were treated with additional stents. CFD technique was used to quantify the displacement forces acting on the aortic wall in the areas of endograft and validated with USG-Doppler data. The aortic segment was extended from the origin of the aortic arch to the aortic bifurcation. Results: Our results indicated that prostheses implantation improved overall aortic blood flow. We observed that blood flow rate was around two-fold higher in branching arteries of the aorta after surgical procedure. The wall shear stress (WSS) values were lower in all analysed areas. Hence, the overall risk of dissection propagation and rupture was decreased. Conclusion: CFD technique may provide qualitative assessment of hemodynamic forces in the aorta before and after prostheses implantation and may have potential in aiding the therapeutic decision-making process after operation.

Keywords CFD simulation · Aortic dissection · True lumen · False lumen · Wall shear stress · Blood flow

A. Polanczyk (✉)
Faculty of Process and Environmental Engineering, Department of Heat and Mass Transfer, Lodz University of Technology, Łódź, Poland
e-mail: andrzej.polanczyk@gmail.com

A. Polanczyk · Ch. Neumayer · I. Huk
Division of Vascular Surgery, Department of Surgery, Medical University of Vienna, Vienna, Austria

A. Piechota-Polanczyk
Faculty of Biochemistry, Biophysics and Biotechnology, Department of Medical Biotechnology, Jagiellonian University, Kraków, Poland

S. Gutschmidt et al. (eds.), *IUTAM Symposium on Recent Advances in Moving Boundary Problems in Mechanics*, IUTAM Bookseries 34,
https://doi.org/10.1007/978-3-030-13720-5_7

7.1 Introduction

Acute dissection, with tear formation in the inner lining of the aorta, is one of the cardiovascular emergencies, associated with high morbidity and mortality [9, 31]. An alternative treatment to open repair is thoracic endovascular aortic repair (TEVAR) for the management of acute type B dissection [5, 16]. Moreover, aortic dissection can be influenced by mechanical factors e.g. blood hemodynamic, vascular geometry and mechanical properties of the aortic wall [3, 10, 18]. Hemodynamic parameters play a crucial role in the formation and the progression of the aortic dissection. Blood flow rate and wall shear stress (WSS) are the main parameters that change after aortic repair (TEVAR) [10]. Blood hemodynamic within the dissected aorta is dominated by locally disturbed flow with areas of recirculation [4, 19]. Therefore, in this study we focus on the evaluation of hemodynamic parameters such as flow rate and WSS pre- and post-TEVAR. Computational fluid dynamic (CFD) technique is one of the engineering applications that allow reconstruction of blood hemodynamic in complex 3D models of cardiovascular system [15, 27, 30, 32]. Application of CFD technique in the topic of blood hemodynamic in vessels is widely described in literature [1, 14, 26]. Previously, the CFD technique has been applied to assess blood flow hemodynamic in vessels after stent-graft implantation in aortic aneurysms [22, 29, 33]. The real three-dimensional models of vessels are usually reconstructed with AngioCT or magnetic resonance imaging [2, 20]. Also, CFD allows to analyse blood hemodynamic changes within the true and false lumen of dissected aorta before and after TEVAR procedure [17]. Therefore, the aim of this study was to prepare a CFD model of chosen blood flow parameters within the aorta and aortic branches in patients with type B aortic dissection (TBAD) before and after TEVAR procedure.

7.2 Materials and Methods

A 39-years old male with acute complicated type B dissection was analysed. Antihypertensive therapy was initiated and AngioCT analysis was performed in which the primary entry tear was identified and substantial flow limitation to the renal arteries was found. TEVAR via a transfemoral approach was performed with intentional coverage of the left subclavian artery (LSA), 2 additional stents were implanted in the left renal artery, and the right common iliac artery (Epic^{TM}, self-expanding stents, Boston Scientific, Natick, MA). Post-operative AngioCT showed significant stenosis of the celiac trunk, which was retreated with the implantation of a balloon expandable stent (Express^{TM}, Boston Scientific, Natick, MA) using a percutaneous approach. The post-operative course was uneventful. Renal function improved during the hospital stay (sCrea: 2.28; GFR: 58.4 ml/min) and improved gradually during follow up. The management of arterial hypertension involved the use of beta blockers, ACE-inhibitors, calcium channel blockers and diuretics. During follow up, so far, no endoleak was found. The intentional coverage of the left subclavian artery

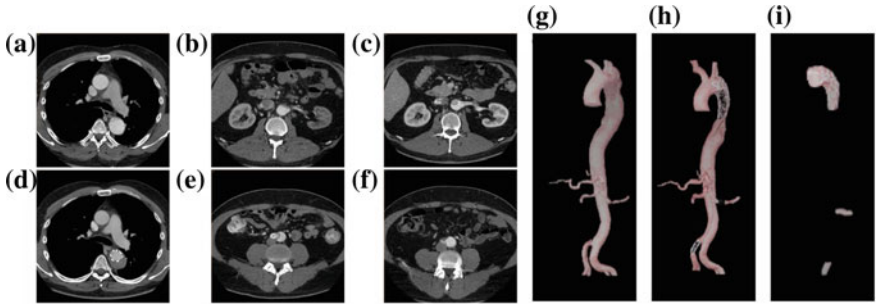

Fig. 7.1 AngioCT data and 3D reconstruction of the dissected aorta from the analysed patient. **a–c** An example of cross-sections before surgical intervention; **d–f** an example of cross-section after surgical intervention; **g** 3D geometry of analysed aorta before surgical intervention; **h** 3D geometry of analysed aorta after surgical intervention; **i** 3D geometries of vascular implant

(LSA) was tolerated well so far and no subsequent revascularisation was required. Anonymized pre-operative and post-operative AngioCT data (512 × 512 × 270 voxels, in-plane resolution of 0.78 × 0.78 mm, slice thickness 2 mm) was performed (Fig. 7.1). The aortic reconstruction comprised implantation of a stent-graft in the distal aortic arch and the descending thoracic aorta (LSA covered) and the implantation of self-expanding stents into the left renal artery and the right common iliac artery. The study was approved by the local Institutional Review Board (2069/2012).

Application of AngioCT data allowed preparation of patient-specific 3D digital geometries of pre- and post-operative aorta with the use of 3DDOCTOR software (Able Software Corp., Lexington, MA, USA) as previously described [21, 28]. Analysed geometries included data from the ascending aorta, aortic arch, descending thoracic aorta, abdominal aorta, iliac arteries, the orifices of the main aortic branches, the brachiocephalic trunk, left common carotid artery, left subclavian artery, renal arteries, iliac arteries, and the endograft and stents placed during TEVAR (Fig. 7.2). A CFD analysis was utilized to simulate blood flow and WSS for one cardiac cycle as previously described [23, 26]. With the use of ANSYS ICEM (ANSYS, USA) we reconstructed the 3D geometries with numerical mesh of analysed aorta for pre- and post-operative conditions (Fig. 7.2a, b). In the first step, we performed mesh independent test for different configuration of numerical grids. Finally, the following properties of numerical grid were considered: (1) elements were tetrahedral; (2) number of grid elements was in range from 900 000 to 1 000 000; (3) three boundary layers were applied; (4) the size of elements was in range from 0.1 to 2 mm (Fig. 7.2c, d). ANSYS FLUENT 18.2 software (ANSYS, USA), using Euler method for solving Navier-Stokes equations, was applied to carry out blood flow simulations. We assumed that the blood flow was incompressible and laminar and used Dirichlet conditions for the description of the mathematical domain. According to it, the following boundary conditions were applied: domain inlet was described with the use of velocity-inlet (v(x, y, z)), outlets from the domain were described with the pressure conditions, and wall was treated as a rigid structure. The investigated

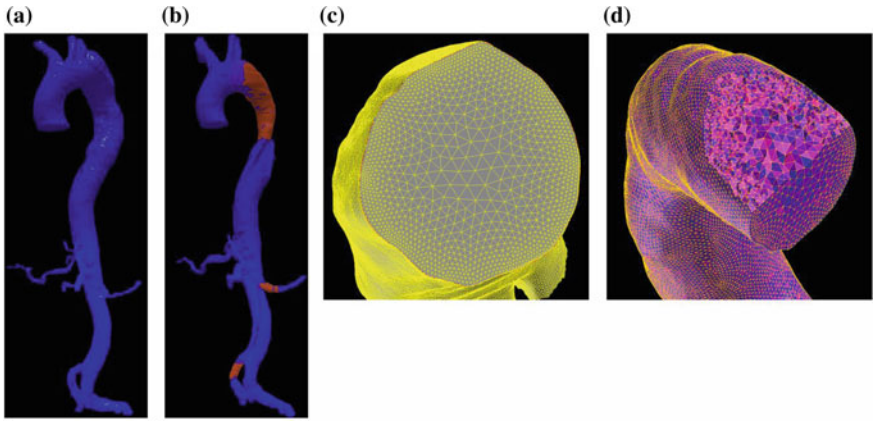

Fig. 7.2 3D virtual geometry of the analysed aorta: **a** before surgical intervention; **b** after surgical intervention; **c**, **d** examples of digital mesh applied for the analysed mathematical domains

spatial configuration of analysed geometries had one inlet at the top, three outlets at the aortic arch, eight outlets at the middle of the aorta and four outlets at the bottom. At the inlet we applied blood velocity profile, acquired from USG-Doppler examination for pre- and post-operative conditions, in a function of time [24]. While, at outlets we assumed an average pressure value equal to 17 332 Pa. Moreover, in our study we focused on blood hemodynamic changes only for arteries where endografts and stents were placed. Following Hoskins et al. [12] blood density was assumed as a constant value of 1 040 kg/m^3. Moreover, blood was treated as non-Newtonian liquid and described with the use of Quemada's model [25, 26]. We concentrated on the comparison of blood flow rate/velocity and WSS for the areas where endografts were placed.

7.3 Results

CFD analysis of pre- and post-operative aortic models indicated that the endografts remodelled the aortic geometry and restored blood flow through the true lumen. To determine how aortic remodelling influences blood hemodynamic, we analysed changes in blood redistribution, flow rate/velocity and WSS. Main flow patterns at the initial examination and after TEVAR were similar. There was high-velocity flow in the ascending aorta, with a pronounced jet into the dissection entry tear from the true lumen to the false lumen, and a slow-flow zone with recirculation patterns adjacent to the false lumen wall. Verification of CFD results with USG-Doppler examination for both cases, before and after TEVAR showed high correlation (accuracy 93 and 97% before TEVAR: thoracic trunk 0.30 m/s (USG-Doppler) and 0.32 m/s (CFD), renal arteries 0.30 m/s (USG-Doppler) and 0.31 m/s (CFD) and iliac arteries 0.028 m/s

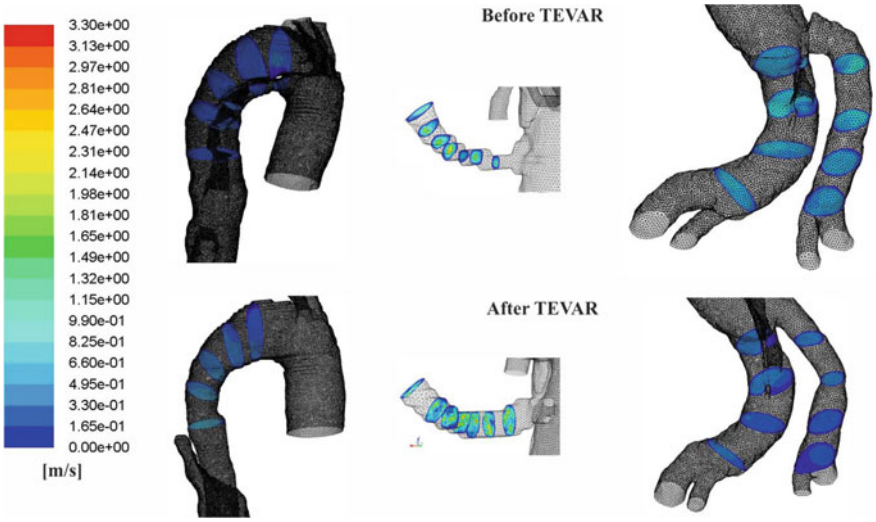

Fig. 7.3 An example of blood flow distribution before and after surgical intervention for aortic arch (left), renal artery (middle), iliac arteries for time of 0.1 s and posterior position (right)

(USG-Doppler) and 0.029 m/s (CFD); after TEVAR: thoracic trunk 0.30 m/s (USG-Doppler) and 0.32 m/s (CFD), renal arteries 0.34 m/s (USG-Doppler) and 0.35 m/s (CFD) and iliac arteries 0.029 m/s (USG-Doppler) and 0.030 m/s (CFD)).

Similarly, in the bottleneck places of renal and iliac arteries areas of a low-velocity (Fig. 7.3) but high-WSS (Fig. 7.4) were observed. The WSS analysis presented that mean WSS values after TEVAR, calculated for one heart cycle, increased slightly from 1.88 to 2.02 Pa. Moreover, post-operative aortic remodelling contributed to flow distribution into aortic branches, which was a result of better perfusion of the true lumen. We observed a 70% increase in blood flow through the true lumen of the thoracic aorta followed by 15% decrease in blood flow through the brachiocephalic trunk, left common carotid artery, left subclavian artery, and iliac arteries. After detailed analysis of flow distribution we decided to concentrate on three trouble-spot areas of the aorta, which included the aortic arch, where aortic dissection begins, the left renal artery and right common iliac artery. We decided to analyse these vascular territories more in detail, since they were strongly affected by the dissection and needed stents insertion.

Analysis of postinterventional remodelling of the aortic arch indicated changes in WSS values before and after TEVAR. The pre-operative aorta had irregular shapes with numerous narrowing areas and unstable flow determined by the appearance of the two lumens (true and false). In our study the dissecting membrane creates an artificial barrier characterized by high-velocity and high-WSS (4.73 Pa) in the areas adjacent to the wall. Therefore, in true lumen the velocity and WSS were much lower than expected. Moreover, the endovascular intervention separated the false lumen and directed blood flow through the true lumen leaving one channel.

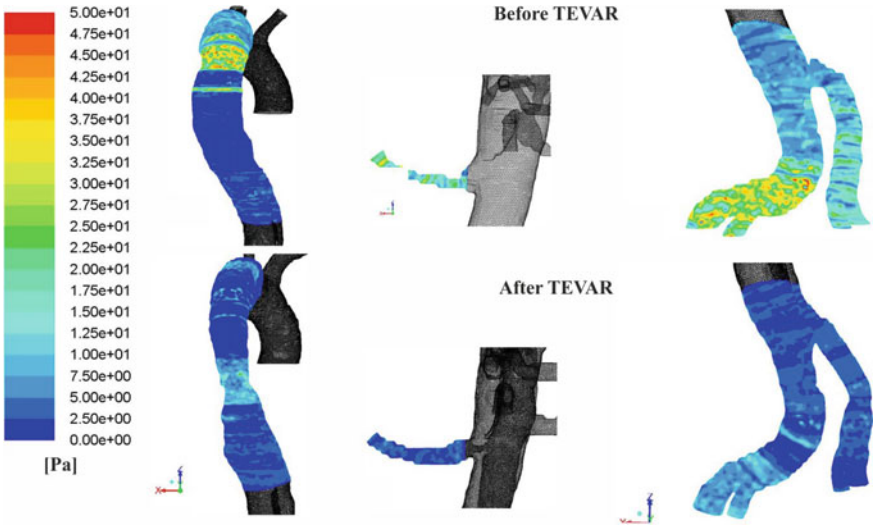

Fig. 7.4 An example of wall shear stress distribution before and after surgical intervention for aortic arch (left), renal artery (middle), iliac arteries for time of 0.1 s and posterior position (right)

This smoothed the blood flow and caused a noticeable change in WSS value with a 3-fold decrease in average WSS from 4.73 to 1.57 Pa after TEVAR. Additionally, post-operative character of velocity counters distribution was more uniform and no cross-sectional flow between the true and false lumen appeared. Post-operative remodelling increased aortic diameter and decreased the average blood flow velocity by 40%. Uneven distribution of blood flow contours accompanied by a thinner aortic wall within the dissection area increases the risk of further aortic wall remodelling. Therefore, in our case, the aortic arch remodelling after insertion of an endograft closed the false lumen and directed blood through the true channel what overall improved blood rheology. Moreover, prior to intervention the left renal artery had an irregular shape with numerous stenotic areas, which resulted in high average WSS values (4.42 Pa). The endovascular intervention led to an alignment of the artery and a 57% increase of the average channel cross-section. Moreover, there was a 3.2-fold decrease in the average WSS from 4.42 to 1.40 Pa. Stent implantation lead to an increased cross-sectional diameter of the left renal artery, therefore, ameliorating blood flow by 2.8-fold and average blood velocity by 1.8-fold. Free passage through the left renal artery also lowered the average WSS in this area. Furthermore, analysis of postinterventional remodelling of the right common iliac artery indicated that the initial artery (prior to TEVAR) had an irregular shape including numerous narrowness which resulted in high average WSS values (4.76 Pa). The endovascular intervention led to an alignment of the artery and a 57% increase of the average channel cross section. Moreover, there was a 2.6-fold decrease in the average WSS from 4.76 to 1.82 Pa. Also, the post-operative remodelling of the right iliac artery resulted in an equal distribution of blood through the branching iliac arteries. The analysis of

velocity contours in time showed a more stable and smoother flow. The average blood velocity in all outlets was reduced by around 50%. The change in the right iliac artery rheology was a consequence of changed overall distribution of blood flow through the aorta and its branches.

7.4 Discussion

This report clearly demonstrates that CFD technique can quantify changes in blood distribution, velocity and wall shear stress resulting from aortic remodelling after TEVAR for acute type B dissection. Aortic repair (TEVAR) led to improvement of blood distribution within the aorta and its branches, as well as stabilization of blood velocity, thereby efficiently reducing overall WSS. Changes in spatial configuration of the geometry of aorta and aortic branches indicated changes in blood velocity profiles. It was indicated in our study that during dissection around 80% of stroke volume enters the false lumen, which may further increase the dilation of the aorta. Moreover, implantation of an endograft in the thoracic aorta closed the primary entry to the false lumen and improved blood flow. Therefore, high flow conditions within the true lumen may limit aneurysm growth, as demonstrated previously [11]. Additionally, our results indicated that post-operative remodelling of the aorta decreased WSS especially in the areas of endograft and stent implantation. Lower-WSS within the aorta was a consequence of closure of the primary entry to the false lumen. Previously, Karmonik et al. [13] described in a patient-derived data model in which the aneurysm entry tear was characterized by high WSS and low total pressure. Also Cheng et al. [4] reported on high values of WSS around the entry tear inside the true lumen which could expand the tear. Moreover, post-operative remodelling of the aorta leads to changes in the lumen cross-sectional diameter, which correlates with WSS [8]. Furthermore, WSS values are influenced by vessel centreline asymmetry and maximum diameter [6].

Our study has some limitations. Firstly, unlike in humans we treated the artery wall as a rigid body, therefore neglecting its influence on blood flow character. However, this approach was in line with [7] who presented that differences between blood flow distribution for rigid and pulsating wall are comparable. Secondly, we described blood using non-Newtonian model. Nevertheless, it was presented by Xiang et al. [34] that non-Newtonian fluid reflects the real properties of blood and does not artificially increase WSS comparing to the Newtonian approach. Finally, the CFD simulations accuracy depends on the resolution of AngioCT data. In our study we applied 2 mm slides which gives acceptable but not perfect resolution. Therefore, it might influence the results.

7.5 Conclusion

With the use of CFD technique it was possible to characterise post-operative remodelling of the aorta after TEVAR for acute type B dissection. Therefore, CFD analysis may become a useful non-invasive tool for the characterization of blood hemodynamic changes before and after endovascular treatment of acute TBAD and may have potential in aiding therapeutic decision making after operation.

Acknowledgements The study was supported by grant number 181110 from the Medical University of Vienna, Department of Surgery.

References

1. Amblard, A., Berre, H.W.L., Bou-Said, B., Brunet, M.: Analysis of type I endoleaks in a stented abdominal aortic aneurysm. Med. Eng. Phys. **31**, 27–33 (2009). https://doi.org/10.1016/j.medengphy.2008.03.005
2. Auer, M., Gasser, T.C.: Reconstruction and finite element mesh generation of abdominal aortic aneurysms from computerized tomography angiography data with minimal user interactions. IEEE Trans. Med. Imaging **29**, 1022–1028 (2010). https://doi.org/10.1109/TMI.2009.2039579
3. Blanco, P.J., Pivello, M.R., Urquiza, S.A., Feijoo, R.A.: On the potentialities of 3D-1D coupled models in hemodynamics simulations. J. Biomech. **42**, 919–930 (2009). https://doi.org/10.1016/j.jbiomech.2009.01.034
4. Cheng, Z., et al.: Analysis of flow patterns in a patient-specific aortic dissection model. J. Biomech. Eng. **132**, 051007 (2010). https://doi.org/10.1115/1.4000964
5. Dake, M.D., et al.: Endovascular stent-graft placement for the treatment of acute aortic dissection. New Engl. J. Med. **340**, 1546–1552 (1999). https://doi.org/10.1056/NEJM199905203402004
6. Doyle, B.J., Callanan, A., Burke, P.E., Grace, P.A., Walsh, M.T., Vorp, D.A., McGloughlin, T.M.: Vessel asymmetry as an additional diagnostic tool in the assessment of abdominal aortic aneurysms. J. Vasc. Surg. **49**, 443–454 (2009). https://doi.org/10.1016/j.jvs.2008.08.064
7. Duvernois, V., Marsden, A.L., Shadden, S.C.: Lagrangian analysis of hemodynamics data from FSI simulation. Int. J. Numer. Methods Biomed. Eng. **29**, 445–461 (2013). https://doi.org/10.1002/cnm.2523
8. Georgakarakos, E., Ioannou, C.V., Kamarianakis, Y., Papaharilaou, Y., Kostas, T., Manousaki, E., Katsamouris, A.N.: The role of geometric parameters in the prediction of abdominal aortic aneurysm wall stress. Eur. J. Vasc. Endovasc. Surg. Off. J. Eur. Soc. Vasc. Surg. **39**, 42–48 (2010). https://doi.org/10.1016/j.ejvs.2009.09.026
9. Hagan, P.G., et al.: The International Registry of Acute Aortic Dissection (IRAD): new insights into an old disease. JAMA J. Am. Med. Assoc. **283**, 897–903 (2000)
10. Herman, I.M., Brant, A.M., Warty, V.S., Bonaccorso, J., Klein, E.C., Kormos, R.L., Borovetz, H.S.: Hemodynamics and the vascular endothelial cytoskeleton. J. Cell Biol. **105**, 291–302 (1987)
11. Hoshina, K., Sho, E., Sho, M., Nakahashi, T.K., Dalman, R.L.: Wall shear stress and strain modulate experimental aneurysm cellularity. J. Vasc. Surg. **37**, 1067–1074 (2003). https://doi.org/10.1067/mva.2003.169
12. Hoskins, P.R.: Simulation and validation of arterial ultrasound imaging and blood flow. Ultrasound Med. Biol. **34**, 693–717 (2008). https://doi.org/10.1016/j.ultrasmedbio.2007.10.017
13. Karmonik, C., et al.: Longitudinal computational fluid dynamics study of aneurysmal dilatation in a chronic DeBakey type III aortic dissection. J. Vasc. Surg. **56**, 260–263, e261 (2012). https://doi.org/10.1016/j.jvs.2012.02.064

14. Kizilova, N.: Computational approach to optimal transport network construction in biomechanics. Lect. Notes Comput. Sci. **3044**, 476–485 (2004)
15. Lam, S.K., Fung, G.S., Cheng, S.W., Chow, K.W.: A computational study on the biomechanical factors related to stent-graft models in the thoracic aorta. Med. Biol. Eng. Comput. **46**, 1129–1138 (2008). https://doi.org/10.1007/s11517-008-0361-8
16. Nienaber, C.A., et al.: Nonsurgical reconstruction of thoracic aortic dissection by stent-graft placement. New Engl. J. Med. **340**, 1539–1545 (1999). https://doi.org/10.1056/NEJM199905203402003
17. Papathanasopoulou, P., et al.: MRI measurement of time-resolved wall shear stress vectors in a carotid bifurcation model, and comparison with CFD predictions. J. Magn. Reson. Imaging JMRI **17**, 153–162 (2003). https://doi.org/10.1002/jmri.10243
18. Piechota, A., Polanczyk, A., Goraca, A.: Role of endothelin-1 receptor blockers on hemodynamic parameters and oxidative stress. Pharmacol. Rep. **62**, 7 (2010)
19. Piechota, A., Polanczyk, A., Goraca, A.: Protective effects of endothelin-A receptor antagonist BQ123 against LPS-induced oxidative stress in lungs. Pharmacol. Rep. **63**, 7 (2011)
20. Polanczyk, A., Klinger, M., Nanobachvili, J., Huk, I., Neumayer, C.: Artificial circulatory model for analysis of human and artificial vessels. Appl. Sci. **8**, 12 (2018). https://doi.org/10.3390/app8071017
21. Polanczyk, A., Piechota-Polanczyk, A., Domenig, C., Nanobachvili, J., Huk, I., Neumayer, C.: Computational fluid dynamic accuracy in mimicking changes in blood hemodynamics in patients with acute type IIIb aortic dissection treated with TEVAR. Appl. Sci. **8**, 14 (2018). https://doi.org/10.3390/app8081309
22. Polanczyk, A., Piechota-Polanczyk, A., Stefanczyk, L.: A new approach for the pre-clinical optimization of a spatial configuration of bifurcated endovascular prosthesis placed in abdominal aortic aneurysms. PloS One **12**, e0182717 (2017). https://doi.org/10.1371/journal.pone.0182717
23. Polanczyk, A., Podgorski, M., Polanczyk, M., Veshkina, N., Zbicinski, I., Stefanczyk, L., Neumayer, C.: A novel methodology for the description of biomechanical properties of aortic wall based on three-dimensional fluid structure interaction model. Interact. Cardiovasc. Thorac. Surg. **10** (2018). https://doi.org/10.1093/icvts/ivy252
24. Polanczyk, A., Podgorski, M., Wozniak, T., Stefanczyk, L., Strzelecki, M.: Computational fluid dynamics as an engineering tool for the reconstruction of hemodynamics after carotid artery stenosis operation: a case study. Medicina **54**, 15 (2018). https://doi.org/10.3390/medicina54030042
25. Polanczyk, A., Podyma, M., Stefanczyk, L., Szubert, W., Zbicinski, I.: A 3D model of thrombus formation in a stent-graft after implantation in the abdominal aorta. J. Biomech. **48**, 425–431 (2015). https://doi.org/10.1016/j.jbiomech.2014.12.033
26. Polanczyk, A., Podyma, M., Stefanczyk, L., Zbicinski, I.: Effects of stent-graft geometry and blood hematocrit on hemodynamic in Abdominal Aortic Aneurysm. Chem. Process Eng. 53–62 (2012). https://doi.org/10.2478/v10176-012-0005-2
27. Polanczyk, A., Podyma, M., Trebinski, L., Chrzastek, J., Zbicinski, I., Stefanczyk, L.: A novel attempt to standardize results of CFD simulations basing on spatial configuration of aortic stent-grafts. PloS One **11**, e0153332 (2016). https://doi.org/10.1371/journal.pone.0153332
28. Polanczyk, A., Strzelecki, M., Wozniak, T., Szubert, W., Stefanczyk, L.: 3D blood vessels reconstruction based on segmented CT data for further simulations of hemodynamic in human artery branches. Found. Comput. Decis. Sci. **42**, 13 (2017). https://doi.org/10.1515/fcds-2017-0018
29. Polanczyk, A., Wozniak, T., Strzelecki, M., Szubert, W., Stefanczyk, L.: Evaluating an algorithm for 3D reconstruction of blood vessels for further simulations of hemodynamic in human artery branches. In: Signal Processing—Algorithms, Architectures, Arrangements, and Applications Conference Proceedings, SPA 5 (2016). https://doi.org/10.1109/spa.2016.7763595
30. Shahcheraghi, N., Dwyer, H.A., Cheer, A.Y., Barakat, A.I., Rutaganira, T.: Unsteady and three-dimensional simulation of blood flow in the human aortic arch. J. Biomech. Eng. **124**, 378–387 (2002)

31. Suzuki, T., et al.: Clinical profiles and outcomes of acute type B aortic dissection in the current era: lessons from the International Registry of Aortic Dissection (IRAD). Circulation **108**(Suppl 1), II312–317 (2003) https://doi.org/10.1161/01.cir.0000087386.07204.09
32. Tse, K.M., Chiu, P., Lee, H.P., Ho, P.: Investigation of hemodynamics in the development of dissecting aneurysm within patient-specific dissecting aneurismal aortas using computational fluid dynamics (CFD) simulations. J. Biomech. **44**, 827–836 (2011). https://doi.org/10.1016/j.jbiomech.2010.12.014
33. Xenos, M., et al.: Patient-based abdominal aortic aneurysm rupture risk prediction with fluid structure interaction modeling. Ann. Biomed. Eng. **38**, 3323–3337 (2010). https://doi.org/10.1007/s10439-010-0094-3
34. Xiang, J., Tremmel, M., Kolega, J., Levy, E.I., Natarajan, S.K., Meng, H.: Newtonian viscosity model could overestimate wall shear stress in intracranial aneurysm domes and underestimate rupture risk. J. Neurointerventional Surg. **4**, 351–357 (2012). https://doi.org/10.1136/neurintsurg-2011-010089

Chapter 8
The Three Dynamical Regimes of a Droplet Driven by Thermocapillarity

Jonatan Raúl Mac Intyre, Juan Manuel Gomba, Carlos Alberto Perazzo, Pablo Germán Correa and Mathieu Sellier

Abstract We study the behaviour of two-dimensional droplets of partially wetting liquids driven by thermocapillary forces. A sessile droplet over a non-uniformly heated surface undergoes a shear stress along the surface of the liquid that moves the droplet from warmer to colder regions. By means of a two-term disjoining pressure model with a single stable energy minimum, we introduce the effect of a non-zero contact angle and two different models are compared. Polar liquids are modelled using London–van der Waals and ionic-electrostatics molecular interactions and, non-polar fluids with long- and short-range molecular forces. The droplet dynamics model is based on the lubrication approximation and the resulting partial differential equation is solved in the Finite Element package COMSOL Multiphysics. As a result of a parametric study on the contact angle, we characterize three different regimes.

Keywords Droplet · Thermocapillarity · Partially wetting

J. R. Mac Intyre · J. M. Gomba · P. G. Correa
Instituto de Física Arroyo Seco - IFAS (UNCPBA) and CIFICEN (UNCPBA-CICPBA-CONICET), Pinto 399, 7000 Tandil, Argentina
e-mail: jmintyre@exa.unicen.edu.ar

J. M. Gomba
e-mail: jgomba@engineering.ucsb.edu

P. G. Correa
e-mail: pcorrea@exa.unicen.edu.ar

C. A. Perazzo
IMeTTyB, Universidad Favaloro-CONICET, Solís 453, C1078AAI Buenos Aires, Argentina
e-mail: perazzo@favaloro.edu.ar

Departamento de Física y Química, FICEN, Universidad Favaloro, Sarmiento 1853, C1044AAA Buenos Aires, Argentina

M. Sellier (✉)
Department of Mechanical Engineering, University of Canterbury, Private Bag 4800, Christchurch 8140, New Zealand
e-mail: mathieu.sellier@canterbury.ac.nz

S. Gutschmidt et al. (eds.), *IUTAM Symposium on Recent Advances in Moving Boundary Problems in Mechanics*, IUTAM Bookseries 34,
https://doi.org/10.1007/978-3-030-13720-5_8

8.1 Introduction

In a variety of industrial applications, such as coating, ink-jet printing, microfluidics, micro-electronics, and medical diagnostics [2], the migration of droplets over a solid substrate is crucial. Among a large range of different physical principles to displace the liquids, we study here the thermocapillary effect, which has been employed in a large number of microfluidic devices to actuate droplets and bubbles given that the change of the surface tension with temperature is observable in most liquids [11].

We focus on droplets on horizontal surfaces that are driven by thermocapillary forces, where a non-uniformly heated substrate induces a shear stress along the surface of the liquid that moves the droplet from warmer to colder regions. Using a precursor film model at the contact line, we solve an initial value problem for the displacement of the droplet, without imposing restrictions on either the shape of the interface or the velocity of the contact lines [8].

We carry out a parametric study using the contact angle and distinguish three different flow regimes. For small contact angles, the drop spreads in the direction of motion, while for large contact angles the liquid migrates steadily preserving its shape. For intermediate contact angles, for both polar and non-polar liquids, the droplet breaks up into smaller droplets or migrates with a stationary profile, although we observe that polar droplets are more likely to break up than non-polar ones.

8.2 Mathematical Model

Figure 8.1 shows a two-dimensional droplet of density ρ and viscosity μ deposited on a non-uniformly heated surface. We reduce the Navier–Stokes equations to a single partial differential equation for the thickness $h = h(x, t)$ of the droplet employing the lubrication approximation [14].

We apply two boundary conditions: no slip at the solid substrate and tangential *Marangoni* stress τ along the liquid-air interface. The surface tension γ is linear in the temperature $T(x, h)$ at the air-liquid interface

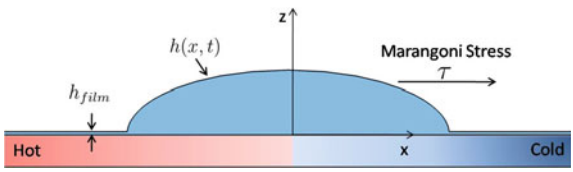

Fig. 8.1 Sketch of the problem: a two-dimensional droplet of thickness $h(x, t)$ resting on a non-uniformly heated surface. The temperature induces a gradient of the surface tension which drives the liquid towards the colder region. The droplet is surrounded by a constant film thickness with an initial (equilibrium) thickness h_{film} [13]

$$\gamma = \gamma_0 - \sigma(T - T_0) \ , \tag{8.1}$$

where γ_0 is the surface tension at $T = T_0$ and σ is a positive constant. Based on experimental data [1, 4], we assume Péclet number $Pe = HU/\delta \ll 1$ (where H is the maximum droplet thickness, U the migration velocity and δ the liquid thermal diffusivity) and Biot number $Bi = Hq_\infty/\kappa_t \ll 1$ (where q_∞ is the interfacial heat transfer coefficient and κ_t the liquid thermal conductivity), that is the conduction is the main heat transfer mechanism within the drop and the conductivity of the liquid is high. Therefore, the fluid temperature is equal to the linear temperature profile at the substrate [3] and the Marangoni stress along the liquid-air interface

$$\tau = \frac{d\gamma}{dT}\frac{dT}{dx} \tag{8.2}$$

is equal to a positive constant.

We scale both space directions with $h_c = x_c = a$, where $a = \sqrt{\gamma_0/\rho g}$ is the capillary length, and define the characteristic time as $t_c = 3\mu a/\gamma_0$. The evolution equation for the thickness $h(x, t)$ is given by [3]

$$\frac{\partial h}{\partial t} + \frac{\partial}{\partial x}\left[h^3 \frac{\partial}{\partial x}\left(\frac{\partial^2 h}{\partial x^2} + K\left[\left(\frac{h_*}{h}\right)^n - \left(\frac{h_*}{h}\right)^m\right]\right) + Bh^2\right] = 0 \ , \tag{8.3}$$

where the constants are

$$K = \frac{\tan^2\theta\ (n-1)(m-1)}{2(n-m)h_*} \ , \quad B = \frac{3a\tau}{2\gamma_0} \ , \tag{8.4}$$

and h_*, the thickness for which the energy of solid-liquid interaction reaches its minimum in units of a [13]. Equation (8.3) is obtained under the lubrication approximation, that assumes small values for the Reynold number and the first derivative (see for example Ref. [15]). The term multiplied by K models the effects of the molecular interactions, which satisfies $n > m > 1$. We focus on two different types of molecular potentials: polar liquids are represented by $(n, m) = (3, 2)$, and non-polar liquids by $(n, m) = (4, 3)$ [13, 14, 18]. The disjoining-conjoining pressure allows us to study droplets of partially wetting liquids and that non-zero contact angle θ is defined as the angle at the inflection point for large drops. The fourth-order differential equation is solved using the finite element technique in COMSOL Multiphysics environment and is subject to periodic boundary conditions at both extremes of the domain for the height of the droplet h. These conditions are equivalent to null first and third derivatives at the extremes of the domain.

The initial condition corresponds to the profile of a static droplet of area A when the temperature gradient is zero. This condition is satisfied employing the static profiles reported in [13] for non-polar liquids, and in [7, 16] for polar ones. We estimate the intensity of the thermal gradient and the area of the droplets as $0.002 \leq B \leq 0.05$ and $0.1 \leq A \leq 10$, respectively, based on experimental data [1, 4]. The use of realistic

values for h_*, typically of $10-100\,\text{nm}$, in problems with moving contact lines is impractical because it requires cell sizes of the order of h_* [6], so that we will use $h_* \geq 5 \times 10^{-3}$ [9, 10]. The effect of non-using realistic values is mainly evidenced as a time shift in the evolution of the flow with minor effects on the morphology of the surface (see Ref. [17] where the breakup of a droplet is reproduced, or Ref. [10] where the instability of a rivulet is reproduced numerically).

8.3 Film Regime

For small contact angles $\tan^2\theta \approx 0$ ($K \approx 0$), the molecular action is negligible. Experimental results for Marangoni films have shown that non-polar liquids under microgravity develop a linear profile [5] similar to the one we report here. Then, we will call this behaviour as *film regime*.

Figure 8.2a shows the numerical solution of Eq. (8.3) for a non-polar liquid with $\theta = 4°$ and $B = 0.01$. The front develops a characteristic capillary ridge and the bulk adopts a linear profile with a slope which decreases with time, while the droplet elongates, its maximum height decreases, and the volume under the linear profile grows. For polar liquids the behaviour is identical to that just described, due to independence of molecular interaction expected when $K \approx 0$.

The numerical solution of the differential equation retaining all terms shows that the long rear part of the drop develops a linear profile which, using the method of characteristics, is given by [8]

$$h = \frac{x - x_0}{2Bt}\,, \tag{8.5}$$

where x_0 is a constant related to the initial position of the rear contact line. Figure 8.2a shows the comparison between the numerical solution of the full Eq. (8.3) with Eq. (8.5). Figure 8.2b shows the evolution of the maximum height h_m for two values of B using both polar and non-polar liquids. At long times, the curves converge to the asymptotic curve $h_m \propto (Bt)^{-1/2}$ independently of the molecular interaction. Note that as the value of B is increased, the duration of the transient stage is reduced.

The bulk region of the droplet can be approximated by a triangular profile of width $x_f - x_a$ and height $(x_f - x_a)/(2Bt)$, where x_f and x_a are the front and rear positions of the drop, respectively. Then the area A of the droplet is given by $A = (x_f - x_a)^2/(4Bt)$. Given that A is almost constant since the capillary ridge is narrow, we can obtain the velocity of the droplet as $U = dx/dt = \sqrt{AB/t}$.

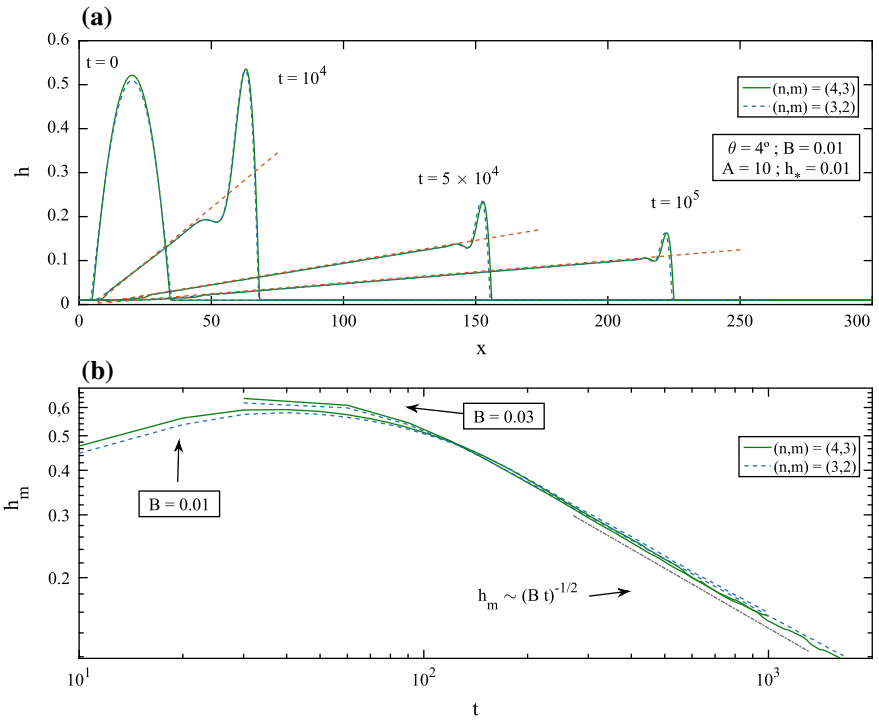

Fig. 8.2 **a** Evolution of the thickness profile for a non-polar (solid green line) and polar (dashed blue line) droplets. The dashed red line is the analytic solution for the rear profile given by Eq. (8.5). Here, $\theta = 4°$, $B = 0.01$, $A = 10$ and $h_* = 0.01$. **b** Evolution of the maximum height h_m for $\theta = 4°$, two values of B, and both molecular potentials. Here, $A = 10$, $h_* = 0.01$

8.4 Transition Regime

For intermediate values of the contact angle θ, the effects of the molecular potential and the Marangoni stress are of the same order. In this *transition regime* the droplet migrates across the plate and, while doing so, exhibits two different dynamics, as shown in Fig. 8.3: either it breaks into two or more smaller volumes or attains some, ultimately steady, profile which then migrates with a constant velocity. Non-polar liquid are more stable, the droplet moves steadily with a profile that consists in a capillary ridge followed by a film of constant thickness. On the contrary polar liquids breaks up more readily, showing a complex behaviour. We observe that in order to detect break up of non-polar liquids we have to increase B beyond the range of parameters reported in the experimental works ($B > 0.03$). Later in the text we analyze the differences between polar and non-polar flows in terms of the linear stability analysis of the flat profile behind the front.

Figure 8.4 shows steady solutions that do not break up, move with a constant velocity and present a characteristic flat thickness h_e. As B increases, the width of

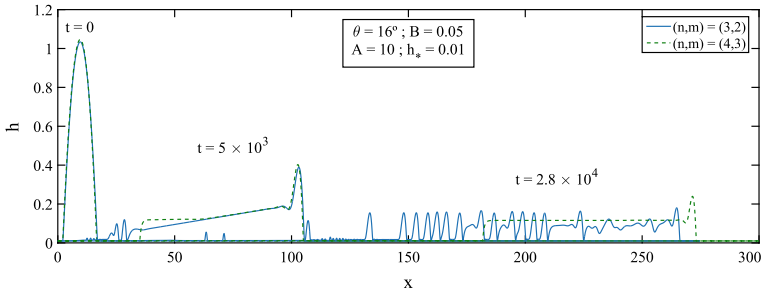

Fig. 8.3 Comparison of a stable (dashed green line) and unstable (solid blue line) droplet migration for $\theta = 16°$ and $B = 0.05$

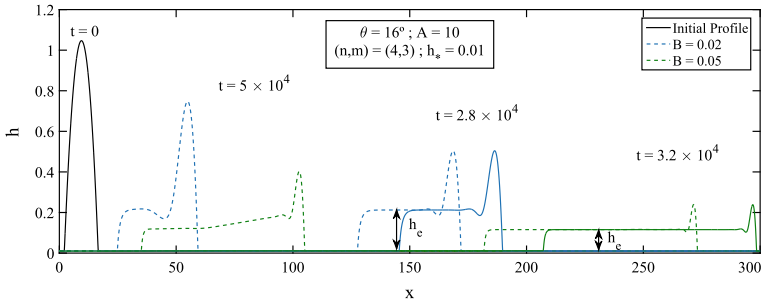

Fig. 8.4 Migration of flat droplets for a initial contact angle $\theta = 16°$, and two different thermal gradients at $\{5; 2.8\} \times 10^4$ in dashed line and 3.2×10^4 in solid line. h_e decreases as B increases

the profile w and the velocity of the droplet U increases, while the thickness h_e decreases. Note that the area below the capillary ridge enlarges as B diminishes and, when most of the fluid is within the capillary ridge, the profile does not present a flat film.

By dimensional analysis and parametric studies on K, B, and A, we find that the dependence of h_e on K and B is given by

$$h_e \propto K B^{-2/3} \propto \tan^2\theta \; B^{-2/3} \; , \tag{8.6}$$

and the width of the droplet w follows the scaling law

$$w \propto \frac{A}{K} B^{2/3} \propto \frac{A}{\tan^2\theta} B^{2/3} \; , \tag{8.7}$$

which are successfully tested. Also, the numerical results show that when A is increased, the width w increases but the thickness h_e remains constant, as expected from Eq. (8.6) to Eq. (8.7). Assuming that the solution is well represented by a travelling wave, we can determine that the velocity of migration is $U = Bh_e$, which is in a good agreement with the numerical data as shown Fig. 8.5. Note that using Eq. (8.6),

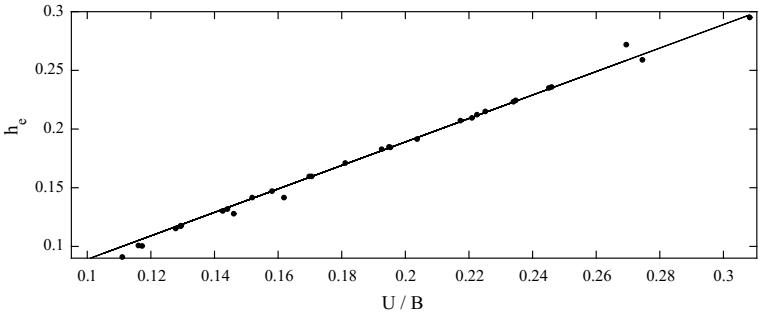

Fig. 8.5 Dependence of the thickness h_e on the velocity U and thermal gradient B. The law (8.8) is valid for the intermediate flow regime when droplets move steadily without ruptures, as shown Fig. 8.4

the velocity of the drop becomes

$$U \propto K B^{1/3} \propto \tan^2\theta \; B^{1/3} \; . \tag{8.8}$$

The nature of polar or non-polar liquid affects the stability of the flat film, as can observed in Fig. 8.3. In order to understand the rupture process, we implement a linear stability analysis using Eq. (8.3) for $h = h_e + \xi \exp(\imath kx + \omega t)$, with $h_e \gg \xi$. The growth rate and the wavenumber are related by [12]

$$\omega = -2i\,B h_e k - h_e^3 k^2 \left[k^2 - K \left(m \frac{h_*^m}{h_e^{m+1}} - n \frac{h_*^n}{h_e^{n+1}} \right) \right] \; . \tag{8.9}$$

A stable constant thickness h_e requires a negative growth rate, which from previous equation implies

$$k > \sqrt{K} \left(m \frac{h_*^m}{h_e^{m+1}} - n \frac{h_*^n}{h_e^{n+1}} \right)^{1/2} \; . \tag{8.10}$$

Note that the minimum unstable wavelength is larger for the case $(n, m) = (4, 3)$, thus non-polar liquids need longer times and larger domains to develop an instability. From Eq. (8.9) we can determinate the wavelength with the largest growth rate as

$$\lambda_m = 2\pi \sqrt{\frac{2}{K}} \left(m \frac{h_*^m}{h_e^{m+1}} - n \frac{h_*^n}{h_e^{n+1}} \right)^{-1/2} \; . \tag{8.11}$$

We implement a Fourier analysis of the thickness profile. Figure 8.6 shows the Fourier transform of the thickness profiles showed in Fig. 8.3 for $(n, m) = (3, 2)$. The position of the vertical line, that indicates the maximum wavelength amplitude $\lambda_m^n = 4.68$, agrees well with the theoretical value $\lambda_m^t = 2\pi/k_m = 3.72$.

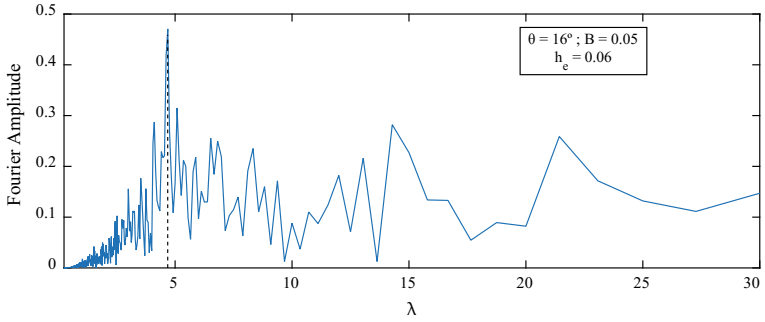

Fig. 8.6 Fourier transform of the thickness profile with a molecular potential $(n, m) = (3, 2)$ shown in Fig. 8.3. The vertical line shows the numerical maximum wavelength, here $\lambda_m^n = 4.68$

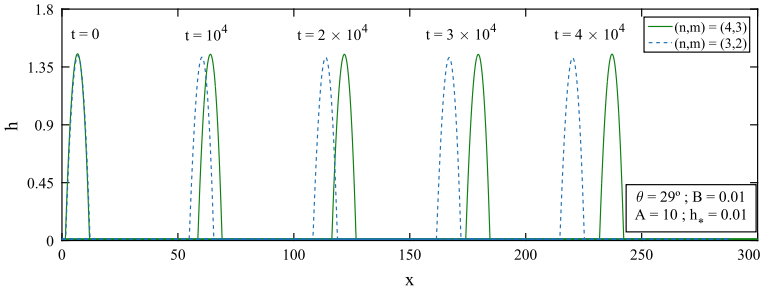

Fig. 8.7 Evolution of the thickness profile for non-polar liquid, $(n, m) = (4, 3)$ (green solid line) and polar liquid, $(n, m) = (3, 2)$ (blue dashed line). The effect of the potential avoids drop stretching due to Marangoni stress

8.5 Droplet Regime

In the *droplet regime*, the molecular potential becomes strong enough to keep the initial shape of the droplet during the migration with constant velocity U. Experimentally, Brzoska et al. [1] and Chen et al. [4] show that droplets migrate keeping their initial shape and the velocities present differences for different liquids, viscosities and thermal gradients. Similar to the experiments, the type of the molecular force modifies the velocity of migration U, as we can see in Fig. 8.7 for droplets with initial contact angle $\theta = 29°$. Note that the velocity of migration U changes with the polarity of the liquid, i.e. with the molecular potential.

Brzoska et al. [1] and Chen et al. [4] have shown that the velocity is proportional to B and inversely proportional to the viscosity. Following the dimensional analysis carried out by Gomba and Homsy [8], we define two Π^* groups to consider different pairs (n, m) depending on the type of liquid and obtain that

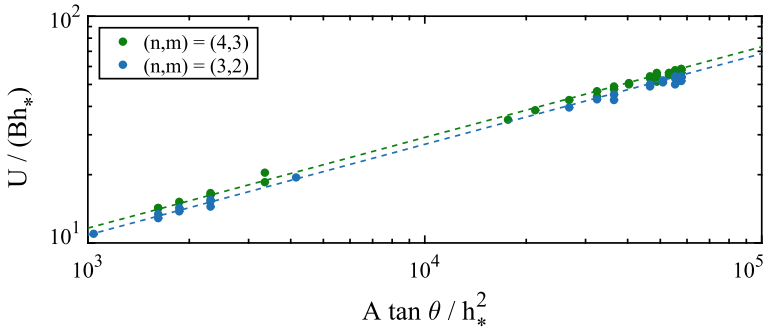

Fig. 8.8 Dependence of the velocity U for several combinations of the parameters (n, m), A, θ, B, and h_*. The exponent in Eq. (8.12) is $\beta = 0.4$ for both liquids

$$\Pi_1^* = \frac{U}{Bh_*} \propto (\Pi_2^*)^\beta \,, \tag{8.12}$$

$$\Pi_2^* = \left(\frac{(n-1)(m-1)}{2(n-m)}\right)^{1/2} \frac{A\tan\theta}{h_*^2} \,, \tag{8.13}$$

with $\beta = 0.4$, independently of the pair (n, m). Therefore, the pre-factor in Eq. (8.13) is responsible for the different velocity for each liquid. Figure 8.8 shows U/Bh_* versus $A\tan\theta/h_*^2$ for several combinations of the parameters (n, m), A, θ, B, and h_*.

8.6 Conclusions

We have explored the dynamics of droplets under the effect of a thermocapillary driving force. In the considered configuration, a droplet over a non-uniformly heated surface experiences a shear-stress that displaces the liquid from warmer to colder regions in a complex way. The droplet dynamics model is based on the lubrication approximation and the resulting partial differential equation is solved in the Finite Element package COMSOL.

For small contact angles, the droplets stretch in such a way that they develop a linear profile in the region behind the capillary ridge. The straight profile is well described by a similarity solution irrespective of the molecular interaction potential which is a consequence of the fact that, for small contact angles, the contribution of the disjoining pressure term is negligible. The asymptotic velocity of the front is given by $U = \sqrt{BA/t}$.

The transition regime occurs for intermediate values of the contact angle. Two characteristic behaviours are found in this regime: droplets travel with a constant profile which is different from the initial one or break up into a series of smaller droplets. Stable droplets migrate with a constant velocity, that scales as the $1/3$ power

of B. Also, it is sensitive to small differences in the contact angle being proportional to K. Unstable droplets are strongly dependent on the type of molecular interaction potential. For polar liquids with a disjoining pressure given by the pair $(n, m) = (3, 2)$, breakup occurs more readily than for non-polar liquids with a disjoining pressure for which $(n, m) = (4, 3)$. In other words, it takes a smaller value of the driving thermocapillary stress to breakup the initial droplets into smaller ones for polar liquids than for non-polar ones. By means of a linear stability analysis, we found that the maximum growth rate of the instability is larger for polar liquids, $(n, m) = (3, 2)$ than for non-polar ones and occurs for shorter wavelengths. That is to say, the instability for non-polar liquids takes longer times and larger distances to develop. The stability analysis also allows a prediction of the number of droplets the parent droplet breaks up into and the distance between them.

Finally, for larger values of the contact angle, the model confirms experimental results showing that the droplet travels with a constant profile and at constant speed. The travelling velocity is found to be greater for non-polar than for polar liquids and scales linearly with the thermocapillary driving force. The constant velocity of the droplet follows a power law with the parameters of the problem (see Eq. (8.13)) but, interestingly, the exponent of the power law is completely independent of the molecular potential.

This study presents new results on the role of the polarity of liquids in the dynamics of droplets driven by thermocapillary stresses. They shed light on how fluid properties and parameter selection are of importance in the context of droplet actuation.

Acknowledgements The authors gratefully acknowledge the funding supports via the CONICET Grants PIP No. 356 and PIP No. 299, the ANPCyP Grant No. 2012-1707 and CICPBA.

References

1. Brzoska, J.B., Brochard-Wyart, F., Rondelez, F.: Motions of droplets on hydrophobic model surfaces induced by thermal gradients. Langmuir **9**(8), 2220–2224 (1993). https://doi.org/10.1021/la00032a052
2. Casadevall i Solvas, X., DeMello, A.: Droplet microfluidics: recent developments and future applications. Chem. Commun. **47**(7), 1936–1942 (2011). https://doi.org/10.1039/C0CC02474K
3. Chaudhury, K., Chakraborty, S.: Spreading of a droplet over a nonisothermal substrate: multiple scaling regimes. Langmuir **31**(14), 4169–4175 (2015). https://doi.org/10.1021/la5047657
4. Chen, J.Z., Troian, S.M., Darhuber, A.A., Wagner, S.: Effect of contact angle hysteresis on thermocapillary droplet actuation. J. Appl. Phys. **97**(1), 014906 (2005). https://doi.org/10.1063/1.1819979
5. Fote, A.A., Slade, R.A., Feuerstein, S.: Thermally Induced Migration of Hydrocarbon Oil. J. Lubr. Technol. **99**(2), 158–162 (1977). https://doi.org/10.1115/1.3453002
6. Gaskell, P.H., Jimack, P.K., Sellier, M., Thompson, H.M.: Efficient and accurate time adaptive multigrid simulations of droplet spreading. Int. J. Numer. Methods Fluids **45**(11), 1161–1186 (2004). https://doi.org/10.1002/fld.632
7. Gomba, J.M., Homsy, G.M.: Analytical solutions for partially wetting two-dimensional droplets. Langmuir **25**(10), 5684–5691 (2009). https://doi.org/10.1021/la804335a

8. Gomba, J.M., Homsy, G.M.: Regimes of thermocapillary migration of droplets under partial wetting conditions. J. Fluid Mech. **647**, 125–142 (2010). https://doi.org/10.1017/S0022112010000078
9. Gomba, J.M., Diez, J.A., González, A.G., Gratton, R.: Spreading of a micrometric fluid strip down a plane under controlled initial conditions. Phys. Rev. E **71**(1), 016304 (2005). https://doi.org/10.1103/PhysRevE.71.016304
10. Gomba, J.M., Diez, J.A., Gratton, R., González, A.G., Kondic, L.: Stability study of a constant-volume thin film flow. Phys. Rev. E **76**(4), 046308 (2007). https://doi.org/10.1103/PhysRevE.76.046308
11. Karbalaei, A., Kumar, R., Cho, H.: Thermocapillarity in microfluidics - a review. Micromachines **7**(1), 13 (2016). https://doi.org/10.3390/mi7010013
12. Mac Intyre, J.R.: Efectos de fuerzas moleculares sobre gotas estáticas y flujos termocapilares. Ph.D. thesis, Universidad Nacional del Centro de la Provincia de Buenos Aires (2017)
13. Mac Intyre, J.R., Gomba, J.M., Perazzo, C.A.: New analytical solutions for static two-dimensional droplets under the effects of long- and short-range molecular forces. J. Eng. Math. **101**(1), 55–69 (2016). https://doi.org/10.1007/s10665-016-9846-x
14. Oron, A., Davis, S.H., Bankoff, S.G.: Long-scale evolution of thin liquid films. Rev. Mod. Phys. **69**(3), 931–980 (1997). https://doi.org/10.1103/RevModPhys.69.931
15. Perazzo, C.A., Gratton, J.: Navier-Stokes solutions for parallel flow in rivulets on an inclined plane. J. Fluid Mech. **507**, 367–379 (2004). https://doi.org/10.1017/S0022112004008791
16. Perazzo, C.A., Mac Intyre, J.R., Gomba, J.M.: Final state of a perturbed liquid film inside a container under the effect of solid-liquid molecular forces and gravity. Phys. Rev. E **89**(4), 043010 (2014). https://doi.org/10.1103/PhysRevE.89.043010
17. Schwartz, L.W., Eley, R.R.: Simulation of droplet motion on low-energy and heterogeneous surfaces. J. Colloid Interface Sci. **202**(1), 173–188 (1998). https://doi.org/10.1006/jcis.1998.5448
18. Starov, V.M., Velarde, M.G., Radke, C.J.: Wetting and Spreading Dynamics. Surfactant Science, vol. 11. CRC Press, Boca Raton (2007)

Chapter 9
Simulation of the Ultrasound-Induced Growth and Collapse of a Near-Wall Bubble

Bradley Boyd and Sid Becker

Abstract The ultrasound-induced growth and collapse of a bubble results from the oscillating position of an ultrasound transducer face in a liquid medium. The current work presents a fully-compressible model that is the first to capture the growth and collapse of a bubble set in a liquid medium subjected to an ultrasound transducer. The oscillating transducer face is represented by an immersed moving reflective boundary. The flow is simulated using a conservative interface capturing method, which includes the use of a high-order WENO reconstruction, a maximum-principle-satisfying and positivity-preserving limiter, and the HLLC approximate Riemann flux. A simulation is conducted of the growth and collapse of an initially spherical bubble with an initial radius of 50 μm near a wall subjected to the acoustic field resulting from a transducer face oscillating with a frequency of 30 kHz and a displacement amplitude of 0.6956 μm. The shape of the bubble during the growth and collapse is found to be qualitatively consistent with previous work, with a flattening of the bubble near the wall after the growth and the formation of a jet during the collapse. The violent collapse of the bubble results in a maximum pressure at the wall of approximately 14 MPa.

Keywords Acoustic cavitation · Bubble collapse · WENO

9.1 Introduction

Ultrasound-induced cavitation (acoustic cavitation) is employed in applications such as ultrasonic surface cleaning [1], water filtration [2], and food processing [3]. The medical field employs ultrasound-induced cavitation in ultrasound lithotripsy [4], the antitumor effect [5], hemostasis [6], phacoemulsification [7], drug and gene delivery [8], sonoporation [9], and cancer immunotherapy [10]. These applications make

B. Boyd (✉) · S. Becker
University of Canterbury, Christchurch, New Zealand
e-mail: bradley.boyd@pg.canterbury.ac.nz

S. Gutschmidt et al. (eds.), *IUTAM Symposium on Recent Advances in Moving Boundary Problems in Mechanics*, IUTAM Bookseries 34,
https://doi.org/10.1007/978-3-030-13720-5_9

use of the violent collapse of cavities (bubbles) that occur as a result of acoustic cavitation.

The ultrasound-induced growth and collapse of a bubble is a result of acoustic cavitation. With a sufficient drop in the fluid pressure, caused by the acoustic field, the fluid undergoes a phase change in localized regions where nucleation is possible: this is described as cavitation [11, 12]. The newly formed air and vapor cavity appears as a bubble in the solution, where it is able to continue to grow in time as air from the solution diffuse into the bubble: this is termed rectified diffusion [11, 12]. If the initial stable cavitation bubble is large enough and the amplitude of the acoustic field is sufficient in magnitude the bubble will respond transiently: often described as the lower transient threshold or Blake threshold [12]. This cavity will then grow rapidly with decreasing fluid pressure to at least twice its initial radius [12]. As the fluid pressure begins to increase, the bubbles rate of growth starts to decelerate until the bubble radius reaches its maximum and the transient collapse begins. The collapse of a cavitation bubble near a wall results in a high pressure experienced by the boundary and, in cases, a jet develops through the center of the bubble toward the boundary and impacts the surface of the boundary [13, 14].

We seek to model the acoustically-driven growth and collapse of a near wall bubble. To capture the violent collapse of a bubble, a fully compressible two-phase model that is capable of capturing shocks is required to represent both the bubble fluid and the surrounding liquid as compressible. In existing fully compressible models, the collapse is either induced by a shock wave traveling through the domain [13–17] or by using an initial condition in which there is a pressure difference between the bubble and the surrounding medium [1, 16, 18], which is referred to as a Rayleigh collapse. However, the shock-induced collapse and the Rayleigh collapse are not intended to capture the collapse of a bubble in a transient acoustic field.

Our previous study [19] worked on developing a model to capture the acoustically-driven collapse of a near wall bubble where the growth phase of the bubble is approximated using the Rayleigh-Plesset equation. Instead of approximating the growth and simulating the collapse, the focus of the present study is to directly simulate both the growth and collapse stages of the near wall bubble.

The field lacks a fully compressible model that is able to capture an acoustically-driven bubble near a wall. The model presented in this paper captures both the growth and collapse phases of a bubble subject to an ultrasound field. The ultrasound field is simulated directly using an immersed moving reflective boundary condition: the immersed boundary simulates the movement of the active face of the ultrasound transducer.

9.2 Methodology

9.2.1 Physical Model

The current study uses some previously validated simplifications to model the ultrasound-induced bubble growth and collapse. The nucleation and formation of the cavity are not considered as they are difficult to model and provide no additional insight into the growth and collapse of a cavity [16]. Instead, we assume the cavitation bubble is already present in the solution. Surface tension, viscous effects, gravity, and heat conduction are considered to be of secondary importance during the collapse [14, 20–24]; thus, they are neglected. We also assume that no mass transport occurs across the interface and that the cavitation bubble is entirely composed of air. Considering the condensation and evaporation of the vapor across the interface and rectified diffusion of air across the interface during the collapse would greatly increase the complexity of the model, with minimal additional insight into the dynamics of the bubble. These assumptions result in the idealized model of an acoustically-driven air bubble, where a compressible multiphase model is used to capture the different fluids and any shock waves that develop.

In practice, the transducer face oscillates sinusoidally in the fluid medium producing the ultrasound field. Thus, the properties of the ultrasound field in the fluid depend on the transducers displacement amplitude (a) and the transducers frequency (f). A representation of an experimental ultrasound-induced cavitation setup (e.g. ultrasonic cleaning [25] or sonoporation [26]) including the transducer, cavitation bubble, surrounding fluid, and the wall is depicted in Fig. 9.1a. The dashed line in this figure represents the physical domain that is modelled in the present study. The width of the domain is smaller than the width of the transducer face to allow the outer boundary to be treated as a reflective boundary, capturing the symmetry across that boundary.

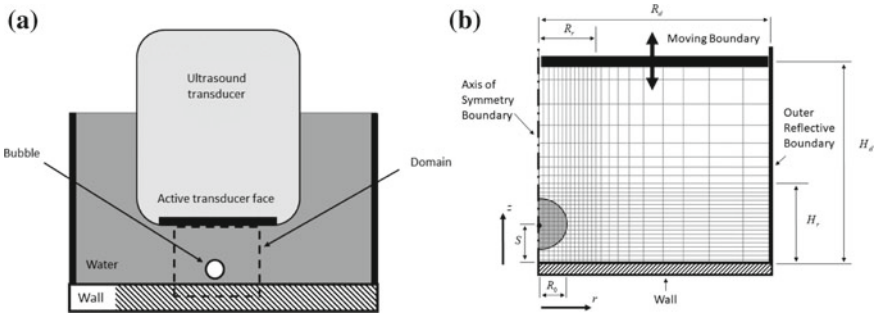

Fig. 9.1 **a** A representative depiction of an ultrasound transducer setup and **b** the computational domain in cylindrical coordinates used to simulate the acoustically-driven bubble

The computational domain for the present study is depicted in Fig. 9.1b. The model uses an axisymmetric cylindrical coordinate system with a growing mesh from the refined region that encompasses the bubble (Fig. 9.1b). Figure 9.1b shows the dimensions of the domain, H_d and R_d, the dimensions of the refined region, H_r and R_r, the standoff distance of the bubble from the wall, S, and the boundary conditions. The ultrasound transducer face is simulated using an immersed moving reflective boundary that oscillates sinusoidally. The wall is represented by a reflective boundary.

9.2.2 Numerical Methods

In this study, we model the acoustically-driven growth and collapse of an air bubble in water exposed to an ultrasound field. The bubble dynamics are modelled using a compressible, inviscid, multiphase model. The two-fluid system, the bubble air and the surrounding water, is described using the five-equation model of [27]. To model a multiphase system containing liquids and gases using the same equation of state (EOS), we use the stiffened equation of state [24].

The numerical scheme consists of a conservative interface capturing scheme which uses the fifth-order WENO reconstruction [24] with a maximum-principle-satisfying and positivity-preserving limiter (developed in [28]), and the HLLC approximate Riemann flux [24]. To model the ultrasound input, an immersed moving reflective boundary oscillates through a fixed grid of finite-volume cells (Fig. 9.1b). A conservative cell mixing method allows the moving boundary to bisect the fixed cells, where the moving boundary-fluid interaction is evaluated using the one-sided Riemann problem [29].

The initial bubble (R_0) in equilibrium with the surrounding fluid ($p_B = p_{atm}$) is superimposed onto the developed ultrasound field (Fig. 9.3) to give the initial condition for the simulation. The superimposing procedure is similar to the method developed in [19]. The key difference is that the bubble is initialized at an equilibrium state, prior to growth (R_0), as opposed to the maximum bubble size, prior to collapse ($R_{\max}$).

9.3 Results

9.3.1 Case Study Parameters

A representative case study is presented to show the application of the model developed. The case study captures the growth and collapse of a bubble that has an initial radius of 50 μm in an ultrasound field where the transducer face is oscillating at

Table 9.1 Model parameters and fluid properties

Symbol	Description	Value
f	Ultrasound frequency	30.0 kHz
a	Amplitude of the transducer face	0.6956 μm
S	Initial bubble standoff distance	116 μm
R_0	Initial bubble radius	50.0 μm
H_d	Domain depth	1.0 cm
R_d	Domain radius	1.0 cm
H_r	Refined region depth	200.0 μm
R_r	Refined region radius	400.0 μm
$\Delta r_{\min}$	Refined cell radius	1.0 μm
$\Delta z_{\min}$	Refined cell depth	1.0 μm
N	Cells	134400
g	Cell growth rate	1.1
CFL	CFL condition (to compute Δt)	0.16
p_{atm}	Atmospheric pressure	101.325 kPa
$\rho_{0,2}$	Density of water (surrounding fluid) at p_{atm}	1000.0 kg/m^3
γ_1	EOS parameter for air [15]	1.4
γ_2	EOS parameter for water [15]	6.12
$\pi_{\infty,1}$	EOS parameter for air [15]	0.0 Pa
$\pi_{\infty,2}$	EOS parameter for water [15]	3.43×10^8 Pa

30 kHz with a displacement amplitude of 0.6956 μm. The model parameters and fluid properties are provided in Table 9.1.

9.3.2 Bubble Growth and Collapse Results

The ultrasound-induced growth and collapse of a bubble is presented in Fig. 9.2, where the bubble interface contours are stepped in time. The growth phase of the simulation shows the rapid non-spherical growth of the near-wall bubble (Fig. 9.2a). The bubble deviates from the spherical shape due to the near-wall boundary hindering the flow, resulting in a flat region of the bubble interface on the side nearest to the

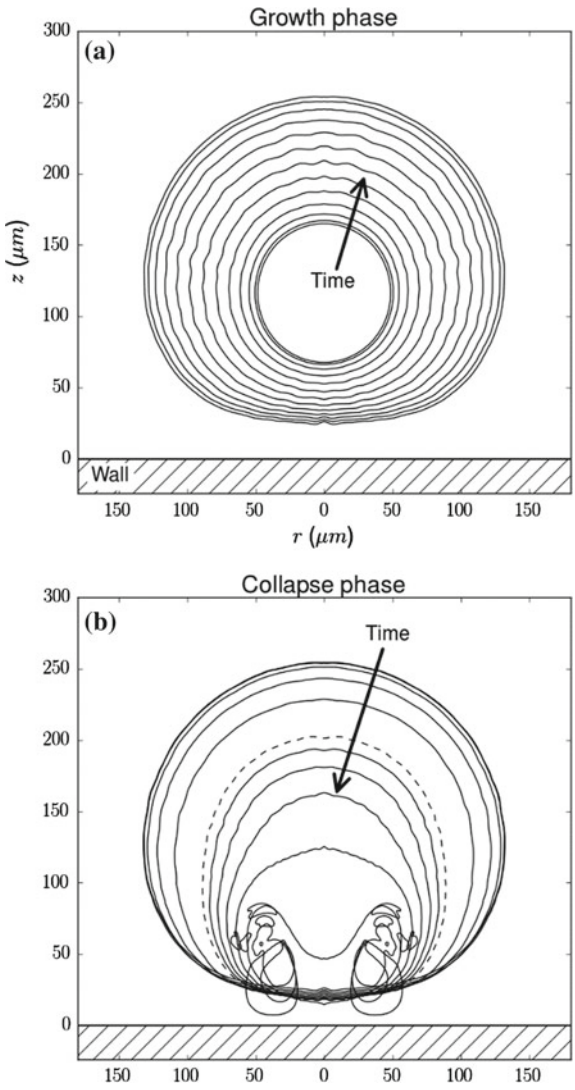

Fig. 9.2 The **a** growth and **b** collapse of a bubble near a wall ($S = 116\,\mu$m). The depiction shows the bubble interface stepped in time in increments of 1.463 μs until the dashed contour line where the interface is then stepped in time in increments of 0.3658 μs

wall (Fig. 9.2a). This leaves a layer of water between the fully grown bubble and the wall, which is observed in experiments [30].

Once the bubble reaches its maximum size and the collapse phase begins, the simulation shows the formation of a jet which penetrates the bubble towards the wall at the later stages of the collapse (Fig. 9.2b). The final three contours of (Fig. 9.2b) show the formation of a toroidal bubble as the jet fully penetrates the bubble, and the rebounding of the bubble (the growth of the toroidal bubble after the collapse). The bubble shape for the majority of the collapse phase is qualitatively consistent with the collapse shape found in multiple studies [1, 21, 31–33].

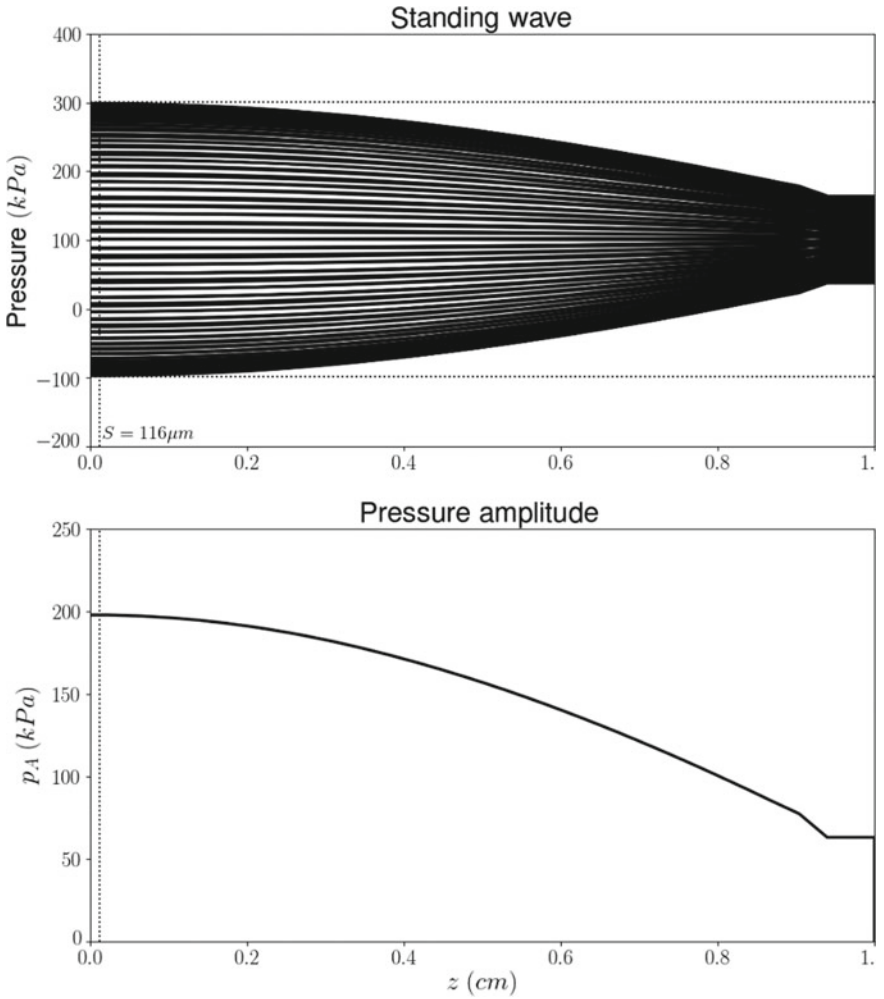

Fig. 9.3 The ultrasound standing pressure wave (quarter wave) between the transducer face (immersed moving boundary condition) ($z \approx 1$ cm) and the wall ($z \approx 0$), without the presence of a bubble. The standing pressure wave is presented by showing the acoustic pressure wave at multiple different instances during the acoustic wave cycle. The local pressure amplitude varies in z direction: $p_A(z) = \big(p_{\max}(z) - p_{\min}(z)\big)/2$

An ultrasound transducer face displacement amplitude of 0.6956 μm resulted in a standing wave between the wall ($z = 0$) and the immersed moving boundary ($z \approx 1$ cm) with no bubble present, see Fig. 9.3. The evolution of the location pressure near the wall gives a pressure amplitude of 200 kPa (Fig. 9.3). The subsequent far-field pressure at $[r = R_d, z = 0]$ during the bubble growth and collapse is sinusoidal with a pressure amplitude of 200 kPa (Fig. 9.4a).

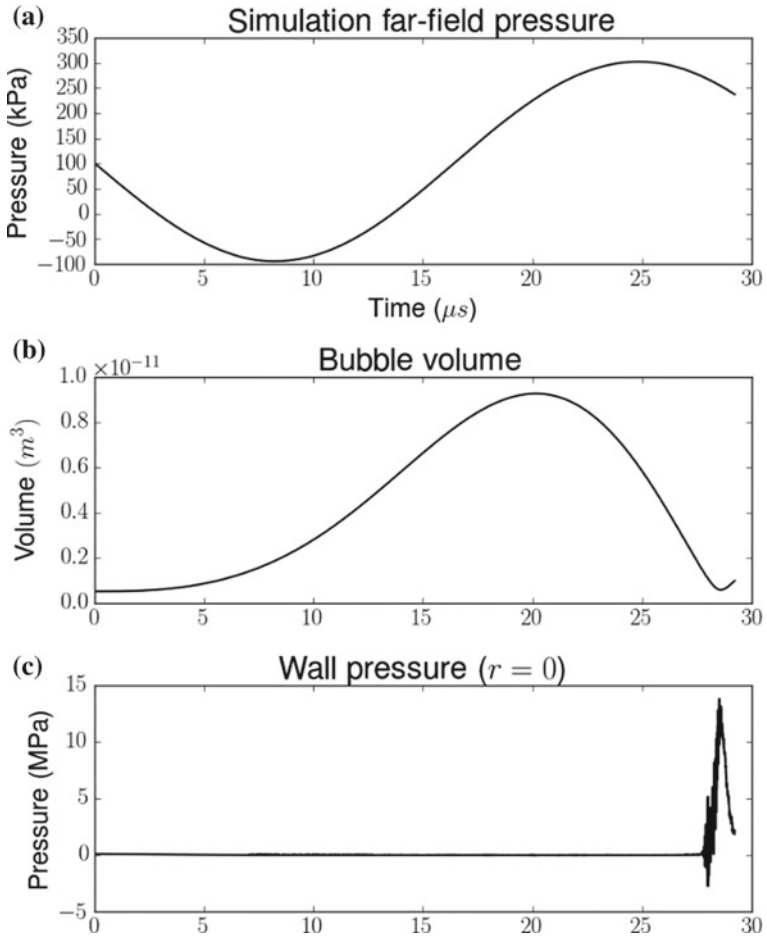

Fig. 9.4 **a** The far-field pressure (at $[r = R_d, z = 0]$ near the wall and the outer boundary, see Fig. 9.1) produced by the immersed moving reflective boundary, used to simulate the ultrasound input, **b** the bubble volume, and **c** the pressure experienced by the wall at $r = 0$

For a bubble with an initial radius of 50 μm and a pressure amplitude of 200 kPa (Fig. 9.4a), the pressure experienced by the wall increased rapidly nearing the end of the collapse, reaching a peak pressure of approximately 14 MPa (Fig. 9.4c).

9.4 Conclusion

To the authors' knowledge, this is the first fully compressible model able to simulate the ultrasound-induced growth and collapse of a bubble near a wall. The case study presented in this paper applies the numerical model to the ultrasound-induced growth

and collapse of a cavitation bubble near a wall. Given an initial bubble ($R_0 = 50\,\mu$m) and the parameters of the ultrasound transducer, frequency of 30 kHz and transducer displacement amplitude of 0.6956 μm, the resulting bubble growth and collapse was simulated and analyzed. The shape of the bubble during growth and collapse was found to be qualitatively consistent with previous work. The pressure experienced by the nearby solid boundary was analyzed and the bubble collapse resulted in the formation of a jet which produced a maximum pressure at the wall of 14 MPa.

References

1. Chahine, G.L., et al.: Modeling of surface cleaning by cavitation bubble dynamics and collapse. Ultrason. Sonochem. **29**, 528–549 (2016)
2. Reuter, F., et al.: Membrane cleaning with ultrasonically driven bubbles. Ultrason. Sonochem. **37**, 542–560 (2017)
3. Chandrapala, J., et al.: Ultrasonics in food processing. Ultrason. Sonochem. **19**(5), 975–983 (2012)
4. Yoshizawa, S., et al.: High intensity focused ultrasound lithotripsy with cavitating microbubbles. Med. Biol. Eng. Comput. **47**(8), 851–860 (2009)
5. Wang, Y.U., et al.: Antitumor effect of microbubbles enhanced by low frequency ultrasound cavitation on prostate carcinoma xenografts in nude mice. Exp. Ther. Med. **3**(2), 187–191 (2012)
6. Feng, G., et al.: Hemostatic effects of microbubble-enhanced low-intensity ultrasound in a liver avulsion injury model. PLoS ONE **9**(5), e95589 (2014)
7. Topaz, M., et al.: Acoustic cavitation in phacoemulsification: chemical effects, modes of action and cavitation index. Ultrasound Med. Biol. **28**(6), 775–784 (2002)
8. Paliwal, S., Mitragotri, S.: Ultrasound-induced cavitation: applications in drug and gene delivery. Expert Opin. Drug Deliv. **3**(6), 713–726 (2006)
9. Tezel, A., Mitragotri, S.: Interactions of inertial cavitation bubbles with stratum corneum lipid bilayers during low-frequency sonophoresis. Biophys. J. **85**(6), 3502–3512 (2003)
10. Unga, J., Hashida, M.: Ultrasound induced cancer immunotherapy. Adv. Drug Deliv. Rev. **72**, 144–153 (2014)
11. Brennen, C.E.: Cavitation and Bubble Dynamics, vol. 44. Oxford University Press, New York (1995)
12. Young, F.R.: Cavitation. Imperial College Press, London (1999)
13. Coralic, V., Colonius, T.: Shock-induced collapse of a bubble inside a deformable vessel. Eur. J. Mech. B. Fluids **40**, 64–74 (2013)
14. Johnsen, E., Colonius, T.: Shock-induced collapse of a gas bubble in shockwave lithotripsy. J. Acoust. Soc. Am. **124**(4), 2011–2020 (2008)
15. Coralic, V.: Simulation of shock-induced bubble collapse with application to vascular injury in shockwave lithotripsy. California Institute of Technology (2015)
16. Johnsen, E., Colonius, T.I.M.: Numerical simulations of non-spherical bubble collapse. J. Fluid Mech. **629**, 231–262 (2009)
17. Quirk, J.J., Karni, S.: On the dynamics of a shock-bubble interaction. J. Fluid Mech. **318**(1), 129–163 (1996)
18. Chahine, G.L.: Modeling of cavitation dynamics and interaction with material. In: Kim, K.-H., et al. (eds.) Advanced Experimental and Numerical Techniques for Cavitation Erosion Prediction, pp. 123–161. Springer Netherlands, Dordrecht (2014)
19. Boyd, B., Becker, S.: Numerical modelling of an acoustically-driven bubble collapse near a solid boundary. Fluid Dyn. Res. (2018)

20. Blake, J., Taib, B., Doherty,G.: Transient cavities near boundaries. Part 1. Rigid boundary. J. Fluid Mech. **170**, p. 479–497 (1986)
21. Zhang, S., Duncan, J.H., Chahine, G.L.: The final stage of the collapse of a cavitation bubble near a rigid wall. J. Fluid Mech. **257**, 147–181 (1993)
22. Plesset, M.S., Chapman, R.B.: Collapse of an initially spherical vapor cavity in the neighborhood of a solid boundary (1970)
23. Naudé, C.F., Ellis, A.T.: On the mechanism of cavitation damage by nonhemispherical cavities collapsing in contact with a solid boundary. J. Basic Eng. **83**(4), 648–656 (1961)
24. Johnsen, E., Colonius, T.: Implementation of WENO schemes in compressible multicomponent flow problems. J. Comput. Phys. **219**(2), 715–732 (2006)
25. Maisonhaute, E., White, P.C., Compton, R.G.: Surface acoustic cavitation understood via nanosecond electrochemistry. J. Phys. Chem. B **105**(48), 12087–12091 (2001)
26. Polat, B.E., et al.: A physical mechanism to explain the delivery of chemical penetration enhancers into skin during transdermal sonophoresis—insight into the observed synergism. J. Control. Release **158**(2), 250–260 (2012)
27. Allaire, G., Clerc, S., Kokh, S.: A five-equation model for the simulation of interfaces between compressible fluids. J. Comput. Phys. **181**(2), 577–616 (2002)
28. Zhang, X., Shu, C.-W.: Maximum-principle-satisfying and positivity-preserving high-order schemes for conservation laws: survey and new developments. In: Proceedings of the Royal Society of London A: Mathematical, Physical and Engineering Sciences. The Royal Society (2011)
29. Hu, X.Y., et al.: A conservative interface method for compressible flows. J. Comput. Phys. **219**(2), 553–578 (2006)
30. Vogel, A., Lauterborn, W., Timm, R.: Optical and acoustic investigations of the dynamics of laser-produced cavitation bubbles near a solid boundary. J. Fluid Mech. **206**, 299–338 (1989)
31. Plesset, M.S., Chapman, R.B.: Collapse of an initially spherical vapour cavity in the neighbourhood of a solid boundary. J. Fluid Mech. **47**(2), 283–290 (1971)
32. Jayaprakash, A., Hsiao, C.-T., Chahine, G.: Numerical and experimental study of the interaction of a spark-generated bubble and a vertical wall. J. Fluids Eng. **134**(3), 031301-031301-12 (2012)
33. Hsiao, C.-T., et al.: Modelling of material pitting from cavitation bubble collapse. J. Fluid Mech. **755**, 142–175 (2014)

Chapter 10
Air Flow Entrainment of Lactose Powder: Simulation and Experiment

Thomas Kopsch, Darragh Murnane and Digby Symons

Abstract Lactose powder is frequently used as an excipient in drug formulations for use in dry powder inhalers (DPIs). As a patient inhales through a DPI the lactose powder is entrained into the airflow, thus enabling delivery of the drug dose to the patient's lungs. Computational fluid dynamics (CFD) can potentially aid the designers of DPIs if the entrainment process can be accurately simulated. In this study we compare CFD simulations and experimental observations of entrainment of lactose powder using an example 2D DPI geometry and typical inhalation airflow profiles. 2D transient CFD simulations were carried out using an Eulerian-Eulerian solver to model the progression of entrainment subject to two example patient inhalation maneuvers: one high and one low flow rate. Experiments used the same 2D geometry laser cut from a 3 mm thick opaque acrylic sheet sandwiched between transparent sheets. A powder dose was pre-loaded before assembly of the geometry. Two different lactose powders were used with particle sizes of 59 and 119 μm. Air flow was provided by a computer controlled pump (a breath simulator). The geometry was back lit and the progression of entrainment was filmed at 1000 fps. Comparison of the CFD simulations and experimental results showed good agreement for the two powders tested.

Keywords Multiphase flow · CFD · Validation

T. Kopsch
Engineering Department, University of Cambridge, Cambridge, UK

D. Murnane
Department of Pharmacy, University of Hertfordshire, Hatfield, UK

D. Symons (✉)
Mechanical Engineering Department, University of Canterbury, Christchurch, New Zealand
e-mail: digby.symons@canterbury.ac.nz

S. Gutschmidt et al. (eds.), *IUTAM Symposium on Recent Advances in Moving Boundary Problems in Mechanics*, IUTAM Bookseries 34,
https://doi.org/10.1007/978-3-030-13720-5_10

10.1 Introduction

10.1.1 Motivation

Dry powder inhalers (DPIs) are used to deliver medicines directly to the lungs to treat both respiratory and systemic diseases. Drug particles are usually micronized to obtain particle sizes of less than 5 μm to maximize pulmonary deposition and minimize tracheobronchial deposition [1]. However, such small particles are typically extremely cohesive: they have poor flowability and form large agglomerates that are difficult to entrain into the airstream. The drug is therefore often pre-mixed with an excipient composed of larger carrier particles. De-agglomeration of the drug from the carrier particles is accomplished (primarily by impacts) as the entrained formulation exits the DPI.

Lactose powder is frequently used as an excipient in drug formulations for use in dry powder inhalers (DPIs). In many DPIs the powder drug dose is stored in a foil sealed "blister" until use. Typically the foil seal is then pierced by an inlet and outlet tube and the blister itself forms the entrainment part of the air path through the DPI, see Fig. 10.1.

Good performance of the entrainment geometry of a DPI is necessary to achieve good drug delivery performance. Computational fluid dynamics (CFD) can potentially aid the designers of DPIs if the entrainment process can be accurately simulated.

10.1.2 Overview of Paper

In this study we compare CFD simulations and some initial experimental observations of entrainment of lactose powder using an example DPI geometry and typical patient inhalation airflow profiles.

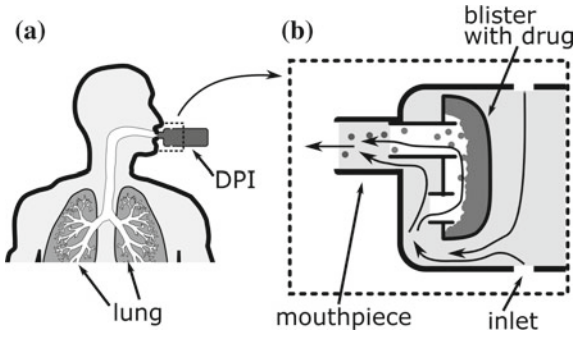

Fig. 10.1 Schematic illustration of the drug delivery process with a DPI. **a** The DPI and the respiratory tract. **b** A close-up view of the DPI

10.2 Methods

10.2.1 Computational Simulation

For this study the example entrainment geometry investigated was a 2D representation of a blister type entrainment geometry with length ~6 mm, see Fig. 10.2 The geometry had previously been computationally optimised to perform consistently, with low sensitivity to the patient's inhalation profile, using a similar process to that described in Kopsch et al. [2].

In CFD analysis for DPIs the particulate (drug) phase can either be ignored (a single phase approach considering air flow only) or modelled using a multiphase approach. The majority of reported studies using multiphase approaches for simulation of DPIs have used Eulerian-Lagrangian (EL), i.e. particle-tracking, approaches [3]. However, EL approaches make it difficult to study the fluidization process of a powder bed due to the large number of particle-particle interactions. It is for this reason that Zimarev et al. [4] introduced an Eulerian-Eulerian (EE) CFD approach to model the entrainment of drug in a DPI and to optimize the entrainment part of a DPI. When the volume fraction of drug is very high, the EE approach is more computationally efficient than an EL particle tracking approach.

In the EE approach, the drug particles are modelled as a second continuous phase and the interaction between the gas and the granular phase is modelled. A new

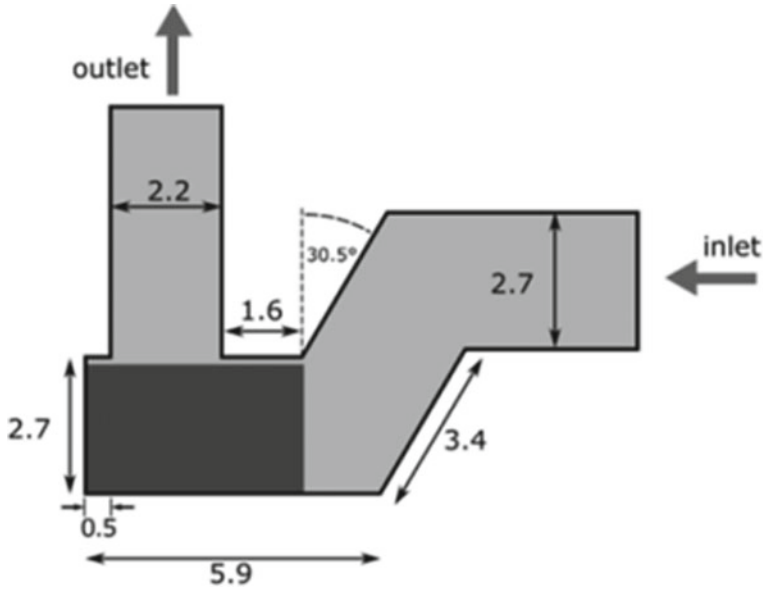

Fig. 10.2 The tested geometry with dimensions in mm indicated. The dark grey area indicates the initial powder load in the CFD simulations

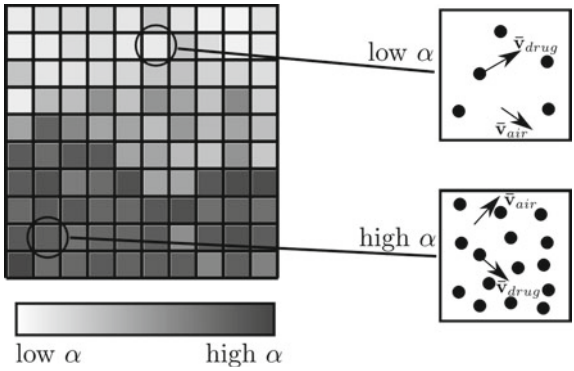

Fig. 10.3 Idealized representation of the Eulerian-Eulerian (EE) approach. The volume fraction α indicates the density of particles

Table 10.1 Settings for the OpenFOAM EE CFD solver

CFD modelling parameter	Sub-model selected
Granular viscosity model	'Gidaspow' [7]
Frictional stress model	'Johnson Jackson' [8]
Conductivity model	'Gidaspow' [7]
Granular pressure model	'Lun' [5, 9]
Radial distribution	'Lun Savage' [5, 9]
Drag coefficient	'GidaspowErgunWenYu' [7]

variable, the volume fraction (α) is introduced to keep track of the local fraction of granular phase. As in other CFD approaches the domain of interest is split into a large number of cells. For each cell the EE algorithm solves for a number of variables including the volume fraction α, the average velocity of drug particles $\bar{\mathbf{v}}_{drug}$ and the average velocity of the gaseous phase $\bar{\mathbf{v}}_{air}$. As shown in Fig. 10.3 the value of α indicates the number of particles in that cell. In an EE approach, all phases, including the particulate phases, are modelled as continuous fluids and consequently mass, momentum and energy conservation laws are applied to all phases. In many cases, these equations look similar to the standard Navier-Stokes equations. The kinetic theory of granular flow (KTGF) [5] is one method to model the constitutive behaviour of a granular phase in the EE approach. KTGF makes predictions about stresses and phase interaction terms in the governing equations of the fluid.

For this study 2D transient CFD simulations were carried out using "twoPhaseEulerFoam": an OpenFoam [6] EE solver with k-ε turbulence modelling. KTGF sub-models of particle-particle interaction were used to provide the constitutive behaviour of the powder phase. The sub-models used in this work are given in Table 10.1.

The powder was modelled as uniform sized particles with diameter equal to the measured D50 size of the lactose powders used in the later experiments, i.e. 59 and 119 μm, see Table 10.2. The simulations modelled the progression of entrainment

Table 10.2 Powder characteristics of two different lactose powders

Manufacturer	DMV-Fonterra Excipients GmbH & Co. KG			
Product name	Respitose® SV003		Respitose® Lactohale 100	
	Measured	Specification	Measured	Specification
D10 (μm)	33.1 ± 0.2	19–43	50.9 ± 0.6	45–65
D50 (μm)	59.2 ± 0.1	53–66	119.4 ± 0.4	125–145
D90 (μm)	89.9 ± 0.3	75–106	200.4 ± 2.4	200–250
Poured density (g/L)		630		690
Tapped density (1250 taps) (g/L)		780		840

subject to two time varying flow rate profiles representative of typical patient inhalation maneuvers: one high and one low flow rate.

10.2.2 Experiment

Lactose Powders

Experiments were carried out with two different powders: Respitose SV003 and Lactohale 100 (measured D50 of 59 and 119 μm respectively, both DMV-Fonterra Excipients GmbH). The material properties as specified by the manufacturer are shown in Table 10.2. Most real pharmaceutical powders, including the lactose powders chosen in this study, are not monodisperse in size (as assumed for the CFD simulations). Instead, they consist of particles of a range of different diameters. Table 10.2 shows the D10, D50 and D90 values for these powders as specified by the manufacturer. To validate these specifications a measurement of particle size distribution was carried out. The particle size distribution for was measured with a laser diffraction system, a Sympatec HELOS laser diffraction sensor [10] together with a Sympatec RODOS dry dispersing unit [11]. Measured values are included in Table 10.2 where the stated error is the standard deviation over four repeated measurements. Measured values are generally in agreement with the specification.

Entrainment Module

Entrainment experiments were carried out with an apparatus based on the same 2D geometry as used for the CFD simulations. The geometry was laser cut from a 3.15 mm thick opaque acrylic sheet that was then clamped between two transparent acrylic sheets, see Fig. 10.4. The experimental powder dose was pre-loaded before assembly of the geometry.

Breathing Simulator

In order to simulate a patient's inhalation maneuver, a breathing simulator (model BRS 3000 [12] from Copley Scientific) was used. The breathing simulator could

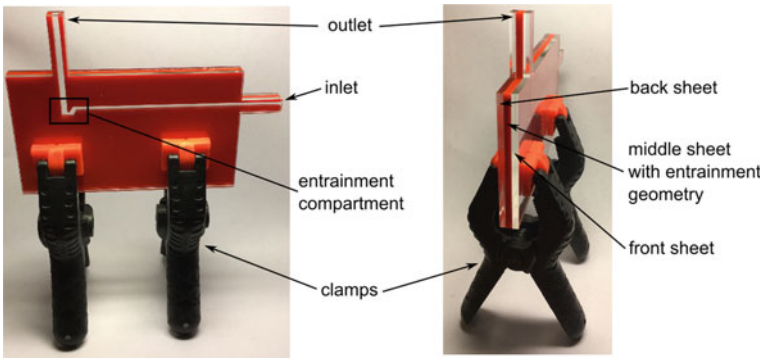

Fig. 10.4 Assembled entrainment module

generate user-defined inhalation flow rate profiles. It consists of a piston whose movement is controlled by a microprocessor. Integrated software allows a flow rate profile to be specified. The breathing simulator was connected to the outlet of the entrainment unit via a filter. The purpose of the filter was to remove powder from the air flow before it entered the breathing simulator. A digital flow meter (Certifier FA Plus Ventilator Test System 4080 [13] by TSI Inc.) was connected to the inlet of the entrainment unit. The flow meter monitored the specified flow rate profile. Figure 10.5 depicts schematically the position of the breathing simulator, the entrainment module and the flow meter.

Camera and Illumination

During the entrainment process, the entrainment compartment was filmed with a high-speed camera. The camera (Casio Exilim EX-FH20 [14]) was set to high-speed mode (1000 frames per second). It was mounted with a tripod screw on a wooden platform to fix the relative position of the camera and the entrainment module. The goal was to obtain the same image section consistently in different experiments. The entrainment module was illuminated from the back. A diffusion panel (a thin sheet of paper) was placed between the lamp and the entrainment module to reduce optical artefacts. Figure 10.6 shows two photos of the complete experimental setup.

Inhalation Flow Rate Profiles

The specified flow rate profiles $Q_{\text{high}}(t)$ and $Q_{\text{low}}(t)$ are shown in Fig. 10.7. Both flow rate profiles started with the inhalation maneuver at time $t = 0$ s. The maximum flow rate of the inhalation profile was reached at time $t = 0.45$ s after the onset of the inhalation. For the 'high' flow rate profile the peak flow was 20 L min^{-1}, for the 'low' flow rate profile the peak was 14 L min^{-1}. Since an air bypass was not incorporated in the entrainment module, the chosen peak values were lower than typical peak values of real patients [15] to account for the absent bypass. For both profiles, inhalation was complete at time t = 3.7 s. At this time, most of the powder

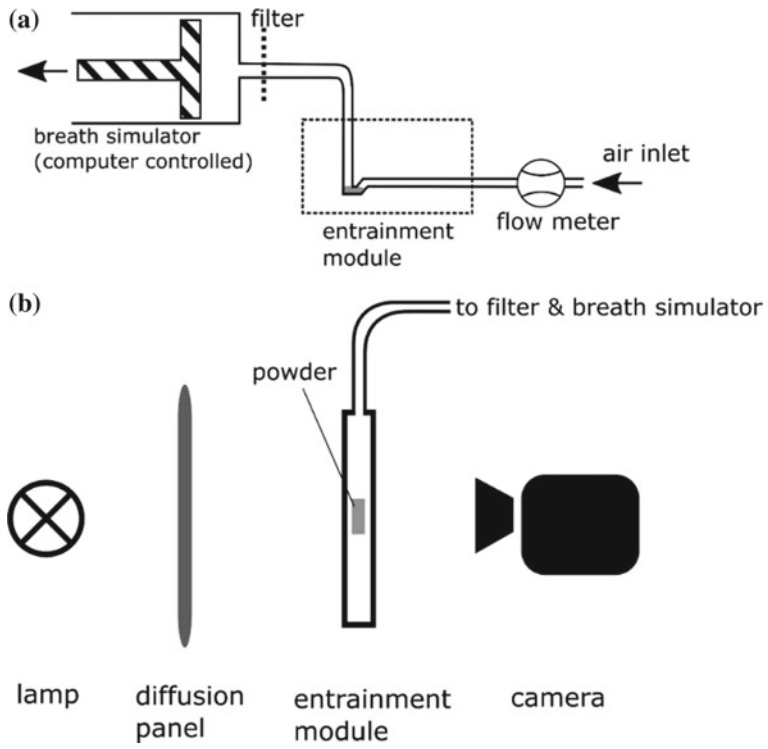

Fig. 10.5 Setup of the entrainment experiment. **a** Front view: the breathing simulator generates a flow through the entrainment module. **b** Side view: a camera records the powder in the entrainment module

was typically entrained. However, video post-processing is simplified if a reference frame with the evacuated entrainment unit is available. Consequently, a high flow rate was applied from time $t = 5$ to 11 s to evacuate the entrainment unit completely. The exact length and strength of the evacuation flow profile was not important as long the compartment was emptied. As an illustration, Fig. 10.7b shows how the distribution of drug in the entrainment compartment may look as a function of time.

Analysis of the Entrainment Videos

The aim of analysing the entrainment videos was to compare the experimental observations of the entrainment process with predictions from CFD simulations. This was done both qualitatively and quantitatively. Qualitatively, individual frames from an entrainment video were compared with the corresponding CFD contour plots of the volume fraction α. Quantitatively, the mass of drug released $M(t)$ as a function of time t was determined from the videos and compared to CFD predictions.

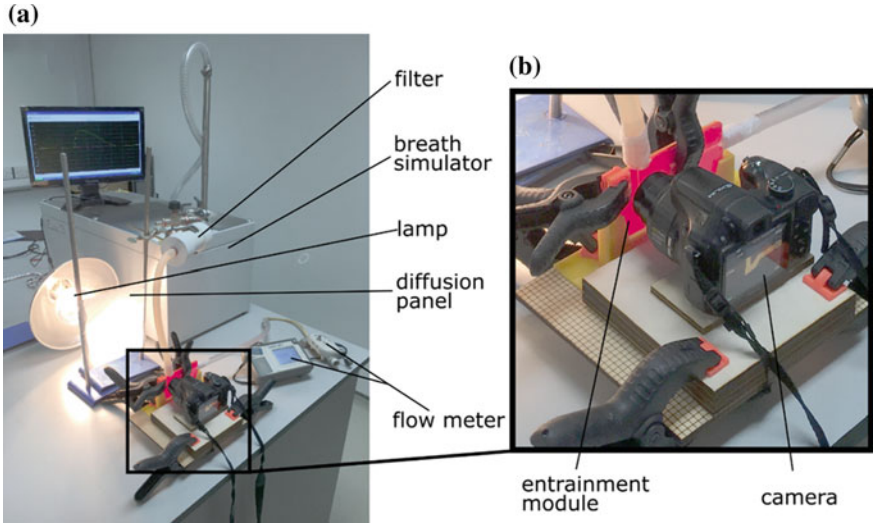

Fig. 10.6 Setup of the entrainment experiment. The breathing simulator generates a flow rate profile through the entrainment module, while a camera records the process

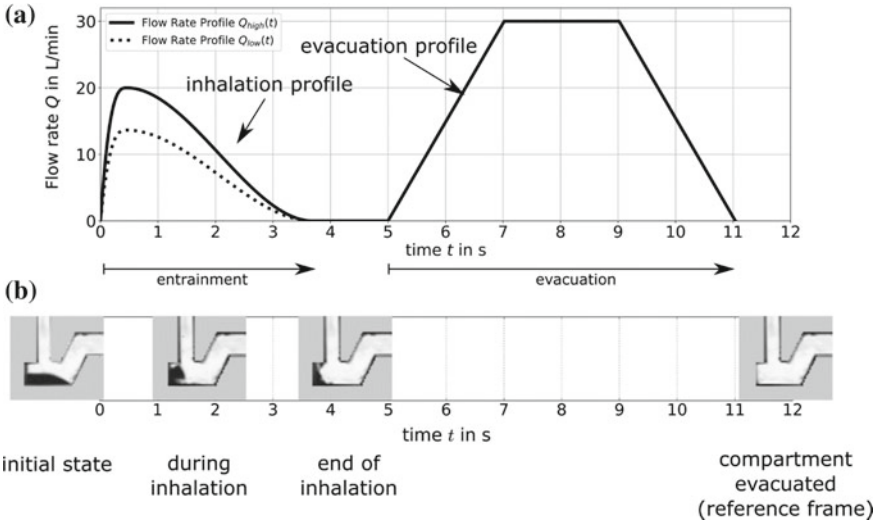

Fig. 10.7 **a** The specified inhalation flow rate profiles $Q_{\text{high}}(t)$ and $Q_{\text{low}}(t)$. The entrainment time interval and the evacuation time interval are indicated. **b** An illustration of the entrainment process as a function of time (sample data for illustration only)

10.3 Results

For both powders SV003 and LH100 experimental entrainment results were compared to CFD predictions. A qualitative comparison of video frames and CFD contour plots of the volume fraction α for the 'high' flow profile are shown in Fig. 10.8. The CFD prediction is in good agreement with the experimental video footage for both powders.

Figure 10.9 compares the predicted mass release profile $M(t)$ and the corresponding experimental measurement for both 'high' and 'low' flow profiles. Each experimental curve is the average of three experiments. Good agreement between the CFD prediction and the experiment is observed.

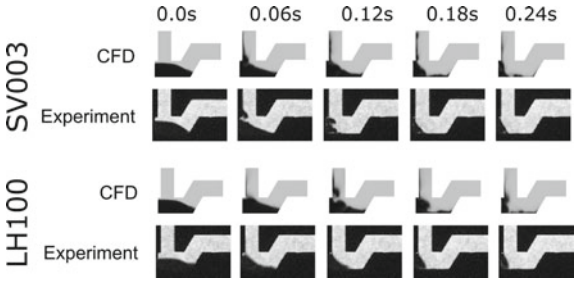

Fig. 10.8 Comparison of CFD and experimental images of entrainment with the high flow profile. Air flow is from right to left

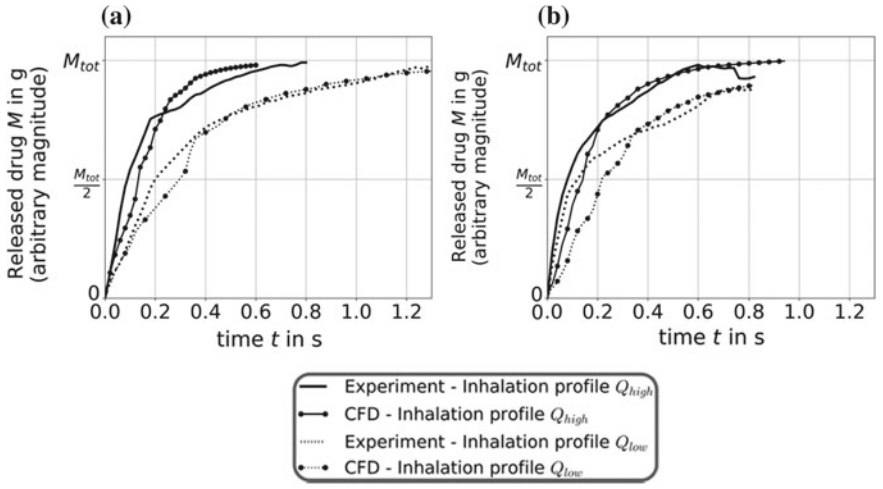

Fig. 10.9 Comparison of predicted (CFD) and experimentally measured drug powder release with both the high and low flow profiles. **a** SV003 **b** LH100

10.4 Conclusions

The aim of this work was to make a preliminary experimental validation of the EE CFD method for simulating entrainment of lactose in an example DPI geometry. This was achieved by conducting entrainment experiments with a transparent entrainment module, two different lactose powders and two different inhalation flow rate profiles. Entrainment processes were recorded with a high-speed camera and the resulting video footage was compared qualitatively and quantitatively with the corresponding CFD prediction. For the quantitative comparison $M(t)$, the mass of released drug, was inferred from the measured intensity distribution.

Limitations of the EE CFD method used were that cohesive interaction and de-agglomeration of particles were not modelled. Nonetheless, the CFD predictions agreed strongly with the experimental results for lactose powders SV003 and LH100.

The experimental validation results reported in this work suggest excellent promise for modelling entrainment of lactose powder drug formulations in DPIs with an EE CFD approach.

References

1. Labiris, N.R., Dolovich, M.B.: Pulmonary drug delivery. Part I: physiological factors affecting therapeutic effectiveness of aerosolized medications. Brit. J. Clin. Pharm. **56**(6), 588–599 (2003)
2. Kopsch, T., Murnane, D., Symons, D.: Optimizing the entrainment geometry of a dry powder inhaler: methodology and preliminary results. Pharm. Res. **33**(11), 2668–2679 (2016)
3. Parisini, I., Cheng, S.J., Symons, D., Murnane, D.: Potential of a cyclone prototype spacer to improve in vitro dry powder delivery. Pharm. Res. **31**(5), 1133–1145 (2014). https://doi.org/10.1007/s11095-013-1236-8
4. Zimarev, D., Parks, G., Symons, D.: Computational modelling and stochastic optimization of entrainment geometries in dry powder inhalers. In: DDL24 Conference (2013)
5. Ding, J., Gidaspow, D.: A bubbling fluidization model using kinetic theory of granular flow. AIChE J. **36**(4), 523–538 (1990). https://doi.org/10.1002/aic.690360404
6. The OpenFOAM Foundation. OpenFOAM 2.4. http://www.openfoam.org/
7. Gidaspow, D., Bezburuah, R., Ding, J.: Hydrodynamics of circulating fluidized beds: kinetic theory approach. In: Proceedings of the Seventh Engineering Foundation Conference on Fluidization (1992)
8. Johnson, P.C., Jackson, R.: Frictional-collisional constitutive relations for granular materials, with application to plane shearing. J. Fluid Mech. **176**(-1), 67 (1987). https://doi.org/10.1017/s0022112087000570
9. Lun, C.K.K., Savage, S.B., Jeffrey, D.J., Chepurniy, N.: Kinetic theories for granular flow: Inelastic particles in Couette flow and slightly inelastic particles in a general flowfield. J. Fluid Mech. **140**, 223–256 (1984). https://doi.org/10.1017/S0022112084000586
10. Sympatec GmbH. http://www.sympatec.com/EN/LaserDiffraction/HELOS.html. Accessed 15 June 2017 (2017)
11. Sympatec GmbH. http://www.sympatec.com/EN/LaserDiffraction/RODOS.html. Accessed 15 June 2017 (2017)
12. Copley Scientific. Quality Solutions for Inhaler Testing (2015)
13. TSI Inc. Certifier FA Ventilator test systems—for gas flow analysis (manual) (2010)

14. Casio Computer Co. Ltd. Digital Camera EX-FH20 User's guide (2008)
15. de Koning, J.P., van Der Mark, T.W., Coenegracht, P.M.J., Tromp, T.F.J., Frijlink, H.W.: Effect of an external resistance to airflow on the inspiratory flow curve. Int. J. Pharm. **234**(1–2), 257–266 (2002). https://doi.org/10.1016/S0378-5173(01)00969-3

Chapter 11
Oblique Impact of a Droplet on a Textured Substrate

Hossein Rashidian and Mathieu Sellier

Abstract This study presents the modelling of an oblique drop impact on a textured substrate using the multiphase lattice Boltzmann method to understand the conditions under which the lamella lifts off the substrate and generates a satellite droplet. Depending on the impact angle and the Weber number, four various outcomes are observed: asymmetric spreading, bilateral splashing including a prompt splash and a corona splash, one-sided coronal splashing and asymmetric break-up. To obtain a better understanding of when splashing is likely to occur, a graph which shows splashing thresholds for a range of normal Weber numbers and impact angles between 5° and 45° is presented. Numerical results show that an increasing proportion of the droplet bounces off the surface in the form of satellite droplets for increasingly tangential impacts. Furthermore, the influence of substrate texture parameters such as the height of posts and wettability of the substrate are investigated. Results show that splashing vanishes as the wettability of the substrate increases. Also, the space between posts and the height of posts is shown to play an important role on the occurrence of splashing.

Keywords Oblique droplet impact · Textured substrate · Multiphase lattice Boltzmann method

11.1 Introduction

The impact of droplets onto solid surfaces has been extensively studied over the past due to its importance in a range of applications such as inject printing or spray coating but also because it encompasses some of the most difficult modelling challenges in fluid mechanics such as a free surface, a wetting front or topography changes. The current state of the knowledge is comprehensively reviewed by Josserand and Thoroddsen [1]. Better understanding how the droplet wets a solid surface after

H. Rashidian · M. Sellier (✉)
University of Canterbury, Christchurch 8041, New Zealand
e-mail: mathieu.sellier@canterbury.ac.nz

S. Gutschmidt et al. (eds.), *IUTAM Symposium on Recent Advances in Moving Boundary Problems in Mechanics*, IUTAM Bookseries 34,
https://doi.org/10.1007/978-3-030-13720-5_11

impact is critical to obtaining a better control in practical applications. For example, one may wish to avoid lamella break-up and the production of satellite droplets post-impact in the application of pesticide on foliage.

For normal impacts on solid surfaces, Rioboo et al. proposed that the wetting outcomes can be broken down into five categories: deposition, rebound, receding break-up, prompt splash and corona splash [2]. The regime of interest here is the splashing because this phenomena, observed in many applications, still remains less understood. As a droplet impacts on a solid surface, the kinetic energy of the droplet is transformed into surface energy (potential energy) and dissipated by the viscous shear. If kinetic energy overcomes surface energy, the lamella may either generate tiny droplets at the contact line (prompt splash) or lifts off and detaches away from the substrate and generates satellite droplets (corona splash). Simple dimensional analysis reveals that the main dimensionless number expressing the ratio of inertia forces to surface tension forces is the Weber number:

$$\mathrm{We} = \frac{\rho V^2 D}{\sigma} \tag{11.1}$$

where ρ and σ are the density and surface tension of the liquid, respectively. D denotes the diameter of the droplet and V refers to the impact velocity.

Several studies have described the dynamics of a droplet which impacts normally onto a textured substrate [3–6]. Generally, at a high enough Weber number, increment of the roughness amplitude of substrates leads eventually to prompt splash [3]. Experiments also demonstrated that the presence of a small vertical obstacle promotes corona splash [4]. Furthermore, the drop splashing threshold is dependent on geometrical parameters of the textured substrate [5]. In addition to surface morphology, the ambient pressure may affect the dynamics of the wetting front so that the splashing vanishes with a decrease in the ambient pressure [6].

In spite of the large number of important applications, the understanding of oblique impacts is, on the other hand, a lot less advanced. For oblique impacts, both the normal and tangential components of the impact velocity are considered and therefore the behaviour of the lamella spreading is more complex. In particular, an important question is how the tangential component of the impact velocity influences the dynamics of the contact line. To address this question, several researchers studied vertical impact onto an inclined stationary surface [7–10] and others investigated the vertical impact of droplets onto a moving surface which equally resulted in a tangential component of the impact velocity [11–13]. Another case for which the tangential component of the impact velocity matters is oblique impact on a horizontal surface. For such impacts, the role of the impact velocity components on the wetting outcomes has not to this day been investigated systematically.

The wettability of the substrate and the impact parameters such as the impact angle and the Weber number may affect the wetting outcome of oblique droplet impacts. Few studies exist on the oblique impact of droplets on super-hydrophobic surfaces. For example; Yeong et al. [8] performed an investigation of the impact and rebound dynamics of droplet impacting at an angle onto a super-hydrophobic surface and

reported that the maximum spread of the droplet is a function of both the normal and tangential components of the impact velocity. Aboud and Kietzig [13] carried out oblique drop impacts onto tilted moving surfaces with various wettability including super-hydrophobic surfaces to obtain the oblique splashing threshold. Although the wettability of the surface was considered in the above studies, the effect of the geometrical parameters of the textured hydrophobic surface such as the space between posts, the height of the posts have not been investigated.

On the other hand, the aforementioned efforts in the literature have been experimental and therefore a numerical modelling of the dynamics of the lamella resulting from the oblique impact of a droplet onto a horizontal textured substrate has not performed yet. Thus, this work is a first attempt to simulate the behaviour of the lamella and investigate numerically the conditions under which it breaks-up and generates a satellite droplet. Furthermore, the influence of geometrical parameters of the textured substrate as well as the impact parameters is studied systematically. Thus, the aim of this contribution is to provide a greater understanding of the relation between the splashing, the impact parameters, and the substrate texture. To achieve this goal, we have developed a two-dimensional multiphase lattice Boltzmann code following the Shan-Chen model [14]. In recent years, the lattice Boltzmann method (LBM) which is based on the mesoscopic kinetic equation has been developed as a powerful tool for simulating multiphase fluid systems.

The remainder of the paper is structured as follows. Section 11.2 describes the multiphase lattice Boltzmann method in details. Then, a validation case is presented in Sect. 11.3. In this section, we perform simulations to calculate the maximum spread of an oblique impacting droplet onto a smooth surface and compare the numerical results with a correlation reported by Yeong et al. [8]. Section 11.4 represents the various possible splashing outcomes of the oblique impact of a droplet onto a textured substrate and investigates the effects of the impact angle, Weber number and wettability of the textured substrate. Finally, Sect. 11.5 presents concluding remarks.

11.2 Computational Algorithm

In the LBM, the simulation domain is divided into lattices which are occupied by either a fluid (liquid or gas) or a solid. The main variable is the density distribution function $f_k(\boldsymbol{x}, t)$ which represents the state of the particle collection. The lattice position vector at time t is represented by $\boldsymbol{x}$ and the velocity direction is denoted by the label k. The density distribution function is discretised using the typical D2Q9 lattice arrangement [15]. This velocity model involves nine microscopic velocity vectors in two space dimensions. For this model, the microscopic velocity vectors $\boldsymbol{e}_k$ and weights ω_k are defined as follows:

$$\boldsymbol{e}_k = \begin{cases} (0,0) & k=0 \\ c\left(\cos\left(\frac{(k-1)\pi}{2}\right), \sin\left(\frac{(k-1)\pi}{2}\right)\right) & k=1,2,3,4 \\ \sqrt{2}c\left(\cos\left(\frac{(k-\frac{9}{2})\pi}{2}\right), \sin\left(\frac{(k-\frac{9}{2})\pi}{2}\right)\right) & k=5,6,7,8 \end{cases} \tag{11.2}$$

$$\omega_k = \begin{cases} 4/9 & k=0 \\ 1/9 & k=1,2,3,4 \\ 1/36 & k=5,6,7,8 \end{cases} \tag{11.3}$$

In the above, c denotes the lattice speed which is given by $c = \frac{\Delta x}{\Delta t}$ where Δx and Δt are the lattice unit (*lu*) and the time step (*ts*), respectively. Within the LBM, a fluid is modelled as a fraction of the distribution functions which streams with $\boldsymbol{e}_k$ from $\boldsymbol{x}$ to its neighbouring lattice $\boldsymbol{x} + \boldsymbol{e}_k \Delta t$ via certain directions k at the following time step Δt. This process is named the streaming step. Another process which is called the collision step occurs since a portion of other particles is moving from various directions to the same lattice simultaneously. The collision step which takes account of the rate of change in the particle distribution can be simplified to the Bhathagar-Gross-Krook (BGK) single relaxation time approximation [15]. Both above-mentioned steps are embodied by the discretized Boltzmann equation:

$$f_k(\boldsymbol{x} + \boldsymbol{e}_k \Delta t, t + \Delta t) - f_k(\boldsymbol{x}, t) = \frac{\Delta t}{\tau}\left[f_k^{eq}(\boldsymbol{x}, t) - f_k(\boldsymbol{x}, t)\right] \tag{11.4}$$

The left hand side of the Eq. 11.4 expresses the streaming step and the right hand side represents the collision step where τ is the relaxation time adjusted to 1. The kinematic viscosity which is related to the relaxation time is defined as $\upsilon = c_s^2(\tau - 0.5)\Delta t$ where the sound speed is determined as $c_s^2 = \frac{c^2}{3}$. In the collision step, the equilibrium distribution function f_k^{eq} is calculated as:

$$f_k^{eq} = \omega_k \rho \left[1 + \frac{\boldsymbol{e}_k.\boldsymbol{u}}{c_s^2} + \frac{1}{2}\left(\frac{\boldsymbol{e}_k.\boldsymbol{u}}{c_s^2}\right)^2 - \frac{\boldsymbol{u}.\boldsymbol{u}}{2c_s^2}\right] \tag{11.5}$$

where ρ and $\boldsymbol{u}$ denote the fluid density and velocity, respectively. These quantities can be determined from the density distributions:

$$\rho = \sum_{k=0}^{8} f_k \tag{11.6}$$

$$\boldsymbol{u} = \frac{1}{\rho}\sum_{k=0}^{8} f_k \boldsymbol{e}_k \tag{11.7}$$

For fluid nodes, an initial velocity u_0 needs to be assigned as well as an initial density ρ_0 which is either the gas density ρ_g or the liquid density ρ_l. The following initial assumption can be applied as the relaxation time is unity:

$$f_k(\boldsymbol{x}, t = 0) = f_k^{eq}(\boldsymbol{x}, t = 0) = f_k^{eq}(\rho_0, \boldsymbol{u}_0) \tag{11.8}$$

Following Benzi et al. [16], the solid nodes possess an artificial wall density ρ_w where $\rho_g \leq \rho_w \leq \rho_l$ to tune the substrate contact angle [17]. It is also important to note that for the lateral sides of the bounding box, periodic boundary conditions are applied for which the distribution functions carry on the opposite wall once they reach the end of the region. We also consider bounce-back boundary conditions at the solid-liquid interface as the known distribution functions from the streaming process hit the wall and scatter back to the fluid via its incoming lattice link. To obtain the inter-particle forces, the single component multiphase Shan-Chen model [14] is used as follows:

$$\boldsymbol{F}(\boldsymbol{x}, t) = -G\psi(\boldsymbol{x}, t) \sum_{k=0}^{8} \omega_k \psi(\boldsymbol{x} + \boldsymbol{e_k}\Delta t, t)\boldsymbol{e}_k \tag{11.9}$$

where G denotes the attraction strength factor and creates the liquid-gas interface with constant surface tension, density gradient and interface thickness. ψ denotes the mean field potential term and is a function of density such that [18]:

$$\psi(\rho) = \sqrt{\frac{2\left(P - c_s^2\rho\right)}{c_s^2 G}} \tag{11.10}$$

where P denotes the pressure and is determined from the Carnahan-Starling (C-S) equation of state (EOS) [19]:

$$P = \rho\gamma T \frac{1 + \frac{\beta\rho}{4} + \left(\frac{\beta\rho}{4}\right)^2 - \left(\frac{\beta\rho}{4}\right)^3}{\left(1 - \frac{\beta\rho}{4}\right)^3} - \alpha\rho^2 \tag{11.11}$$

where T denotes the temperature and can be obtained by $T = 0.0943T_0$ as $\alpha = 1\ lu^5/(mu.ts^2)$, $\beta = 4\ lu^3/mu$ and $\gamma = 1\, lu^2/(ts^2.tu)$ [19]. mu and tu are the mass unit and the temperature unit, respectively.

An alternative velocity named the equilibrium velocity is considered for calculating the equilibrium distribution function [14]:

$$\boldsymbol{u}^{eq} = \boldsymbol{u} + \frac{\boldsymbol{F}\tau}{\rho} \tag{11.12}$$

where $\boldsymbol{u}^{eq}$ denotes the equilibrium velocity and replaces $\boldsymbol{u}$ in Eq. 11.5.

After collision, a new collection of distribution functions can leave this collision lattice and another streaming step starts. These steps are performed until a final desired time is reached. Finally, the density contours can be plotted to show the liquid behaviour during its interaction with the gas and the solid. During our simulation, default values of the liquid density and gas density are $0.285\, mu/lu^3$ and

$0.0285\, mu/lu^3$, respectively. Furthermore, the effect of gravity is neglected as it is assumed to be negligible compared to inertia and surface tension.

11.3 Validation

The maximum spread which occurs when an impacting droplet deforms to its largest extent along a substrate is considered as a validation case. For an oblique impact, the maximum spread is the outcome of an asymmetric behaviour created by the tangential component of the impact velocity. Since the tangential momentum affect such drop impacts, a normal and tangential Weber number is defined through the normal impact velocity V_n and the tangential impact velocity V_t:

$$\mathrm{We}_n = \frac{\rho V_n^2 D}{\sigma} \tag{11.13}$$

$$\mathrm{We}_t = \frac{\rho V_t^2 D}{\sigma} \tag{11.14}$$

The impact angle, illustrated in Fig. 11.3, is defined as:

$$\Phi = \tan^{-1} \frac{V_n}{V_t} \tag{11.15}$$

Yeong et al. [8] obtained a relationship between the normalized maximum spread D_{max}/D and the Weber numbers:

$$(D_{max}/D) = 0.9\, \mathrm{We}_n^{0.25} + C\, \mathrm{We}_t \tag{11.16}$$

where C is a constant equal to 0.005. It should be noted that this correlation is valid for $We_n < 60$ since break-up occurs beyond this value.

We now model the impact of a droplet with a diameter of $D = 200\, lu$ and impact velocity V under an initial impact angle $\Phi = 30°$ onto a smooth substrate with an equilibrium contact angle of $\theta = 150°$. Figure 11.1 shows the droplet at maximum spread when the Weber number is 50. For this case, the non-dimensional maximum spread calculated via correlation 15 yields 3.14, while our simulation gives 3.17 (error is around 1%).

Numerical simulations are performed for a various range of the normal Weber numbers from 10 to 50. A comparison between the normalized maximum spread determined numerically (the blue line) and Eq. 11.16 (the black spot) is shown in Fig. 11.2. It can be seen that a good agreement is found. The maximum error is 3.7% as $\Phi = 10°$.

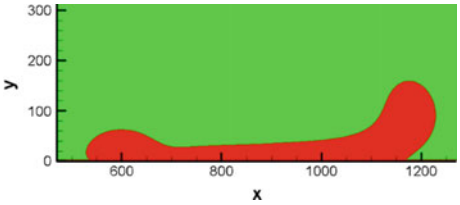

Fig. 11.1 Numerical simulation of the maximum spread of a droplet when the normal Weber number and the impact angle are 50° and 30°, respectively

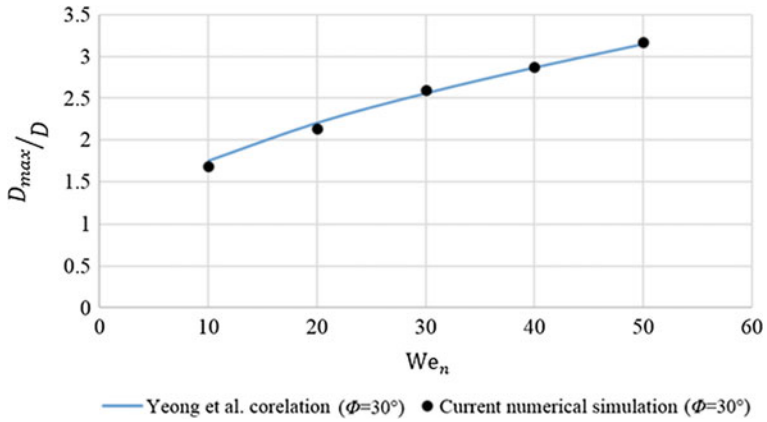

Fig. 11.2 Comparison between the current numerical simulations and the correlation reported by Yeong et al. [8] for the maximum spread of an oblique impact drop on a super-hydrophobic surface when the impact angle is 30°

11.4 Results and Discussion

11.4.1 Outcomes Classification

We consider now an oblique droplet impacts on a textured substrate as is shown in Fig. 11.3. The size of the droplet is $D = 200lu$ during all simulations and because of its diagonal motion, the impact velocity of the droplet contains two components: $V_n = V \sin \Phi$ and $V_t = V \cos \Phi$. The textured substrate features an array of identical posts. To restrict the number of independent parameters, posts have unit aspect ratio and unit spacing ratio. Therefore the width of posts W, the space between posts S, and the height of posts H are equal and such that $W = S = H = 10\,lu$. The equilibrium contact angle of the substrate is set to $\theta = 150^{\circ}$ which is referred to a super-hydrophobic surface.

First, we investigate the possible outcomes which are observed during our simulations. Four possible outcomes are illustrated in Fig. 11.4: (a) an asymmetric spreading occurs as the lamella may spread onto substrate in an asymmetrically without splash-

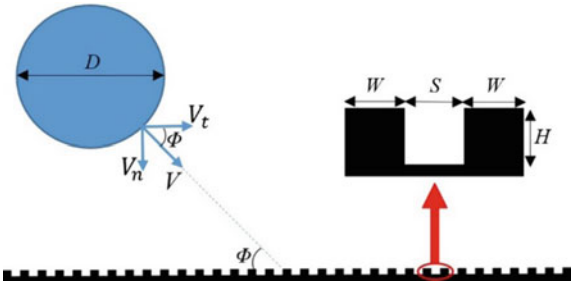

Fig. 11.3 Schematic of an oblique impacting droplet with a diameter of D and an impact angle Φ onto a substrate. V, V_n and V_t denote the impact velocity, the normal component and tangential components of the impact velocity, respectively

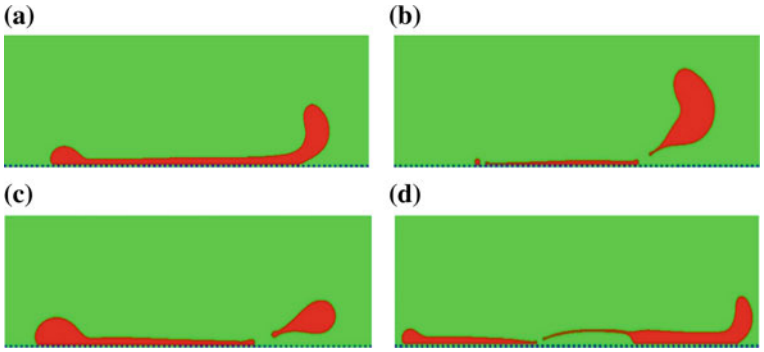

Fig. 11.4 Four various possible outcomes of the oblique impact of a droplet onto a superhydrophobic textured substrate: **a** asymmetric spreading ($We_n = 125$ and $\Phi = 30°$), **b** bilateral splashing includes simultaneous occurrence of both the prompt splash and the corona splash ($We_n = 140$ and $\Phi = 20°$), **c** one-sided corona splashing ($We_n = 140$ and $\Phi = 30°$) and **d** asymmetric break-up ($We_n = 690$ and $\Phi = 60°$)

ing, (b) bilateral splashing including a prompt splash which generates tiny droplets onto the substrate from the receding contact line of the lamella and a corona splash which launches a satellite droplet from the advancing contact line of the lamella, (c) one-sided corona splashing which only occurs at the advancing contact line of the lamella and finally (d) an asymmetric break-up which takes place as an air pocket appears and grows underneath the lamella and causes a break-up at maximum spread. It is also worth noting that the combination outcome of (c) and (d) in Fig. 11.4 may occur. This combination happens when the normal Weber number increases in Case (d) and as a consequence in addition to the occurrence of the asymmetric break-up, the one-sided corona splashing also takes places in the separated right hand part of the lamella.

11.4.2 Effect of Impact Parameters on Splashing

The impact angle of the droplet as well as its normal Weber number lead to different wetting outcomes as mentioned in previous section. Numerical results demonstrate that the asymmetric spreading can be observed so long as the normal weber number is insufficient to trigger splashing. Therefore, such outcome may occur for any impact angle. If the normal Weber number is high enough, splashing and asymmetric break-up take place. While bilateral splashing only takes place as long as the impact angle is $\Phi \leq 20°$, the one-sided corona splashing happens for an impact angle between $25° \leq \Phi \leq 45°$. When the impact angle becomes $\Phi \geq 50°$ the asymmetric break-up can occur.

Figure 11.5 illustrates the splashing threshold values for an oblique impact with an impact angle of $5° \leq \Phi \leq 45°$. There is no splash in the area located on the left hand side of the line. It can be seen that splashing is likely to occur with a decrease in the impact angle (i.e. increasingly tangential impact). In other words, with a lower normal weber number, splashing takes place for smaller impact angles.

During corona splashing, amount of the mass which detaches away from the lamella is also an interesting quantity. In thermal spraying and for a smooth surface, Sobolev and Guilemany [20] reported that the ratio χ of the mass of the droplet which remains onto the substrate to the initial mass of the droplet is dependent on the impact angle as follows:

$$\chi \sim \sin \Phi$$

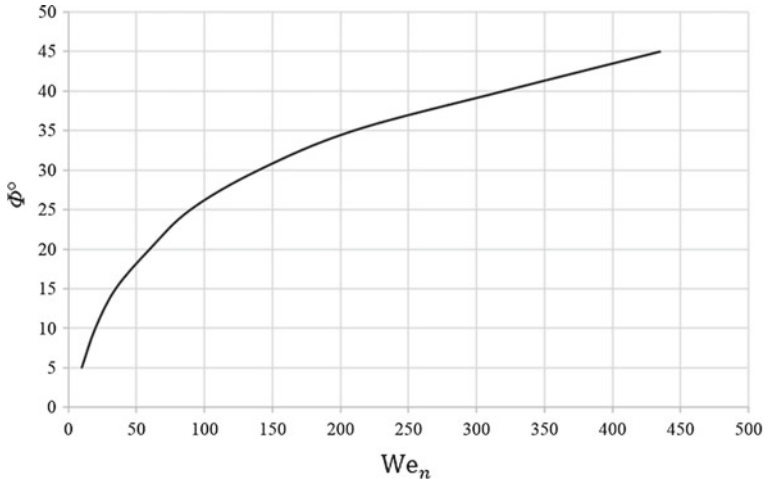

Fig. 11.5 Corona splashing threshold for an oblique impact with a range of the impact angle between 5° and 45°. On left hand side of the line splashing does not occur

From the above relation, it is obvious that the loss of the droplet mass due to splashing decreases as the impact angle increases. To confirm this trend, we compared two different cases with the same normal Weber number ($We_n = 140$) and different impact angles ($\Phi = 20°$ Case (b) and $\Phi = 30°$ for Case (c) in Fig. 11.4). It can be seen that with an increase in the impact angle from $\Phi = 20°$ to $\Phi = 30°$, the mass of the satellite droplet generated during splashing decreases as predicted.

11.4.3 Effect of Texture Parameters on Splashing

In addition to the impact parameters, the substrate parameters such as texture and wettability may influence on splashing. In this section, the normal Weber number and the impact angle are kept constant and equal to $We_n = 140$ and $\Phi = 30°$ (Case (c) in Fig. 11.4) and numerical simulation were performed for a range of substrate parameters.

First of all, the effect of texture on splashing is investigated. When the substrate does not feature posts, splashing does not occur for a contact angle of 150° with $We_n = 140$ and $\Phi = 30°$ as seen in Fig. 11.6. Conversely, the presence of texture with $W = S = H = 10\,lu$ was shown to trigger the splash for the same conditions (Case c in Fig. 11.4). To understand the role of the space between posts (S), the height of post (H), and the wettability of the substrate (θ) in appearance of splashing, we now simulate six different cases as are reported in Table 11.1 and compare these numerical results with Case (c) in Fig. 11.4. The simulation results for Case 1 and Case 2 for which only the space between posts is varied are depicted in Fig. 11.7. It can be seen that with S equal to 5 lu (Case 1) the splashing is unlikely to occur (see Fig. 11.7a), whereas with an increase in this parameter to 20 lu (Case 2) the splashing is observed (see Fig. 11.7b) as was seen for Case (c) for which S was 10 lu. The difference between Case 2 and Case (c) is that splashing occurs earlier (17,000 ts for Case 2 against 20,000 ts for Case (c)). This means that the space between posts affects the time and the likelihood of splashing.

Beside the space between posts, the height of the posts also plays an important role in splashing. Our numerical results demonstrate that for Case 3 for which the height of posts is $H = 5\,lu$ splashing does not happen as shown in Fig. 11.8a, while as previously observed in Fig. 11.4c splashing occurs when $H = 10\,lu$. Splashing takes

Fig. 11.6 Although the equilibrium contact angle of the substrate is $\theta = 150°$ splashing does not occur for an oblique impact on a smooth substrate with the impact parameters $We_n = 140$ and $\Phi = 30°$

Table 11.1 Six simulation cases with different substrate parameters

Case	Impact parameters		Substrate parameters				Status
	We_n	Φ (°)	W (lu)	S (lu)	H (lu)	θ (°)	
1	140	30	10	5	10	150	No splashing
2	140	30	10	20	10	150	Splashing
3	140	30	10	10	5	150	No splashing
4	140	30	10	10	20	150	Splashing
5	140	30	10	10	25	150	No splashing
6	140	30	10	10	10	110	No splashing
c in Fig. 11.4	140	30	10	10	10	150	Splashing

These simulation cases are compared with Case (c) in Fig. 11.4 of Sect. 4.1 for which the one-sided corona splashing took place

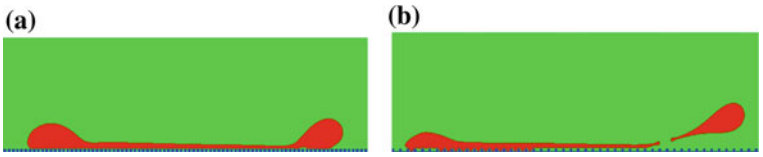

Fig. 11.7 The effect of the space between posts (S) on the occurrence of splashing for an oblique impact with $We_n = 140$ and $\Phi = 30°$ on a textured substrate with an equilibrium contact angle $\theta = 150°$: **a** the splashing is does not occur for Case 1 for which $S = 5\ lu$ and the height of posts (H) and the width of posts (W) are 10 lu but **b** splashing occurs for Case 2 which $S = 20\ lu$ and $H = W = 10\ lu$

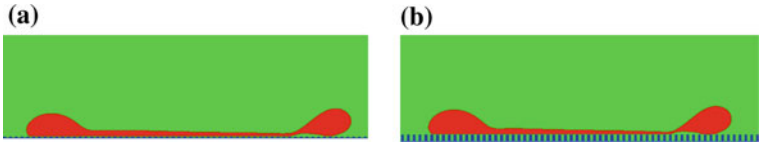

Fig. 11.8 For an oblique impacting droplet with $We_n = 140$ and $\Phi = 30°$ onto a textured substrate with $S = W = 10\ lu$, the splashing is unlikely to occur as the height of the posts are either **a** $H = 5\ lu$ or **b** $H = 25\ lu$

place until $H = 20\ lu$ (Case 4). When the height of posts reaches $H = 25\ lu$ (Case 5), splashing is once more prevented as shown in Fig. 11.8b. Thus, splashing occurs between two thresholds of post height. To investigate the effect of the wettability of the substrate on splashing, we consider another case (Case 6) for which the impact parameters ($We_n = 140$ and $\Phi = 30°$) and texture parameters ($W = S = H = 10\ lu$) are similar to Case c in Fig. 11.4. The equilibrium contact angle of the substrate is set to $\theta = 110°$. Figure 11.4c showed that splashing occurs when the equilibrium substrate contact angle is 150°. With a reduction in the contact angle from 150° to 110°, the splashing is seen to be prevented since wettability of the substrate increases (Fig. 11.9).

Fig. 11.9 Simulation result for an oblique impacting droplet with an impact angle of 30° and normal Weber number of 140. The equilibrium contact angle of the substrate is $\theta = 110°$. The numerical results show that the splashing vanishes with an increase in wettability of the substrate to $\theta = 110°$

11.5 Conclusion

In this numerical study, we have developed a multiphase lattice Boltzmann code to investigate how the lamella of an oblique impacting droplet behaves onto a textured super-hydrophobic substrate. For oblique impacts, an asymmetric behaviour has been observed due to the tangential component of the impact velocity. First, as a validation case, we have performed simulations to calculate the maximum spread for an oblique impacting droplet onto a smooth surface. The numerical results have been compared with a correlation reported by Yeong et al. [8] and a good agreement has been found.

Then, numerical simulations were performed for oblique impacts on a textured substrate. Four various wetting outcomes have been identified for such impacts. The asymmetric spreading happens for any impact angle Φ as the normal Weber is sufficiently low such that surface tension prevents splashing. Depending on the impact angle, other wetting outcome occur with an increase in the normal Weber number. Bilateral splashing including prompt and corona splash is observed for an impact angle $\Phi \leq 20°$, one-sided corona splash for $25° \leq \Phi \leq 45°$ and the asymmetric break-up for $\Phi \geq 50°$. We have also presented a graph which illustrates splashing threshold values for impact angles $5° \leq \Phi \leq 45°$. Results show that splashing is more likely to occur for smaller impact angle. Moreover, we have demonstrated that the mass of the satellite droplet generated during corona splashing decreases as the impact angle increases as predicted by others. In addition to the impact parameters, we have studied the influence of the geometrical parameters of the textured substrate (the space between posts and the height of the posts) and also the wettability of the surface on the occurrence of splashing. We observed that the time and the occurrence of splashing are influenced by the distance between posts. Furthermore, corona splashing only occurs in a limited range of post heights. Finally, our result show that with a decrease of the substrate contact angle from $\theta = 150°$ to $\theta = 110°$, splashing is prevented as intuitively expected.

Acknowledgements The authors gratefully acknowledge the support of MBIE through the Smart Ideas Endeavour fund for the project “Impact for Spray Drying”.

References

1. Josserand, C., Thoroddsen, S.T.: Drop impact on a solid surface. Annu. Rev. Fluid Mech. **48**, 365–391 (2016)
2. Rioboo, R., Tropea, C., Marengo, M.: Outcomes from a drop impact on solid surfaces. Atomization Sprays **11**(2) (2001)
3. Xu, L.: Liquid drop splashing on smooth, rough, and textured surfaces. Phys. Rev. E **75**(5), 056316 (2007)
4. Josserand, C., Lemoyne, L., Troeger, R., Zaleski, S.: Droplet impact on a dry surface: triggering the splash with a small obstacle. J. Fluid Mech. **524**, 47–56 (2005)
5. Kim, H., Park, U., Lee, C., Kim, H., Hwan Kim, M., Kim, J.: Drop splashing on a rough surface: how surface morphology affects splashing threshold. Appl. Phys. Lett. **104**(16), 161608 (2014)
6. Tsai, P., CA van der Veen, R., van de Raa, M., Lohse, D.: How micropatterns and air pressure affect splashing on surfaces. Langmuir **26**(20), 16090–16095 (2010)
7. Šikalo, Š., Tropea, C., Ganić, E.N.: Impact of droplets onto inclined surfaces. J. Colloid Interface Sci. **286**(2), 661–669 (2005)
8. Yeong, Y.H., Burton, J., Loth, E., Bayer, I.S.: Drop impact and rebound dynamics on an inclined super-hydrophobic surface. Langmuir **30**(40), 12027–12038 (2014)
9. LeClear, S., LeClear, J., Park, K.C., Choi, W.: Drop impact on inclined super-hydrophobic surfaces. J. Colloid Interface Sci. **461**, 114–121 (2016)
10. Liu, J., Vu, H., Yoon, S.S., Jepsen, R.A., Aguilar, G.: Splashing phenomena during liquid droplet impact. Atomization Sprays **20**(4) (2010)
11. Chen, R.H., Wang, H.W.: Effects of tangential speed on low-normal-speed liquid drop impact on a non-wettable solid surface. Exp. Fluids **39**(4), 754–760 (2005)
12. Bird, J.C., Tsai, S.S., Stone, H.A.: Inclined to splash: triggering and inhibiting a splash with tangential velocity. New J. Phys. **11**(6), 063017 (2009)
13. Aboud, D.G., Kietzig, A.M.: Splashing threshold of oblique droplet impacts on surfaces of various wettability. Langmuir **31**(36), 10100–10111 (2015)
14. Shan, X., Chen, H.: Simulation of nonideal gases and liquid-gas phase transitions by the lattice Boltzmann equation. Phys. Rev. E **49**(4), 2941 (1994)
15. Mohamad, A.A.: Lattice Boltzmann Method: Fundamentals and Engineering Applications with Computer Codes. Springer Science & Business Media, London (2011)
16. Benzi, R., Biferale, L., Sbragaglia, M., Succi, S., Toschi, F.: Mesoscopic modelling of a two-phase flow in the presence of boundaries: the contact angle. Phys. Rev. E **74**(2), 021509 (2006)
17. Rashidian, H., Sellier, M.: Modeling an impact droplet on a pair of pillars. Interfacial Phenom. Heat Transf. **5**(1), 43–57 (2017)
18. Huang, H., Krafczyk, M., Lu, X.: Forcing term in single-phase and Shan-Chen-type multiphase lattice Boltzmann models. Phys. Rev. E **84**(4), 046710 (2011)
19. Yuan, P., Schaefer, L.: Equations of state in a lattice Boltzmann model. Phys. Fluids **18**(4), 042101 (2006)
20. Sobolev, V., Guilemany, J.M.: Effect of droplet impact angle on flattening of splat in thermal spraying. Mater. Lett. **32**(2–3), 197–201 (1997)

Chapter 12
Numerical Simulation in Coupled Hydroelastic Problems by Using the LS-STAG Immersed Boundary Method

Ilia K. Marchevsky and Valeria V. Puzikova

Abstract A software package is developed for numerical simulation in coupled hydroelastic problems by using the modified LS-STAG immersed boundary method. In the case of moving immersed boundary, Arbitrary Lagrangian Eulerian method idea is used. It allows solution of problems when domain shape changes in the simulation process due to hydroelastic body motion without mesh reconstruction at each time step. The flow past an in-line oscillating circular airfoil was computed to verify the numerical method and the developed software package. Some numerical results are also presented for simulation of a circular airfoil wind resonance phenomenon, wind turbine rotors autorotation, buffeting phenomenon and tube-bundle flow-induced vibrations. Computational results are in good qualitative agreement with the experimental data. Obtained results demonstrate the extensive possibilities of the developed numerical method and its effectiveness.

Keywords Immersed boundary method · The LS-STAG method · Coupled hydroelastic problem · Flow-induced vibrations · Airfoil · Wind resonance · Buffeting · Autorotation

12.1 Introduction

Coupled hydroelastic problems appear when simulating autorotation and auto-oscillations phenomena. Such problems are complicated for numerical solution, since it is necessary to take into account interference between the flow and moving immersed body. In the case of a sufficiently massive body, coupled hydroelastic

I. K. Marchevsky (✉) · V. V. Puzikova
Bauman Moscow State Technical University,
2nd Baumanskaya, 5, 105005 Moscow, Russia
e-mail: iliamarchevsky@mail.ru

I. K. Marchevsky · V. V. Puzikova
Ivannikov Institute for System Programming of the RAS,
Alexander Solzhenitsyn st., 25, 109004 Moscow, Russia

S. Gutschmidt et al. (eds.), *IUTAM Symposium on Recent Advances in Moving Boundary Problems in Mechanics*, IUTAM Bookseries 34,
https://doi.org/10.1007/978-3-030-13720-5_12

problems can be solved using a step-by-step numerical algorithm, firstly simulating flow around a body moving with known parameters and then computing the dynamics of the body with known hydrodynamic loads.

Immersed boundary methods [1] are useful for numerical simulation in coupled hydroelastic problems, since they do not require a coincidence of cell edges and boundaries of the computational domain, and allow the solution of problems when domain shape is irregular or it changes in the simulation process due to hydroelastic body motion. The main advantage of these methods is that mesh reconstruction is not needed at each time step.

The LS-STAG cut-cell immersed boundary method [2] for viscous incompressible flow simulations combines the advantages of immersed boundary methods and the level-set method. This method allows the solution of problems on a Cartesian grid. In contrast to classical immersed boundary methods, the flow variables are computed in the cut-cells, and not interpolated. Numerical analogues of conservation laws satisfaction in all fluid domain cells is a basis of LS-STAG discretization construction, which allows one to obtain physically realistic numerical solutions. For these reasons, the LS-STAG method is used in the present study for simulation in coupled hydroelastic problems. The immersed boundary is represented with the level-set function [3]. Due to this fact the LS-STAG method allows to easy simulale the flow past an airfoils system [4, 5]. Linear systems resulting from the LS-STAG discretization of the Navier-Stokes or Reynolds-averaged Navier-Stokes equations, are solved using the BiCGStab method [6] with the ILU- and multigrid [7] preconditioning [8].

12.2 Governing Equations

The problem is considered for the 2D unsteady case when the flow around an airfoil (or airfoils system) is assumed to be viscous and incompressible. The continuity and momentum equations are the following:

$$\nabla \cdot \mathbf{v} = 0, \quad \frac{\partial \mathbf{v}}{\partial t} + (\mathbf{v} \cdot \nabla)\mathbf{v} = -\frac{1}{\rho}\nabla p + \nu \Delta \mathbf{v}. \tag{12.1}$$

The boundary conditions on the external boundaries of the computational domain are the following:

$$\mathbf{v}\big|_{\text{inlet}} = \mathbf{v}_\infty, \quad \frac{\partial \mathbf{v}}{\partial \mathbf{n}}\Big|_{\text{outlet}} = 0, \quad \frac{\partial p}{\partial \mathbf{n}}\Big|_{\text{inlet\&outlet}} = 0, \tag{12.2}$$

and the boundary conditions on the camber line of each airfoil are no-slip conditions:

$$\mathbf{v}\big|_{\text{airfoil}} = \mathbf{v}^{\text{ib}}, \quad \frac{\partial p}{\partial \mathbf{n}}\Big|_{\text{airfoil}} = 0. \tag{12.3}$$

Here $\mathbf{v}^{\text{ib}}$ is the velocity of the immersed boundary. The airfoil is assumed to be rigid and it can oscillate with 1, 2 or 3 degrees of freedom. Such problem can be considered as coupled hydroelastic one, despite the fact that the airfoil itself is non-deformable, because its motion in the flow domain depends on hydrodynamic loads. The airfoil's motion is described by dynamics equations which in the most common form can be written down as the following:

$$\ddot{\mathbf{q}} = \Phi(\mathbf{q}, \dot{\mathbf{q}}) + \mathbf{Q}^{\text{flow}} + \mathbf{Q}^{\text{ext}}. \tag{12.4}$$

Here $\mathbf{q}$ is the airfoil generalized coordinates vector, $\Phi(\mathbf{q}, \dot{\mathbf{q}})$ is determined by elastic and viscous constraints imposed on the airfoil, $\mathbf{Q}^{\text{flow}}$ is the generalized aerodynamic force, $\mathbf{Q}^{\text{ext}}$ is the external mass forces vector.

If the ith airfoil can oscillate along Ox then the airfoil constraint is assumed to be linear viscoelastic of Kelvin—Voigt type and their motion (12.4) is described by the following equation:

$$m_i \ddot{x}_{*,i} + b\dot{x}_{*,i} + cx_{*,i} = F_{x,i}. \tag{12.5}$$

Here m_i is the airfoil mass, b_i is the damping factor, c_i is the constraints rigidity; $F_{x,i}$ is the drag force; $x_{*,i}$ is the deviation from the equilibrium on Ox.

Similarly, if the ith airfoil can oscillate along Oy then the airfoil constraint is assumed to be linear viscoelastic and their motion (12.4) is described by the following equation:

$$m_i \ddot{y}_{*,i} + b\dot{y}_{*,i} + cy_{*,i} = F_{y,i}. \tag{12.6}$$

Here $F_{y,i}$ is the lift force; $y_{*,i}$ is the deviation from the equilibrium on Oy.

If the ith airfoil can autorotate then the following dynamics equation (12.4) is to be solved:

$$I_i \ddot{\alpha}_i + k_i \dot{\alpha}_i = M_i^{\text{flow}}. \tag{12.7}$$

Here α_i is the rotation angle of the airfoil; I_i is the polar moment of inertia of the airfoil; k_i is the viscous friction coefficient in the axis; M_i^{flow} is the hydrodynamic moment. Since the two-dimensional problem is considered, $M_i^{\text{flow}} = M_{z,i}$. In addition, the airfoil angular velocity is $\omega_i = \dot{\alpha}_i$, so (12.7) can be rewritten as the following:

$$I_i \dot{\omega}_i + k_i \omega_i = M_{z,i}. \tag{12.8}$$

12.3 Numerical Method

A Cartesian mesh with cells $\Omega_{i,j} = (x_{i-1}, x_i) \times (y_{j-1}, y_j)$ is introduced in the rectangular computational domain. It is denoted that $\Gamma_{i,j}$ is the face of $\Omega_{i,j}$ and $\mathbf{x}^c_{i,j} = (x^c_i, y^c_j)$ is the center of this cell. According to the concept of the LS-STAG method, normal stress components are sampled on this mesh (similar to pressure discretization) and shear ones are sampled in the upper right corners of the mesh cells. Unknown components $u_{i,j}$ and $v_{i,j}$ of velocity vector $\mathbf{v}$ are computed in the middle of fluid parts of the cell faces. These points are the centers of control volumes $\Omega^u_{i,j} = (x^c_i, x^c_{i+1}) \times (y_{j-1}, y_j)$ and $\Omega^v_{i,j} = (x_{i-1}, x_i) \times (y^c_j, y^c_{j+1})$ with faces $\Gamma^u_{i,j}$ and $\Gamma^v_{i,j}$, respectively.

Cells which the immersed boundary intersects are the so-called 'cut-cells'. These cells $\Omega^{ib}_{i,j}$ contain the solid part together with the liquid one. The level-set function φ is used for immersed boundary Γ^{ib} description. The boundary Γ^{ib} is represented by a line segment on the cut-cell $\Omega_{i,j}$. Locations of this segment endpoints are defined by linear interpolation of the variable $\varphi_{i,j} = \varphi(x_i, y_j)$. The cell-face fraction ratios $\vartheta^u_{i,j}$ and $\vartheta^v_{i,j}$ are introduced. They take values in the interval [0, 1] and represent the fluid parts of the east and north faces of $\Gamma_{i,j}$, respectively. One-dimensional linear interpolation of $\varphi(x_i, y)$ on the segment $[y_{j-1}, y_j]$ and $\varphi(x, y_j)$ on the segment $[x_{i-1}, x_i]$ is used for the cell-face fraction ratios computing.

The hydrodynamic moment on the nth time step for each airfoil can be computed in the following way:

$$M^n_z = \sum_{\text{Cut-cells } \Omega^{ib}_{i,j}} [(x^c_i - X_C)F_y|^n_{i,j} - (y^c_j - Y_C)F_x|^n_{i,j}]. \tag{12.9}$$

Here (X_C, Y_C) are coordinates of the airfoil center, around which the rotation takes place, $F_x|^n_{i,j}$ and $F_y|^n_{i,j}$ are the portion of drag and lift acting on the solid part of the cut-cell $\Omega_{i,j}$ on the nth time step:

$$F_x|_{i,j} = (\vartheta^u_{i-1,j} - \vartheta^u_{i,j})\Delta y_j \Big(p_{i,j} - \nu \frac{\partial u}{\partial x}\Big|_{i,j}\Big) - \nu \text{Quad}^{ib}_{i,j}\Big(\frac{\partial u}{\partial y}\mathbf{e}_y \cdot \mathbf{n}\Big), \tag{12.10}$$

$$F_y|_{i,j} = -\nu \text{Quad}^{ib}_{i,j}\Big(\frac{\partial v}{\partial x}\mathbf{e}_x \cdot \mathbf{n}\Big) + (\vartheta^v_{i,j-1} - \vartheta^v_{i,j})\Delta x_i \Big(p_{i,j} - \nu \frac{\partial v}{\partial y}\Big|_{i,j}\Big). \tag{12.11}$$

Here $\Delta y_j = y_j - y_{j-1}$, $\Delta x_i = x_i - x_{i-1}$, $\text{Quad}^{ib}_{i,j}$ are the quadratures of the shear stress which depend on the cut-cells [2]. Respectively, hydrodynamic force can be computed as the following:

$$F_x = \sum_{\text{Cut-cells } \Omega^{ib}_{i,j}} F_x|_{i,j}, \qquad F_y = \sum_{\text{Cut-cells } \Omega^{ib}_{i,j}} F_y|_{i,j}. \tag{12.12}$$

We denote that the deviations from the equilibrium on the nth step of computation are $x^n_{*,i} = X^n_{C,i} - X^0_{C,i}$, $y^n_{*,i} = Y^n_{C,i} - Y^0_{C,i}$. Here $(X^0_{C,i},\ Y^0_{C,i})$ are coordinates of the ith airfoil center at the initial time and $(X^n_{C,i},\ Y^n_{C,i})$ are coordinates of this airfoil center at the nth step of computation. Difference analogues of Eqs. (12.5), (12.6) can be written down in the following form:

$$m_i \cdot \frac{X^{n+1}_{C,i} - 2X^n_{C,i} + X^{n-1}_{C,i}}{(\Delta t)^2} + b_i \cdot \frac{X^{n+1}_{C,i} - X^{n-1}_{C,i}}{2\Delta t} + c_i \cdot x^n_{*,i} = F_{x,i}|^n, \quad (12.13)$$

$$m_i \cdot \frac{Y^{n+1}_{C,i} - 2Y^n_{C,i} + Y^{n-1}_{C,i}}{(\Delta t)^2} + b_i \cdot \frac{Y^{n+1}_{C,i} - Y^{n-1}_{C,i}}{2\Delta t} + c_i \cdot y^n_{*,i} = F_{y,i}|^n. \quad (12.14)$$

Here Δt is a time discretization step. Position of the airfoil center at the next time step can be easily obtained from this equation on every computational step after computing the lift force acting on the airfoil. It allows the reconstruction of the level-set function and all matrices required for the computation and to compute the immersed boundary velocity $\mathbf{v}^{ib}$ for recalculation the source terms.

The difference analogue of Eq. (12.7) for the kth airfoil can be written down in the following form:

$$I_k \frac{\omega^{n+1}_k - \omega^n_k}{\Delta t} + k_k \omega^n_k = M^n_{z,k}. \quad (12.15)$$

The value of the airfoil angular velocity at the next time step can be easily computed after (12.15). New airfoil position and the immersed boundary velocity can be defined by using this value:

$$\alpha^{n+1}_k = \alpha^n_k + \omega^n_k \Delta t, \quad (12.16)$$

$$\mathbf{v}^{ib,n+1}_k|_{i,j} = \left\{ -\frac{y^c_j - Y_{C,k}}{|y^c_j - Y_{C,k}|} \cdot \omega^{n+1}_k |x^c_i - X_{C,k}|,\ \frac{x^c_i - X_{C,k}}{|x^c_i - X_{C,k}|} \cdot \omega^{n+1}_k |y^c_j - Y_{C,k}| \right\}.$$

The Arbitrary Lagrangian-Eulerian method [9] is widely used by finite-volume methods on body-conformal meshes. This method considers a computational domain that tracks the moving boundary, such that the grid follows the boundary motion in the Lagrangian fashion, while it is held fixed in an Eulerian manner sufficiently far from it. The ALE equations of the flow motion written in the computational domain are similar to the Navier—Stokes equations except for the convective term

$$\int_{\Gamma^*(t)} ([\mathbf{v} - \mathbf{v}^g] \cdot \mathbf{n})\mathbf{v}\, dS. \quad (12.17)$$

In a series of papers, Farhat and co-workers have shown that an ALE numerical scheme preserves the accuracy and stability of its fixed grid counterpart if the grid

velocity and mesh update procedure are designed such that the so-called geometric conservation law is enforced at the discrete level [10]:

$$\frac{d}{dt}\int\limits_{\Omega^*(t)} dV = \int\limits_{\Gamma^*(t)} \mathbf{v}^g \cdot \mathbf{n}\, dS. \tag{12.18}$$

This equation is obtained by requiring that a uniform flow is a solution to the ALE equations, and states that the change in volume of a cell during a time interval must be equal to the volume that has been swept by the cell boundary. For immersed boundary methods the geometric conservation law is easy to fulfill because only the grid nodes on the solid part of a cut-cell are moving and the computational grid is not deformed by the immersed boundary motion.

The time integration is performed with a semi-implicit Euler scheme. The predictor step leads to discrete analogues of the Helmholtz equation for velocities prediction $\widetilde{U}_x, \widetilde{U}_y$ at the time $t_{n+1} = (n+1)\Delta t$. The corrector step leads to a discrete analogue of the Poisson equation for pressure correction $\Phi = \Delta t(P^{n+1} - P^n)$.

12.4 Numerical Experiments

All computations were performed on a server based on the Intel C610 platform using the Intel Xeon E5-1620 V3 4-core processor (3.5 GHz) with HyperThreading support (8 logical cores). The server is equipped with 16 GB of ECC DDR4-2133 RAM and two hard drives (2 TB), united in a RAID1 disk volume. This server is running Windows Server 2012 R2 operating system.

12.4.1 In-Line Oscillating Circular Airfoil in a Free-Stream

To validate the developed implementation of the LS-STAG method the flow past an in-line oscillating circular airfoil was computed. The in-line motion of the airfoil center is given by:

$$\begin{aligned} X_C &= X_C^0 + \begin{cases} A, & t < 10D/V_\infty, \\ A\cos\left(2\pi S_e \left[tV_\infty - 10D\right]/D\right), & t \geq 10D/V_\infty, \end{cases} \\ Y_C &= Y_C^0. \end{aligned} \tag{12.19}$$

Here A is the amplitude of oscillations, S_e is the exciting Strouhal number, (X_C, Y_C) are coordinates of the airfoil center at the current time moment, (X_C^0, Y_C^0) are coordinates of the airfoil center at the initial time.

This problem has been numerically solved in [11–14] and it also has been studied by Dutsch et al. [15] in experiment with the following dimensionless parameters:

Table 12.1 Comparison of time averaged drag coefficient $\bar{C}_x$ with established results from the literature

Study	Dutsch (experiment) [15]	The present	Guilmineau & Queutey [12]		
Mesh	–	240 × 296	120 × 100	240 × 200	480 × 400
$\bar{C}_x$	2.090	2.075	2.059	2.078	2.080

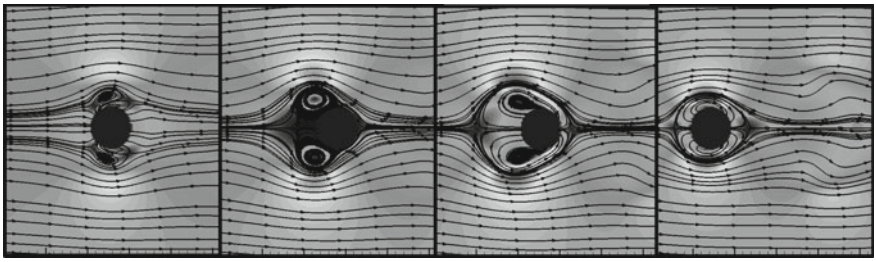

Fig. 12.1 Dynamics of vortex formation and shedding from an in-line oscillating circular airfoil (the shown pictures correspond to sixth parts of the period)

$$V_\infty = 1.0, \quad D = 1.0, \quad \mathrm{Re} = 100, \quad A = 0.8D, \quad S_e = 0.2.$$

This flow is characterized by stable, symmetric and periodic vortex shedding.

Computations were performed on a non-uniform grid 240 × 296 with time discretization step $\Delta t = 0.005$. Computed time averaged drag coefficient $\bar{C}_x$ differs from the experimentally defined value [15] by less than 1% (Table 12.1).

Vortex dynamics is shown in Fig. 12.1. As the airfoil moves from the initial position downstream, vortices begin to form on the top and bottom of it. Vortices increase in size when the airfoil is close to the rightmost position and reach their maximum radius when the airfoil is in the rightmost position. Then the airfoil starts its backward motion, creating the same vortex formation on the other side of it. As the direction of the airfoil motion changes again, the resulting pair of vortices is shed from the airfoil. The described process begins again when the airfoil is returned to its initial position.

12.4.2 Circular Airfoil Wind Resonance

To simulate wind resonance phenomenon we considered the motion of the circular airfoil with diameter D across the stream with one degree of freedom (12.6). The natural frequency of the system $\omega \approx \sqrt{c/m}$ can be set by varying the coefficient c. A number of computations have been performed on a non-uniform grid 272 × 292 with time discretization step $\Delta t = 0.0001$ and the following dimensionless parameters:

$$V_\infty = 3.0, \quad \rho = 1.0, \quad \nu = 0.003, \quad D = 1.0, \quad m = 39.75, \quad b = 0.731.$$

These parameters correspond to a Reynolds number $\mathrm{Re} = 1000$. The dimensionless natural frequency of the system is in the following range:

$$\mathrm{St}_\omega = \frac{\omega}{2\pi} \cdot \frac{D}{V_\infty} = 0.150 \ldots 0.280.$$

Computational results are in good agreement with the previous studies [16]. Maximal amplitude is about $0.4D$ and it occurs when the natural frequency of the system St_ω is close to the Strouhal number, calculated for a fixed airfoil $\mathrm{St} \approx 0.24$ [2, 17, 18].

12.4.3 Circular Airfoil Buffeting

To simulate the buffeting phenomenon we considered the motion of two equal circular airfoils with diameter $D = 1.0$ across the stream at $V_\infty = 1.0$ with two degrees of freedom (12.5), (12.6). The distance between airfoil centers is equal to $L = 5.5$ on the horizontal and $T = 0.7$ on the vertical at the initial time. The dimensionless natural frequency of the system was in the range

$$\mathrm{St}_\omega / \mathrm{St} = 0.50 \ldots 2.00.$$

Here St is the Strouhal number, calculated for a fixed airfoil at the corresponding Reynolds number.

A number of computations have been performed on a non-uniform grid 666×344 at $\mathrm{Re} = 100$ and $\mathrm{Re} = 1000$ and the following dimensionless parameters:

$$\rho = 1.0, \quad m = 4.7273, \quad b = 4\pi m \xi \mathrm{St}_\omega, \quad \xi = 3.3 \cdot 10^{-4}, \quad c = m(2\pi \mathrm{St}_\omega)^2.$$

The time discretization step was equal to $\Delta t = 10^{-4}$ ($\Delta t = 5 \cdot 10^{-5}$ at $\mathrm{Re} = 1000$) at $\mathrm{St}_\omega / \mathrm{St} = 0.85 \ldots 1.15$ and $\Delta t = 5 \cdot 10^{-4}$ ($\Delta t = 10^{-4}$ at $\mathrm{Re} = 1000$) at other values. A uniform mesh block with spatial discretization step $h = D/64$ was used in the proximity of the airfoil.

Since the distance between the airfoil centers along the Ox axis is large enough ($>5D$), the upstream airfoil (K_1) behaves like a single airfoil and the downstream airfoil (K_2) performs forced oscillations due to periodic vortex-shedding flow past airfoil K_1. Thus, buffeting of airfoil K_2 is observed. The maximal amplitude of the airfoil K_2 oscillations significantly exceeds the amplitude of the airfoil K_1 oscillations at the $\mathrm{Re} = 100$ (Fig. 12.2). The maximal amplitude of the airfoil K_1 oscillations appear at $\mathrm{St}_\omega \approx \mathrm{St}$ ($\mathrm{St} \approx 0.162$ at $\mathrm{Re} = 100$) as in [19]. This corresponds to the single airfoil behavior in the flow. Maximal amplitude of the airfoil K_2 oscillations along the Oy axis appears at $\mathrm{St}_\omega \approx 0.85\mathrm{St}$.

The amplitude of airfoil K_2 oscillations along the Oy axis is less than the amplitude of airfoil K_1 oscillations (Fig. 12.3) at $\mathrm{Re} = 1000$ as in [20]. In this case the maximal

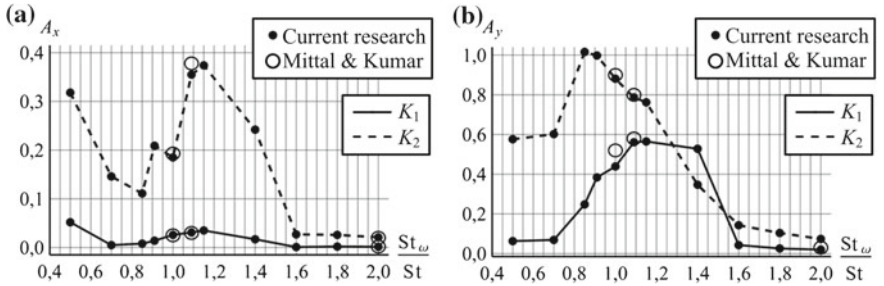

Fig. 12.2 Maximal amplitude of the circular airfoils oscillations at Re = 100: **a** along the Ox axis; **b** along the Oy axis

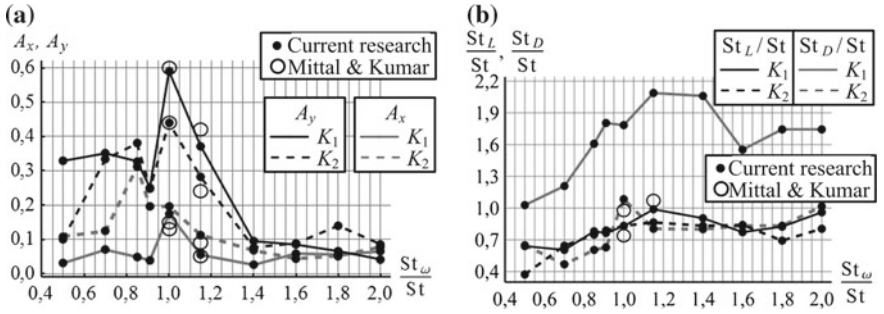

Fig. 12.3 Characteristics of the circular airfoils oscillations at Re = 1000: **a** maximal amplitude of the circular airfoils oscillations; **b** frequences of lift and drag forces oscillations

amplitude of the circular airfoil oscillations appears at $\mathrm{St}_\omega \approx \mathrm{St}$ both along the Oy axis and the Ox axis.

12.4.4 Tube-Bundle Flow-Induced Vibrations

We considered the motion of circular airfoils with diameter $D = 1.0$ across the stream at $V_\infty = 1.0$ with two degrees of freedom (12.5), (12.6). Tubes can be destroyed at $\mathrm{St}_\omega \approx \mathrm{St}$ with damping, which corresponds to $b < 0.1$ [21]. Therefore, simulations were performed at $m = 40$ and $\xi = 3.3 \cdot 10^{-3}$ in this research. These values correspond to the damping coefficient $b = 4\pi m \xi \mathrm{St}_\omega > 0.14$ at $\mathrm{St}_\omega > 0.09$.

The flow pattern depends on the arrangement of the tubes and their locations in the bundle [21]. For this reason, we considered flow around six columns of tubes in a staggered arrangement and flow around five columns of tubes in an in-line arrangement (Fig. 12.4).

The distance between airfoil centers is equal to L on the horizontal and T on the vertical at the initial time. When the simulation was performed at $T/D > 4$, vortex streets between the rows do not affect each other, as in [21]. When $L/D > 4$, tubes

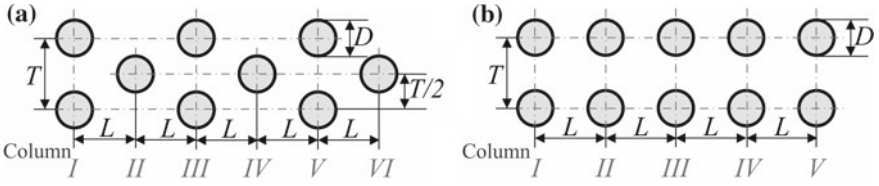

Fig. 12.4 Considered tube arrangements: **a** staggered tube arrangement; **b** in-line tube arrangement

in the bundle behave as single airfoils. So, tube-bundles behave as a single system at lower values of L, T.

As an example, here we present computational results at $T/D = 2.0$, $L = T$ in the case of an in-line tube arrangement and $L = T\sqrt{3}/2$ in the case of a staggered tube arrangement. Thus, in the first case airfoils in adjacent columns are in the corners of a square, and in the second case they are located at the vertices of an equilateral triangle.

A number of computations have been performed at $\mathrm{Re} = 1000$ on a non-uniform grid 846×424 in the case of a staggered tube arrangement and on a non-uniform grid 816×424 in the case of an in-line tube arrangement. A uniform mesh block with space discretization step $h = D/64$ was used in the vicinity of the airfoil. The time discretization step was equal to $\Delta t = 5 \cdot 10^{-5}$. To simulate 50 dimensionless time units is required about 137 h.

The natural frequency of the system was in the range $\mathrm{St}_\omega/\mathrm{St} = 0.50 \ldots 2.00$. Here St is the Strouhal number, calculated for a fixed tube-bundle at the corresponding Reynolds number. Our simulations showed that $\mathrm{St} \approx 0.205$ in the case of an in-line tube arrangement. This is in agreement with the fact that for this arrangement in the experiments [21] $\mathrm{St} = \mathrm{St}(T/D) = 0.2 + \exp[-1.2(T/D)^{1.8}]$, i.e. $\mathrm{St}(2.0) \approx 0.215$. In the case of a staggered arrangement two different frequencies are observed for tubes from even and odd columns (Fig. 12.4) as in [21]. Upper frequency is observed in the tubes from odd columns. This frequency is considered as the vortex shedding frequency. So, we obtain that $\mathrm{St} \approx 0.280$ in the case of a staggered tube arrangement. This is in agreement with the fact that in the experiments [21] the maximum amplitude of oscillation occurs at a frequency equal to $(0.4 + 2\exp[-0.44(T/D)^{1.8}])/3$, i.e the Strouhal number $\mathrm{St} \approx 0.277$ at $T/D = 2.0$. Lower frequency is observed in the tubes from even columns and it is equal $\mathrm{St}/2$. It corresponds to the frequency of vortex street interaction.

Computational results (Fig. 12.5) are in qualitative agreement with the experimental data [21]. Tubes from the first column behave like a single airfoil. In the case of a staggered tubes arrangement the amplitude of the tube oscillations along the Oy axis significantly decreases with increasing column number.

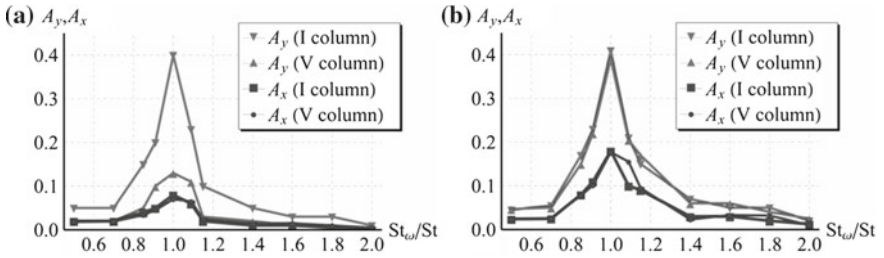

Fig. 12.5 Maximal amplitude of the tube oscillations at Re = 1000: **a** staggered tube arrangement; **b** in-line tube arrangement

12.4.5 Airfoils Autorotation

To simulate the airfoil autorotation of wind turbine rotors, the dynamics equation (12.7) has been solved. Algorithm of level-set function construction for complex-shaped airfoils, based on Bezier curves, was proposed in [22]. Also, algorithm for the level-set function recalculation at any time without reconstructing the Bezier curve for each new airfoil position was described. The designed second-order Butterworth low-pass filter for aerodynamic torque filtration for simulations using coarse grids was presented. Simulation of flow past autorotating Savonius rotor with two blades by using the modified LS-STAG method was presented. Computational results [22] were in good qualitative agreement with the experimental data.

12.5 Conclusions

- A software package was developed for the numerical simulation of airfoil motion in a viscous incompressible flow using the LS-STAG method.
- Simulation of circular airfoil wind resonance and buffeting phenomena, tube-bundle flow-induced vibrations and airfoil autorotation were considered. The LS-STAG method allows the simulation of these phenomenons on a very coarse mesh.
- Computational results were in good qualitative agreement with the experimental data.

Acknowledgements The work was supported by the Russian Science Foundation Grant (proj. No 17-79-20445).

References

1. Mittal, R., Iaccarino, G.: Immersed boundary methods. Annu. Rev. Fluid Mech. **37**, 239–261 (2005). https://doi.org/10.1146/annurev.fluid.37.061903.175743
2. Cheny, Y., Botella, O.: The LS-STAG method: a new immersed boundary/level-set method for the computation of incompressible viscous flows in complex moving geometries with good

conservation properties. J. Comput. Phys. **229**, 1043–1076 (2010). https://doi.org/10.1016/j.jcp.2009.10.007
3. Osher, S., Fedkiw, R.P.: Level Set Methods and Dynamic Implicit Surfaces. Springer, Berlin (2003). https://doi.org/10.1115/1.1760520
4. Marchevskii, I.K., Puzikova, V.V.: Numerical simulation of the flow around two fixed circular airfoils positioned in tandem using the LS-STAG method. J. Mach. Manuf. Reliab. **45**, 130–136 (2016). https://doi.org/10.3103/S1052618816020084
5. Marchevskii, I.K., Puzikova, V.V.: Numerical simulation of the flow around two circular airfoils positioned across the stream using the LS-STAG method. J. Mach. Manuf. Reliab. **46**, 114–119 (2017). https://doi.org/10.3103/S105261881702011X
6. Van der Vorst, H.A.: Bi-CGSTAB: a fast and smoothly converging variant of Bi-CG for solution of non-symmetric linear systems. SIAM J. Sci. Stat. Comput. **2**, 631–644 (1992). https://doi.org/10.1137/0913035
7. Wesseling, P.: An introduction to multigrid methods. Willey, Hoboken (1991)
8. Van Kan, J., Vuik, C., Wesseling, P.: Fast pressure calculation for 2D and 3D time dependent incompressible flow. Numer. Linear Algebr. Appl. **7**, 429–447 (2000). https://onlinelibrary.wiley.com/doi/abs/10.1002/1099-1506%28200009%297%3A6%3C429%3A%3AAID-NLA204%3E3.0.CO%3B2-8
9. Donea, J., Huerta, A., Ponthot, J-Ph, Rodriguez-Ferran, A.: Arbitrary Lagrangian-Eulerian methods. In: Stein, E., de Borst, R., Hughes, T.J.R. (eds.) Encyclopedia of Computational Mechanics. Fundamentals, vol. 1, pp. 413–437. (2004). https://doi.org/10.1002/0470091355.ecm009
10. Lesoinne, M., Farhat, C.: Geometric conservation laws for flow problems with moving boundaries and deformable meshes, and their impact on aeroelastic computations. Comput. Method Appl. Mech. Eng. **134**, 71–90 (2003). https://doi.org/10.1016/0045-7825(96)01028-6
11. Gu, W., Chyu, C., Rockwell, D.: Timing of vortex formation from an oscillating cylinder. Phys. Fluids **6**, 3677–3682 (1994). https://doi.org/10.1063/1.868424
12. Guilmineau, E., Queutey, P.: On numerical simulation of vortex shedding from an oscillating circular. J. Fluid Struct. **16**, 773–794 (2002). https://doi.org/10.1006/jfls.2002.0449
13. Yang, J., Balaras, E.: An embedded-boundary formulation for large-eddy simulation o turbulent flows interacting with moving boundaries. J. Comput. Phys. **215**, 12–40 (2006). https://doi.org/10.1016/j.jcp.2005.10.035
14. Udaykumar, H.S., Mittal, R., Rampunggoon, P., Khanna, A.: A sharp interface Cartesian grid method for simulating flows with complex moving boundaries. J. Comput. Phys. **174**, 345–380 (2001). https://doi.org/10.1006/jcph.2001.6916
15. Dutsch, H., Durst, F., Becker, S., Lienhart, H.: Low-Reynolds-number flow around an oscillating circular cylinder at low Keulegan-Carpenter numbers. J. Fluid Mech. **360**, 249–271 (1998). https://doi.org/10.1017/S002211209800860X
16. Klamo, J.T., Leonard, A., Roshko, A.: On the maximum amplitude for a freely vibrating cylinder in cross flow. J. Fluids Struct. **21**, 429–434 (2005). https://doi.org/10.1016/j.jfluidstructs.2005.07.010
17. He, J.W., Glovinski, R., Metcalfe, R., Nordlander, A., Triaux, J.P.: Active control and drag optimization for flow past a circular cylinder. Part I: Oscillatory cylinder rotation. J. Comput. Phys. **163**, 87–117 (2000)
18. Henderson, R.D.: Nonlinear dynamics and pattern formation in turbulent wake transition. J. Fluid Mech. **352**, 65–112 (1997). https://doi.org/10.1017/S0022112097007465
19. Mittal, S., Kumar, V.: Flow-induced oscillations of two cylinders in tandem and staggered arrangements. J. Fluids Struct. **15**, 717–736 (2001). https://doi.org/10.1006/jfls.2000.0376
20. Mittal, S., Kumar, V.: Vortex induced vibrations of a pair of cylinders at Reynolds number 1000. Int. J. Comput. Fluid Dyn. **18**, 601–614 (2004). https://doi.org/10.1080/10618560310001370 17
21. Zukauskas, A., Ulinskas, R., Katinas, V.: Fluid Dynamics and Flow-Induced Vibrations of Tube Banks [in Russian]. Vil'nyus (1984)

22. Marchevsky, I.K., Puzikova, V.V.: Numerical simulation of wind turbine rotors autorotation by using the modified LS-STAG immersed boundary method. Int. J. Rotating Mach. 1–7 (2017). https://doi.org/10.1155/2017/6418108

Chapter 13
On the Efficiency of the Parallel Algorithms in VM2D Open Source Code for 2D Flows Simulation Using Vortex Methods

Kseniia Kuzmina and Ilia K. Marchevsky

Abstract VM2D is an open-source software being developed by the authors for two-dimensional incompressible flows simulations around airfoils. VM2D is based on meshless Lagrangian vortex methods. The main operations of the algorithm are pointed out, and the estimations of their computational complexity are given. Two model problems with different parameters are considered in order to analyze the ratio between computational complexities of the operations. Parallel algorithms are implemented for all time-consuming operations to perform the simulations on CPU and GPU. Test problems show that VM2D is efficiently parallelized; the accelerations achieved on GPUs are comparable to acceleration on hundreds and even thousands of CPU cores.

Keywords Vortex Methods · VM2D Code · CPU · GPU · MPI · OpenMP · NVidia CUDA

13.1 Introduction

In many engineering applications Fluid–Structure Interaction problems appear, when it is necessary to calculate the loads acting on the construction being immersed into the flow. Such problems become especially complicated when we deal with essentially unsteady flow with intensive vortex shedding: in this case, it is impossible to use approximate models based on stationary aerodynamic characteristics, so, the only way is to perform direct numerical simulation of the flow. Moreover, when designing a structure, it is necessary to perform a large number of numerical experiments; and

K. Kuzmina (✉) · I. K. Marchevsky
Bauman Moscow State Technical University, 2-nd Baumanskaya st., 5,
105005 Moscow, Russia
e-mail: kuz-ksen-serg@yandex.ru

K. Kuzmina · I. K. Marchevsky
Ivannikov Institute for System Programming of the RAS, Alexander Solzhenitsyn st., 25,
109004 Moscow, Russia
e-mail: iliamarchevsky@mail.ru

S. Gutschmidt et al. (eds.), *IUTAM Symposium on Recent Advances in Moving Boundary Problems in Mechanics*, IUTAM Bookseries 34,
https://doi.org/10.1007/978-3-030-13720-5_13

in spite of large number of commercial and open-source codes for flow simulation based on different numerical methods, there is relevant problem of developing of efficient methods for direct numerical simulation in FSI problems.

Most of the existing methods for numerical simulation in FSI problems belong to the class of Eulerian or hybrid Eulerian/Lagrangian methods and require mesh generation in the flow domain; in case of moving or deformable body the mesh should be modified at every time step (except immersing boundary methods [1, 2]). In case of small body displacements we can do with mesh deformation; but if the body has significant displacement or rotation, it is necessary to reconstruct the mesh, at least after several time steps, what reduces essentially the efficiency of the numerical method. From this point of view, the class of meshless Lagrangian methods which doesn't require fluid domain meshing and permits arbitrary displacements of the body is preferable.

In the present research the efficiency of meshless Lagrangian vortex method and its software implementation is investigated. It should be noted that the range of applicability of vortex methods is restricted by rather low Reynolds numbers (up to 10^5) and incompressible flow model. However, many problems which arise in engineering practice, satisfy such conditions and can be efficiently solved numerically using vortex methods.

The main idea of vortex methods [3–7] is the considering of the vorticity as the primary calculated variable. The body is replaced with three thin sheets on its surface: an attached vortex sheet, an attached source sheet and a free vortex sheet. The intensities of the attached sheets are expressed through the velocity of the body surface; free vortex sheet intensity can be found from the no-slip boundary condition satisfaction on the body surface. To satisfy the no-slip boundary condition the ideas of vortex panel methods are used [8]: the airfoil surface line is discretized into rectilinear panels, the solution on each panel is represented by a constant distribution. The main differences of the approach used in this paper from the classical approach are the following: instead of the equality of the normal velocity components at the airfoil surface line, the equality of the tangent components is required [9], and the boundary condition is satisfied not in collocation points, bat on average at the panels [10]. So, at every time step we should satisfy boundary condition, which is represented by integral equation, and find the intensity of the free vortex sheet; and then this vorticity sheds to the vortex wake in form of separate vortex elements and become part of the vortex wake behind the body.

It should be noted that vortex methods are especially efficient in comparison with mesh methods when we simulate external flow around the structures, since in this case the boundary condition of perturbations decay at infinity is satisfied automatically and there is no need to limit the computational domain artificially and set some boundary conditions on its outer boundaries. Moreover, in most cases of the external flow simulation the domain with non-zero vorticity is localized around and behind the body, so computational resources can be "concentrated" in this domain.

Vortex methods are well-investigated and they are rather popular in engineering community. There are various modifications of vortex methods both for numerical simulation in 3D and 2D problems. Nevertheless, vortex methods are still not imple-

mented in any known software packages: both commercial and freely distributed. Of course, many researchers have their own "in-house" codes, however, such software is usually used only by small groups of scientists working also on their development. This fact negatively effects the popularity of vortex methods.

Therefore, having some research experience in vortex methods, as well as the experience of their software implementation in our "in-house" software [11], the authors have started to develop new software package **VM2D—Open source code for two-dimensional flows simulation using vortex methods** [12]. Source code is available on GitHub: `https://github.com/vortexmethods/VM2D`. In [12] the general structure of the VM2D code and main approaches implemented there are described. The current paper does not aim to re-describe VM2D software; the main purpose is to analyze the efficiency of the VM2D code and its parallel properties.

The VM2D software is based on the method of Viscous vortex domains (VVD), developed by prof. G.Ya. Dynnikova [7]. Well known models and numerical algorithms as well as the authors' advancements are implemented in the VM2D code [10, 13–15]. At the present moment, it is expected that the code is used for external flows simulation, however, problems solution which require internal flow simulation is also possible, maybe after some modification of the algorithm for higher efficiency achievement.

It should also be noted that in order to provide the simplicity of program modification, both by the authors and other users, and the possibility of new approaches and features addition, we have adhered to the principles of the object-oriented approach, and the VM2D code has modular structure. The main purpose of the VM2D development is to create a tool for the engineering problems numerical solution in a short time, so, it is important to provide the possibility of computations performing in parallel mode. In this paper, we study the efficiency of parallel algorithms in the VM2D.

13.2 Main Computational Blocks in the VM2D Algorithm

There are 7 basic computational blocks in the vortex method algorithm implemented in the VM2D. Their detailed description can be found in [11, 13], here we will give only their brief description and point out the main operations in these blocks and estimate their computational complexities, which depend primarily on the airfoil discretization.

1. *Vorticity generation on the airfoil surface.* In order to calculate the free vortex sheet intensity on the airfoil surface line, we solve the integral equation, which follows from the no-slip boundary condition on the airfoil surface line. There are two approaches to derive such integral equation: by satisfying the boundary condition for normal or tangential components of flow velocity [9]. The right-hand side of these integral equations depends on the velocity, generated on the airfoil surface by all the vortex elements, which model the vortex wake in the flow. All the vortices contributions computation makes this procedure time-consuming. For the numerical solution

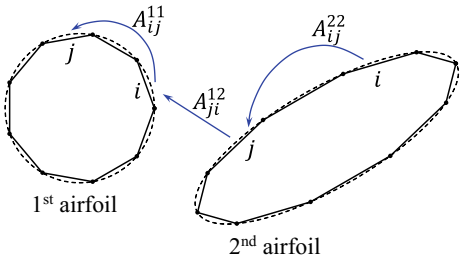

Fig. 13.1 Two airfoils approximated with rectilinear panels

of the integral equation, the airfoils are usually approximated by polygons consist of rectilinear panels (Fig. 13.1); then linear algebraic equations system is generated according to the chosen numerical scheme. There are number of different numerical schemes for the integral equation approximation, they have different computational complexities (with regard to coefficients computations) and lead to linear systems of different sizes, but in all the known scheme system size is commensurate with number of panels. In [14] a hierarchy of such schemes is described, all of those schemes are based on the ideas of Galerkin approach, continuous or discontinuous. In the current version of the VM2D code the numerical scheme with constant basis and projection functions in the framework of tangential components approach is used, as well as some less accurate schemes.

In order to estimate the computational complexities of the operations, we use hereinafter the following designations:

N is number of vortex elements in the flow domain;

n is total number of panels on the surface lines of all the airfoils.

In accordance with the described numerical scheme and formulae for calculating of the matrix and right-hand side coefficients given in [14], the following estimates for the computational complexity of this block can be obtained:

- the matrix coefficients computation: $Q_1 = 83n^2$,
- the right-hand side vector computation: $Q_2 = 30Nn + 85n^2$,
- linear system solving: $Q_3 = n^3/3$.

In the most general case of flow simulation around m deformable airfoils, it is necessary to recompute and solve the linear system at every time step of the simulation. The structure of the matrix can be schematically represented as the following:

$$\begin{pmatrix} A^{11} & A^{12} & \dots & A^{1m} \\ A^{21} & A^{22} & \dots & A^{2m} \\ \vdots & \vdots & \ddots & \vdots \\ A^{m1} & A^{m2} & \dots & A^{mm} \end{pmatrix},$$

where blocks A^{kk} express the self-influence of the k-th airfoil, and blocks A^{kp} express the contribution of the vorticity, being generated on the surface of the p-th airfoil, to limit value of the flow velocity on the k-th airfoil surface line.

The coefficients which form the corresponding blocks, depend on the relative positions of the panels only; therefore, in case of non-deformable (rigid) airfoils maintaining their positions relative to each other, the system matrix remains constant, that allows to calculate all the coefficients only once, then reverse the matrix (only at the first time step, computational complexity $Q_{rev} = O(n^3)$, and solve the system by its multiplying the right-hand side ($Q_{mult} = O(n^2)$ operations). In case of non-deformable airfoils being moved relative to each other, diagonal blocks A^{kk} remain constants, while the other (non-diagonal) blocks should be recalculated.

2. *Velocities computation.* The velocities of the vortex elements within the VVD approach [7] consist of two components: convective velocities and diffusive (caused by viscosity) velocities. When calculating the convective velocity, it is necessary to take into account the mutual influence of all vortex elements (i.e., to calculate the contributions of all the other vortices), according to the Bio—Savart law. The diffusive velocities are also calculated by taking into account the mutual influence of all vortex elements.

Computational complexities of these operations are the following:

- convective velocities computation: $Q_4 = 6N^2 + 8Nn$,
- diffusive velocities computation: $Q_5 = 9N^2 + 14Nn$.

Note, that complexity of diffusive velocities computation can be reduced by taking into account that vortices contributions to the diffusive velocity decrease exponentially with distance increase, so in practice it is necessary to calculate the influences only from the vortex elements, placed not very far one from others.

It also should be noted, that the surfaces of the airfoils also make a contribution to diffusive velocity of vortices in the flow. It should be taken into account only for vortices which are placed close to the airfoil surface, so the computational complexity of this procedure is proportional to n^2 and it can be neglected since $n \ll N$. In practice, however, this operation is important and in order to achieve high efficiency of parallel implementation, it also should be parallelized.

3. *Hydrodynamic loads computation.* In this block we compute hydrodynamic loads (forces and torque) acting the airfoils. For such purposes it is possible to use integral formulae, which are derived by prof. G.Ya. Dynnikova and adapted to several types of problems being solved by using vortex methods [16]. Note, that computational complexity of this block is much less in comparison with the other operation, so we will not take it into account.

4. *Vorticity evolution.* In this block vortices in the vortex wake are just being transferred along the calculated velocity field (recall, that it is superposition of convective and diffusive velocity fields). We use explicit Euler integration method, so it is necessary just to multiply vortices velocities by the time step value and add it to the current vortices positions. So the computational complexity of the block 4 is also much less than for the other operations, and normally it can be neglected.

5. *No-throw control.* In this operation we exclude vortex elements that penetrate the airfoil. Its complexity depends on the implementation; in the first approximation $Q_6 \sim n^2$, and the proportionality coefficient is of the order of 10.

6. *Vortex wake restructuring.* Closely placed vortex elements can be merged, and vortex elements which move far away from the airfoil, can be excluded. The computational complexity of this algorithm, as calculations show, is of the order of $Q_7 \sim N^2$, the proportionality coefficient is relatively small.

Thus, the computational complexity of the last two operations, although it may be high, is much lower than the total complexity of the other operations, so their complexities can be taken into account approximately: we set $Q_6 = Q_1$ and $Q_7 = 0.2\, Q_4$.

13.3 Model Problems Description

In order to estimate the possible ratios of computational complexities of the above mentioned operations for different types of problems, we consider two model problems:

Problem 13.1 (*Hydroelastic oscillations simulation for circular cylinder*) We consider flow around movable circular cylinder (Fig. 13.2) when vortex sheet on the surface line of cylinder is modeled with $n_{p0} = 200$ vortex elements. We assume that the vortex wake after the airfoil is simulated by $N_0 = 10\,000$ vortex elements, and number of time steps is $T_0 = 30\,000$. Such estimates are taken from practical simulation and correspond to the parameters of the real algorithm.

In order to improve the accuracy of simulation, which is necessary for flow simulation at rather high Reynolds numbers (number of vortices $n_{p0} = 200$ is considered to be more or less enough only for $\mathrm{Re} \le 10^3$), number of vortex elements on the airfoils surfaces n_p should be increased. Total number of vortices in the flow domain N we assume to be proportional to n^2, time step should be proportionally decreased and number of steps—proportionally increased:

$$n = n_p, \quad N = N_0 \cdot \left(\frac{n_p}{n_{p0}}\right)^2, \quad T = T_0 \cdot \left(\frac{n_p}{n_{p0}}\right). \tag{13.1}$$

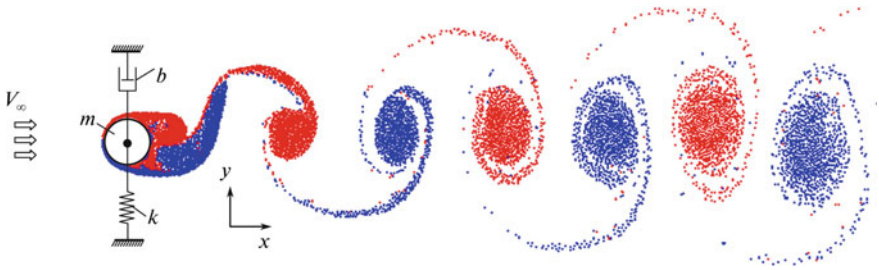

Fig. 13.2 Model problem 13.1 statement

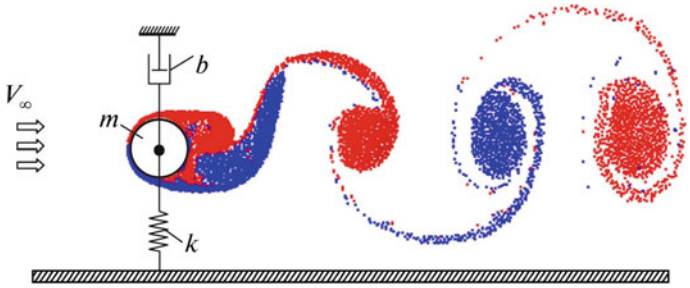

Fig. 13.3 Model problem 13.2 statement

Problem 13.2 (*Circular cylinder hydroelastic oscillations simulation in the presence of the screen*) The mentioned problem (Fig. 13.3) is considered in [17, 18]. In numerical simulation, the flow around the airfoil which models the screen, can be considered as flow without separation, that makes it possible to decrease number of vortices in the flow domain due to vorticity flux simulating only on the cylinder surface (vortex sheet on the screen surface is attached). As basic parameters of the numerical scheme, we consider the following: vortex sheet on the cylinder surface is modeled with $n_{p0} = 200$ vortex elements, vortex sheet on the screen surface—with $n_{e0} = 3n_{p0} = 600$ vortex elements, number of vortices in the wake in flow domain $N_0 = 10\,000$.

As the result, for arbitrary value of n_p we obtain

$$n = 4n_p, \quad N = N_0 \cdot \left(\frac{n_p}{n_{p0}}\right)^2, \quad T = T_0 \cdot \left(\frac{n_p}{n_{p0}}\right).$$

Computational complexities of the considered model problems for $n_p = 200$ are the following:

$$S_1(200) = \sum_{r=1}^{3} Q_r(n,\ N) + \sum_{r=4}^{7} Q_r(n,\ N) \cdot T_0 = 5.0 \cdot 10^{13},$$

$$S_2(200) = \sum_{r=1}^{7} Q_r(n,\ N) \cdot T_0 = 7.1 \cdot 10^{13}.$$

Estimations for computational complexities of these problems at different values of n_p (being normalized to $S(n_p = 200)$) are shown in Table 13.1.

The diagrams in the Figs. 13.4 and 13.5 show how the shares of separate operations vary for the considered problems with different n_p.

It is clear from the diagrams, that for different problems with different parameters the distribution of the total computational complexity over the operations can vary significantly. Figure 13.4 shows the ratio of the complexities of the operations for

Table 13.1 Computational complexity of the algorithm for different values of n_p in comparison with $S(200)$

n_p	100	200	400	600	800	1 000
$\frac{S_1(n_p)}{S_1(200)}$	0,03	1	32	240	1000	3050
$\frac{S_2(n_p)}{S_2(200)}$	0,05	1	26	188	766	2293

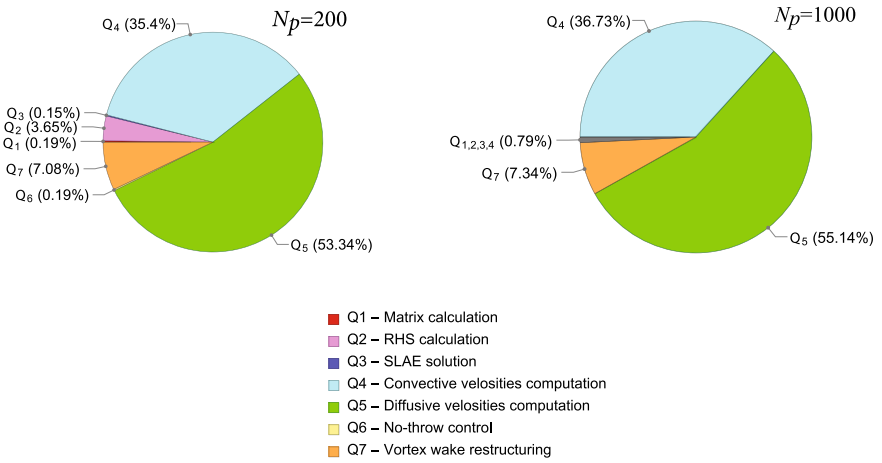

Fig. 13.4 The shares of separate operations for the Problem 13.1 with $n_p = 200$ and $n_p = 1000$

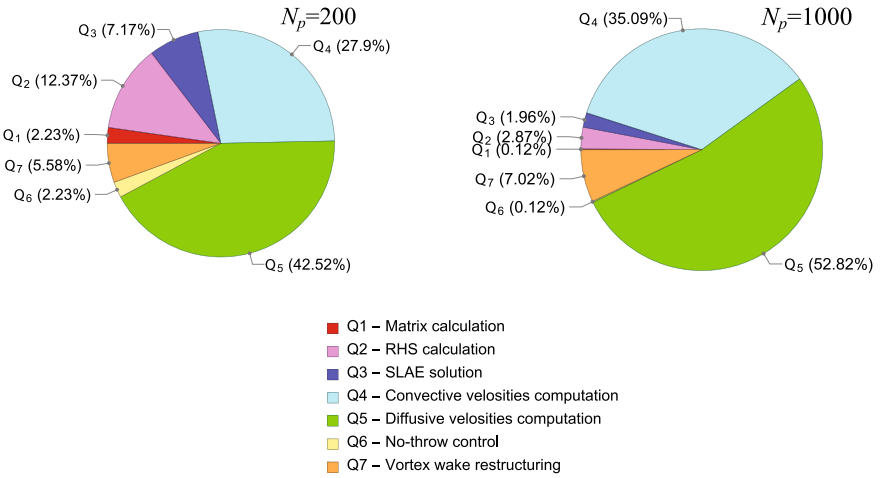

Fig. 13.5 The shares of separate operations for the Problem 13.2 with $n_p = 200$ and $n_p = 1000$

Problem 13.1: it is evident that in the case of $n_p = 1000$ panels, only operations 4, 5 and 7 have significant complexities, while all the other operations takes only about 0.2 %. However, for $n_p = 200$, the operation 3 also becomes significant. In the case of Problem 13.2, when there is large number of panels on the airfoils, some of which do not shed to the flow, for $n_p = 1000$, complexities of operations 2, 3, 4, 5, 7 are essential, while it seems that complexities of the 1 and 6 operations still can be neglected. However, if we consider the same problem with $n_p = 200$, all the operations are essential, and in order to obtain an efficient acceleration of computations, it is necessary to perform parallelization of all the listed operations.

13.4 Parallel Technologies Implemented in the VM2D Code

In the VM2D code parallel algorithms based on the MPI, OpenMP and Nvidia CUDA technologies are implemented, which allow one to perform simulations on multiprocessor computers with different architectures: on CPUs (with distributed and shared memory), and of hybrid systems with CPUs + GPUs. To achieve high acceleration and high efficiency, all the operations listed above are parallelized for all the mentioned parallel technologies.

13.4.1 MPI + OpenMP Parallelization

Parallelization for distributed memory systems is performed using MPI technology, computations within one node are parallelized using OpenMP technology. To estimate the efficiency of parallelization, the test simulations for four problems similar to Problem 13.1 have been performed with the following parameters: (1) $n_p = 1000$, $N_1 = 80\,000$; (2) $n_p = 2000$, $N_2 = 160\,000$; (3) $n_p = 4000$, $N_3 = 320\,000$; (4) $n_p = 6000$, $N_4 = 480\,000$.

The computations have been performed on two cluster systems:

1. Cluster with HP Blade Servers BL2x220c G7, Ivannikov Institute for System Programming of the RAS (Infiniband QDR, 2 × Intel Xeon X5670 (6 cores), 2.93 GHz).
2. Cluster HPC1 in National Research Center “Kurchatov Institute” (Infiniband QDR, 2 × Intel Xeon E5345 (4 cores), 2.33 GHz).

Figure 13.6 shows the acceleration of computations on the BL2x220c G7 system. The black line shows the acceleration level for the “ideally parallelized” code with 0.1 % of non-parallel (sequential) code calculated according to the Amdahl’s law [19]. It can be seen, that parallelization is the more efficient, the more vortex elements are in the vortex wake. Note, that for the considered problems we reach absolute efficiency 0.75 . . . 0.79 at 96 cores and 0.62 . . . 0.75 at 228 cores. If we normalize our acceleration to the acceleration of the code with 0.1 % of sequential code, we

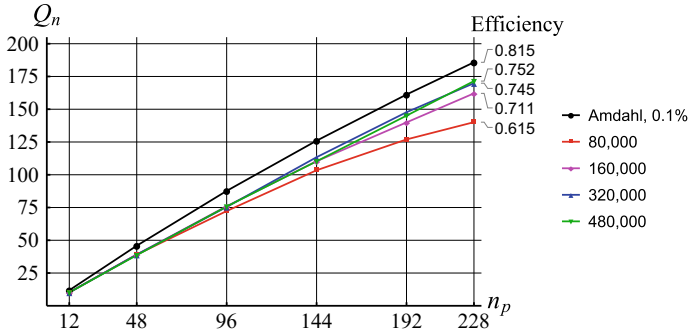

Fig. 13.6 Acceleration of the computations obtained for different number of cores for problems with different parameters on BL2x220c G7

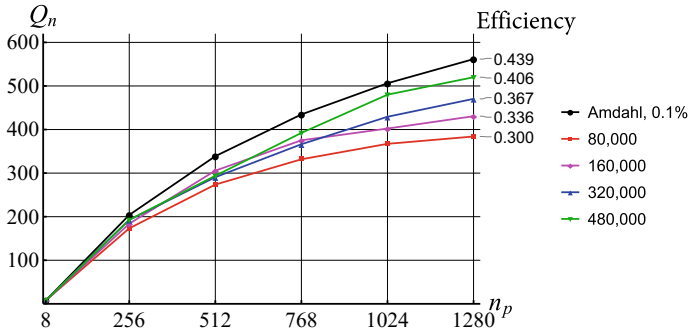

Fig. 13.7 Acceleration of the computations obtained by different number of cores for problems with different parameters on HPC1

obtain efficiency 0.82 . . . 0.92 at 96 cores and 0.75 . . . 0.88 at 228 cores. Finally, we reach 140 . . . 170 times acceleration of the algorithm at 228 nodes.

Figure 13.7 shows the acceleration of computations on the Claster HPC1 in National Research Center "Kurchatov Institute". As earlier, the black line shows the acceleration of the "ideally parallelized" code with 0.1 % sequential code calculated according to the Amdahl's law. For the considered problems we reach absolute efficiency 0.68 . . . 0.76 at 256 cores and 0.30 . . . 0.41 at 1280 cores. If we normalize our acceleration to the acceleration of the code with 0.1 % sequential code, we obtain efficiency 0.84 . . . 0.94 at 256 cores and 0.68 . . . 0.93 at 1280 cores. Finally, we reach 380 . . . 520 times acceleration of the algorithm at 1280 nodes.

Table 13.2 Comparison of performances of GPUs and BL2x220c G7

Acceleration	1	12	48	G970	96	144	192	228	K40
$N = 80\,000$	1	10.2	39.1	**58.7**	72.3	103.4	127.0	140.1	**158.9**
$N = 480\,000$	1	10.2	38.6	**66.1**	75.8	110.3	145.1	171.5	**162.6**

Table 13.3 Comparison of performances of GPUs and HPC1

Acceleration	1	8	G970	256	512	768	1024	K40	1280
$N = 80\,000$	1	7.2	**127.9**	173.3	273.7	331.7	367.2	**467.6**	468.6
$N = 480\,000$	1	7.3	**190.8**	192.8	294.0	392.3	463.0	**469.0**	565.9

13.4.2 Nvidia CUDA and MPI + CUDA Parallelization

All the algorithms for the described operations have been adapted for hybrid computer systems with GPU accelerators. Test simulations were performed by using two GPUs:

	GeForce GTX 970	Tesla K40c
Number of multiproc./cores	13/1664	15/2880
DRAM Memory	4 Gb (3.5 Gb)	12 Gb

Tables 13.2 and 13.3 show a comparison of the VM2D code performance on GPUs with its performance on CPUs. It can be seen that in the framework of VM2D one GPU GeForce GTX 970 can replace dozens or even hundreds of CPU cores. GPU Tesla K40c replaces hundreds or even more than 1000 CPU cores. It is also possible to perform calculations on several graphical cards that are located on different nodes, their communication takes place with the help of MPI. Test calculations show that if you use two graphical cards, you can get an acceleration of 1.6 times, and for three cards—2.2 times compared with the calculation on a single graphical card.

13.5 Conclusions

Parallel algorithms for VM2D open-source code were implemented using three technologies: MPI, OpenMP and CUDA. It is shown that ratio between computational complexities of the operations of the algorithm can vary significantly for different problems statements. Test problems shown that VM2D is efficiently parallelized: we achieve 75 . . . 79% efficiency of parallelization at 96 CPU cores, 0.68 . . . 0.76% efficiency at 256 cores and 0.30 . . . 0.41% efficiency at 1280 cores. It is shown that the acceleration achieved on one GPU is comparable to acceleration on hundreds and

even thousands of CPU cores. At the same time, the acceleration of calculations on GPU can be further increased due to the fact that it is possible to perform calculations on several cards simultaneously.

Acknowledgements The research is supported by the Russian Foundation for Basic Research (projects no. 17-08-01468 and 18-31-00245). The authors express their gratitude to Ivannikov Institute for System Programming of the Russian Academy of Sciences and to National Research Center "Kurchatov Institute" for providing the computational resources.

References

1. Mittal, R., Iaccarino, G.: Immersed boundary methods. Annu. Rev. Fluid Mech. **37**, 239–261 (2005). https://doi.org/10.1146/annurev.fluid.37.061903.175743
2. Marchevskii, I.K., Puzikova, V.V.: Numerical simulation of the flow around two fixed circular airfoils positioned in tandem using the LS-STAG method. J. Mach. Manuf. Reliab. **45**, 130–136 (2016). https://doi.org/10.3103/S1052618816020084
3. Cottet, G.-H., Koumoutsakos, P.D.: Vortex Methods: Theory and Practice. Cambridge University Press, Cambridge (2000)
4. Saffman, P.G.: Vortex Dynamics. Cambridge University Press, Cambridge (1992)
5. Lifanov, I.K.: Singular Integral Equations and Discrete Vortices. Walter de Gruyter, Utrecht (1996)
6. Lighthill, M.: Introduction. In: Rosenhead, J. (ed.) Boundary Layer Theory. Oxford University Press, Oxford (1963)
7. Dynnikova, G.Ya.: Vortex motion in two-dimensional viscous fluid flows. Fluid Dyn. **38**(5), 670–678 (2003). https://doi.org/10.1023/B:FLUI.0000007829.78673.01
8. Katz, J., Plotkin, A.: Low-speed aerodynamics. From wing theory to panel methods. McGraw-Hill, International Edition, New York (1991)
9. Kempka, S.N., Glass, M.W., Peery, J.S., Strickland, J.H., Ingber, M.S.: Accuracy considerations for implementing velocity boundary conditions in vorticity formulations. Sandia Report Sand 96-0583 UC-700 (1996). https://doi.org/10.2172/242701
10. Kuzmina, K.S., Marchevskii, I.K., Moreva, V.S.: Vortex sheet intensity computation in incompressible flow simulation around an airfoil by using vortex methods. Math. Model. Comput. Simul. **10**(3), 276–287 (2018). https://doi.org/10.1134/S2070048218030092
11. Kuzmina, K.S., Marchevsky, I.K., Moreva, V.S.: Parallel implementation of vortex element method on CPUs and GPUs. Procedia Comput. Sci. **66**, 73–82 (2015). https://doi.org/10.1016/j.procs.2015.11.010
12. Kuzmina, K.S., Marchevsky, I.K., Ryatina, E.P.: Open Source Code for 2D Incompressible Flow Simulation by Using Meshless Lagrangian Vortex Methods. IEEE Xplore Digital Library. Ivannikov ISPRAS Open Conference. 97–103 (2017). https://doi.org/10.1109/ISPRAS.2017.00023
13. Kuzmina, K.S., Marchevskii, I.K., Moreva, V.S., Ryatina, E.P.: Numerical scheme of the second order of accuracy for vortex methods for incompressible flow simulation around airfoils. Russ. Aeronaut. **60**(3), 398–405 (2017). https://doi.org/10.3103/S1068799816030114
14. Kuzmina, K.S., Marchevsky, I.K., Ryatina, E.P.: Exact analytical formulae for linearly distributed vortex and source sheets influence computation in 2D vortex methods. J. Phys. Conf. Ser. **918**, art. 012013 (2017). https://doi.org/10.1088/1742-6596/918/1/012013
15. Kuzmina, K.S., Marchevsky, I.K., Milani, D., Ryatina, E.P. Accuracy comparison of different approaches for vortex sheet discretization on the airfoil in vortex particles method. In: Proceedings of 5th International Conference on Particle-Based Methods, Particles-2017, pp. 691–702. Hannover, Germany (2017)

16. Dynnikova, G.Ya.: An analog of the Bernoulli and Cauchy – Lagrange integrals for a time-dependent vortex flow of an ideal incompressible fluid. Fluid Dyn. **35**(1), 24–32 (2000). https://doi.org/10.1007/BF02698782
17. Bearman, P.W., Zdravkovich, M.M.: Flow around a circular cylinder near a plane boundary. J. Fluid Mech. **89**(1), 33–47 (1978). https://doi.org/10.1017/S002211207800244X
18. Lei, C., Cheng, L., Kavanagh, K.: Re-examination of the effect of a plane boundary on force and vortex shedding of a circular cylinder. J. Wind. Eng. Ind. Aerodyn. **80**(3), 263–286 (1999). https://doi.org/10.1016/S0167-6105(98)00204-9
19. Amdahl, G.: Validity of the single processor approach to achieving large-scale computing capabilities. AFIPS Conf. Proc. **30**, 483–485 (1967). https://doi.org/10.1145/1465482.1465560

Chapter 14
A Geometry-Adaptive Immersed Boundary–Lattice Boltzmann Method for Modelling Fluid–Structure Interaction Problems

Lincheng Xu, Li Wang, Fang-Bao Tian, John Young and Joseph C. S. Lai

Abstract The immersed boundary method has been extensively used in many areas. However, there are two typical challenges for modelling fluid-structure problems at moderate and high Reynolds numbers (e.g. 10^3–10^5). One is the size of mesh at high Reynolds numbers when the standard immersed boundary method is applied. The other is the numerical instability associated with the partitioned coupling for fluid-structure interaction problems involving small structure-to-fluid mass ratios. To address the challenges, a novel computational framework which combines the lattice Boltzmann method and an improved immersed boundary method based on a dynamic geometry-adaptive Cartesian grid is presented. A few classic validations are conducted to demonstrate the accuracy of the current method.

Keywords Adaptive mesh · Immersed boundary method · Lattice Boltzmann method · Fluid-structure interaction

14.1 Introduction

Many biological systems and flows in nature involve fluid-structure interactions (FSIs) such as flag flapping, vocal-fold vibration, insect wing and fish fin (see e.g. [1–8]). Study of FSIs within these flows is of great significance to understand the fundamentals and improve engineering designs. For example, the knowledge of flag flapping is able to provide inspiration to designing the flexible plate energy harvester by using piezoelectric materials [1, 3, 4, 6, 9–11]. The flexibility of flapping wings/foils is able to enhance the aerodynamic performance [5, 8, 12–14]. Therefore, great effort has been dedicated to develop numerical methods for modelling FSI problems [15–18].

Due to the complexity of FSI flows, various numerical methods have been developed. Each method is suitable for a group of topics. Some of these were summarized

L. Xu · L. Wang · F.-B. Tian (✉) · J. Young · J. C. S. Lai
School of Engineering and Information Technology, University of New South Wales, Canberra, ACT 2600, Australia
e-mail: f.tian@adfa.edu.au

S. Gutschmidt et al. (eds.), *IUTAM Symposium on Recent Advances in Moving Boundary Problems in Mechanics*, IUTAM Bookseries 34,
https://doi.org/10.1007/978-3-030-13720-5_14

by Deng et al. [15]. Among these methods, there are two typical types of approaches: body-fitted grid methods and Cartesian grid methods. In body-fitted grid methods, one needs to generate a mesh to fit the boundaries immersed in the fluid. The advantages of body-fitted grid methods are associated with the facts that the boundary conditions can be directly applied at the fluid-structure boundaries and that it is easy to apply a very fine mesh around the boundaries to resolve the boundary layer [15, 19–25]. However, it is time consuming to generate a proper mesh for problems involving complex geometries and to handle moving mesh for problems involving large deformation. On the other hand, these challenges are avoided in Cartesian grid methods where the fluid governing equations are discretized on a Cartesian mesh which does not conform to the immersed boundaries. The immersed boundary method (IBM), first developed by Peskin [26, 27] and recently a popular approach of Cartesian grid methods, has attracted growing interest on expanding its applications and proposing new features [28–31] and has been extensively used in many areas (see e.g. [3, 31–37]). There are two typical challenges for modelling FSI problems at moderate and high Reynolds numbers (e.g. 10^3–10^5) by using IBM and partitioned FSI coupling strategy. One is the size of mesh at high Reynolds numbers when the standard IBM is applied. The other is the numerical instability for FSI problems involving small structure-to-fluid mass ratios [38, 39].

In this work, we present a novel computational framework which combines the lattice Boltzmann method (LBM) and an improved IBM based on a dynamic geometry-adaptive Cartesian grid. In addition, the heat transfer, solved by a finite difference method, is coupled with the fluid and structure dynamics. A few classic validations are conducted to demonstrate the accuracy of the current method.

14.2 Numerical Method

In this work, the fluid dynamics, structure dynamics and heat transfer are coupled in a partitioned way, so that each component can be solved separately, and coupled via boundary conditions handled by the IBM.

In the current work, the fluid dynamics is obtained by solving the discrete lattice Boltzmann equation [40], i.e.

$$m_i\left(\boldsymbol{x}+\boldsymbol{e}\delta_t, t+\delta_t\right)-m_i\left(\boldsymbol{x}, t\right)=s_i\left(m_i^{eq}-m_i\left(\boldsymbol{x}, t\right)\right)+\left(1-\frac{s_i}{2}\right)\left(\mathbf{M}\boldsymbol{G}\right)_i, \quad (14.1)$$

$$\boldsymbol{m}=\mathbf{M}\boldsymbol{g}, \qquad \boldsymbol{m}^{eq}=\mathbf{M}\boldsymbol{g}^{eq}, \quad (14.2)$$

where $\boldsymbol{m}$ represents the velocity moment, $\boldsymbol{m}^{eq}$ is the equilibrium moment, $\boldsymbol{g}$ is the distribution function, $\boldsymbol{g}^{eq}$ is the equilibrium function, $\boldsymbol{e}$ is the discrete velocity, $\boldsymbol{x}$ is the space coordinate, δ_t is the time step size, s_i is a series of relaxation rates, $\mathbf{M}$ is the moment matrix, and jth component of $\boldsymbol{G}$ is given by $\omega_j\left[\delta_t\boldsymbol{f}\cdot\left(\boldsymbol{e}_j-\boldsymbol{u}\right)/{c_s}^2+\left(\delta_t\boldsymbol{f}\cdot\boldsymbol{e}_j\right)\left(\boldsymbol{u}\cdot\boldsymbol{e}_j\right)/{c_s}^4\right]$, with $\boldsymbol{f}$ being an external body force, macroscopic variables including the fluid density, velocity and pressure values

respectively calculated by $\rho = \sum \boldsymbol{g}_j$, $\boldsymbol{u} = \left(\sum \boldsymbol{g}_j \boldsymbol{e}_j + 0.5\delta_t \boldsymbol{f}\right)/\rho$, $p = \rho {c_s}^2$, and c_s being the lattice sound speed given by $\delta_x/\left(\sqrt{3}\delta_t\right)$ with δ_x being the mesh spacing. The equilibrium function ${\boldsymbol{g}_j}^{eq}$ is determined by ${\boldsymbol{g}_j}^{eq} = \omega_j \rho[1 + \boldsymbol{u} \cdot \boldsymbol{e}_j/{c_s}^2 + \left(\boldsymbol{u} \cdot \boldsymbol{e}_j\right)^2/(2{c_s}^4) - \boldsymbol{u}^2/(2{c_s}^2)]$, where ω_j is the jth weight. In the above calculations, i and j indicate the ith component of velocity moment and jth discrete velocity, respectively.

The heat transfer, governed by an unsteady convection-diffusion equation, is solved by using a finite difference method. In this method, the second-order upwind scheme is used to discretize the convection term, and the second-order central difference scheme is adopted for the diffusion term. In addition, a second-order explicit scheme is used for the temporal discretization.

The structure dynamics can be solved by the finite element method (as used in Ref. [36]), finite difference method (as used in Refs. [22, 39]) or meshfree material point method [41]. In this paper, filament/thin plate structure in our FSI validation cases is solved by the finite difference method.

Both LBM for the fluid dynamics and finite difference method for the heat transfer are solved on a dynamic geometry-adaptive Cartesian mesh which is applied to provide fine resolution around the immersed geometries and coarse resolution in the far field. The overlapping grids between two adjacent refinements consist of two layers. In order to enhance the numerical stability, two-layer "ghost nodes" are generated within the immersed body domain which is a non-fluid area. The movement of fluid–structure interfaces only causes adding or removing grids at the boundaries of refinements and consequently a high mesh-update efficiency is guaranteed.

The boundary conditions of fluid dynamics at the FSI interfaces are handled by an improved IBM, which drives the predicted flow velocity (calculated after the LBM stream process [42] without the IBM body force) to match the solid velocity. In the present IBM, the feedback coefficient is mathematically derived and explicitly approximated, i.e.

$$k = k_0/(1 - \Delta U_1/\Delta U) = 2/(1 - C_{UR}), \tag{14.3}$$

where C_{UR} is an approximation of the relative velocity residual. The Lagrangian force is divided into two parts, i.e.

$$\begin{aligned} \boldsymbol{F}_{IB} &= \bar{k}\left(\boldsymbol{U}_b^{n+1} - \mathbf{A}\boldsymbol{u}^*\right)\delta_x/\delta_t \\ &= \bar{k}\left(\boldsymbol{U}_b^{n+1} - \boldsymbol{U}_b^n + \boldsymbol{U}_b^n - \mathbf{A}\boldsymbol{u}^*\right)\delta_x/\delta_t \\ &= \bar{k}\left(\boldsymbol{U}_b^n - \mathbf{A}\boldsymbol{u}^*\right)\delta_x/\delta_t + \bar{k}\delta_x \boldsymbol{a}, \end{aligned} \tag{14.4}$$

where $\bar{k} = k\delta_t/\delta_x$ and $\boldsymbol{a}$ is the acceleration of the flexible structure. The first part is the driving force caused by the predicted flow velocity, and the other part is caused by the acceleration of the immersed boundary. Such treatment significantly enhances the numerical stability for modelling FSI problems involving small structure-to-fluid mass ratios. The Lagrangian force is then spread onto the fluid nodes around the

boundary according to

$$\boldsymbol{f}(\boldsymbol{x},t)=\int_{\Gamma}\boldsymbol{F}_{IB}\delta_h(\boldsymbol{X}(s,t)-\boldsymbol{x})ds, \tag{14.5}$$

where δ_h is a smooth approximation of Dirac's delta function [43].

For the heat transfer, similar technique is applied to modify the heat source around the boundary [44]

$$q=\int_{\Gamma}Q(s,t)\delta_h(\boldsymbol{X}(s,t)-\boldsymbol{x})ds, \tag{14.6}$$

where Q is the Lagrangian heat source. For the first type of boundary condition, Q can be calculated according to

$$Q=\alpha_T(T_{ib}-T_0), \tag{14.7}$$

where α_T is a large factor, T_0 is the boundary condition on the immersed boundary, and T_{ib} is the temperature on the surface interpolated by

$$T_{ib}(s,t)=\int_{V}T(x,t)\delta_h(\boldsymbol{X}(s,t)-\boldsymbol{x})d\boldsymbol{x}. \tag{14.8}$$

In Eq. (14.1), the fluid kinematic viscosity ν is reflected in values of s_i. It could be a constant (for Newtonian fluid) or a function of shear rate (for non-Newtonian fluid) [20, 39, 45–48]. If the large eddy simulation (LES) model is applied, it also includes turbulent viscosity component. In our work, the classic Smagorinsky LES model [49], the Germano–Lilly model [50] and the Lagrangian dynamic subgrid-scale model [51] have been incorporated into the framework to model turbulent flows at relatively high Reynolds numbers.

14.3 Validation

14.3.1 Fluid-Structure-Heat Interaction of Flow Around a Filament in the Wake of a Stationary Cylinder

A filament in the wake of a stationary cylinder located in a uniform flow, which has been extensively used to study fish behaviors in a street wake [3, 7, 52, 53], is coupled with heat transfer and power-law fluid. The problem configuration is shown in Fig. 14.1, where D is the diameter of the cylinder, L is the length of the filament and l is the distance from the origin of the cylinder to the fixed leading edge of the filament. Simulations are performed at $l/D=3.0, m_s=0, L/D=2.5$ and Re=100. The non-dimensional stretching coefficient defined by $K_s^*=K_s/(\rho U^2 D)$ is 1000,

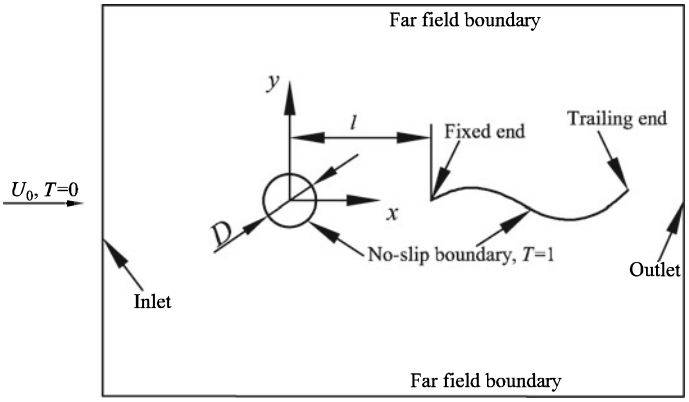

Fig. 14.1 Schematic of fluid-structure-heat interaction of a filament in the wake of a stationary cylinder located in a uniform flow

Table 14.1 Mean drag coefficient ($\overline{C_D}$), Strouhal number (St) and mean Nusselt number ($\overline{Nu}$) of the cylinder, and the lateral flapping amplitude A/D of the trailing end of the filament

Sources	n	C_D	St	Nu	A/D
Present	0.6	1.25	0.175	5.881	1.10
Present	1.0	1.38	0.156	5.407	1.11
Sui et al. [52]		1.41	0.156	–	1.14
Present	1.4	1.51	0.143	5.077	1.10

and the non-dimensional bending rigidity defined by $K_b^* = K_b/(\rho U^2 D^3)$ is 10^{-4}. The mesh size around the cylinder and filament is $D/160$. The dimensionless time step $\Delta t^* = \Delta t U_0/D = 6.25 \times 10^{-4}$. Three power-law indices $n = 0.6$, 0.8 and 1.0 are considered.

Table 14.1 shows the mean drag coefficient ($\overline{C_D}$), Strouhal number (St) and mean Nusselt number ($\overline{Nu}$) of the cylinder, and the lateral flapping amplitude (A/D) of the trailing end of the filament. For $n = 1.0$ (Newtonian flow), results of Ref. [52] are listed in the table for comparison. First, our results for $n = 1$ are in good agreement with those predicted by Sui et al. [52]. Second, $\overline{C_D}$ increases with n, while St and $\overline{Nu}$ decrease with n. This is quite similar to that of a single cylinder in power-law flow [39, 45, 46]. Finally, A/D is almost independent of power-law index. The instantaneous vorticity and temperature contours are presented in Fig. 14.2. The non-Newtonian results presented here can be used to extend the limited database of fluid-structure-heat interaction.

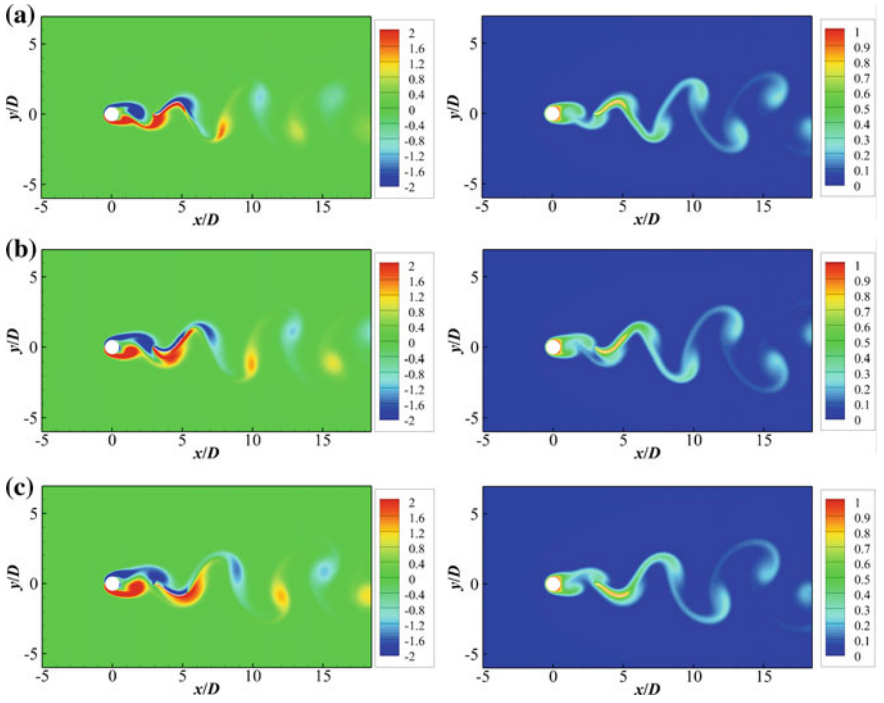

Fig. 14.2 Instantaneous vorticity (left column) and temperature (right column) contours at Re = 100, Pr = 1.0: **a** $n = 0.6$, **b** $n = 1.0$ and **c** $n = 1.4$

14.3.2 A Hovering Dragonfly

A hovering dragonfly is simulated to validate a three-dimensional complex case. The wings undergo both body axis-centered stroke motion and pitching motion around their spanwise torsion axes, with a frequency of about 36 Hz and a stroke plane angle of 60° [54]. The stroke kinematics can be described as

$$\varphi(t) = 0.5(\varphi_{max} + \varphi_{min}) + 0.5(\varphi_{max} - \varphi_{min})\cos(2\pi f t), \tag{14.9}$$

where f is the frequency, and φ_{min} and φ_{max} are respectively $-25°$ and 35° for forewings and $-15°$ and 45° for hindwings. The pitching kinematics is approximated by (measured in degrees) [55]

$$\theta(t) = 105 + 54\cos(2\pi f t + 1.55) + 2\cos(4\pi f t + 1.53) + 7\cos(6\pi f t + 0.91). \tag{14.10}$$

Here the Reynolds number, defined by $\mathrm{Re} = 2\rho(\varphi_{max} - \varphi_{min}) f L_w \bar{c}/\mu$, is about 2500, where f is the flapping frequency, and L_w and $\bar{c}$ are respectively the spanwise length and the mean chord length of a wing. The phase difference between forewings

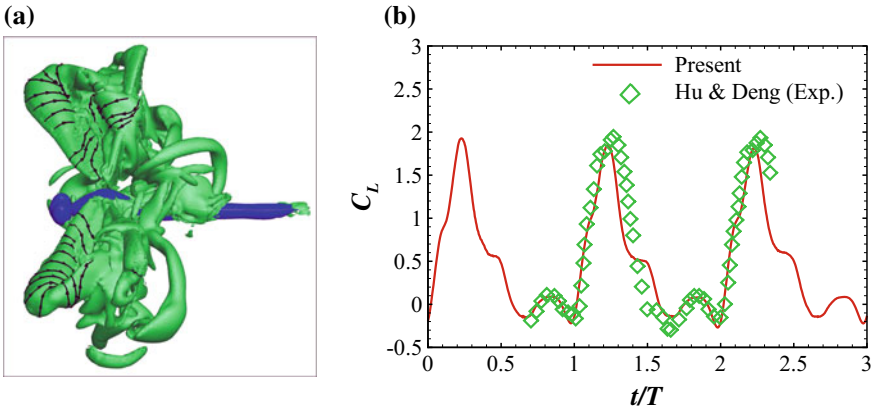

Fig. 14.3 Flow around hovering dragonfly: **a** Vortex structure of an integrated dragonfly model during hovering flight; **b** Lift coefficient of hindwings. Experimental data conducted by Hu and Deng [55] is shown for comparison

and hindwings is 180°. The vortical structures and lift coefficient of a pair of hindwings are shown in Fig. 14.3. It shows that the current result is in good agreement with the experimental data in Ref. [55].

14.3.3 Turbulence Flow Over a Wavy Wall

A pressure-driven turbulent flow over a wavy wall [56, 57] is conducted to validate the turbulence modelling capability. The bottom wavy wall is described by $y = a\cos(2\pi x/\lambda)$, where a is the amplitude of the wave, x is the streamwise coordinate, and λ is the wave length. Following Refs. [56, 57], we set $h/\lambda = 0.4, a/\lambda = 0.05$ and $l_w/\lambda = 0.944$, where h and l_w are respectively the half height and the spanwise length of the channel. No-slip condition is applied on the wavy wall; periodic boundary conditions are applied on all of the lateral walls; and symmetric boundary condition is applied on the top wall. A constant streamwise pressure gradient is applied over the whole domain. The Reynolds number based on the half channel height h and the mean streamwise velocity on the top wall is around 2400 which is achieved by adjusting the pressure gradient.

Figure 14.4 shows the mean streamwise velocity, velocity profiles within sublayers, turbulent statistics and energy spectrum. For comparison, the LES result from Ref. [57] and experimental data from Ref. [56] are shown in the picture. From Fig. 14.4a, it is found that our results are in good agreement with those from Refs. [56, 57]. The turbulent models [49–51] implemented in this framework are able to predict reliable results, as demonstrated by Fig. 14.4a, b. Regarding turbulent statistics shown in Fig. 14.4c, results of three models are comparable. But we also notice

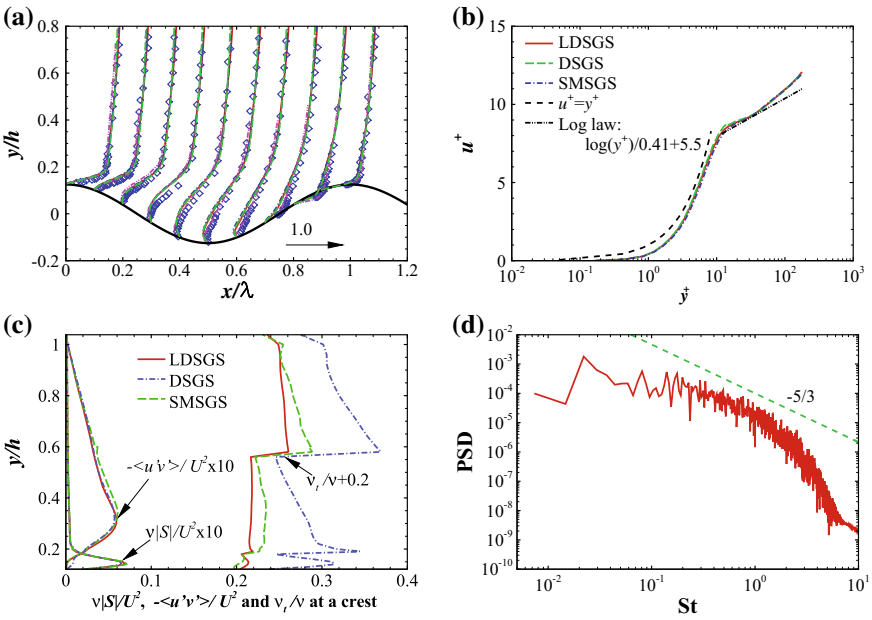

Fig. 14.4 Turbulence flow over a wavy wall: **a** Mean streamwise velocity; **b** Velocity profiles within sublayers; **c** $\nu|S|/U^2 \times 10$, $- < u'v' > /U^2 \times 10$ and $\nu_t/\nu + 0.2$; and **d** Energy spectrum. In **a**, the LES result from Ref. [57] (pink dash-double dotted line) and experimental data from Ref. [56] (blue diamond symbol) are presented for comparison. Other line legends in **a** are the same as those in **c**. In order to optimise that visualisation, the stresses in **c** are amplified by 10 times and the turbulent viscosity is shifted by 0.2. SMSGS, DSGS and LDSGS represent the classic Smagorinsky LES model [49], the Germano–Lilly model [50] and the Lagrangian dynamic subgrid-scale model [51], respectively

that the turbulent viscosities predicted by the Germano–Lilly model [50] and the Lagrangian dynamic subgrid-scale model [51] are lower compared to that predicted by the classic Smagorinsky LES model [49], and approach zero on the wall. Finally, the $-5/3$ Kolmogorov law is well captured, as shown in Fig. 14.4d.

14.4 Conclusion

In this work, a novel geometry-adaptive IB-LBM has been introduced to model FSI problems involving heat transfer, non-Newtonian flow and turbulence. Benchmark cases including fluid-structure-heat interaction of flow around a filament in the wake of a stationary cylinder, a hovering dragonfly and turbulence flow over a wavy wall have been conducted to validate the current solver. Results show that the current solver is reliable. In addition, the results presented in this work can be used to extend the limited database of fluid-structure-heat interaction.

Acknowledgements Mr L. Xu acknowledges the support of the University International Postgraduate Award by University of New South Wales. Dr. F.-B. Tian is the recipient of an Australian Research Council Discovery Early Career Researcher Award (project number DE160101098).

References

1. Zhu, L., Peskin, C.S.: Simulation of a flapping flexible filament in a flowing soap film by the immersed boundary method. J. Comput. Phys. **179**, 452–468 (2002)
2. Tian, F.B., Luo, H., Zhu, L., Lu, X.Y.: Interaction between a flexible filament and a downstream rigid body. Phys. Rev. E **82**, 026,301 (2010)
3. Tian, F.B., Luo, H., Zhu, L., Liao, J.C., Lu, X.Y.: An immersed boundary-lattice Boltzmann method for elastic boundaries with mass. J. Comput. Phys. **230**, 7266–7283 (2011)
4. Tian, F.B., Lu, X.Y., Luo, H.: Onset of instability of a flag in uniform flow. Theor. Appl. Mech. Lett. **2**, 022,005 (2012)
5. Tian, F.B., Luo, H., Song, J., Lu, X.Y.: Force production and asymmetric deformation of a flexible flapping wing in forward flight. J. Fluids Struct. **36**, 149–161 (2013)
6. Tian, F.B.: Role of mass on the stability of flag/flags in uniform flow. Appl. Phys. Lett. **103**, 034,101 (2013)
7. Stewart, W.J., Tian, F.B., Akanyeti, O., Walker, C., Liao, J.C.: Refusing rainbow trout selectively exploit flows behind tandem cylinders. J. Exp. Biol. **219**, 2182–2191 (2016)
8. Shahzad, A., Tian, F.B., Young, J., Lai, J.C.S.: Effects of flexibility on the aerodynamic performance of flapping wings with different shapes and aspect ratios in hover. J. Fluids Struct. **81**, 69–96 (2018)
9. Tezduyar, T.E., Sathe, S., Keedy, R., Stein, K.: Space-time finite element techniques for computation of fluid-structure interactions. Comput. Methods Appl. Mech. Eng. **195**, 2002–2027 (2006)
10. Tian, F.B., Luo, H., Zhu, L., Lu, X.Y.: Coupling modes of three filaments in side-by-side arrangement. Phys. Fluids **23**, 111,903 (2011)
11. Akcabay, D.T., Young, Y.L.: Scaling the dynamic response and energy harvesting potential of piezoelectric beams. Appl. Phys. Lett. **101**, 264,104 (2012)
12. Tian, F.B., Young, J., Lai, J.C.S.: Improving power-extraction efficiency of a flapping plate: From passive deformation to active control. J. Fluids Struct. **51**, 384–392 (2014)
13. Wu, J., Shu, C., Zhao, N., Tian, F.B.: Numerical study on the power extraction performance of a flapping foil with a flexible tail. Phys. Fluids **27**, 013,602 (2015)
14. Wu, J., Wu, J., Tian, F.B., Zhao, N., Li, Y.D.: How a flexible tail improve the power extraction efficiency of a semi-activated flapping foil system: a numerical study. J. Fluids Struct. **54**, 886–899 (2015)
15. Deng, H.B., Xu, Y.Q., Chen, D.D., Dai, H., Wu, J., Tian, F.B.: On numerical modeling of animal swimming and flight. Comput. Mech. **52**, 1221–1242 (2013)
16. Takizawa, K., Bazilevs, Y., Tezduyar, T.E., Long, C.C., Marsden, A.L., Schjodt, K.: ST and ALE-VMS methods for patient-specific cardiovascular fluid mechanics modeling. Math. Model. Methods Appl. Sci. **24**, 2437–2486 (2014)
17. Takizawa, K., Bazilevs, Y., Tezduyar, T.E., Hsu, M.C., Øiseth, O., Mathisen, K.M., Kostov, N., McIntyre, S.: Engineering analysis and design with ALE-VMS and space-time methods. Arch. Comput. Methods Eng. **21**, 481–508 (2014)
18. Liska, S., Colonius, T.: A fast immersed boundary method for external incompressible viscous flows using lattice Green's functions. J. Comput. Phys. **331**, 257–279 (2017)
19. Tian, F.B., Lu, X.Y., Luo, H.: Propulsive performance of a body with a traveling wave surface. Phys. Rev. E **86**, 016,304 (2012)
20. Tian, F.B., Bharti, R.P., Xu, Y.Q.: Deforming-spatial-domain/stabilized space-time (DSD/SST) method in computation of non-Newtonian fluid flow and heat transfer with moving boundaries. Comput. Mech. **53**, 257–271 (2014)

21. Tian, F.B., Xu, Y.Q., Tang, X.Y., Deng, Y.L.: Study on a self-propelled fish swimming in viscous fluid by a finite element method. J. Mech. Med. Biol. **13**, 1340,012 (2013)
22. Tian, F.B.: FSI modeling with the DSD/SST method for the fluid and finite difference method for the structure. Comput. Mech. **54**, 581–589 (2014)
23. Tian, F.B.: A numerical study of linear and nonlinear kinematic models in fish swimming with the DSD/SST method. Comput. Mech. **55**, 469–477 (2015)
24. Tian, F.B., Wang, Y., Young, J., Lai, J.C.S.: An FSI solution technique based on the DSD/SST method and its applications. Math. Model. Methods Appl. Sci. **25**, 2257–2285 (2015)
25. Xu, Y.Q., Jiang, Y.Q., Wu, J., Sui, Y., Tian, F.B.: Benchmark numerical solutions for two-dimensional fluid-structure interaction involving large displacements with the deforming-spatial-domain/stabilized space-time and immersed boundary-lattice Boltzmann methods. Inst. Mech. Eng. C: J. Mech. Eng. Sci. **232**, 2500–2514 (2018)
26. Peskin, C.S.: Flow patterns around heart valves: a numerical method. J. Comput. Phys. **10**, 252–271 (1972)
27. Peskin, C.S.: Numerical analysis of blood flow in the heart. J. Comput. Phys. **25**, 220–252 (1977)
28. Griffith, B.E., Hornung, R.D., McQueen, D.M., Peskin, C.S.: An adaptive, formally second order accurate version of the immersed boundary method. J. Comput. Phys. **223**, 10–49 (2007)
29. Ghias, R., Mittal, R., Dong, H.: A sharp interface immersed boundary method for compressible viscous flows. J. Comput. Phys. **225**, 528–553 (2007)
30. Wang, W., Yan, Y., Tian, F.B.: A simple and efficient implicit direct forcing immersed boundary framework for simulations of complex flow. Appl. Math. Model. **43**, 287–305 (2017)
31. Wang, L., Currao, G.M.D., Han, F., Neely, A.J., Young, J., Tian, F.B.: An immersed boundary method for fluid-structure interaction with compressible multiphase flows. J. Comput. Phys. **346**, 131–151 (2017)
32. Mittal, R., Iaccarino, G.: Immersed boundary method. Annu. Rev. Fluid Mech. **37**, 239–261 (2005)
33. Xu, Y.Q., Tian, F.B., Li, H.J., Deng, Y.L.: Red blood cell partitioning and blood flux redistribution in microvascular bifurcation. Theor. Appl. Mech. Lett. **2**, 024,001 (2012)
34. Xu, Y.Q., Tian, F.B., Deng, Y.L.: An efficient red blood cell model in the frame of IB-LBM and its application. Int. J. Biomath. **6**, 1250,061 (2013)
35. Xu, Y.Q., Tang, X.Y., Tian, F.B., Peng, Y.H., Xu, Y., Zeng, Y.J.: IB-LBM simulation of the haemocyte dynamics in a stenotic capillary. Comput. Methods Biomech. Biomed. Eng. **17**, 978–985 (2014)
36. Tian, F.B., Dai, H., Luo, H., Doyle, J.F., Rousseau, B.: Fluid-structure interaction involving large deformations: 3D simulations and applications to biological systems. J. Comput. Phys. **258**, 451–469 (2014)
37. Sotiropoulos, F., Yang, X.: Immersed boundary methods for simulating fluidcstructure interaction. Prog. Aerosp. Sci. **65**, 1–21 (2014)
38. Xu, L., Tian, F.B., Young, J., Lai, J.C.S.: A novel geometry-adaptive cartesian grid based immersed boundary-lattice Boltzmann method for fluid-structure interactions at moderate and high reynolds numbers. J. Comput. Phys. **375**, 22–56 (2018)
39. Wang, L., Tian, F.B.: Heat transfer in non-newtonian flows by a hybrid immersed boundary-lattice Boltzmann and finite difference method. Appl. Sci. **8**, 559 (2018)
40. d'Humières, D.: Generalized lattice Boltzmann equation. AIAA Rarefied Gas Dyn. Theory Simul. **159**, 450–458 (1992)
41. Sulsky, D., Chen, Z., Schreyer, H.L.: A particle method for history-dependent materials. Comput. Mechods Appl. Mech. Eng. **118**, 179–196 (1994)
42. Chen, S., Doolen, G.D.: Lattice Boltzmann method for fluid flows. Annu. Rev. Fluid Mech. **30**, 329–364 (1998)
43. Peskin, C.S.: The immersed boundary method. Acta Numer. **11**, 479–517 (2002)
44. Ren, W., Shu, C., Wu, J., Yang, W.: Boundary condition-enforced immersed boundary method for thermal flow problems with dirichlet temperature condition and its applications. Comput. Fluids **57**, 40–51 (2012)

45. Bharti, R., Sivakumar, P., Chhabra, R.: Forced convection heat transfer from an elliptical cylinder to power-law fluids. Int. J. Heat Mass Transf. **51**, 1838–1853 (2008)
46. Patnana, V.K., Bharti, R.P., Chhabra, R.P.: Two-dimensional unsteady flow of power-law fluids over a cylinder. Chem. Eng. Sci. **64**, 2978–2999 (2009)
47. Tian, F.B., Zhu, L., Fok, P.W., Lu, X.Y.: Simulation of a pulsatile non-Newtonian flow past a stenosed 2D artery with atherosclerosis. Comput. Biol. Med. **43**, 1098–1113 (2013)
48. Tian, F.B.: Deformation of a capsule in a power-law shear flow. Comput. Math. Methods Med. **2016**, 7981,386 (2016)
49. Smagorinsky, J.: General circulation experiments with the primitive equations: I. The basic experiment. Mon. Weather Rev. **91**(3), 99–164 (1963)
50. Lilly, D.K.: A proposed modification of the Germano subgrid-scale closure method. Phys. Fluids Fluid Dyn. **4**, 633–635 (1992)
51. Meneveau, C., Lund, T.S., Cabot, W.H.: A lagrangian dynamic subgrid-scale model of turbulence. Journal of Fluid Mechanics **319**, 353–385 (1996)
52. Sui, Y., Chew, Y.T., Roy, P., Low, H.T.: A hybrid immersed-boundary and multi-block lattice Boltzmann method for simulating fluid and moving-boundaries interactions. Int. J. Numer. Meth. Fluids **53**, 1727–1754 (2007)
53. Alben, S.: Wake-mediated synchronization and drafting in coupled flags. J. Fluid Mech. **641**, 489–496 (2009)
54. Norberg, R.: Hovering flight of the dragonfly Aeschna juncea L., kinematics and aerodynamics. Swimming and Flying in Nature, pp. 763–781. Springer, Berlin (1975)
55. Hu, Z., Deng, X.Y.: Aerodynamic interaction between forewing and hindwing of a hovering dragonfly. Acta Mech. Sin. **30**(6), 787–799 (2014)
56. Hudson, J.D., Dykhno, L., Hanratty, T.J.: Turbulence production in flow over a wavy wall. Exp. Fluids **20**, 257–265 (1996)
57. Calhoun, R.J., Street, R.L.: Turbulent flow over a wavy surface: neutral case. J. Geophys. Res. Ocean. **106**, 9277–9293 (2001)

Chapter 15
Toward the Problem of Low Re Flows Through Linearly Elastic Porous Media

Sid Becker

Abstract An isotropic elastic porous structure whose initial geometry is regular (periodically uniform) will experience non-uniform deformation when a viscous fluid flows through the matrix under the influence of an externally applied pressure difference. In such a case, the flow field will experience a non uniform pressure gradient whose magnitude increases in the direction of bulk flow. The closed solution to the problem of low Re flow through deformable porous media requires the simultaneous solution of the flow field in the void space and of the stress distribution in the solid matrix. The focus of the current study is to attempt to predict the pressure distribution of the flow field based only on the geometry of the media. The intention is to eventually simplify the coupled fluid-solid problem by replacing explicitly solution of the flow field with a pressure boundary condition in the stress distribution of the solid matrix.

Keywords Non-uniform · Porous media · Parallelepiped · Viscous

15.1 Introduction

At low Re and in a uniform porous medium, the flow rate is directly proportional to the pressure gradient (Darcy's Law). The permeability, K, of the medium characterizes this relationship and it is determined experimentally or numerically from the relation:

$$K = U\mu\left(\frac{\Delta P}{\Delta L}\right)^{-1} \tag{15.1}$$

Here U is the seepage velocity, μ is the dynamic viscosity, ΔL represents the length of the porous medium and ΔP is the difference in average pressure experienced by the fluid. The permeability is always a function of geometry regardless of

S. Becker (✉)
University of Canterbury, Christchurch, New Zealand
e-mail: sid.becker@canterbury.ac.nz

S. Gutschmidt et al. (eds.), *IUTAM Symposium on Recent Advances in Moving Boundary Problems in Mechanics*, IUTAM Bookseries 34,
https://doi.org/10.1007/978-3-030-13720-5_15

any heterogeneity in the flow field [1]. The importance of considering the local pore structure for media with geometry that varies in the direction perpendicular to the direction of bulk flow has been well studied, see for example the seminal work by Vafai in [2]. The descriptions of slurry flow through evolving dendritic structures in [3, 4] emphasize that macroscopic modelling is greatly improved when local heterogeneity in the structure is taken into account. One of the pore structures presented therein is represented by bundles of capillary tubes that experience periodic constrictions and expansions. Permeability predictions that consider such serial type changes in tube geometry have been presented that relate the permeability to the pore diameters, porosity, and a pore size density [5–8]. When the porous medium is not uniform in the direction of bulk flow, the permeability varies in this direction as well. In a recent publication, a method is presented that allows the prediction of local losses of low Re flow through a porous matrix composed of layers of orthogonally oriented parallelepipeds for which the local geometry varies discreetly in the direction of bulk flow [9, 10]. The important take-away from these works is that even in the presence of non-uniform periodic matrix geometry, it is possible to predict the local losses as long as there is full knowledge of the geometry.

With this in mind, consider the case of an initially uniform porous medium that is composed of a linearly elastic material. It is anticipated that the local pore structure of such a matrix may deform under the stresses associated with the pressure drop experienced by the fluid as it passes through the medium. In this case, the linear relationship between flow rate and pressure drop that is exhibited by non-deformable media is not preserved. As the total pressure drop is increased, the matrix experiences local pore structure deformations (constrictions) resulting in increased local resistance to the flow. This result has been shown experimentally [11, 12]. The deformation of an elastic porous media is non-uniform. At the inlet of the media (free surface), deformations are smallest and lateral displacement of the media is the largest. Conversely, at the outlet of the media (a fixed surface), the deformations are the largest while the displacement is zero. This was illustrated in the work by Munro et al. [13] that considered the low Re flow of glycerol through elastic porous media in an experimental test rig that relates global pressure drop to flow rate. Using that experiment, we found that the deformation of an elastic porous media is non-uniform. Unpublished results of related experiments are shown in Fig. 15.1. At the inlet of the media (this corresponds to the highest layer number), the deformations are smallest and lateral displacement of the media is the largest. Conversely, at the outlet of the media (a fixed surface represented in Fig. 15.1 by the lowest layer number), the deformations are the largest while the displacement is nearly zero.

This work is motivated by the complexity of the problem of incompressible low Re flow through a deformable porous media. The solution to this problem requires the simultaneous solution of the flow field in the void space and of the stress distribution in the solid matrix. Previously, attempts have been made to address the solution theoretically [14–17]. The relatively recent review by Hou et al. provides a clear description of the numerical requirements of the Fluid-Solid Interaction (FSI) [18]. A summary of the FSI problem outlined in that paper follows.

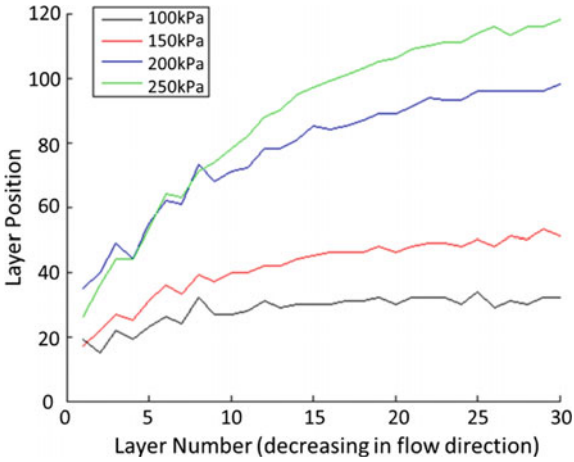

Fig. 15.1 Relative displacement of different layers of an elastic porous media subjected to flows with different total pressure drops

The equations of motion in the fluid domain is:

$$\rho^f \left(\partial_t v_i^f + v_j^f \partial_j v_i^f\right) - \partial_j \sigma_{ij}^f - b_i^f = 0 \tag{15.2}$$

If the flow is incompressible, the conservation of mass of the flow states that:

$$\partial_i v_i^f = 0 \tag{15.3}$$

For an incompressible Newtonian flow the fluid stress is represented by:

$$\sigma_{ij}^f = -p\delta_{ij} + \tau_{ij} \tag{15.4}$$

where p is the static pressure and the fluid shear is determined by:

$$\tau_{ij} = 2\mu\left(e_{ij} - \delta_{ij} e_{kk}/3\right) \tag{15.5}$$

Here $e_{ij} = \partial_j v_i^f + \partial_i v_j^f$.
The equation of motion for the solid matrix is:

$$\rho^s \left(\partial_t v_i^s + v_j^s \partial_j v_i^s\right) - \partial_j \sigma_{ij}^s - b_i^s = 0 \tag{15.6}$$

Here the superscript f denotes association with the flow field, the superscript s denotes association with the solid matrix, and b is a body force. The solid side velocity is the total time derivative of the solid displacement field $v_i^s = \dot{u}_i^s$. For the elastic solid, the structural stress obeys Hooke's law:

$$\sigma_{ij}^s = \lambda \delta_{ij} \varepsilon_{kk} + 2G\varepsilon_{ij} \tag{15.7}$$

where the strain is $\varepsilon_{ij} = \left(\partial_j u_i + \partial_i u_j\right)/2$, the Lame constant is $\lambda = E\nu/[(1+\nu)(1-2\nu)]$ and the shear modulus is $G = E/(2(1+\nu))$, E is the Young's Modulus, and ν is the Poisson's ratio.

The interface conditions at the fluid-solid interfaces are:

$$v_i^f = v_i^s \tag{15.8}$$

$$\sigma_{ij}^f \cdot n = \sigma_{ij}^s \cdot n \tag{15.9}$$

There are obvious inherent complications of this problem; in particular, that the location at which these interface conditions are applied will change as the solid experiences elastic deformation. Consider that many applications of this problem seek only to know the final state of the flow field. In such cases the question might be asked: "Given an applied pressure, and the initial geometry of the solid matrix, what is the final geometry of the solid and the resulting flow rate of the fluid?" The motivation behind the current paper is to take a step toward the approximation of the final flow configuration without explicitly solving Eqs. (15.2)–(15.9).

Consider the problem of the response of the solid matrix to a known stress field at the solid-fluid interface. In such a case the term $\sigma_{ij}^f \cdot n$ is known everywhere on the fluid solid interface so that Eq. (15.9) may be treated as a boundary condition in order to determine the solution of Eqs. (15.6)–(15.7). This paper considers a recent publication [9] that develops a correlation that can return the fluid stress distribution at the fluid-solid interface given the geometry of the solid, the total pressure drop experienced by the fluid, and the fluid viscosity. In the following text, a summary of the correlation developed in Ref. [9] is presented. The suggestion here is that in the future, researchers could use such correlations as a simplification to determine an approximate solution to the FSI problem of viscous low Re flow through an elastic porous medium.

15.2 The Geometry

This section describes the regular periodic Cartesian geometry that was developed and tested in [13]. The uniform version of this geometry is introduced in order to highlight its important characteristics. Then a manner of describing the variation in this geometry is presented. Consider the regular periodic geometry representative of the Cartesian matrix structure depicted in Fig. 15.2. The longitudinal axis directions of adjacent layers are perpendicular to one another. In order to introduce tortuosity, parallel layers are offset by a single pore thickness. The colored regions correspond to the space occupied by the solid matrix and the clear regions correspond to the pore space.

The anticipated symmetry of the flow may be used in order to simplify the geometry to a single representative pore structure. This is depicted in Fig. 15.3. In order to

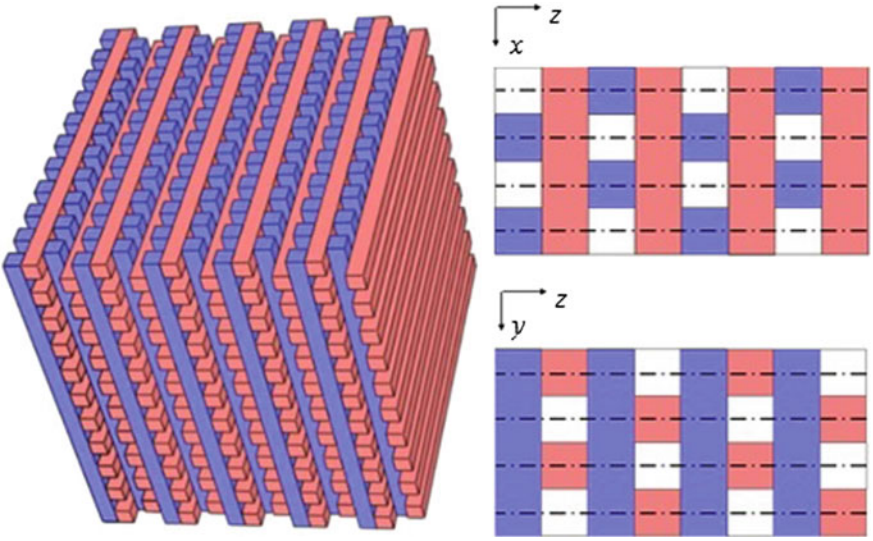

Fig. 15.2 Porous Structure (left); Side views in the x-z and y-z planes with dash-dot lines indicating planes of symmetry (right). Note that the planes of symmetry bisect the pores in laternating directions

introduce porosity variation in the direction of bulk flow, the geometry of each solid layer is varied. Consider Fig. 15.3 depicting representative views of a single pore channel through the matrix. In Fig. 15.3c a depiction of a pore channel through a non-uniform matrix geometry is presented. Here each solid layer experiences a decrease in its characteristic geometry in the direction of bulk flow, ℓ_z, and this decrease is proportional to a variation parameter, ε. Simultaneously each solid layer also experiences an increase in its characterizing length perpendicular to the direction of bulk flow (ℓ_x in this view) and this increase is also proportional to the variation parameter ε.

The parameter, ε, whose influence on the local pore geometry is depicted in Fig. 15.3c, is analogous to the strain experienced in an elastic deformation. In this way the variation parameter of each layer may be defined by the relation:

$$\varepsilon \equiv \left(\frac{\Delta \ell_z}{L_0}\right)_{\text{SOLID}} = \left(\frac{L_0 - \ell_z}{L_0}\right)_{\text{SOLID}} \tag{15.10}$$

where L_0 is the characteristic length when $\varepsilon = 0$.

The lateral expansion may also be related to this longitudinal compression by a parameter, ν, that is analogous to the Poisson ratio. It is defined as:

$$\nu \equiv \left(\frac{\Delta \ell_x}{\Delta \ell_z}\right)_{\text{SOLID}} = \left(\frac{\Delta \ell_y}{\Delta \ell_z}\right)_{\text{SOLID}} \tag{15.11}$$

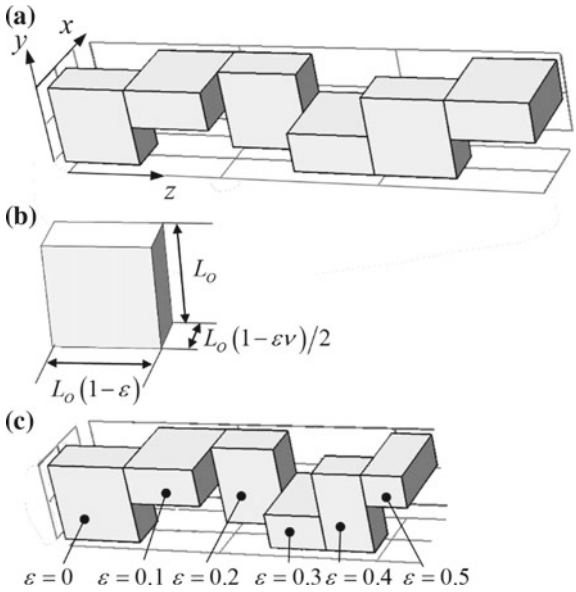

Fig. 15.3 **a** The representative pore structure through the uniform Cartesian matrix (constant β), **b** the geometric characterization of the pore structure in a single layer, **c** the representative pore structure for a non-uniform medium in which each layer's variation parameter, ε, increases in the direction of flow

In this way the pore structure and the porosity of each layer are also related directly to the parameters through the parameters ε and ν. In the direction of bulk flow, the characteristic pore length of the *i*th layer is:

$$L_{z,i} = L_0(1 - \varepsilon_i) \tag{15.12}$$

Consider next the lengths of the pore sides that are perpendicular to the direction of flow (oriented respectively along the x and y coordinates). The length of one of these sides is always equal to the constant L_0 while the length of the other side may vary between layers and the orientations of these side lengths alternate coordinate directions (x or y) between adjacent layers. The length of the side that is free to experience a contraction or an expansion is linearly related to the variation parameter by some positive constant, ν. In this way, the *i*th layer's pore length perpendicular to the direction of bulk flow may be described by the relation:

$$\ell_i = \frac{L_0}{2}(1 - \varepsilon_i \nu) \tag{15.13}$$

In the work done in this study the parameter ν does not vary. However the variation parameter ε will change between layers. When the value of ε in the medium varies discreetly between layers of the medium, and when its value in each layer is known, the permeability of any layer "*i*" may be described to be dependent only on the values of the variation parameter (i) of that layer ε_i, (ii) of its upstream neighbor ε_{i-1}, and (iii)

of its downstream neighbor ε_{i+1}. The study [9] determines the functional relationships between the dimensionless parameters:

$$\frac{K_i}{L_0^2} = f(\varepsilon_{i-1}, \varepsilon_i, \varepsilon_{i+1}) \tag{15.14}$$

If the permeability can be determined from knowledge of the matrix geometry, then it is results of numerical simulations are used to investigate the nature of this dependence and then these results are used to determine a best fit curve to predict the dependence of permeability on the local variation parameters.

15.3 Simulations

While numerical simulations are not the focus of this study, we later develop correlations using the results of numerical simulations, and thus we provide some details of the numerical computations here. These simulations were conducted using the Software COMSOL® Multiphysics version 4.3. An Intel® Core™ i7-3770 CPU @ 3.40 GHz with 32.0 GB RAM was used to run the simulations. The stationary "laminar Flow" model was used to simulate the steady solution. Symmetry boundary conditions were implemented on surfaces corresponding to planes of symmetry and no slip boundary conditions were imposed on surfaces corresponding to the fluid-solid interfaces. A tetrahedral mesh was used. Grid refinement studies were conducted and the mesh was refined until there a was a less than 0.1% difference in flow solutions. This was listed as an "extra fine" mesh in the mesh settings.

At the inlet and outlet of the pore structure, uniform pressures were specified. To ensure that the permeabilities of our correlation have no Re dependency, the inlet and outlet pressures were chosen so that the local Reynolds number remained below about 0.1. We simulated the laminar Newtonian flow of a viscous incompressible liquid with a density of 10^3 kg m^{-3} and a viscosity of 0.1 Pa s^{-1}.

In the correlations discussed later, local pressure losses are related to pore geometry. The numerical results of the flow field were post processed for use in the correlations as follows. At specified cross sections of the pore structure, average pressures were determined from the simulated results using the COMSOL® "Surface Average" tool. The results at each cross section were saved in a table and exported. We used the "Surface Integration" tool to determine the total flow rate at some cross sections perpendicular to the direction of bulk flow. The "Surface Average" tool is used to determine the average pressure along the planes in the fluid domain that correspond to the interfaces between the layers. For each geometric configuration, the flow rate and average pressures are exported and then in a MatLab script the permeability of each simulation is calculated. The MatLab function "lsqcurvefit" is used to determine the least squares best fit curve for the correlations which are described next.

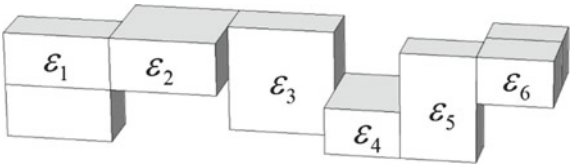

Fig. 15.4 The geometry of the pore structure used in the simulations to determine in the permeability data used in the correlations

15.4 Correlations

It is anticipated that at very low Re, the dimensionless permeability is dependent only on the local pore geometry; the lateral the dimensionless permeability of any particular layer depends only on the relative variation in the pore geometry of that layer and of those associated with the adjacent layers as implied by Eq. (15.14). Simulations are conducted of flows through different pore structure geometries of 6 layers. There first 3 layers always have the same value of the variation parameter, ε. The last 3 layers share an identical variation parameter that. In this way, there is a change in the variation parameter at the interface between layer 3 and layer 4 as depicted in Fig. 15.4. In all simulations, the parameter characterizing lateral variation in geometry that appears in Eq. (15.13) is constant and equal to $\nu = 0.4$

In order to simplify the subsequent analysis, the downstream change in the variation parameter of layer "i" is introduced:

$$\Delta\varepsilon_i^- \equiv \varepsilon_{i-1} - \varepsilon_i \tag{15.15}$$

and the upstream change in the variation parameter of layer "i" is:

$$\Delta\varepsilon_i^+ \equiv \varepsilon_{i+1} - \varepsilon_i \tag{15.16}$$

In this way, from the each simulation, two values of the local permeability may be estimated (one for layer $i = 3$ and one for layer $i = 4$) from the relation:

$$K_{SIM,i} = \frac{U\mu}{(\Delta P_i / L_i)} \tag{15.17}$$

The simulated permeability values may be explicitly linked to their corresponding variation parameter values ε, ε^+, ε^-. In the simulations that are used to develop the correlation, the variation in geometry is constrained such that $0 \leq \varepsilon \leq 0.6$ and $0 \leq \varepsilon^{\pm} \leq 0.6$. From the data of 11 simulations in this range, a good representation of the permeability's dependence on geometry is:

$$\frac{K}{L_0^2} = a_1 + a_2\beta + a_3\beta^2 + \Delta\beta^-(a_4 + a_5\beta) + \Delta\beta^+(a_6 + a_7\beta) \tag{15.18}$$

The constants $a_1 - a_7$ of Eq. (15.18) are then determined using the method of least squares from this data and are:

$$\begin{aligned} a_1 &= 9.802E{-}03 \quad a_2 = -2.478E{-}02 \quad a_3 = 1.614E{-}02 \\ a_4 &= -2.774E{-}03 \quad a_5 = 4.556E{-}03 \\ a_6 &= -2.790E{-}03 \quad a_7 = 4.586E{-}03 \end{aligned} \tag{15.19}$$

15.5 Test Case

In this section, the prediction of the pressures resulting from flows through the geometry depicted in Fig. 15.5 is presented. The geometry of the pore channel the total pressure drop ΔP_T over the porous medium are specified. The predicted permeability of each layer of the structure is first evaluated from constants of Eq. (15.19) with the correlation:

$$\frac{K_i}{L_0^2} = a_1 + a_2\beta_i + a_3\beta_i^2 + \Delta\beta_i^+(a_4 + a_5\beta_i) + \Delta\beta_i^-(a_6 + a_7\beta_i) \quad i = 1, 2, \ldots, 11 \tag{15.20}$$

The upstream change in the variation parameter of the first layer and the downstream change in the variation parameter of the last layer are set to zero $\Delta\varepsilon_1^- = \Delta\varepsilon_N^+ = 0$. The volumetric flow rate is related to the total pressure drop using a simple resistor representation:

$$Q = \frac{\Delta P_T A_T}{\mu} \frac{1}{\sum_{i=1}^{N} (L_i/K_i)} \tag{15.21}$$

Here A_T is the total area perpendicular to the direction of flow, and the height of each layer, L_i, may be determined from that layer's variation parameter by Eq. (15.12). The prediction of the drop in the average pressures across each layer may then be evaluated from the relation:

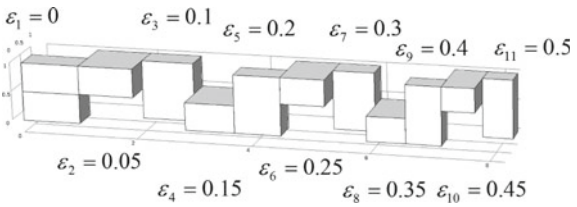

Fig. 15.5 A depiction of the geometry of 11 layer structure with a uniform change in variation parameter $\Delta\varepsilon^+ = -\Delta\varepsilon^- = 0.05$

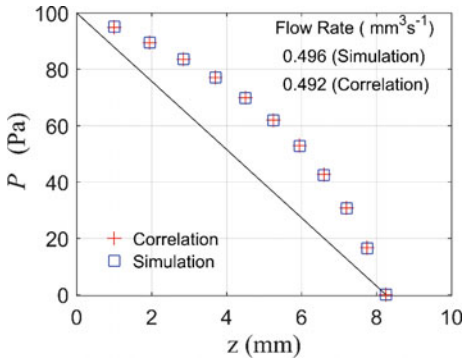

Fig. 15.6 The comparison between the pressure at the layer interfaces determined by the numerical simulation and by the correlation of Eq. (15.20) of the predict the reduced correlation of Eq. (15.18) of **a** the difference in average pressure across each layer, and **b** the pressure at each layer outlet

$$\Delta P_i = \frac{\mu}{(K_i/L_i)} \frac{Q}{L_0^2} \quad i = 1, 2, \ldots, 12 \tag{15.22}$$

The inlet and outlet pressures (gage) are specified to be 100 and 0 Pa respectively and gravitational effects are neglected. The fluid density is 10^3 kg m^{-3} and the fluid viscosity is 0.1 Pa s^{-1}. The geometric parameters used are $L_0 = 10^{-3}$ m and $\nu = 0.4$.

The test case geometry that is depicted in 5, represents an 11 layer structure that has a uniformly increasing value of the variation parameter so that the first layer has a variation parameter of $\beta_1 = 0$ and each subsequent layer's variation parameter increases by 0.05 ($\Delta\varepsilon_i^+ = 0.05 \quad i = 1, \ldots, 10$ and $\Delta\varepsilon_i^- = -0.05 \quad i = 2, \ldots, 11$).

A comparison between the results of the numerical simulations conducted in COMSOL and the predictions of the correlation resulting from Eqs. (15.20)–(15.22) are presented in Fig. 15.6. The pressure drop over each layer increases with increasing ε in a quadratic manner (as is anticipated) and the correlation's predictions agree well with the simulation. The calculated average pressure at each layer's outlet is depicted explicitly in Fig. 15.6 in showing excellent agreement. A solid line has been added here to accentuate the deviation of this pressure distribution from that represented by a flow exhibiting a uniform pressure gradient (the magnitude of the slope of this line is proportional to the effective permeability of the medium). The correlation's predicted volumetric flow rate of Eq. (15.21) agrees to within 1% of that determined from the results of the numerical simulation.

15.6 Conclusions

An empirical correlation is presented that relates the dimensionless permeability to the local pore geometry. Given only the information of the fluid viscosity, the local matrix geometry, and total pressure drop, the correlation is able to predict global flow rate and the average pressure at any cross section. It is the intent of this research that in the future such correlations will be applied to the FSI problem of laminar flows

through elastic porous media. It is anticipated that it will be possible to estimate the solution of the solid matrix without explicitly solving the CFD problem by focusing only on the solution to the solid matrix in a computational mechanics model. The correlation developed in this study should be applied to estimate the average pressure at each solid-liquid interfacial surface within each layer of the matrix. In this way the pressure boundary condition of these faces will be dependent on the deformation associated with each layer its adjacent layers.

References

1. Mathieu-Potvin, F., Gosselin, L.: Impact of non-uniform properties on governing equations for fluid flows in porous media. Transp. Porous Media **105**(2), 277–314 (2014)
2. Vafai, K.: Convective flow and heat transfer in variable-porosity media. J. Fluid Mech. **147**(1), 233–259 (1984)
3. Goyeau, B., et al.: Numerical calculation of the permeability in a dendritic mushy zone. Metall. Mater. Trans. B **30**(4), 613–622 (1999)
4. Goyeau, B., et al.: Averaged momentum equation for flow through a nonhomogenenous porous structure. Transp. Porous Media **28**(1), 19–50 (1997)
5. Azzam, M.I.S., Dullien, F.A.L.: Flow in tubes with periodic step changes in diameter: a numerical solution. Chem. Eng. Sci. **32**(12), 1445–1455 (1977)
6. Dullien, F.A.L., Azzam, M.I.S.: Effect of geometric parameters on the friction factor in periodically constricted tubes. AIChE J. **19**(5), 1035–1036 (1973)
7. Dullien, F.A.L., Azzam, M.I.S.: Comparison of pore size as determined by mercury porosimetry and by miscible displacement experiment. Ind. Eng. Chem. Fundam. **15**(2), 147–147 (1976)
8. Dullien, F.A.L., Elsayed, M.S., Batra, V.K.: Rate of capillary rise in porous-media with nonuniform pores. J. Colloid Interface Sci. **60**(3), 497–506 (1977)
9. Becker, S.M.: Prediction of local losses of low Re flows in non-uniform media composed of parrallelpiped structures. Transp. Porous Media **122**(1), 185–201 (2018)
10. Becker, S.M., Gasow, S.: Prediction of local losses of low Re flows in elastic porous media **2017**(58066), V01CT23A009 (2017)
11. Beavers, G.S., Wittenberg, K., Sparrow, E.M.: Fluid-flow through a class of highly-deformable porous-media. 2. Experiments with water. J. Fluids Eng. Trans. ASME. **103**(3), 440–444 (1981)
12. Siddique, J.I., Anderson, D.M., Bondarev, A.: Capillary rise of a liquid into a deformable porous material. Phys. Fluids **21**(1) (2009)
13. Munro, B., et al.: Fabrication and characterization of deformable porous matrices with controlled pore characteristics. Transp. Porous Media **107**(1), 79–94 (2015)
14. Chen, H., et al.: A numerical algorithm for single phase fluid flow in elastic porous media. In: Chen, Z., Ewing, R.E., Shi, Z.-C. (eds.) Numerical Treatment of Multiphase Flows in Porous Media: Proceedings of the International Workshop Held a Beijing, China, 2–6 August 1999, pp. 80–92. Springer, Berlin (2000)
15. Spiegelman, M.: Flow in deformable porous media. Part 1 simple analysis. J. Fluid Mech. **247**(1), 17–38 (1993)
16. Cao, Y., Chen, S., Meir, A.J.: Steady flow in a deformable porous medium. Math. Methods Appl. Sci. **37**(7), 1029–1041 (2014)
17. Bociu, L., et al.: Analysis of nonlinear poro-elastic and poro-visco-elastic models. Arch. Rat. Mech. Anal. **222**(3), 1445–1519 (2016)
18. Hou, G., Wang, J., Layton, A.: Numerical methods for fluid-structure interaction—a review. Commun. Comput. Phys. **12**(2), 337–377 (2012)

Chapter 16
Approximate Analytic Solution of the One Phase Stefan Problem for the Sphere

R. B. Shorten

Abstract This paper presents an approximate analytic solution for the (well-posed) one phase Stefan problem for the sphere using homotopy analysis. Unlike prior studies, the analytic approximation presented here uses homotopy analysis to deal with the non-linearity associated with the moving boundary; at no point in the analysis are any changes made to either the governing heat equation or the boundary and initial conditions. Explicit analytic expressions are developed in the form of separate Taylor series for the moving boundary location and the temperature profile within the sphere up to and including the fourth term in each series. The approximations are found to be in good agreement with the results from a number of prior studies.

Keywords Single phase Stefan problem · Sphere · Approximation · Homotopy analysis

16.1 Introduction

This paper outlines an analysis of the one phase Stefan problem for the sphere (which is known to be well-posed: see [1] at p. 2350)[1] through an application of homotopy analysis.[2] Unlike prior studies (see, for example, [1, 3–7]), the analytic approximation presented here uses homotopy analysis to deal with the non-linearity associated with

[1] The velocity of the moving boundary is unbounded at $t = 0$ but is finite for all t up to (but not including) the point when the moving boundary reaches the centre of the sphere (which point in time is denoted by t_e). Practically speaking, the moving boundary problem exists for all times between $t = 0$ and $t = t_e$. Beyond this point, the solution for the temperature profile is still well defined and, in this sense, the problem is "well behaved" for all values of $t > t_e$.

[2] For a detailed discussion of "homotopy analysis" including worked examples, see [2].

R. B. Shorten (✉)
Sirius Corporate Advisory Services Pty Ltd, 2nd Floor, 123 Camberwell Road, Hawthorn East, VIC 3123, Australia
e-mail: rob.shorten@scas.net.au

S. Gutschmidt et al. (eds.), *IUTAM Symposium on Recent Advances in Moving Boundary Problems in Mechanics*, IUTAM Bookseries 34,
https://doi.org/10.1007/978-3-030-13720-5_16

the moving boundary based on the methods outlined in [8]. As far as the author is aware, homotopy analysis has not been applied to the single phase Stefan problem for the sphere.

Explicit analytic expressions are developed in the form of separate Taylor series for the moving boundary location and the temperature profile within the sphere up to and including the fourth term in each series—the Taylor series are based on the corresponding short time solutions (see [3] for details of the short time solution[3]) for the moving boundary and the temperature profile. The paper discusses the relationship between the four term approximations presented here and the corresponding exact solution. It also outlines how the analytic approximations presented here may be made arbitrarily accurate (relative to the exact solution) by the addition of extra terms in the respective Taylor series.

Instances where the analysis outlined in this paper may be of practical use include: (i) applications involving suspended liquid droplets in air (e.g., inkjet printing) or other gases where the spherical droplet vaporises as time passes; (ii) applications in minerals processing and chemical and electro-chemical processes where there is an unreacted core surrounded by a reacted outer layer; and (iii) cases where the analysis can serve as a starting point for the solution of more complex problems involving moving boundaries in a sphere (e.g., the analysis of melting spherical nano-particles where surface tension effects are included in a single phase setting).

The nomenclature is as follows:

α	Stefan number where $\alpha > 0$
r	dimensionless spatial variable where $s(t) \leq r \leq 1$
t	dimensionless time variable where $0 < t \leq t_e$
t_e	extinction time when the moving boundary reaches the centre of the sphere[a]
$u(r, t)$	dimensionless temperature profile
$s(t)$	position of the moving boundary
q	embedding parameter
c_0	convergence control parameter
$w(r, t)$	transformed dimensionless temperature profile
z	transformed dimensionless spatial variable
λ	solution to the transcendental equation arising for the short time solution to the underlying boundary value problem

[a]Refer to footnote 1

16.2 Outline of the Mathematical Problem

The mathematical problem analysed here is as follows:

[3]The short time solutions are shown in [3] as Eqs. (4.3) and (4.4) and the leading term of Eq. (7.3).

$$u_t(r,\ t)\ =\ u_{rr}(r,\ t) + (2/r)u_r(r,\ t) \tag{16.1}$$

$$u(s(t),\ t) = 0 \tag{16.2}$$

$$u(1,\ t) = 1 \tag{16.3}$$

$$u_r(s(t),\ t) = -\alpha.s_t(t) \tag{16.4}$$

$$s(0) = 1 \tag{16.5}$$

where both $u(r,\ t)$ and $s(t)$ are unknown. At $r = 1$ the temperature is set equal to 1 and the melting temperature at the moving boundary is assumed to be equal to 0. Equation (16.4) is the Stefan condition which reflects the absorption of latent heat at the moving boundary arising from the change of phase. This boundary value problem in Eqs. (16.1)–(16.5) corresponds to the dimensionless problem set out as Eqs. (1.6) to (1.8) in [3].

An initial transformation is used to simplify Eqs. (16.1)–(16.5) by letting $u\ (r,\ t) = w(r,\ t)/r$ such that Eqs. (16.1)–(16.5) are now:

$$w_t(r,\ t) = w_{rr}(r,\ t) \tag{16.6}$$

$$w(s(t),\ t) = 0 \tag{16.7}$$

$$w(1,\ t) = 1 \tag{16.8}$$

$$w_r(s(t),\ t) = -\alpha.s(t)s_t(t) \tag{16.9}$$

$$s(0) = 1 \tag{16.10}$$

where both $w(r,\ t)$ and $s(t)$ are unknown.

A further transformation is required in order to reduce the problem in Eqs. (16.6)–(16.10) to one involving fixed spatial boundaries. The specific transformation involves the introduction of a new spatial variable, z, where $z = (1 - r)/(1 - s(t))$ such that $0 \leq z \leq 1$. The transformed boundary value problem (i.e., Eqs. (16.6)–(16.10)) is as follows:

$$(1-s(t))^2.w_t(z,\ t) = w_{zz}(z,\ t) - z.(1-s(t)).s_t(t).w_z(z,\ t) \tag{16.11}$$

$$w(1,\ t) = 0 \tag{16.12}$$

$$w(0,\ t) = 1 \tag{16.13}$$

$$w_z(1,\ t) = \alpha.(1-s(t)).s(t).s_t(t) \tag{16.14}$$

$$s(0) = 1 \tag{16.15}$$

16.3 Development of an Approximate Analytic Solution to Eqs. (16.11)–(16.15) Using Homotopy Analysis

16.3.1 Preliminaries

Consider the following "generalised" PDE and associated boundary and initial conditions for the unknown functions for the temperature profile, *w(z, t; q),* and the position of the moving boundary, *s(t; q)*:

$$\begin{aligned}(1-q).[w_{zz}(z,t;q) - z.(1-s(t;0)).s_t(t;0).w_z(z,t;0) - (1-s(t;0))^2.w_t(z,t;0)] \\ = c_0.q.[w_{zz}(z,t;q) - z.(1-s(t;q)).s_t(t;q).w_z(z,t;q) \\ -(1-s(t;q))^2.w_t(z,t;q)]\end{aligned} \tag{16.16}$$

$$w(1,\ t;\ q) = 0 \tag{16.17}$$

$$w(0,\ t;\ q) = 1 \tag{16.18}$$

$$\begin{aligned}w_z(1,\ t;\ q) = \alpha.(1-s(t;\ q)).s(t;\ q).s_t(t;\ q) \\ + (1-q).[w_z(1,\ t;0) - \alpha.(1-s(t;0)).s(t;0).s_t(t;0)]\end{aligned} \tag{16.19}$$

$$s(0;\ q) = 1 \tag{16.20}$$

The solutions to the generalised PDE subject to the associated boundary and initial conditions (i.e., Eqs. (16.16)–(16.20)) are assumed to be both capable of representation as a Taylor series in q about the point $q = 0$ and convergent for $0 \le q \le 1$:

$$w(z,t;\ q) = \sum_{n=0}^{\infty} [d^n w(z,\ t;0)/dq^n]q^n/n! \quad s(t;\ q) = \sum_{n=0}^{\infty} [d^n s(t;0)/dq^n]q^n/n!$$

When $q = 1$, the above PDE's and associated boundary and initial conditions (i.e., Eqs. (16.16)–(16.20)) correspond to Eqs. (16.11)–(16.15) and the Taylor series for *w(z, t;* 1*)* and *s(t;* 1*)* represent the solutions to Eqs. (16.11)–(16.15). Accordingly, the practical task is to develop expressions for the coefficients in each of the above Taylor series. This is done by successively differentiating Eqs. (16.16)–(16.20) with respect to q, setting q equal to 0 and then solving the resultant "subsidiary" problems.

The constant in Eq. (16.12), c_0, is referred to as the "convergence control parameter" which is independent of q. By changing c_0, the rate of convergence of the Taylor series can be varied allowing the range of values of c_0 for which the Taylor

series converges[4] to be identified. It emerges that in this particular case a further simplification can be effected[5] by letting $c_0 = -1$. When this substitution is made, Eqs. (16.16)–(16.20) reduce to the following:

$$w_{zz}(z,\ t;\ q) - (1-q).[z.(1-s(t;\ 0)).s_t(t;\ 0).w_z(z,\ t;\ 0) + (1-s(t;0))^2.w_t(z,\ t;\ 0)] = q.[z.(1-s(t;\ q)).s_t(t;\ q).w_z(z,\ t;\ q) + (1-s(t;\ q))^2.w_t(z,\ t;\ q)] \tag{16.21}$$

$$w(1,\ t;\ q) = 0 \tag{16.22}$$

$$w(0,\ t;\ q) = 1 \tag{16.23}$$

$$w_z(1,\ t;\ q) = \alpha.(1-s(t;\ q)).s(t;\ q).s_t(t;\ q) + (1-q).[w_z(1,\ t;\ 0) - \alpha.(1-s(t;\ 0)).s(t;\ 0).s_t(t;\ 0)] \tag{16.24}$$

$$s(0;\ q) = 1 \tag{16.25}$$

When $q = 1$, Eqs. (16.26)–(16.30) below correspond to the problem to be solved (i.e., Eqs. (16.11) to (16.15) above):

$$w_{zz}(z,\ t;\ 1) = z.(1-s(t;\ 1)).s_t(t;\ 1).w_z(z,\ t;\ 1) + (1-s(t;\ 1))^2.w_t(z,\ t;\ 1) \tag{16.26}$$

$$w(1,\ t;\ 1) = 0 \tag{16.27}$$

$$w(0,\ t;\ 1) = 1 \tag{16.28}$$

$$w_z(1,\ t;\ 1) = \alpha.(1-s(t;\ 1)).s(t;\ 1).s_t(t;\ 1) \tag{16.29}$$

$$s(0;\ 1) = 1 \tag{16.30}$$

This implies that the Taylor series expressions for $w(z,\ t;\ q)$ and $s(t;\ q)$ at $q = 1$ correspond to the solution to the Stefan problem to be solved subject to the following conditions: (i) each Taylor series converges for all values of q between and including 0 and 1; and (ii) at least one point in the t space (usually at $t = 0$) the respective Taylor series for the cases where $q = 0$ and $q = 1$ are solutions to the Stefan problem being analysed (i.e., Eqs. (16.6)–(16.10)). If these two conditions are met, we can say that when q moves from 0 to 1 there is a continuous change between the solutions to the two problems where $q = 0$ and $q = 1$ (i.e., the two solutions are "homotopic").

[4]Refer to [2] for a detailed discussion of the role of the convergence control parameter in the homotopy analysis method.

[5]Based on the comparison of the four term approximations for both the temperature and the moving boundary position against results set out in prior works (e.g., [1, 4]) it is clear that the Taylors series expressions for both are convergent where $c_0 = -1$.

Explicit expressions for the coefficients of the two Taylor series can be derived by: (i) successively differentiating Eqs. (16.21) to (16.25) with respect to q, setting $q = 0$; and (ii) solving the resulting boundary value problems starting with the determination of the first term in each Taylor series, namely, $w(z,\ t;\ 0)$ and $s(t;\ 0)$.

16.3.2 Expressions for w(z, t; *0) and* s(t; *0)*

The first step in the analysis of Eqs. (16.21)–(16.25) is to develop explicit expressions for the first term in each Taylor series for the moving boundary and the underlying temperature profile, namely: $w(z,\ t;\ 0)$ and $s(t;\ 0)$. When $q = 0$, Eqs. (16.21)–(16.25) are as follows[6]:

$$(1-s(t;0))^2.w_t(z,\ t;\ 0) = w_{zz}(z,\ t;\ 0) - z.(1-s(t;\ 0)).s_t(t;\ 0).w_z(z,\ t;\ 0) \tag{16.31}$$

$$w(1,\ t;\ 0) = 0 \tag{16.32}$$

$$w(0,\ t;\ 0) = 1 \tag{16.33}$$

$$w_z(1,\ t;\ 0) = w_z(1,\ t;\ 0) \tag{16.34}$$

$$s(0;\ 0) = 1 \tag{16.35}$$

While the homotopy analysis method allows for considerable flexibility in terms of the choice of $w(z,\ t;\ 0)$ and $s(t;\ 0)$, the choice made must (as noted above) be a solution of both Eqs. (16.31)–(16.35) and the problem being analysed (i.e., Eqs. (16.6)–(16.10)) for at least one point in the t space. The small time solution to Eqs. (16.6)–(16.10), which is denoted by $f(r,\ t)$ for the temperature profile and $s^*(t)$ for the moving boundary location, is as follows[7]:

$$f(r,\ t) = \left(1-K.Erf\left([1-r]/2t^{1/2}\right)\right) \tag{16.36}$$

$$s^*(t) = 1-2\lambda t^{1/2} \tag{16.37}$$

where $K = 1/Erf(\lambda)$ and λ is the solution to the transcendental equation: $e^{-\lambda^2} = \alpha\pi^{1/2}\lambda.Erf(\lambda)$. The small time solution set out in Eqs. (16.36)–(16.37) is straightforward and matches the actual solution including the corresponding Stefan condition exactly at $t = 0$ but not for $t > 0$.

---

[6]The conditions set out in Eq. (16.34) will, of course, be automatically satisfied by the choice of $w(z,\ t;\ 0)$.

[7]This is sometimes referred to as the "Neumann solution". It matches Eqs. (16.6)–(16.8), and (16.10) for all t but Eq. (16.9) only at $t = 0$. Refer also to footnote 3 above.

As a practical matter, the Taylor series for the moving boundary will display singular behaviour at the point in time where the small time solution for the moving boundary is equal to zero. This behavior occurs because the small time solution for the moving boundary appears in the denominator of all higher order terms for the Taylor series for the moving boundary. This does not present a practical difficulty provided the moving boundary reaches the centre of the sphere before the small time solution does. Fortunately, other studies (e.g., [3, 4]) confirm that the moving boundary does indeed reach the centre of the sphere ahead of the corresponding small time solution. If this were not the case, a more appropriate choice for the initial term must be found (as was the case in the analysis in [8]).

With this in view, Eqs. (16.36) and (16.37) can be used as the basis for $w(z,\ t;\ 0)$ and $s(t;\ 0)$ respectively. Using the substitution $z = (1 - r)/(1 - s(t;\ 0))$ to transform $f(r,\ t)$ into $w(z,\ t;\ 0)$ we obtain the following expressions for $w(z;\ t;\ 0)$ and $s(t;\ 0)$:

$$w(z,\ t;\ 0) = 1 - K.Erf[\lambda z] \tag{16.38}$$

$$s(t;\ 0) = (1 - 2\lambda t^{1/2}) \tag{16.39}$$

With this result, further terms in each Taylor series can be identified as outlined above. It emerges that these higher order terms are: (i) in the case of the temperature profile, the solutions to a series of well-posed second order linear ODE's in z (although the time variable, t, also appears in σ each ODE); and (ii) in the case of the moving boundary, the solutions to a series of well-posed first order linear ODE's in t.

16.3.3 Expressions for $\mathbf{w_q(z, t; 0)}$ *and* $\mathbf{s_q(t; 0)}$

The development of explicit expressions for the second term in each Taylor series for $w(z,\ t;\ 1)$ and $s(t;\ 1)$, namely $w_q(z,\ t;\ 0)$ and $s_q(t;\ 0)$, begins by differentiating Eqs. (16.21)–(16.25) once with respect to q and setting q equal to zero to yield the following:

$$w_{zzq}(z,\ t;\ 0) = 0 \tag{16.40}$$

$$w_q(0,\ t;\ 0) = 0 \tag{16.41}$$

$$w_q(1,\ t;\ 0) = 0 \tag{16.42}$$

$$\begin{aligned}&\alpha.s_q(t;\ 0)^2\left(s_t(t;\ 0) + s_{tq}(t;\ 0)\right) + w_z(1,\ t;\ 0) + w_{zq}(1,\ t;\ 0) = \\ &\alpha.s_q(t;\ 0).s_t(t;\ 0) + \alpha.s(t;\ 0).\left(\left(1 - 2.s_q(t;\ 0)\right).s_t(t;\ 0) + s_{tq}(t;\ 0)\right)\end{aligned} \tag{16.43}$$

$$s_q(0;\,0) = 0 \tag{16.44}$$

The solution to Eq. (16.40) (which is a second order linear ODE) subject to the conditions set out in Eqs. (16.41)–(16.42) is as follows:

$$w_q(z,\,t;\,0) = 0 \tag{16.45}$$

Taking this result and substituting it into Eq. (16.43) yields a first order linear ODE for $s_q(t;\,0)$ subject to the condition in Eq. (16.44). This is easily solved given that $s(t;\,0)$, $s_t(t;\,0)$, $w_z(1,\,t;\,0)$ and $w_{zq}(1,\,t;\,0)$ are already known:

$$s_q(t;\,0) = -(4\lambda^2 t)/(3(1-2\lambda t^{1/2})) \tag{16.46}$$

16.3.4 Expressions for $\mathbf{w_{qq}(z,\,t;\,0)}$ and $\mathbf{s_{qq}(t;\,0)}$

The development of explicit expressions for the third term in each Taylor series for $w(z,\,t;\,1)$ and $s(t;\,1)$, namely $w_{qq}(z,\,t;\,0)$ and $s_{qq}(t;\,0)$, begins by differentiating Eqs. (16.21)–(16.25) twice with respect to q and setting q equal to zero.

Applying the corresponding boundary conditions for the second order ordinary differential equation for $w_{qq}(z,\,t;\,0)$ yields the following expression:

$$\frac{d^2 w(z,t;0)}{dq^2} = -\frac{4\lambda\sqrt{t}\left(3-4\sqrt{t}\lambda\right)(Erf[z\lambda]-zErf[\lambda])}{3Erf[\lambda]\left(1-2\sqrt{t}\lambda\right)^2} \tag{16.47}$$

The first order ordinary differential equation for $s_{qq}(t;\,0)$, can then be solved subject to the initial condition that $s_{qq}(t=0;\,0)=0$:

$$\frac{d^2 s(t;0)}{dq^2} = -\frac{2\lambda t\left(3\lambda\left(3-4\lambda\sqrt{t}\right)+e^{\lambda^2}\sqrt{\pi}\left(-6+3\alpha\lambda^2+16t\alpha\lambda^4-4\sqrt{t}\lambda\left(-3+4\alpha\lambda^2\right)\right)Erf[\lambda]\right)}{9\left(1-2\lambda\sqrt{t}\right)^3} \tag{16.48}$$

16.3.5 Expressions for $\mathbf{w_{qqq}(z,\,t;\,0)}$ and $\mathbf{s_{qqq}(t;\,0)}$

The development of explicit expressions for the fourth term in each Taylor series for $w(z,\,t;\,1)$ and $s(t;\,1)$, namely $w_{qqq}(z,\,t;\,0)$ and $s_{qqq}(t;\,0)$, begins by differentiating Eqs. (16.21)–(16.25) three times with respect to q and setting q equal to zero.

Applying the corresponding boundary conditions for the second order ordinary differential equation for $w_{qqq}(z,\,t;\,0)$ yields the following expression:

$$\frac{d^3 w(z,t;0)}{dq^3}$$
$$= \frac{\sqrt{\pi}\alpha}{6\left(1-2\sqrt{t}\lambda\right)^4} e^{-z^2\lambda^2}\Big(e^{(3+z^2)\lambda^2}\pi z\alpha\lambda\Big(64t^2\alpha\lambda^6\Big(-7+2\Big(-1+z^2\Big)\lambda^2\Big)+3\sqrt{t}\lambda\Big(-24$$
$$+87\alpha\lambda^2+4\Big(5-8z^2\Big)\alpha\lambda^4\Big)+6\Big(3+2\alpha\lambda^2\Big(-3+\Big(-1+z^2\Big)\lambda^2\Big)\Big)-8t^{3/2}\lambda^3\Big(6+\alpha\lambda^2\Big(-115$$
$$+6\Big(-5+6z^2\Big)\lambda^2\Big)\Big)+16t\lambda^2\Big(6+\alpha\lambda^2\Big(-45+2\Big(-5+8z^2\Big)\lambda^2\Big)\Big)\Big)Erf[\lambda]^3$$
$$+9e^{(1+z^2)\lambda^2}\lambda\Big(-4+5\sqrt{t}\lambda\Big)Erf[z\lambda]+3Erf[\lambda]\Big(3e^{\lambda^2}z\lambda\Big(-4e^{\lambda^2}\sqrt{t}\alpha\lambda^3\Big(3-8\sqrt{t}\lambda$$
$$+4t\lambda^2\Big)+e^{z^2\lambda^2}\Big(4-32t\alpha\lambda^4+16t^{3/2}\alpha\lambda^5+\sqrt{t}\lambda\Big(-5+12\alpha\lambda^2\Big)\Big)\Big)-2e^{(2+z^2)\lambda^2}\sqrt{\pi}\Big(-3$$
$$+8t\alpha\lambda^4\Big(1-6z^2\lambda^2\Big)+4t^{3/2}\alpha\lambda^5\Big(-1+6z^2\lambda^2\Big)+6\sqrt{t}\Big(\lambda-\alpha\lambda^3+3z^2\alpha\lambda^5\Big)\Big)Erf[z\lambda]\Big)$$
$$+\sqrt{\pi}Erf[\lambda]^2\Big(6z\Big(2e^{3\lambda^2}\sqrt{t}\alpha^2\lambda^5\Big(3-8\sqrt{t}\lambda+4t\lambda^2\Big)+e^{(2+z^2)\lambda^2}\Big(-3-2\Big(-1+z^2\Big)\alpha\lambda^4$$
$$+8t\alpha\lambda^4\Big(1+\Big(-2-4z^2+2\alpha\Big)\lambda^2\Big)-4t^{3/2}\alpha\lambda^5\Big(1+\Big(-2-4z^2+2\alpha\Big)\lambda^2\Big)+2\sqrt{t}\lambda\Big(3$$
$$-3\alpha^2\lambda^4+\alpha\lambda^2\Big(-3+\lambda^2+8z^2\lambda^2\Big)\Big)\Big)\Big)+e^{(3+z^2)\lambda^2}\sqrt{\pi}\alpha\lambda\Big(-18+36\alpha\lambda^2+448t^2\alpha\lambda^6$$
$$-48t\lambda^2\Big(2+\alpha\lambda^2\Big(-15+2z^2\lambda^2\Big)\Big)+9\sqrt{t}\lambda\Big(8+\alpha\lambda^2\Big(-29+4z^2\lambda^2\Big)\Big)+8t^{3/2}\lambda^3\Big(6$$
$$+\alpha\lambda^2\Big(-115+6z^2\lambda^2\Big)\Big)\Big)Erf[z\lambda]\Big)\Big) \tag{16.49}$$

The first order ordinary differential equation for $s_{qqq}(t;\,0)$, can then be solved subject to the initial condition that $s_{qqq}(t=0;\,0)=0$ to give:

$$\frac{d^3 s(t;0)}{dq^3}$$
$$= \frac{1}{108\lambda\left(-1+2\sqrt{t}\lambda\right)^5}\sqrt{t}\Big(27\lambda^2\Big(15-32\sqrt{t}\lambda+16t\lambda^2\Big)-27e^{\lambda^2}\sqrt{\pi}\lambda\Big(18-15\alpha\lambda^2$$
$$+128t^{3/2}\alpha\lambda^5+6\sqrt{t}\lambda\Big(-9+20\alpha\lambda^2\Big)-4t\lambda^2\Big(-9+58\alpha\lambda^2\Big)\Big)Erf[\lambda]-9e^{2\lambda^2}\pi\Big(768t^2\alpha^2\lambda^8$$
$$-16t^{3/2}\alpha\lambda^5\Big(15+2(-3+55\alpha)\lambda^2\Big)-24\sqrt{t}\lambda\Big(-3+4\alpha\lambda^2-5\alpha\lambda^4+25\alpha^2\lambda^4\Big)+3\Big(-6$$
$$-8\alpha\lambda^4+27\alpha^2\lambda^4\Big)+8t\lambda^2\Big(-9+39\alpha\lambda^2-24\alpha\lambda^4+194\alpha^2\lambda^4\Big)\Big)Erf[\lambda]^2$$
$$+e^{3\lambda^2}\pi^{3/2}\alpha\lambda\Big(2560t^{5/2}\alpha^2\lambda^9-64t^2\alpha\lambda^6\Big(-99+2(18+55\alpha)\lambda^2\Big)-27\Big(6+3\alpha^2\lambda^4$$
$$+2\alpha\lambda^2\Big(-9+4\lambda^2\Big)\Big)+54\sqrt{t}\lambda\Big(16+16\alpha^2\lambda^4+\alpha\lambda^2\Big(-71+28\lambda^2\Big)\Big)+48t^{3/2}\lambda^3\Big(18$$
$$+154\alpha^2\lambda^4+3\alpha\lambda^2\Big(-95+34\lambda^2\Big)\Big)-36t\lambda^2\Big(42+102\alpha^2\lambda^4+\alpha\lambda^2\Big(-305$$
$$+112\lambda^2\Big)\Big)\Big)Erf[\lambda]^3\Big) \tag{16.50}$$

16.3.6 Approximate Solution

Using the above expressions the four term approximation for the temperature profile in terms of the variables z and t is:

$$w(z,\ t;\ 1) = w(z,\ t;\ 0)/0! + w_q(z,\ t;\ 0)/1! + w_{qq}(z,\ t;\ 0)/2! + w_{qqq}(z,\ t;\ 0)/3! + \ldots \tag{16.51}$$

and the four term approximation for the moving boundary is:

$$s(t;\ 1) = s(t;\ 0)/0! + s_q(t;\ 0)/1! + s_{qq}(t;\ 0)/2! + s_{qqq}(t;\ 0)/3! + \ldots \tag{16.52}$$

16.3.7 Higher Order Terms, Approximate and Exact Solutions

The steps outlined in the sections immediately above can be repeated to allow for the derivation of higher order terms within each Taylor series expression for $w(z,\ t;\ 1)$ and $s(t;\ 1)$.

The subsidiary PDE's and associated boundary and initial conditions for all the higher order terms (i.e., for $n \geq 2$) for the temperature profile are of the following general form[8]:

$$d^2[d^n w(z,\ t;\ 0)/dq^n]/dz^2 = g_n(z,\ t) \tag{16.53}$$

where $g_n(z,\ t)$ is: (i) the nth derivative with respect to q evaluated at $q = 0$ of a suitably rearranged Eq. (16.21) excluding the second order spatial derivative; and (ii) calculated from the results for the previous terms for the Taylor series for each of $w(z,\ t;\ 1)$ and $s(t;\ 1)$ that have already been determined.

The corresponding boundary conditions are $d^n w(z = 0,\ t;\ 0)/dq^n = 0$ and $d^n w(z = 1, t;\ 0)/dq^n = 0$ and the initial condition is $d^n w(z,\ t = 0;\ 0)/dq^n = 0$. Furthermore, the subsidiary ODE's for all the higher order terms for the moving boundary position are of the following general form (i.e., for $n \geq 2$):

$$d\left[d^n w(z = 1,\ t;\ q)/dq^n\right]/dz = d^n[\alpha.(1 - s(t;\ q)).s_t(t;\ q)]/dq^n \tag{16.54}$$

evaluated at $q = 0$ and are subject to the initial condition $d^n s(t = 0;\ q)/dq^n = 0$ at $q = 0$.

---

[8]The convergence control parameter, c_0, does not appear explicitly given the assumption that $c_0 = -1$. However, in the general case represented by Eqs. (16.16)–(16.20) it does appear other than in the first two terms of the Taylor series for $w(z,\ t;\ 1)$ and $s(t;\ 1)$.

If the Taylor series for each of $w(z, t; 1)$ and $s(t; 1)$ is truncated at a finite number of terms, the result will be a fully analytic approximation of the solution to the original boundary problem (as represented by Eqs. (16.11)–(16.15)). This approximation may be made arbitrarily more accurate by the addition of extra terms in each Taylor series to produce an exact analytic solution. To recover the solution to the temperature profile in the original spatial variable, r, the substitution, $z = (1 - r)/(1 - s(t; 1))$ must be made and the function $w(r, t; 1)$ divided by r.

16.4 Comparison with Other Studies

16.4.1 Basic Results

Figure 16.1 shows the location of the moving boundary over time (based on the four term approximation of the solution) superimposed on the results set out in [4] which were derived using a number of different analytic approximation and numerical methods for $\alpha = 10$.

Figure 16.2 shows the temperature profile for various times (based on the four term approximation of the solution) superimposed on the results set out in [1] such that the moving boundary, $s(t)$, is equal to 0.9, 0.7, 0.5, 0.3 and 0.1 respectively for $\alpha = 10$.

The temperature profiles in the original graph in [1] were derived using both a front fixing numerical scheme and the enthalpy method (see [9–11] for details). The

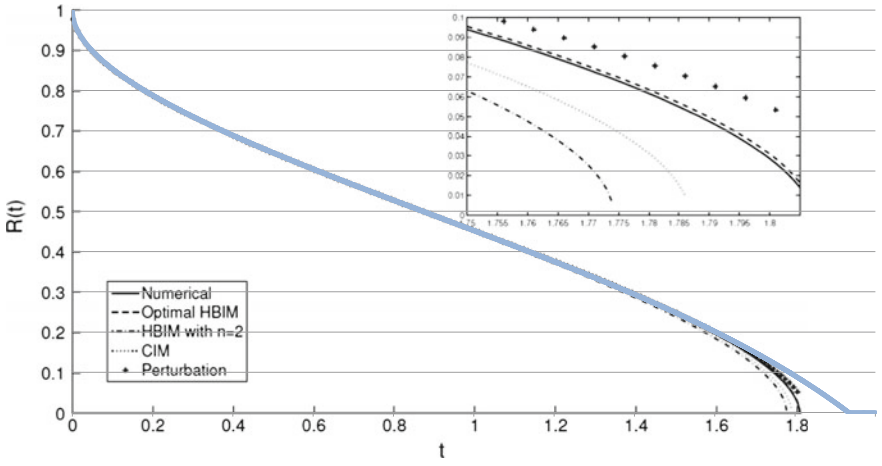

Fig. 16.1 This figure compares the four term homotopy approximation for the moving boundary (shown in blue) against results presented in [4]. The graph against which the comparison has been made here has been reproduced from Fig. 3.1 on page 52 of [4] with the kind permission of the author

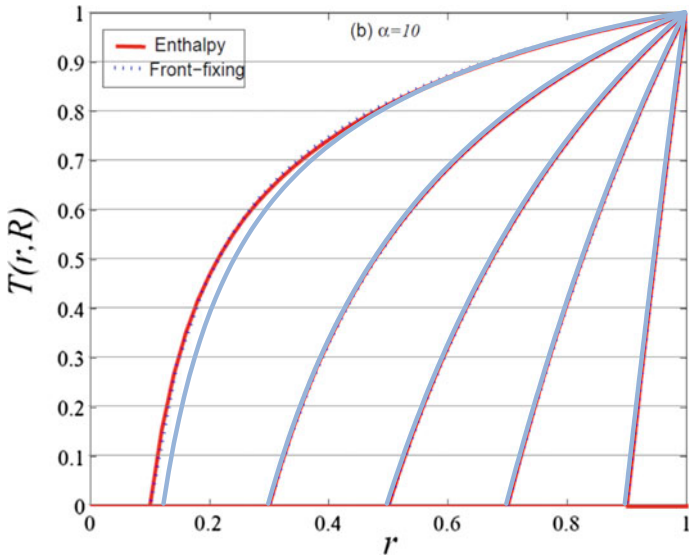

Fig. 16.2 This figure compares the four term homotopy approximation for the temperature profile (shown in blue) against results presented in [1] in Fig. 2, Part (b). The graph against which the comparison has been made here has been reprinted from [1], copyright 2009, with permission from Elsevier

fit between the analytic approximations and the results from the prior studies shown in Figs. 16.1 and 16.2 depend on how close the moving boundary is to the centre of the sphere (the closer the moving boundary is to the centre the worse the fit).

16.4.2 Convergence Behaviour

As noted above, the single phase Stefan problem for the sphere analysed here is well-posed as are the individual component parts of each of the Taylor series for $u(r;\, t;\, 1)$ and $s(t;\, 1)$. This and the equivalence, when $q = 1$, of Eqs. (16.16)–(16.20) and Eqs. (16.11)–(16.15) collectively imply the smoothness and convergence of the Taylor series solutions for both $u(r;\, t;\, 1)$ and $s(t;\, 1)$ and the respective approximations of each; furthermore, the graphical comparisons shown in Figs. 16.1 and 16.2 support this conclusion.

Figures 16.3 and 16.4 below show the 1st, 2nd, 3rd, and 4th order approximations against one another for the moving boundary position and temperature profile respectively—the convergence behaviour of the four term approximation for the moving boundary position is affected by value of the Stefan number and how close the boundary is to the centre of the sphere.

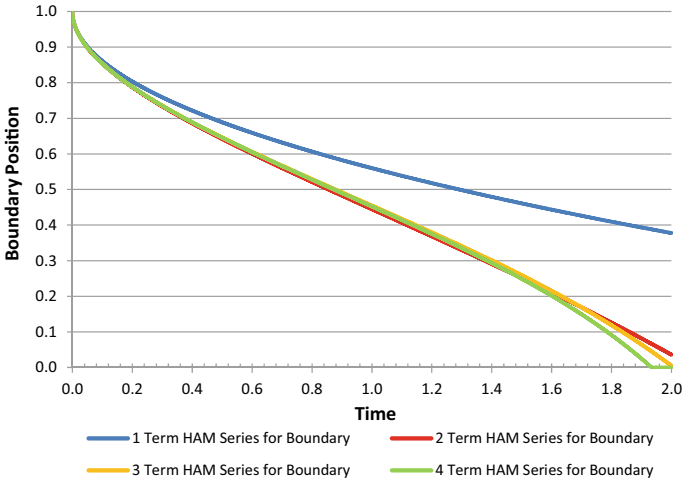

Fig. 16.3 Comparison of the 1st, 2nd, 3rd, and 4th order approximations for the moving boundary. Note for the above graph $\alpha = 10$

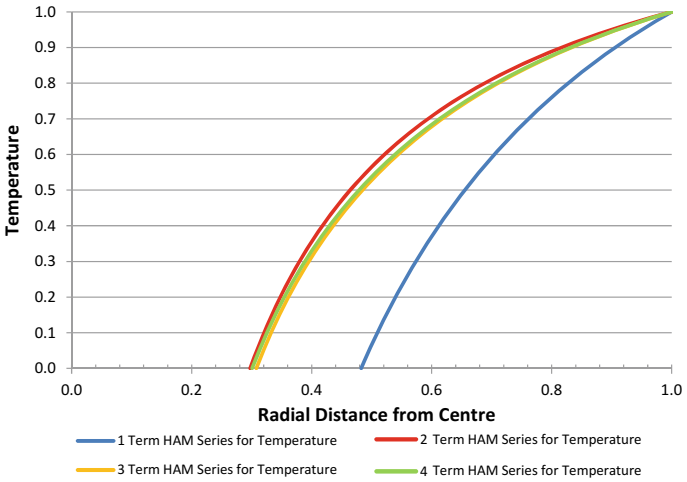

Fig. 16.4 Comparison of the 1st, 2nd, 3rd, and 4th order approximations for the temperature profile. Note that for the above graph, $\alpha = 10$ and $t = 1.3831$

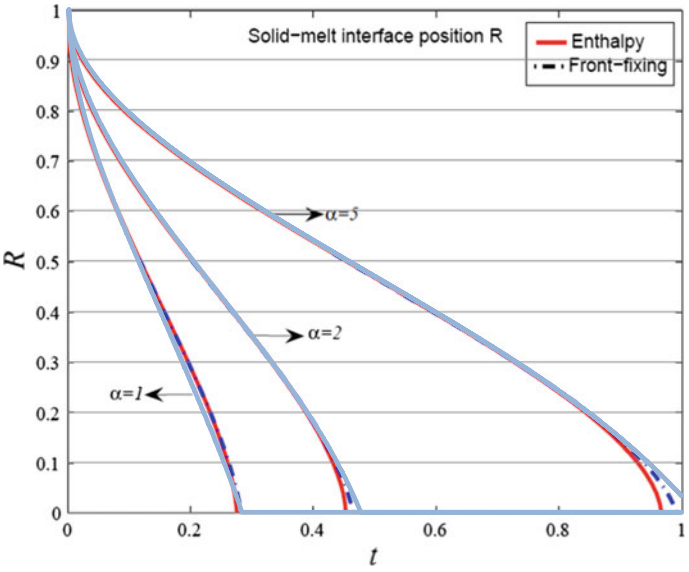

Fig. 16.5 This figure compares the four term homotopy approximation for the moving boundary (shown in blue) for $\alpha = 1$, 2 and 5 against results presented in [1] in Fig. 3. The graph against which the comparison has been made here has been reprinted from [1], copyright 2009, with permission from Elsevier

Figures 16.1 and 16.2 indicate that as t approaches t_e, the four term approximation for the both the moving boundary and the temperature profile worsen which implies that additional terms in each Taylor series are required. Figure 16.5 shows the four term approximation for the moving boundary for smaller Stefan numbers ($\alpha = 1$, 2 and 5):

The four term approximation for the moving boundary for smaller Stefan numbers ($\alpha = 2$ and $\alpha = 5$) is a relatively good fit against the results shown in [1]; in the case where $\alpha = 1$, the fit implies that additional terms are required.

16.4.3 Relationship to Other Solution Methods

The homotopy analysis method as outlined above is not the only strategy available for developing an approximate analytic solution to Eqs. (16.1)–(16.5). Apart the various analytic approximations covered in [1, 3–7], a recently published paper (refer to [12]) employs an interesting approach to the mathematical modelling of the growth of a spherical crystal in a metastable liquid and, accordingly, has relevance to the problem set out above in Eqs. (16.1)–(16.5).

The specific problem studied in [12] shares some similarities to the problem analysed in this paper—the governing PDE in [12], when transformed into dimensionless

co-ordinates, is of the same form as the PDE considered here. However, the boundary conditions applicable to the problem in [12] are different:

- the moving boundary starts at the centre of sphere and moves outwards;
- the Stefan condition imposed at the moving boundary point links the velocity of the boundary to: (i) the difference in temperature between the phase transition temperature and the temperature at the moving boundary; and, separately, (ii) the temperature gradient at the moving boundary point; and
- there is an additional condition such that the movement of the solid/liquid interface ceases when the spherical crystal radius reaches a pre-determined size (which is when in the radius of the spherical crystal, in terms of the dimensionless spatial variable, equals 1).

The key point of interest in [12] insofar as the analysis in this paper is concerned relates to the approach used to solve for the temperature profile and the moving boundary location. The analysis in [12] begins with the assumption that the solution to the heat transfer problem can be represented by a Taylor series in the spatial variable around the point of maximum growth of the crystal sphere after imposing the Stefan condition applicable at the point of maximum growth. The coefficients in this Taylor series representation of the temperature profile are then translated, based on the governing PDE, into the corresponding ascending time derivatives for the temperature profile at the point of maximum growth for the sphere.

The functional dependency of this solution for the temperature profile on the time variable is still "implicit" in that the coefficients involving the dimensionless time variable for the series are, at this point in the analysis, unknown—the next step is to solve for both the coefficients and the moving boundary as explicit functions of the dimensionless time variable. Substituting the Taylor series solution for the temperature profile into the two separate Stefan conditions at the moving boundary point yields two equations involving the moving boundary location and the temperature at the point where the dimensionless spatial variable equals 1.

Separate expressions for the moving boundary location and the temperature at the point where the dimensionless spatial variable equals 1 are constructed as infinite series involving ascending powers of the difference (represented by the symbol β_0 in [12]) between:

- the phase change temperature; and
- the temperature at the point where the dimensionless spatial variable equals 1 when the dimensionless time equals zero,

coupled with an assumption that this difference is very much smaller than 1 (to ensure the two power series in β_0 are convergent and, as a result, remain bounded for all values of the dimensionless time until the maximum size of the spherical crystal is reached).

The coefficients of each series are taken to be functions of the dimensionless time variable—the coefficients are determined by substituting the two power series into the two previous expressions involving the moving boundary location and the tem-

perature at the point where the dimensionless spatial variable equals 1 and equating like powers of β_0 in each series.

It is interesting to note that the "Taylor series" approach such as that used in [12] may (but not necessarily always) give the same result as a suitably constructed application of the homotopy analysis method—this is because, as explained in [13], the homotopy analysis method is more general than and conceptually distinct from the Taylor series approach. The author in [13] notes (see p. 154 in [13]) that while the homotopy analysis method requires the Taylor series in the embedding parameter to be analytic, it does not require the original basis functions (e.g., the short time solutions in the present case of the single phase Stefan problem for the sphere) to be analytic for all values of the underlying independent variables.[9] In contrast, the Taylor series expression used for the temperature profile used in [13] must be analytic over the range of the underlying independent variables under consideration for the Taylor series approach to be valid over that range.[10]

16.5 Concluding Remarks

This paper analyses the single phase Stefan problem for the sphere using homotopy analysis; in particular, an explicit approximate solution has been developed and the relationship between this approximation and the corresponding exact solution presented. The approximation may be made arbitrarily accurate by adding extra terms to the approximation to produce an exact, albeit complicated, analytic solution. Finally, there is scope for the methods outlined to be applied to other Stefan problems (subject to appropriate adjustments to accommodate differences in the governing equations).[11]

[9] An example is given in Sect. 5 of [13] of a nonlinear PDE boundary value problem with a non-analytic, global solution (obtained using homotopy analysis) where the corresponding Taylor series solution can only be defined locally.

[10] The problem in [12] appears to be well behaved (and, by implication, the power series solutions for the temperature profile and the moving boundary location presented in [12] will be correspondingly well behaved) due to: (i) the condition that the crystal sphere stops growing when the maximum size of the sphere is reached; (ii) the constraint imposed on β_0 that β_0 is $\ll 1$; and (iii) the spherical symmetry of the heat transfer problem. These features allow for only one (bounded) solution for each of the location of the moving boundary and the temperature profile at any given point in time up to and including the point in time where the spherical crystal reaches its maximum size.

[11] For example, the corresponding classical two phase Stefan problem for the sphere can be analysed using this approach (see [5] for details of the underlying problem). A suitable set of short time solutions for the classical two phase Stefan problem for the sphere are identified in [5] on pages 2068 and 2069 (see Eqs. 5.5 and 5.6 in [5] for the details).

References

1. Wu, B., McCue, S.W., Tillman, P., Hill, J.M.: Single phase limit for melting nanoparticles. Appl. Math. Model. **33**, 2349–2367 (2009)
2. Liao, S.J.: Notes on the homotopy analysis method: some definitions and theorems. Commun. Nonlinear Sci. Numer. Simul. **14**, 983–997 (2009)
3. Davis, G.B., Hill, J.M.: A moving boundary problem for the sphere. IMA J. Appl. Math. **29**, 99–111 (1982)
4. MacDevette, M.M.: Heat transfer analysis of nanofluids and phase change materials. PhD Dissertation, Facultat de Matematiques Aplicadas at Universitat Politecnica de Catalunya, Barcelona, Spain (2013)
5. McCue, S.W., Wu, B., Hill, J.M.: Classical two-phase Stefan problem for spheres. Proc. R. Soc. A **464**, 2055–2076 (2008)
6. Soward, A.M.: A unified approach to Stefan's problem for spheres and cylinders. Proc. R. Soc. A **373**, 131–147 (1980)
7. Stewartson, K., Waechter, R.T.: On Stefan's Problem for Spheres. Proc. R. Soc. A **348**, 415–426 (1976)
8. Shorten, R.B.: Approximate analytic solution of the one phase superheated Stefan problem. In: Proceedings of the 20th Australasian Fluid Mechanics Conference (AFMC): 5–8 December, 2016, Perth, Western Australia. Australasian Fluid Mechanics Society, Melbourne (2016)
9. Crank, J.: Free and Moving Boundary Problems. Oxford University Press, Oxford (1984)
10. Hu, H., Argyropoulos, S.A.: Mathematical modelling of solidification and melting: a review. Modell. Simul. Mater. Sci. Eng. **4**, 371–396 (1996)
11. Voller, V., Cross, M.: Accurate solutions of moving boundary problems using the enthalpy method. Int. J. Heat Mass Transf. **24**, 545–556 (1981)
12. Alexandrov, D.V.: Nucleation and evolution of spherical crystals with allowance for their unsteady-state growth rates. J. Phys. A Math. Theor (51), 075102 (2018)
13. Van Gorder, R.A.: On the utility of the homotopy analysis method for non-analytic and global solutions to nonlinear differential equations. Numer. Algorithms **76**, 151–162 (2017)

Chapter 17
Selection Criterion of Stable Mode of Dendritic Growth with n-Fold Symmetry at Arbitrary Péclet Numbers with a Forced Convection

Dmitri V. Alexandrov and Peter K. Galenko

Abstract A stable mode of anisotropic dendrite growing in a forced convective flow with n-fold crystalline symmetry is studied for low, moderate and rapid tip velocities (for arbitrary Péclet numbers). A generalized selection criterion determining a stable combination for the dendrite tip velocity and dendrite tip diameter is obtained.

Keywords Moving boundary problem · Crystal growth · Dendrites · Solvability theory · Selection criterion

17.1 Introduction

It is well-known that crystallization processes occurring in undercooled or supersaturated systems are described by the evolution of a very complex crystal structure with lateral branches which is called a dendrite [1–4]. From the mathematical point of view, the growing dendritic shape is the solution of moving boundary problem (see, among others, [5–10]). This shape highly depends on the heat and mass transfer mechanisms, hydrodynamic flows, anisotropies of surface energy and atomic kinetics as well as on the growth Péclet number P_g. One of the important problems in dendritic theory which describes a particular crystal structure of solidified materials (e.g. monocrystal or polycrystal) is connected with the selection of stable mode of dendritic growth. In other words, we need to determine a stable combination $\sigma^* = 2d_0 D_T/(\rho^2 V)$ between the dendrite tip velocity V and tip diameter ρ (here

D. V. Alexandrov (✉)
Laboratory of Multi-Scale Mathematical Modeling, Department of Theoretical and Mathematical Physics, Ural Federal University, Yekaterinburg 620000, Russian Federation
e-mail: Dmitri.Alexandrov@urfu.ru

P. K. Galenko
Friedrich-Schiller-Universität Jena, Physikalisch-Astronomische Fakultät, 07743 Jena, Germany
e-mail: Peter.Galenko@uni-jena.de

S. Gutschmidt et al. (eds.), *IUTAM Symposium on Recent Advances in Moving Boundary Problems in Mechanics*, IUTAM Bookseries 34,
https://doi.org/10.1007/978-3-030-13720-5_17

D_T and d_0 are the thermal diffusivity and capillary constant). This combination can be found on the basis of solvability and stability theories [11–13]. It is important to note that the selection problem has been solved by a number of authors in the case of four- and six-fold symmetries and moderate growth Péclet numbers [14–26]. The present paper extends this solution to more general case of n-fold symmetry of crystalline anisotropy, binary systems, forced convection and arbitrary Péclet numbers including the rapid crystallization scenario.

17.2 Marginal Growth Mode

Let us consider a two-dimensional growth of a needle-like dendritic crystal in a single-component undercooled liquid (the case of a two-component undercooled mixture is studied below). In addition, we consider the growth process in the presence of a forced (convective) flow that is directed toward the crystal growth direction z (Fig. 17.1). The present theory is based on the morphological stability analysis carried out by Bouissou and Pelcé [17] and by ourselves [22]. The dispersion relation determining the marginal growth mode of the wave number k_m and taking into account n-fold crystalline symmetry can be written out as [17, 22]

$$k_m^3 = \frac{V\exp(i\theta)}{2d(\theta)D_T}k_m + \frac{iaU\sin\theta\cos\theta}{8\rho D_T}k_m - \frac{iV\sin\theta}{2D_T}k_m^2 + \frac{V^2\cos\theta\exp(i\theta)}{4d(\theta)D_T^2} + \frac{iV\tilde{\beta}(\theta)\sin\theta}{d(\theta)T_Q}k_m^2, \tag{17.1}$$

where U is the fluid velocity at infinity, i is the imaginary unit, θ is the angle between the growth axis and the normal to the dendrite surface, $T_Q = Q/c_p$, Q is the latent heat parameter, and c_p is the specific heat.

Note that the dispersion relation (17.1) determines the marginal mode of the wave number of morphological perturbations superimposed on the surface of a dendrite growing with a constant velocity (a detailed analysis of morphological stability leading to expression (17.1) is carried out in Refs. [12, 13, 22]).

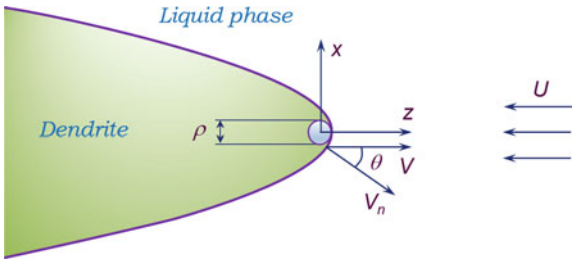

Fig. 17.1 A scheme of growing dendrite in a forced convective flow (V_n is the normal velocity to the interface)

In the case of n-fold symmetry, the anisotropic capillary length $d(\theta)$ and anisotropic growth coefficient $\beta(\theta)$ have the form [27]

$$\begin{aligned} d(\theta) &= d_0 \{1 - \alpha_d \cos[n(\theta - \theta_d)]\}, \\ \tilde{\beta}(\theta) &= \beta_0 T_Q \left\{1 - \alpha_\beta \cos\left[n\left(\theta - \theta_\beta\right)\right]\right\}, \end{aligned} \tag{17.2}$$

where β_0 is the kinetic constant. Expressions (17.2) assume that the anisotropy parameters α_d and α_β are small so that $\alpha_d \ll 1$ and $\alpha_\beta \ll 1$. Note that the parameter n determines the order of crystalline symmetry: $n = 2$ (whiskers), $n = 3$ (triangles), $n = 4$ (rectangles), $n = 5$ (disclinations), $n = 6$ (snowflakes), and $n = 10$ (quasicrystals) [28–31].

The parameter a in expression (17.1) describes the effect of a viscous flow and has the form (on the basis of the Oseen hydrodynamic equations) [32]

$$a(\mathrm{Re}) = \sqrt{\frac{\mathrm{Re}}{2\pi}} \frac{\exp(-\mathrm{Re}/2)}{\mathrm{erfc}\sqrt{\mathrm{Re}/2}}, \quad \mathrm{Re} = \frac{\rho U}{\nu}, \tag{17.3}$$

where ν stands for the kinematic viscosity and Re is the Reynolds number.

The first contribution in the right-hand side (r.h.s.) of expression (17.1) leads to the classical wave number at the neutral stability curve found by Mullins and Sekerka (see, among others, [12, 33])

$$k_{mMS} = -\sqrt{\frac{V \exp(i\theta)}{2d(\theta) D_T}}, \tag{17.4}$$

The first and second contributions (r.h.s., expression (17.1)) lead to the Bouissou and Pelcé wave number [13, 17]

$$k_{mBP} = k_{mMS} \sqrt{1 + \frac{iaUd(\theta)}{8\rho V} \sin(2\theta) \exp(-i\theta)}. \tag{17.5}$$

The first four contributions in the r.h.s. of expression (17.1) correspond to the case of rapid dendritic growth (high growth Péclet number limit) with allowance for the effect of atomic kinetics at the dendrite surface [22]

$$k_{mAG} = k_{mBP} + \frac{V \exp(-i\theta)}{4D_T}. \tag{17.6}$$

In addition, the contribution arising from the first and fifth summands in the r.h.s. of expression (17.1) was studied by Brener (kinetic effects without convection) [18].

Equation (17.1) can be solved on the basis of Cardano's formula ($d_0 \neq 0$) in the spirit of our previous theory [22]. Considering now the case of n-fold symmetry, we get

$$k_m = k_{mAG} + \frac{iV\tilde{\beta}(\theta)\sin\theta}{2d(\theta)T_Q}. \tag{17.7}$$

If the growth of dendrite is controlled by the atomic kinetics at its surface ($d_0 \to 0$), one can find

$$k_m = \frac{iT_Q \exp(i\theta)}{2D_T\tilde{\beta}(\theta)\sin\theta} + \frac{V\cos\theta}{2D_T}. \tag{17.8}$$

The present analysis leaning upon the wave numbers (17.7) and (17.8) generalizes all previously known results for the case of n-fold crystalline anisotropy.

17.3 Solvability Condition

The anisotropy of surface energy for different faces of a growing crystal is no more than 1.5–2% for metals and alloys and not more than 5% for strongly anisotropic materials. With such a small anisotropy, analytical solutions describing the growth of a crystal with a constant velocity are found near the classical Ivantsov solutions for a parabolic (paraboloidal) dendrite. From the mathematical point of view, this means fulfilling the condition of microscopic solvability, which is an approximate solution of the axisymmetric problem with the linearization of the heat and mass transfer conditions on the surface of the parabolic (paraboloidal) dendrite. To select a stable mode of dendritic growth with a constant velocity V near unstable solutions derived by Ivantsov for the parabolic platelet [34, 35], one can use the solvability condition written out with allowance for the effects of crystalline anisotropy. This condition derived by Pelcé and Bensimon [12, 33] takes the form

$$\int_{-\infty}^{\infty} G\left[X_0(l)\right] \exp\left[i\int_0^l k_m(l_1)dl_1\right] dl = 0, \tag{17.9}$$

where G represents the curvature operator, and $X_0(l)$ is a continuum of solutions from which the marginal mode of the wave number k_m is determined. Note that k_m is given by solutions (17.7) and (17.8) in the case of dendritic growth.

Let us now consider the thermally-controlled growth regime of needle-like dendrites when the wave number is described by expression (17.7), $\theta_d = 0$, and the anisotropy parameters are small enough. Also, we use the following variables [17]

$$l = -\frac{\rho}{2}\left[\frac{\tan\theta}{\cos\theta} + \ln\left(\frac{1}{\cos\theta} + \tan\theta\right)\right], \quad \eta = \tan\theta. \tag{17.10}$$

Substituting the wave number (17.7) into the solvability integral (17.9) and using variables (17.10), we arrive at

$$\int_{-\infty}^{\infty} d\eta G\left[X_0(\eta)\right] \exp\left\{-i\int_0^{\eta}\left[\frac{P_g(1-i\eta_1)}{2}+\frac{i\rho V\beta_0\eta_1}{2d_0}\right.\right.$$
$$\left.\left.-\sqrt{\frac{(1+i\eta_1)\left(1+\eta_1^2\right)^{\lambda_n}+i\alpha\eta_1 B_n(\eta_1)}{\sigma^* B_n(\eta_1)}}\right]d\eta_1\right\}=0, \tag{17.11}$$

where l_1 and η_1 are defined by formulas (17.10), and

$$B_n(\eta)=\left(1+\eta^2\right)^{n/2}-\alpha_d\sum_{k=0}^{n}\binom{n}{k}\eta^{n-k}\cos\frac{(n-k)\pi}{2},$$
$$dl_1=-\rho\sqrt{1+\eta_1^2}d\eta_1,\ \alpha=\frac{aUd_0}{4\rho V},\quad \lambda_n=\frac{n+1}{2},\quad \sigma^*=\frac{2d_0D_T}{\rho^2V}. \tag{17.12}$$

Note that the solvability integral (17.11) transforms to the previous theory detailed for $n=4$ [17, 21, 22].

Let us now consider the growth mode controlled by kinetics when the wave number is defined by expression (17.8). Combining expressions (17.8)–(17.10) and assuming that $\theta_\beta=0$, we have

$$\int_{-\infty}^{\infty} d\eta G\left[X_0(\eta)\right]\exp\left\{-i\int_0^{\eta}\left[P_g+\frac{i\rho\left(1+i\eta_1\right)\left(1+\eta_1^2\right)^{\lambda_n}}{2D_T\beta_0\eta_1 B_n'(\eta_1)}\right]d\eta_1\right\}=0, \tag{17.13}$$

$$B_n'(\eta)=\left(1+\eta^2\right)^{n/2}-\alpha_\beta\sum_{k=0}^{n}\binom{n}{k}\eta^{n-k}\cos\frac{(n-k)\pi}{2}.$$

An important point is that the solvability integrals (17.11) and (17.13) coincide with integrals (20) and (24) in Ref. [22] if $n=4$. In addition, if $n=6$ in the absence of kinetics $\beta_0=0$ and impurity concentration, the solvability integral (17.11) corresponds to expressions (8) and (12) from Refs. [24, 25], respectively.

17.4 Selection Criterion

In this section, we discuss the selection criteria (the stable combinations between the dendrite tip velocity V and its tip diameter ρ) for (i) purely thermal growth and (ii) thermo-solutal growth with moderate Péclet numbers as well as (iii) their modification in the case of rapid crystallization scenario.

17.4.1 Thermally-Controlled Dendritic Growth

Let us evaluate the solvability integral (17.11) by means of the previously developed approach [17, 22]. At first, we neglect the kinetic contribution ($\sim\beta_0$) in Eq. (17.11) and arrive at the following criterion

$$\sigma^* = \frac{2d_0 D_T}{\rho^2 V} = \frac{\sigma_0 \alpha_d^{7/n} A_n^{7/n}}{\left(1 + a_1 \alpha_d^{2/n} A_n^{2/n} P_g\right)^2 \left(1 + b\tau_n^{\upsilon_n}\right)}, \tag{17.14}$$

$$\tau_n = \alpha \alpha_d^{-3/n} A_n^{-3/n}, \quad \upsilon_n = \frac{n+7}{2(n+3)},$$

$$A_n = 2^{-3n/4} \sum_{k=0}^{n} \binom{n}{k} i^{n-k} \cos\frac{(n-k)\pi}{2},$$

where σ_0 and b stand for the selection constants. It is significant to note that the selection criterion (17.14) transforms to the previously found criterion for $n = 4$ (criterion (17.6) in Ref. [21] and criterion (25) in Ref. [22]). In this case (see, for details, Ref. [21])

$$a_1 = (8\sigma_0/7)^{1/2} (3/56)^{3/8},$$

and $A_4 = 1$, $\upsilon_4 = 11/14$. An important point is that the parameter n determining the order of crystalline symmetry takes only certain values so that A_n is real (Table 17.1).

Now we consider the next possible case if the kinetic contribution in (17.11) (the term containing β_0) is much greater than the other contribution proportional to P_g. Thus, neglecting the first summand in curly brackets in (17.11), we get

$$\sigma^* = \frac{\sigma_0 \alpha_d^{7/n} A_n^{7/n}}{\left[1 + a_1' \alpha_d^{2/n} P_g D_T \beta_0 A_n^{2/n}/d_0\right]^2 \left(1 + b\tau_n^{\upsilon_n}\right)}, \tag{17.15}$$

Table 17.1 Parameters determining the selection criterion

Symmetry order n	Crystals	Parameter A_n
2	Whiskers [28]	$2^{-1/2}$
3	Triangles [28]	$2^{-1/4}$
4	Rectangles [28]	1
5	Disclinations [29]	$2^{1/4}$
6	Snowflakes [28]	$2^{1/2}$
10	Quasicrystals [30, 31]	$2^{3/2}$

where a_1' is a constant of selection analysis. Note that $a_1' = 20\sqrt{\sigma_0/3}$ if $n = 4$ [18, 22]. The obtained selection criterion (17.15) contains the previously known results. Namely, if $n = 4$ and $U = 0$ in the low Péclet number limit, expression (17.15) corresponds to expression (25) from Ref. [18]. In addition, setting $n = 4$ in (17.15), we arrive at expression (26) from Ref. [22].

An important point is that two selection criteria (17.14) and (17.15) can be represented in a combined form as

$$\sigma^* = \frac{\sigma_0 \alpha_d^{7/n} A_n^{7/n}}{\left[1 + a_1 \alpha_d^{2/n} A_n^{2/n} P_g \left(1 + \delta_0 D_T \beta_0 / d_0\right)\right]^2 \left(1 + b\tau_n^{\upsilon_n}\right)}, \tag{17.16}$$

where $a_1' = a_1 \delta_0$. Two selection parameters σ_0 and b entering in this criterion can be found from experimental data or phase-field computations as in the previously studied case, $n = 4$ [36–40].

The thermally-controlled selection criterion (17.16) can be rewritten in terms of the dendritic tip velocity V

$$V = \frac{2 D_T P_g^2 \sigma_0 \alpha_d^{7/n} A_n^{7/n} / d_0}{\left[1 + a_1 \alpha_d^{2/n} A_n^{2/n} P_g \left(1 + \delta_0 D_T \beta_0 / d_0\right)\right]^2 \left(1 + b\tau_n^{\upsilon_n}\right)}, \tag{17.17}$$

where the definition of σ^* in terms of V and P_g, $2 D_T P_g^2 \sigma^* = d_0 V$, is taken into account. Expression (17.17) transforms to the criterion $V \propto D_T \alpha_d^{3/4} d_0^{-1} f\left(\sqrt{\alpha_d} P_g\right)$ derived in Ref. [41] for $n = 4$ and $U = 0$. Note that function f is demonstrated in Fig. 8 in Ref. [41].

Expressions (17.16) and (17.17) enable us to select the dendrite tip velocity V and dendrite tip diameter ρ with allowance for the undercooling balance condition. They correspond to expressions (29) and (30) deduced in Ref. [22] for the case $n = 4$ and expressions (10) and (14) deduced in Refs. [24, 25] for the case $n = 6$. If we are dealing with arbitrary crystalline symmetry (parameter n is listed in Table 17.1), criteria (17.16) and (17.17) essentially differ from the previously known theory [22]. The main difference consists in the powers of α_d and τ_n dependent on n.

Now we pay our attention to the case completely controlled by the anisotropy of atomic kinetics. The solvability integral (17.13) can be evaluated in the spirit of previous theory [22] for $\alpha_\beta \ll 1$ and different parameters n given in Table 17.1

$$V = \frac{\sigma_0 \alpha_\beta^{5/n} A_n^{5/n} P_g}{\beta_0 \left(1 + h_n \alpha_\beta^{2/n} A_n^{2/n} P_g\right)}, \tag{17.18}$$

where h_n is a constant. It is significant to note that expression (17.18) represents the selection criterion in the large Péclet number limit when the process of dendritic growth is controlled by the effects of atomic kinetics. Taking this into account we

consider the large Péclet number limit in criteria (17.17) and (17.18) to find the unknown constant h_n. The result is

$$h_n = \frac{d_0 \alpha_\beta^{3/n} a_1^2 \left(1 + \delta_0 D_T \beta_0 / d_0\right)^2}{2 D_T \beta_0 \alpha_d^{3/n}}.$$

If $n = 4$ this formula coincides with the previously known expression found in Ref. [22]. Expression (17.18) in terms of dendritic tip diameter ρ reads as

$$\rho = \frac{2 D_T \beta_0 \left(1 + h_n \alpha_\beta^{2/n} A_n^{2/n} P_g\right)}{\sigma_0 \alpha_\beta^{5/n} A_n^{5/n}}. \tag{17.19}$$

Note that criteria (17.18) and (17.19) transform to criteria (35) and (36) from Ref. [22] if $n = 4$. Moreover, criterion (17.18) coincides with expression (16) from Ref. [18] in the limiting case $P_g \ll 1$. Concluding this subsection we especially emphasize that expressions (17.18) and (17.19) underline a key contribution arising in kinetically-controlled growth mode of rapid crystallization [42, 43].

17.4.2 Chemical Dendrite

Let us now consider the case of so-called "chemical dendrite" growing in a binary system at a constant temperature in the presence of a forced convective flow. The difference between the aforementioned purely "thermal" problem and purely "chemical" problem under consideration consists in the fact that the "chemical" problem is one-sided because we neglect the diffusion field in the solid phase. This leads to a scale factor 2 in the selection criterion (17.16). In addition, the factor $\Lambda = mC_i(1 - k_0)/T_Q$ appears as a result of symmetry of temperature and concentration models. Taking this into account and definition $\sigma_{CD}^* = 2 d_0 D_C / (\rho^2 V)$, we rewrite criterion (17.16) in the form

$$\sigma_{CD}^* = \frac{2 \Lambda \sigma_0 \alpha_d^{7/n} A_n^{7/n}}{\left[1 + a_2 \alpha_d^{2/n} A_n^{2/n} P_C \left(1 + \delta_0 D_C \beta_0 / d_{0CD}\right)\right]^2 \left(1 + b \tau_{nCD}^{\upsilon_n}\right)}, \tag{17.20}$$

where m is the equilibrium liquidus slope, C_i is the concentration at the dendrite surface, k_0 is the partition coefficient, D_C is the diffusion coefficient, $P_C = \rho V / (2 D_C)$ is the chemical Péclet number, and

$$\tau_{nCD} = \alpha_{CD} \alpha_d^{-3/n} A_n^{-3/n}, \ \alpha_{CD} = \frac{a U d_{0CD}}{2 \rho V}, \ d_{0CD} = \frac{T_Q d_0}{2 m C_i (1 - k_0)}.$$

The surface concentration C_i and constant $a_2 = \sqrt{2}a_1$ are determined in Refs. [13, 21]. Note that the "chemical" selection criterion (17.20) coincides with the previous theory at $n = 4$ [22].

17.4.3 Thermo-Solutal Dendritic Growth

The selection criteria (17.16) and (17.20) corresponding to the thermally- and chemically-controlled regimes of dendritic growth can be generalized for binary non-isothermal liquids. Such a generalized selection criterion describes the effects of anisotropies of the surface energy and growth kinetics, different growth symmetries (Table 17.1), forced convective flow, arbitrary Péclet numbers (within the framework of local-equilibrium crystallization scenario) and takes the form

$$\sigma^* = \frac{\sigma_0 \alpha_d^{\frac{7}{n}} A_n^{\frac{7}{n}}}{1 + b\bar{\tau}_n^{\upsilon_n}} \left[\frac{1}{\left(1 + a_1 \alpha_d^{\frac{2}{n}} A_n^{\frac{2}{n}} P_g \zeta_T\right)^2} + \frac{2\Lambda D_T}{\left(1 + a_2 \alpha_d^{\frac{2}{n}} A_n^{\frac{2}{n}} P_C \zeta_C\right)^2 D_C} \right], \quad (17.21)$$

$$\bar{\tau}_n = \frac{aUd_0}{4\rho V P \alpha_d^{\frac{3}{n}} A_n^{\frac{3}{n}}} \left(1 + \frac{2D_T}{D_C}\right), \ \zeta_T = 1 + \frac{\delta_0 D_T \beta_0}{d_0}, \ \zeta_C = 1 + \frac{\delta_0 D_C \beta_0}{d_{0CD}},$$

where $P = 1 + 2D_T\Lambda/D_C$, n, A_n, and υ_n are determined in Table 17.1 and expressions (17.14). We especially note that the obtained selection criterion (17.21) includes all previously known criteria, namely

(i) the criterion derived by Ben Amar and Pelcé [16] for crystal growth without kinetics ($\beta_0 = 0$) and forced convective flow ($U = 0$) in the case of small Péclet numbers ($P_g \ll 1$ and $P_C \ll 1$) and $n = 4$;
(ii) the criterion deduced by Bouissou and Pelcé [17] for thermally controlled dendritic growth ($C_i = 0$) without kinetics ($\beta_0 = 0$) in the case of small Péclet numbers ($P_g \ll 1$ and $P_C \ll 1$) and $n = 4$;
(iii) the criterion obtained by Müller-Krumbhaar with co-authors [19] for crystal growth with the four-fold symmetry ($n = 4$) in a stagnant liquid ($U = 0$) without kinetics ($\beta_0 = 0$);
(iv) the criterion derived by Alexandrov and Galenko [21] for dendritic growth with the four-fold symmetry ($n = 4$) without growth kinetics ($\beta_0 = 0$);
(v) the criterion deduced by Brener [18] for crystal growth in a single-component liquid ($C_i = 0$) with $n = 4$ in the absence of convective flow ($U = 0$) and in the limit of small Péclet number ($P_g \ll 1$) (criterion (17.21) coincides with criterion (25) in Ref. [18] in the limit $\mu \equiv \beta_0 \rho V \sqrt{\alpha_d}/d_0 \gg 1$);
(vi) the criterion obtained by Alexandrov and Galenko [22] for the four-fold crystalline symmetry ($n = 4$);

(vii) the criterion derived by Alexandrov and Galenko [24, 25] for dendritic growth in single-component and binary liquids with the six-fold symmetry ($n = 6$) in the absence of kinetics ($\beta_0 = 0$);
(viii) the criterion deduced by Alexandrov and Galenko [44] for thermally-controlled crystal growth ($C_i = 0$) with n-fold symmetry;
(ix) the criterion (17.23) coincides with criterion (24) obtained by Alexandrov and Galenko [47] for rapidly growing dendrites if $n = 4$.

17.4.4 Rapid Thermo-Solutal Dendritic Growth at High Péclet Numbers

It is well-known that the growth of crystals at high solidification rates should be described by the hyperbolic equation for the solute concentration in the liquid phase while the heat transfer equation is of parabolic type (see, among others, [45, 46]). Recently, based on the analysis of the boundary integral equation for the curvilinear crystallization front, it was shown that the following substitutions

$$\frac{\rho}{\sqrt{1-W^2}} \text{ by } \rho_{\text{new}} \text{ and } (1-W^2)V \text{ by } V_{\text{new}} \tag{17.22}$$

must be taken into account if we consider the local nonequilibrium rapid regime of dendritic solidification [47]. Here $W = V/V_D$ and V_D is the bulk diffusion velocity. Expressions (17.22) show that the chemical Péclet number $P_C = \rho V/(2D_C)$ transforms as $P_C^* = \rho_{\text{new}} V_{\text{new}} / \left(2D_C\sqrt{1-W^2}\right)$. Taking this into account and omitting subscript "new", we rewrite the selection criterion (17.21) as

$$\begin{aligned}
\sigma^* = \frac{2d_0 D_T}{\rho^2 V} = \frac{\sigma_0 \alpha_d^{\frac{7}{n}} A_n^{\frac{7}{n}}}{1 + b\bar{\tau}_n^{\upsilon_n}} \Bigg[& \frac{1}{\left(1 + a_1 \alpha_d^{\frac{2}{n}} A_n^{\frac{2}{n}} P_g \zeta_T\right)^2} \\
& + \frac{2\Lambda_V D_T}{\left(1 + a_2 \alpha_d^{\frac{2}{n}} A_n^{\frac{2}{n}} P_C^* \zeta_C\right)^2 D_C} \Bigg], \quad V < V_D, \\
\sigma^* = \frac{2d_0 D_T}{\rho^2 V} = \frac{\sigma_0 \alpha_d^{\frac{7}{n}} A_n^{\frac{7}{n}}}{1 + b\bar{\tau}_n^{\upsilon_n}} & \frac{1}{\left(1 + a_1 \alpha_d^{\frac{2}{n}} A_n^{\frac{2}{n}} P_g \zeta_T\right)^2}, \quad V \geq V_D,
\end{aligned} \tag{17.23}$$

where $\Lambda_V = m_V C_i (1 - k_V)/T_Q$, m_V, k_V and C_i are determined in Ref. [47]. Selection criterion (17.23) extends the theory of Ref. [47] to the case of n-fold symmetry.

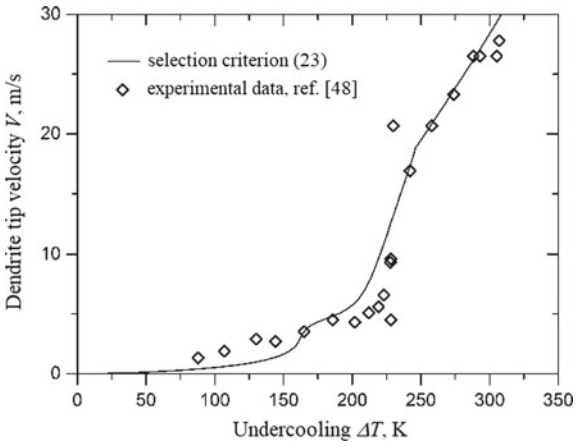

Fig. 17.2 The dendrite tip velocity V as a function of total undercooling ΔT is compared with experimental data [48] of rapidly solidified Ni-0.7 at%B liquid droplets

17.5 Conclusion

The selection criteria derived in Sect. 17.4 define an additional expression connecting the dendrite tip velocity V and dendrite tip diameter ρ. To find V and ρ independently as functions of the system driving force—undercooling ΔT, one can use the corresponding balance of undercoolings. This balance equation contains the different contributions stemming from the thermal, concentration, kinetic and interface curvature undercoolings (see, among others, [13, 24, 25, 44, 47]). Figure 17.2 compares the theory under consideration with experimental data. It is easily seen that the selection criterion (17.23) describes the experimental breakpoint appearing at large undercooling ΔT.

Acknowledgements This work is supported by the Russian Science Foundation (grant 16-11-10095).

References

1. Trivedi, R., Kurz, W.: Dendritic growth. Int. Mater. Rev. **39**, 49–74 (1994). https://doi.org/10.1179/imr.1994.39.2.49
2. Kurz, W.: Fundamentals of Solidification. Trans Tech Publications, Aedermannsdorf (1989)
3. Galenko, P.K., Zhuravlev, V.A.: Physics of Dendrites. World Scientific, Singapore (1994)
4. Galenko, P.K., Alexandrov, D.V.: From atomistic interfaces to dendritic patterns. Phil. Trans. R. Soc. A **376**, 20170210 (2018). https://doi.org/10.1098/rsta.2017.0210
5. Brener, E.A., Mel'nikov, V.I.: Pattern selection in two-dimensional dendritic growth. Adv. Phys. **40**, 53–97 (1991). https://doi.org/10.1080/00018739100101472
6. Almgren, R., Dai, W.-S., Hakim, V.: Scaling behavior in anisotropic Hele-Shaw flow. Phys. Rev. Lett. **71**, 3461–3464 (1993). https://doi.org/10.1103/PhysRevLett.71.3461
7. Brener, E.A.: Needle-crystal solution in three-dimensional dendritic growth. Phys. Rev. Lett. **71**, 3653–3656 (1993). https://doi.org/10.1103/PhysRevLett.71.3653

8. Brener, E.A.: Pattern formation in three-dimensional dendritic growth. Phys. A **263**, 338–344 (1999). https://doi.org/10.1016/S0378-4371(98)00488-9
9. Alexandrov, D.V., Galenko, P.K.: Boundary integral approach for propagating interfaces in a binary non-isothermal mixture. Phys. A **469**, 420–428 (2017). https://doi.org/10.1016/j.physa.2016.11.062
10. Alexandrov, D.V., Galenko, P.K., Titova, E.A.: The boundary integral theory for slow and rapid curved solid/liquid interfaces propagating into binary systems. Phil. Trans. R. Soc. A **376**, 20170218 (2018). https://doi.org/10.1098/rsta.2017.0218
11. Langer, J.S., Hong, D.C.: Solvability conditions for dendritic growth in the boundary-layer model with capillary anisotropy. Phys. Rev. A **34**, 1462–1471 (1986). https://doi.org/10.1103/PhysRevA.34.1462
12. Pelcé, P., Bensimon, D.: Theory of dendrite dynamics. Nucl. Phys. B **2**, 259–270 (1987). https://doi.org/10.1016/0920-5632(87)90022-3
13. Alexandrov, D.V., Galenko, P.K.: Dendrite growth under forced convection: analysis methods and experimental tests. Phys.-Usp. **57**, 771–786 (2014). https://doi.org/10.3367/UFNe.0184.201408b.0833
14. Kessler, D.A., Koplik, J., Levine, H.: Pattern selection in fingered growth phenomena. Adv. Phys. **37**, 255–339 (1988). https://doi.org/10.1080/00018738800101379
15. Ben Amar, M.: Theory of needle-crystal. Phys. D **31**, 409–423 (1988). https://doi.org/10.1016/0167-2789(88)90006-1
16. Ben Amar, M., Pelcé, P.: Impurity effect on dendritic growth. Phys. Rev. A **39**, 4263–4269 (1989). https://doi.org/10.1103/PhysRevA.39.4263
17. Bouissou, Ph, Pelcé, P.: Effect of a forced flow on dendritic growth. Phys. Rev. A **40**, 6673–6680 (1989). https://doi.org/10.1103/PhysRevA.40.6673
18. Brener, E.A.: Effects of surface energy and kinetics on the growth of needle-like dendrites. J. Cryst. Growth **99**, 165–170 (1990). https://doi.org/10.1016/0022-0248(90)90505-F
19. Müller-Krumbhaar, H., Abel, T., Brener, E., Hartmann, M., Eissfeldt, N., Temkin, D.: Growth-morphologies in solidification and hydrodynamics. JSME Int. J. Ser. B **45**, 129–132 (2002). https://doi.org/10.1299/jsmeb.45.129
20. Alexandrov, D.V., Galenko, P.K., Herlach, D.M.: Selection criterion for the growing dendritic tip in a non-isothermal binary system under forced convective flow. J. Cryst. Growth **312**, 2122–2127 (2010). https://doi.org/10.1016/j.jcrysgro.2010.03.036
21. Alexandrov, D.V., Galenko, P.K.: Selection criterion of stable dendritic growth at arbitrary Péclet numbers with convection. Phys. Rev. E **87**, 062403 (2013). https://doi.org/10.1103/PhysRevE.87.062403
22. Alexandrov, D.V., Galenko, P.K.: Thermo-solutal and kinetic regimes of an anisotropic dendrite groving under forced convective flow. Phys. Chem. Chem. Phys. **17**, 19149–19161 (2015). https://doi.org/10.1039/c5cp03018h
23. Alexandrov, D.V., Galenko, P.K.: Selection criterion for the growing dendritic tip at the inner core boundary. J. Phys. A: Math. Theor. **46**, 195101 (2013). https://doi.org/10.1088/1751-8113/46/19/195101
24. Alexandrov, D.V., Galenko, P.K.: Dendritic growth with the six-fold symmetry: theoretical predictions and experimental verification. J. Phys. Chem. Solids **108**, 98–103 (2017). https://doi.org/10.1016/j.jpcs.2017.04.016
25. Alexandrov, D.V., Galenko, P.K.: Thermo-solutal growth of an anisotropic dendrite with six-fold symmetry. J. Phys.: Condens. Matter **30**, 105702 (2018). https://doi.org/10.1088/1361-648X/aaab7b
26. Alexandrov, D.V., Galenko, P.K., Toropova, L.V.: Thermo-solutal and kinetic modes of stable dendritic growth with different symmetries of crystalline anisotropy in the presence of convection. Phil. Trans. R. Soc. A **376**, 20170215 (2018). https://doi.org/10.1098/rsta.2017.0215
27. Karma, A., Kotliar, B.G.: Pattern selection in a boundary-layer model of dendritic growth in the presence of impurities. Phys. Rev. A **31**, 3266–3275 (1985). https://doi.org/10.1103/PhysRevA.31.3266

28. Vainstein, B.K.: Modern Crystallography, vol. 1. Fundamentals of Crystals, Symmetry, and Methods of Structural Crystallography. Springer, Berlin (1982)
29. Ye, H.Q., Wang, D.N., Kuo, K.H.: Fivefold symmetry in real and reciprocal spaces. Ultramicroscopy **16**, 273–277 (1985). https://doi.org/10.1016/0304-3991(85)90083-X
30. Zou, X.D., Fung, K.K., Kuo, K.H.: Orientation relationship of decagonal quasicrystal and tenfold twins in rapidly cooled Al-Fe alloy. Phys. Rev. B **35**, 4526–4528 (1987). https://doi.org/10.1103/PhysRevB.35.4526
31. Hornfeck, W., Kobold, R., Kolbe, M., Herlach, D.: Quasicrystal nucleation in an intermetallic glass-former (2014). arXiv:1410.2952
32. Dash, S.K., Gill, W.N.: Forced convection heat and momentum transfer to dendritic structures (parabolic cylinders and paraboloids of revolution). Int. J. Heat Mass Trans. **27**, 1345–1356 (1984). https://doi.org/10.1016/0017-9310(84)90062-0
33. Pelcé, P.: Dynamics of Curved Fronts. Academic Press, Boston (1988)
34. Ivantsov, G.P.: Temperature field around spherical, cylinder and needle-like dendrite growing in supercooled melt. Dokl. Akad. Nauk SSSR **58**, 567–569 (1947)
35. Ivantsov, G.P.: On a growth of spherical and needle-like crystals of a binary alloy. Dokl. Akad. Nauk SSSR **83**, 573–575 (1952)
36. Bouissou, P., Perrin, B., Tabeling, P.: Influence of an external flow on dendritic crystal growth. Phys. Rev. A **40**, 509–512 (1989). https://doi.org/10.1103/PhysRevA.40.509
37. Tong, X., Beckermann, C., Karma, A., Lee, Q.: Phase-field simulations of dendritic crystal growth in a forced flow. Phys. Rev. E **63**, 061601 (2001). https://doi.org/10.1103/PhysRevE.63.061601
38. Jeong, J.-H., Goldenfeld, N., Dantzig, J.A.: Phase field model for three-dimensional dendritic growth with fluid flow. Phys. Rev. E **64**, 041602 (2001). https://doi.org/10.1103/PhysRevE.64.041602
39. Gao, J., Han, M., Kao, A., Pericleous, K., Alexandrov, D.V., Galenko, P.K.: Dendritic growth velocities in an undercooled melt of pure nickel under static magnetic fields: a test of theory with convection. Acta Mater. **103**, 184–191 (2016). https://doi.org/10.1016/j.actamat.2015.10.014
40. Gao, J., Kao, A., Bojarevics, V., Pericleous, K., Galenko, P.K., Alexandrov, D.V.: Modeling of convection, temperature distribution and dendritic growth in glass-fluxed nickel melts. J. Cryst. Growth **471**, 66–72 (2017). https://doi.org/10.1016/j.jcrysgro.2016.11.069
41. Brener, E.A., Mel'nikov, V.I.: Two-dimensional dendritic growth at arbitrary Peclet number. J. Phys. Fr. **51**, 157–166 (1990). https://doi.org/10.1051/jphys:01990005102015700
42. Bragard, J., Karma, A., Lee, Y.H., Plapp, M.: Linking phase-field and atomistic simulations to model dendritic solidification in highly undercooled melts. Interface Sci. **10**, 121–136 (2002). https://doi.org/10.1023/A:101581592
43. Nestler, B., Danilov, D., Galenko, P.: Crystal growth of pure substances: phase-field simulations in comparison with analytical and experimental results. J. Comput. Phys. **207**, 221–239 (2005). https://doi.org/10.1016/j.jcp.2005.01.018
44. Alexandrov, D.V., Galenko, P.K.: Selected mode of dendritic growth with n-fold symmetry in the presence of a forced flow. EPL **119**, 16001 (2017). https://doi.org/10.1209/0295-5075/119/16001
45. Galenko, P.K., Danilov, D.A.: Local nonequilibrium effect on rapid dendritic growth in a binary alloy melt. Phys. Lett. A **235**, 271–280 (1997). https://doi.org/10.1016/S0375-9601(97)00562-8
46. Galenko, P.K., Danilov, D.A.: Selection of the dynamically stable regime of rapid solidification front motion in an isothermal binary alloy. J. Cryst. Growth **216**, 512–526 (2000). https://doi.org/10.1016/S0022-0248(00)00338-9
47. Alexandrov, D.V., Galenko, P.K.: Selected mode for rapidly growing needle-like dendrite controlled by heat and mass transport. Acta Mater. **137**, 64–70 (2017). https://doi.org/10.1016/j.actamat.2017.07.022
48. Eckler, K., Cochrane, R.F., Herlach, D.M., Feuerbacher, B., Jurisch, M.: Evidence for a transition from diffusion-controlled to thermally controlled solidification in metallic alloys. Phys. Rev. B **45**, 5019–5022 (1992). https://doi.org/10.1103/PhysRevB.45.5019

Chapter 18
Evolution of a Melting Sphere in Cross Flow Using an Arbitrary Mesh Topology

James N. Hewett and Mathieu Sellier

Abstract The melting front of a sphere of ice was simulated using the finite volume method where the water-ice interface was explicitly tracked over time as a domain boundary. We used our previously developed node shuffle algorithm—for improving mesh quality as the interface transforms—and extended this algorithm into 3-D. A hemispherical shape formed in the case of forced convection and a balloon-like shape formed when natural convection occurred; these results were also observed from existing experiments. The melting bodies became less streamlined for both cases, resulting in higher drag coefficients, although their Nusselt numbers decreased. Deformation of the computational mesh was significant, with the melting sphere reducing in volume by up to 85.3% and its surface greatly changing shape, demonstrating that the algorithm is capable of enhancing mesh transformations in moving boundary problems on 3-D unstructured grids.

Keywords Node shuffle algorithm · Evolving boundary · Stefan problem · Dynamic mesh

18.1 Introduction

Moving boundary problems are abundant in nature and industry, for example: melting ice caps, lava flows and injection moulding. These problems consist of a moving interface driven by flow dynamics or a physical mechanism such as melting. Accurately modelling the moving interface requires capturing the sharp boundary for the duration of the problem. In this paper we apply a moving boundary along with our node shuffle algorithm [7], extended to 3-D, to solve a Stefan problem involving a melting sphere in cross flow. The contribution of this work is the development and

J. N. Hewett (✉) · M. Sellier
Department of Mechanical Engineering, University of Canterbury, Christchurch 8140, New Zealand
e-mail: james@hewett.nz

S. Gutschmidt et al. (eds.), *IUTAM Symposium on Recent Advances in Moving Boundary Problems in Mechanics*, IUTAM Bookseries 34,
https://doi.org/10.1007/978-3-030-13720-5_18

validation of this 3-D extension; our simulation results are compared with existing experiments [2, 3].

18.2 Methods

18.2.1 Problem Description and Governing Equations

We modelled the melting of a spherical block of ice immersed in an infinite stream of warm water with a temperature of T_∞ at a low Reynolds number

$$\mathrm{Re} = \frac{2au_\infty}{\nu} \tag{18.1}$$

where a is the effective radius of the body, u_∞ the freestream speed and ν the kinematic viscosity of the surrounding fluid. As the block of ice melts over time, both the morphology as well as the volume of the body change; consequently, a and therefore Re reduce over time. Initial states of geometrical parameters are subscripted with a zero (for example a_0). The effective radius a was measured normal to the flow because the flow regime is sensitive to this dimension [6], and was calculated with $a = \sqrt{A_x/\pi}$ where A_x is the projected area in the x-direction (streamwise). Fluid properties of the water were evaluated at the local temperature by using empirical formulas [12], and were evaluated at the freestream temperature for dimensionless numbers as recommended by Whitaker [14].

The flow regime explored in this study was steady and axisymmetric which occurs for approximately $\mathrm{Re} < 210$ [10]. The initial Reynolds number was typically $Re_0 = 200$, and with a monotonically decreasing geometry (irreversible melting), Re was always in this flow regime. Therefore we assumed a laminar, incompressible and steady state flow field for each discrete melting time step Δt_{melt}. We assumed that the temperature at the water-ice interface, as well as within the body of ice, was constant and at the melting temperature $T_m = 0^\circ$ C, such that the thermal flux from the warm water was exclusively contributing to the melting rate. Specifically, no energy was expended for heating the ice from below T_m, which was the case for the experiments by Hao and Tao [3].

The Navier–Stokes equations, with the above assumptions, are

$$\mathbf{u} \cdot \nabla \mathbf{u} = -\frac{1}{\rho}\nabla p + \nu \nabla^2 \mathbf{u} + \mathbf{g} \tag{18.2}$$

where $\mathbf{u}$ is the velocity of the fluid, ρ the fluid density, p the pressure and $\mathbf{g}$ the acceleration due to gravity. The continuity equation (conservation of mass) is

$$\nabla \cdot \mathbf{u} = 0 \tag{18.3}$$

and the temperature equation, from conservation of energy assuming negligible viscous heating, is given by

$$\mathbf{u} \cdot \nabla T = \alpha \nabla^2 T \tag{18.4}$$

where T is the temperature of the fluid, $\alpha = k/\rho c_p$ the thermal diffusivity with k the thermal conductivity and c_p the specific heat. The melting interface velocity is calculated using the Stefan condition with

$$\mathbf{v}_i = \frac{-k}{\rho_{\text{ice}} \Delta h_f} \left. \frac{dT}{dn} \right|_i \hat{\mathbf{n}} \tag{18.5}$$

where ρ_{ice} is the density of the ice, Δh_f the latent heat of fusion and $\hat{\mathbf{n}}$ the unit normal vector at the water-ice interface and is directed toward the ice. The continuous motion of the moving water-ice interface was discretised by displacing each interface boundary node with

$$\Delta \mathbf{x}_i = \Delta t_{\text{melt}} \mathbf{v}_i \tag{18.6}$$

for each melting time step Δt_{melt}. Although the flow field was treated as steady state for each Δt_{melt}, the surrounding flow evolved with the body over the duration of the melting process. Here, we made the assumption that the local heat flux at the melting interface was approximately constant for the duration of Δt_{melt}.

The Nusselt number describes the ratio between convective and conductive heat transfer and can be defined locally as

$$\text{Nu}_i = \frac{2a_v}{T_\infty - T_i} \left. \frac{dT}{dn} \right|_i \tag{18.7}$$

where a_v is the radius of the body based on an equivalent sphere of the same volume and $T_i = T_m$ the temperature at the interface. The Prandtl number is the ratio between momentum diffusivity and thermal diffusivity and is evaluated with

$$\text{Pr} = \frac{\nu}{\alpha} \tag{18.8}$$

The drag coefficient is defined as

$$C_D = \frac{F_D}{\frac{1}{2}\rho {u_\infty}^2 A_x} \tag{18.9}$$

where F_D is the drag force composed of both pressure and viscous forces.

18.2.2 Numerical Scheme and Discretisation

The governing equations outlined above were solved by the finite volume method using the software ANSYS Fluent R17.0 and analysis of results were processed with MATLAB R2017a. The pressure-based solver was used with the laminar viscous model and SIMPLEC pressure-velocity coupling, second-order pressure and third-order MUSCL spatial discretisation schemes were employed for the momentum and energy equations. The transient solver with the dynamic mesh model was enabled to apply Eqs. 18.5 and 18.6 with user-defined functions, instead of choosing a less accurate method such as changing cell types [5]. Two time scales were utilised in our study: (1) the surrounding flow field with t; and (2) the melting time step Δt_{melt}. The steady state assumption was enforced with a pseudo-infinite time step of $t = 1 \times 10^8$ s; we have verified this approach by comparing results with the steady state solver both here and in a previous study [8]. The dynamic mesh is deployed at the beginning of each time step in Fluent and therefore Eq. 18.6 with Δt_{melt} was calculated for every time step after the first.

The boundary condition at the inlet was a uniformly applied normal velocity with a magnitude of u_∞ with $T = T_\infty$, while the outlet condition had a zero gauge pressure applied. The boundary of the melting body had a no slip condition with $T = T_i$ and the far-field boundary had a symmetry boundary condition (zero temperature and velocity gradients enforced). Initial conditions were calculated from the field properties from the inlet boundary. Iterative convergence was assessed on area-weighted average Nusselt number at the interface and was achieved for all simulations.

18.2.3 Meshing Strategy

The computational domain was comprised of a cylinder surrounding the initially spherical body which was subtracted with a boolean operation, leaving only the exterior flow field to be modelled. The exterior cylinder had a radius of $20a_0$, an upstream length of $20a_0$ and downstream of $40a_0$ which were all sufficiently large in order to reduce blockage, entrance and exit effects respectively. Accurately resolving the thermal boundary layer at the melting interface was the primary objective for our simulations, and therefore inflation layers (up to 20) were applied on the surface of the sphere. The y^+ is a dimensionless number describing the cell resolution near a boundary and is defined as

$$y^+ = \frac{\Delta n}{\nu}\sqrt{\frac{\tau_w}{\rho}} \tag{18.10}$$

where Δn is the distance between centroids of the boundary face and its neighbouring cell, τ_w the wall shear stress and the fluid properties are evaluated at the temperature of the neighbouring cell. Mesh convergence of the results were analysed for the static

(non-deforming) sphere case in Sect. 18.3.1 with a particular attention to the thermal boundary resolution through measuring $y^+_{\max}$.

An unstructured mesh was selected to validate and apply our model to this type of grid, and this mesh was generated with ANSYS Meshing R17.0. Tetrahedral cells are composed of four triangular faces, and consequently, domain boundaries are a set of stitched triangular faces with an average interior angle of 60° and have a relatively high number of valence nodes (when compared to other geometries such as squares or polygons). This dense clustering of boundary nodes may lead to bunching and ultimately numerical issues as discussed in our previous work on erosion of a cylinder in cross flow [6]. In order to mitigate this problem we transformed the mostly tetrahedral-based mesh into a polyhedral mesh in Fluent; resulting in a mean minimum interior angle of approximately 114° for all boundary faces. The conversion to a polyhedral grid reduced the number of cells by a factor of approximately 3.7: from 385684 to 103449 cells for the chosen (mesh converged) grid. Evolutions of the mesh at the water-ice boundary are shown in Figs. 18.7 and 18.8.

18.2.4 Node Shuffle Algorithm in 3-D

The primary contribution for this work is the extension and validation of our node shuffle algorithm into 3-D; the algorithm was originally designed for a cylindrical deforming boundary which had a 2-D shape evolution [6]. The algorithm involves an iterative procedure which for each iteration loops through every boundary node and: (1) shifts the node between the neighbouring nodes; then (2) projects the node back onto a sphere fitted to neighbouring nodes. The second step is critical for preserving the overall profile of the boundary; for example without this step, convex bodies such as a sphere would always reduce in volume which would artificially enhance the melting rate as modelled in our simulations.

First, each node is shifted in a similar way to Laplacian smoothing [4] with

$$\mathbf{x}_j^{n+1} = \mathbf{x}_j^n + \gamma \frac{1}{N_j} \sum_{k=1}^{N_j} (\mathbf{x}_k^n - \mathbf{x}_j^n) \tag{18.11}$$

with the shuffled node using index j, where n is the iteration number, N the number of valence nodes, k the index of the valence nodes and γ the under-relaxation factor ($0 < \gamma \leqslant 1$ and typically $\gamma = 1$). Second, the shuffled node is projected back onto a sphere by holding the spherical angles constant. This fitted sphere is defined by four points in space: the shuffled node and three nearest valence node coordinates.

Table 18.1 Mesh convergence of boundary layer resolution and face sizing on sphere. Re = 200 and Pr = 0.72 with $\langle y^+ \rangle$ as the mean y^+ at the sphere boundary, N_{CV} the total number of control volumes, $N_{CN,S}$ the number of cell nodes on the sphere and $N_{CF,S}$ the number of cell faces on the sphere

Mesh	$\langle y^+ \rangle$	y^+_{max}	N_{CV}	$N_{CN,S}$	$N_{CF,S}$	C_D	Nu
1	0.298	0.501	95098	5508	2756	0.782	9.116
2	0.148	0.250	103449	5508	2756	0.780	9.159
3	0.058	0.099	114084	5508	2756	0.780	9.198
4	0.137	0.238	46018	1394	699	0.793	9.221
5	0.150	0.251	294110	21632	10818	0.777	9.148

18.3 Results

18.3.1 Validation of Flow Past a Static Sphere

The first task of this study before undertaking the melting sphere cases was to validate the computational model for flow around a static sphere. As mentioned earlier in the methods, the thermal boundary layer is the critical region of the flow to accurately model for capturing the local temperature gradient, and consequently the local melting rate. The governing equations employed in our model can be non-dimensionalised [1] and results in two dimensionless parameters: Re and Nu. In this section, we set Pr = 0.72, Re = 50, 100, 200 with $a = 18$ mm, and the fluid properties to their respective freestream temperature values of $\rho(\mathbf{x}, t) = \rho_\infty$, $\mu(\mathbf{x}, t) = \mu_\infty$, $c_p(\mathbf{x}, t) = c_{p,\infty}$ and $k(\mathbf{x}, t) = k_\infty$, in order to quantitatively compare our results with existing simulations and experiments.

A suitable grid, Mesh 2, was chosen based on a mesh convergence study with a summary of results shown in Table 18.1. The convergence of Nu for boundary layer resolution is shown between Mesh 1, 2 and 3 where the differences are less than 0.5% between each subsequent refinement, and the influence of face sizing chosen for the sphere boundary is shown between Mesh 4, 2 and 5 with differences less than 0.7%.

A range of Reynolds number flows were compared against existing simulations, as shown in Fig. 18.1, in order to validate our model for the range of flow dynamics experienced during the melting process. The angle θ is measured from the geometric centroid of the body, between the x-axis and the yz-plane with $\theta = 0$ corresponding to the stagnation point on the fore. Our results have an excellent agreement with existing simulation results [1]. The maximum local heat transfer (related to Nu, and is proportional to melting rate) is found at the fore stagnation point and Nu decreases for lower Re with a lower limit of Nu = 2 which corresponds to the case of heat transfer purely by conduction [14].

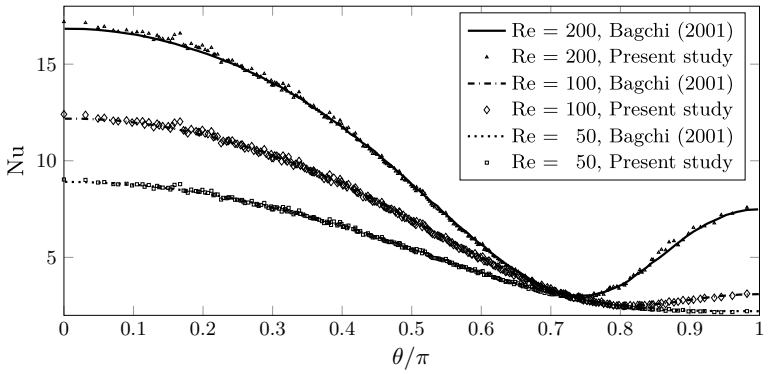

Fig. 18.1 Nusselt number distributions around the static (non-deforming) sphere for several Reynolds number in the axisymmetric flow regime with Pr = 0.72, compared with existing simulation results [1]

18.3.2 Melting Sphere Due to Forced Convection

The first melting sphere case we modelled was with forced convection; isolating the melting rate from gravitational effects by setting $\mathbf{g} = \mathbf{0}$. The fluid was water with Pr = 6.78, variable fluid properties were as described in Sect. 18.2.1, $\mathrm{Re}_0 = 200$ and $a_0 = 18\,\mathrm{mm}$. A melting time step of $\Delta t_{\mathrm{melt}} = 2\,\mathrm{s}$ yielded a converged profile evolution and was used for both melting cases. An axisymmetric shape evolution was obtained, as shown in Fig. 18.2, where a flat surface emerges on the aft of the body; forming a hemispherical shape. The formation of this flat aft was also observed in experiments [3] for relatively high Re cases where natural convection plays only a minor role in the melting process.

The melting water-ice interface receded quickest on the fore of the sphere, with a peak melting rate found at the stagnation point as presented in Fig. 18.3. The minimum melting rate occurs immediately downstream of the separation point of $\theta_{\mathrm{sep}} \approx 2\pi/3$.

18.3.3 Melting Sphere with Mixed Convection

The second case we investigated was for mixed convection which had the same parameters as for Sect. 18.3.2, except that the natural convection due to density variations causing buoyancy effects were included by applying the gravitational forcing term **g**. Axial symmetry of the melting sphere was lost for this case as the warm water climbed up around the body, in the positive y-direction, resulting in a balloon-like shape as shown in Fig. 18.4. The balloon is tilted upstream and the centroid recedes both downstream and in the direction of gravity.

18.3.4 Heat Transfer and Drag Trends

The mean Nu for the mixed convection case was significantly higher than for the case of purely forced convection as shown in Fig. 18.5. This result was expected because the mixed convection case is a combination of both the natural and forced heat transfer types, and the natural convection plays a major role for slowly moving flows. Heat transfer by natural convection was greatest for the initial spherical body and then decreased as the melting ice transformed into a balloon shape. Both the magnitude of Nu and its gradient with Re match reasonably well with extrapolating the results from experiments [3], indicating that our melting model is generally accurate.[1]

Trends of the drag coefficient are shown in Fig. 18.6 where C_D is defined in Eq. 18.9 with a time-dependent cross-sectional area. Particularly, the C_D always increased for both cases, although F_D decreased except at $t_{\text{melt}} < 42$ s for the mixed convection case where the drag force slightly increased. Interestingly, under forced convection $C_{D,0} = 0.849$ which is slightly higher than the $C_D = 0.780$ calculated when all fluid properties were evaluated at $T = T_\infty$ (Table 18.1). Natural convection adversely affected the drag on the melting sphere due to the additional motion of water climbing around the body caused by buoyancy effects, increasing $C_{D,0}$ by 167%. Both melting cases experienced an increase in C_D as their bodies became less streamlined as shown in Figs. 18.2 and 18.4. Particularly, the mixed convection case

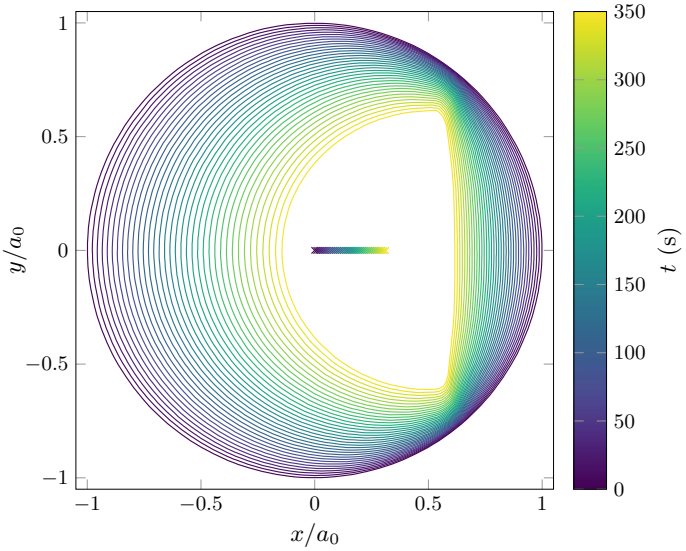

Fig. 18.2 Profile evolution of the forced convection case with $\text{Re}_0 = 200$. The centroid of the melting sphere is denoted with the crossed marks

[1] A quantitative comparison between our results and their experiments was not undertaken because Re_0 was lower in our simulations than the cases they investigated.

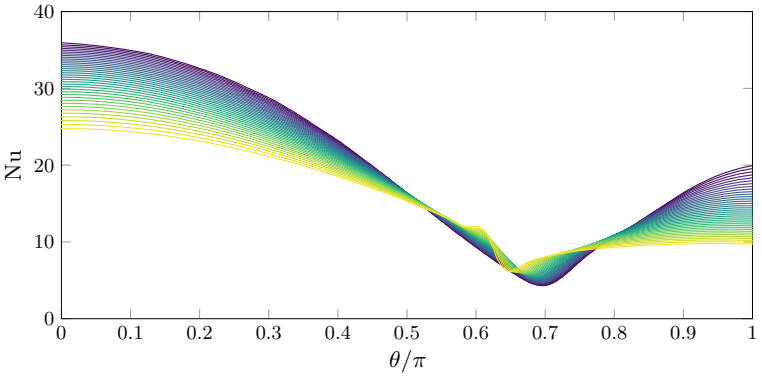

Fig. 18.3 Nusselt number distribution around the melting sphere for the forced convection case. Shade of lines correspond to Fig. 18.2

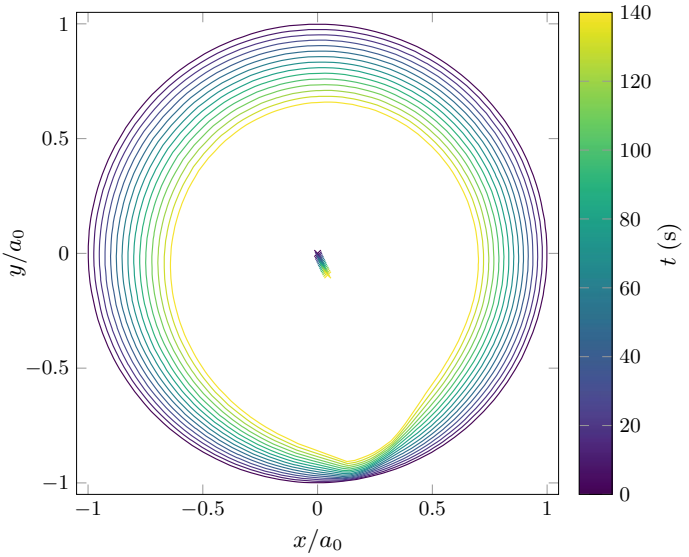

Fig. 18.4 Profile evolution of the mixed convection case with $\mathrm{Re}_0 = 200$. The centroid of the melting sphere is denoted with the crossed marks

developed a pair of protrusions at the base of the sphere; as shown in Fig. 18.8 with the dark regions corresponding to the slowest melting rate.

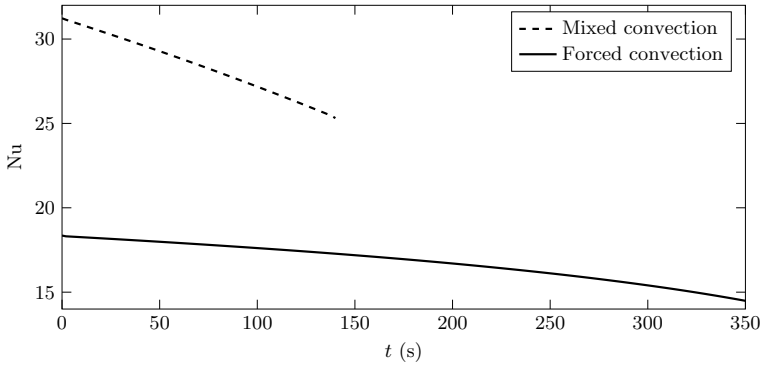

Fig. 18.5 Mean Nusselt number (surface area-averaged) over time for both melting sphere cases where $\mathrm{Re}_0 = 200$

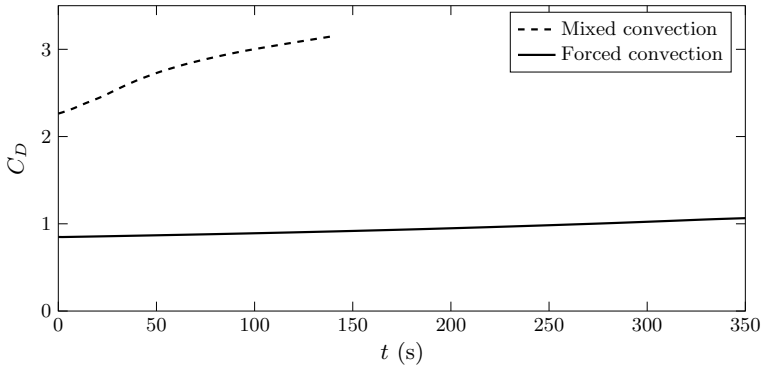

Fig. 18.6 Drag coefficient over time for both melting sphere cases where $\mathrm{Re}_0 = 200$

18.4 Discussion

18.4.1 Symmetric and Asymmetric Profiles

Without natural convection, the flow and consequently the melting rate was axisymmetric throughout the melting process as expected for $\mathrm{Re} \leqslant 200$ conditions [10]. Recirculation behind the aft of the sphere enhanced the melting rate, resulting in a flat profile with a sharp ridge located at the separation point; separating the curved fore and flat aft. A similar phenomena was observed with experiments for the dissolution of hard candy in flowing water [9] where a roughly hemispherical shape was formed at $\mathrm{Re} = \mathcal{O}(10^4)$. The physical mechanisms responsible for driving the moving interface in both melting and dissolution problems are similar [11], inasmuch as the constitutive equations include a problem dependent constant multiplied by the temperature or concentration gradients respectively.

Both the symmetric and asymmetric profiles resulted in an increased drag coefficient; a phenomena in contrast to what we found for the case of an eroding cylinder [6]. The eroding cylinder surface was driven by wall shear stress (function of velocity gradient) instead of heat flux (function of temperature gradient), causing different shape dynamics. Although the Nusselt number, which is dependent on the temperature gradient, decreases for both cases; indicating that the profiles become less prone to melting.

18.4.2 Node Shuffling in 3-D Space

This study has proven that the node shuffle algorithm extends to three spatial coordinates on arbitrary meshes (unstructured grids including nodes with an arbitrary number of valences), and we found that including this algorithm delayed the onset of mesh degradation. One key benefit of employing this algorithm is the retention of node connectivity between time steps; such that recreating the mesh after each shape change is not required (computationally expensive). Another primary benefit is that the surface profile is preserved over many deformation steps; accurately capturing the melting body evolution without artificially under or overestimating the melting rate. The volume V of the void within the computational domain, representing the melting body, shrunk to $0.374V_0$ (mixed convection) and $0.147V_0$ (forced convection); a significant volume change for the mesh to tackle.

Polyhedral cells were chosen over tetrahedral cells, as reasoned in Sect. 18.2.3, and several snapshots of the mesh at the interface are shown in Figs. 18.7 and 18.8. The naturally larger interior angles of the polygons were more effective at node shuffling than the triangular boundary faces when compared in preliminary tests; where the tetrahedral grids tended to bunch and cause numerical issues earlier than the polyhedral grids. The resolution of the ridge which formed on the hemispherical body was limited by the boundary nodes. Either refining the mesh or switching to a structured grid would help capture this geometric feature. Typically, a structured grid, decomposed of several subdomain blocks, would be suitable for modelling flow past a sphere [13] in order to limit numerical diffusion. Our node shuffle algorithm could be directly applied to unstructured grids with the same procedure.

Regions which caused numerical issues were located where the curvature changed significantly: the ridge around the hemisphere (forced convection) and the base of the balloon (mixed convection). Boundary faces at the water-ice interface appear well defined and of good quality, although the interior mesh cells became significantly skewed and of poor quality. A diffusion based smoothing method was applied on the interior cells with the dynamic mesh model of Fluent; however, we found that a linearly elastic solid model (not available for polyhedral grids in Fluent) performs better in cases with non-uniform shape deformations including node shuffling which effectively pulls the nodes around the body. The simulations could be prolonged by improving how the interior mesh deforms over time, with the aim of reducing the cell skewness near the water-ice interface.

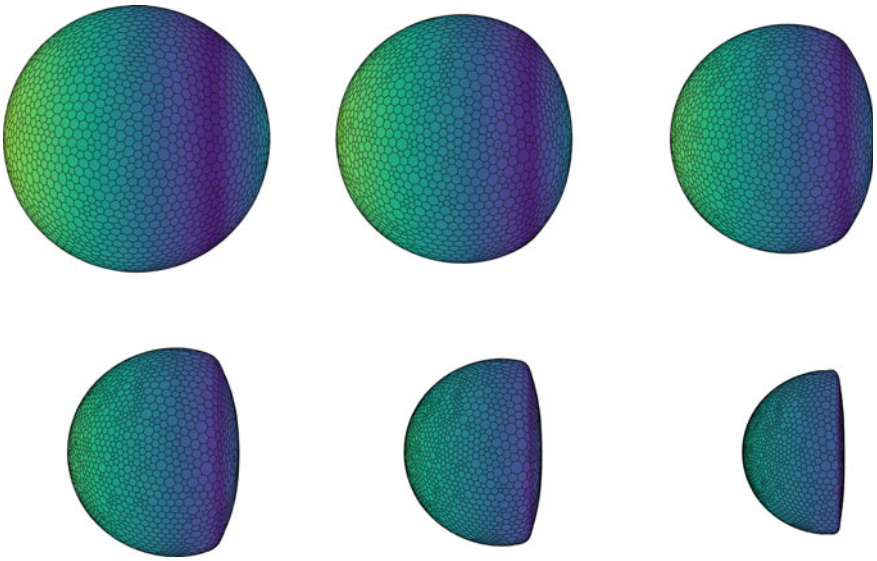

Fig. 18.7 Shape evolution of a melting body of ice under forced convection. The snapshots correspond to $t = 0\,\text{s}$, $70\,\text{s}$, $140\,\text{s}$, $210\,\text{s}$, $280\,\text{s}$ and $350\,\text{s}$. Boundary faces are shaded based on Nu from dark (low Nu) to light (high Nu)

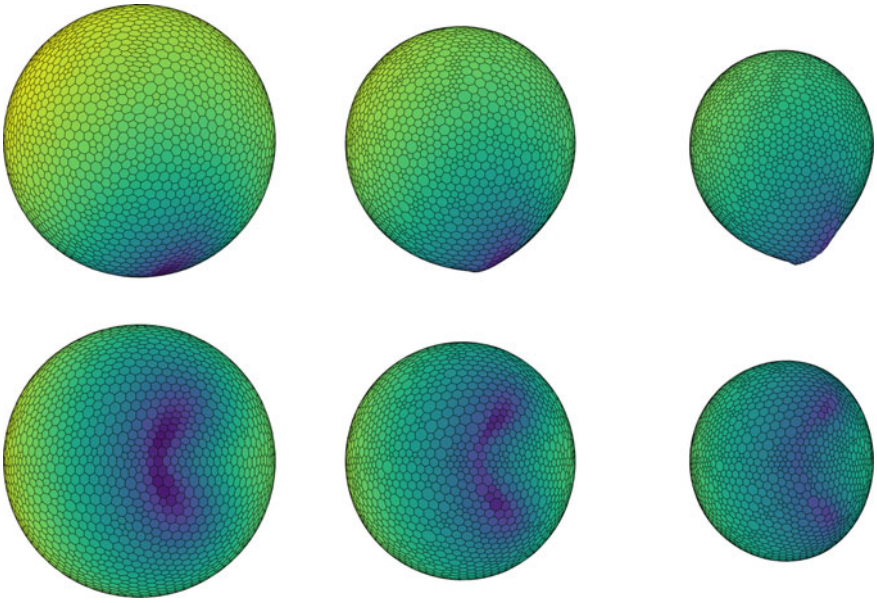

Fig. 18.8 Shape evolution under mixed convection. The snapshots correspond to $t = 0\,\text{s}$ (left), $70\,\text{s}$ (center) and $140\,\text{s}$ (right). Boundary faces are shaded based on Nu with the same scale as Fig. 18.7

18.5 Conclusion

In this work we extended our node shuffle algorithm from 2-D to 3-D and applied this algorithm to model a melting sphere of ice in cross flow. Polyhedral meshes were employed for the simulations in order to validate our model with unstructured grids; and the algorithm could also be applied to a structured grid. The volume of melted ice was up to 85.3% and the final geometries were significantly different from their initial spheres; demonstrating that a single mesh can be deformed for large volume and shape changes without the requirement of completely remeshing the domain.

References

1. Bagchi, P., Ha, M.Y., Balachandar, S.: Direct numerical simulation of flow and heat transfer from a sphere in a uniform cross-flow. J. Fluids Eng. **123**, 347–358 (2001). https://doi.org/10.1115/1.1358844
2. Hao, Y.L., Tao, Y.X.: Melting of a solid sphere under forced and mixed convection: flow characteristics. J. Heat Transf. **123**, 937–950 (2001). https://doi.org/10.1115/1.1389466
3. Hao, Y.L., Tao, Y.X.: Heat transfer characteristics of melting ice spheres under forced and mixed convection. J. Heat Transf. **124**, 891–903 (2002). https://doi.org/10.1115/1.1494090
4. Hewett, J.N.: Modelling evolving boundary problems in fluid mechanics. Ph.D. thesis, University of Canterbury (2017). https://doi.org/10092/14650
5. Hewett, J.N., Sellier, M.: Transient simulation of accumulating particle deposition on a cylinder in cross-flow. In: Eleventh International Conference on CFD in the Minerals and Process Industries. CSIRO, Melbourne, Australia (2015)
6. Hewett, J.N., Sellier, M.: Evolution of an eroding cylinder in single and lattice arrangements. J. Fluids Struct. **70**, 295–313 (2017). https://doi.org/10.1016/j.jfluidstructs.2017.01.011
7. Hewett, J.N., Sellier, M.: The pear-shaped fate of an ice melting front. In: Twelfth International Conference on CFD in the Oil & Gas, Metallurgical and Process Industries, pp. 423–429. SINTEF, Trondheim, Norway (2017)
8. Hewett, J.N., Sellier, M.: Modelling ripple morphodynamics driven by colloidal deposition. Comput. Fluids. **163**, 54–67 (2018). https://doi.org/10.1016/j.compfluid.2017.12.017
9. Huang, J.M., Moore, M.N.J., Ristroph, L.: Shape dynamics and scaling laws for a body dissolving in fluid flow. J. Fluid Mech. **765**, R3 (2015). https://doi.org/10.1017/jfm.2014.718
10. Johnson, T.A., Patel, V.C.: Flow past a sphere up to a Reynolds number of 300. J. Fluid Mech. **378**, 19–70 (1999). https://doi.org/10.1017/S0022112098003206
11. Moore, M.N.J.: Riemann-Hilbert problems for the shapes formed by bodies dissolving, melting, and eroding in fluid flows. Commun. Pure Appl. Math. **70**, 1810–1831 (2017). https://doi.org/10.1002/cpa.21689
12. Popiel, C.O., Wojtkowiak, J.: Simple formulas for thermophysical properties of liquid water for heat transfer calculations (from 0°C to 150 °C). Heat Transf. Eng. **19**, 87–101 (1998). https://doi.org/10.1080/01457639808939929
13. Richter, A., Nikrityuk, P.A.: Drag forces and heat transfer coefficients for spherical, cuboidal and ellipsoidal particles in cross flow at sub-critical Reynolds numbers. Int. J. Heat Mass Transf. **55**, 1343–1354 (2012). https://doi.org/10.1016/j.ijheatmasstransfer.2011.09.005
14. Whitaker, S.: Forced convection heat transfer correlations for flow in pipes, past flat plates, single cylinders, single spheres, and for flow in packed beds and tube bundles. AIChE J. **18**, 361–371 (1972). https://doi.org/10.1002/aic.690180219

Chapter 19
Analysis of 3D Crack Boundary Problems by Means of the Enriched Scaled Boundary Finite Element Method

Sascha Hell and Wilfried Becker

Abstract In fracture mechanics, a demanding challenge is the analysis of truly three-dimensional crack boundary value problems. For instance laminate structures composed of fiber-reinforced plies are typically prone to the formation of inter-fiber cracks because of the given strongly anisotropic stiffness and strength properties. These inter-fiber cracks commonly run through complete plies but are stopped at the ply interfaces. This leads to non-standard three-dimensional crack configurations with locally singular stress fields which should be investigated in regard of their criticality. For that purpose, the Scaled Boundary Finite Element Method turns out to be an appropriate and effective analysis method that permits solving linear elastic mechanical problems including stress singularities with comparably little effort. Only the boundary is discretized by two-dimensional finite elements while the problem is considered analytically in the direction of the dimensionless radial coordinate ξ. A corresponding separation of variables representation for the displacement field employed in the virtual work equation leads to a system of differential equations of Cauchy-Euler type. This differential equation system can be converted into an eigenvalue problem and solved by standard eigenvalue solvers for non-symmetric matrices. Depending on the given load the respective 3D stress singularities may lead to subsequent crack initiation and propagation, i.e. secondary moving cracks (with correspondingly moving boundaries). For the analysis of these secondary 3D crack configurations the Scaled Boundary Finite Element Method has been extended by an appropriate enrichment of the displacement representations. This leads to a clearly better numerical performance and computational efficiency compared to the standard Scaled Boundary Finite Element Method.

Keywords 3D crack problem · Scaled boundary finite element method · Enrichment · Finite fracture mechanics

S. Hell · W. Becker (✉)
TU Darmstadt, 64287 Darmstadt, Germany
e-mail: becker@fsm.tu-darmstadt.de

S. Hell
e-mail: hell@fsm.tu-darmstadt.de

S. Gutschmidt et al. (eds.), *IUTAM Symposium on Recent Advances in Moving Boundary Problems in Mechanics*, IUTAM Bookseries 34,
https://doi.org/10.1007/978-3-030-13720-5_19

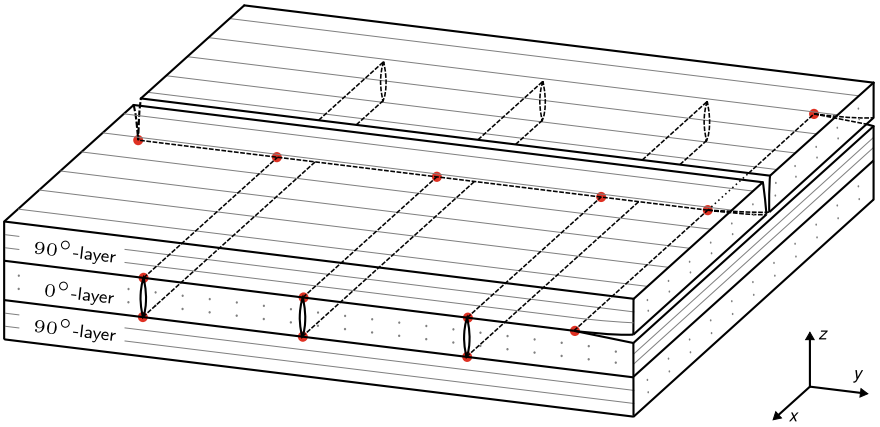

Fig. 19.1 Three-dimensional crack configurations in a cross-ply laminate with locations of stress-singularities

19.1 Introduction

In laminate structures composed of unidirectionally reinforced single plies the occurrence of inter-fiber cracks is very common because of the typically highly anisotropic stiffness and strength properties. This may happen from mechanical, but also from thermomechanical or hygromechanical loading. The inter-fiber cracks commonly run through complete plies and then are stopped at the ply interfaces where they may meet. In addition delamination cracks may occur. This results in non-standard three-dimensional crack configurations as they are depicted schematically in Fig. 19.1. At the red-dotted points in Fig. 19.1 three-dimensional stress singularities arise, not only when two crack fronts meet but also when a crack front meets a free laminate edge. All these 3D configurations are of high interest in regard of their criticality [1–5].

19.2 The Scaled Boundary Finite Element Method

The Scaled Boundary Finite Element Method (SBFEM) [6, 7] is a semi-analytical method which combines the advantages of the Boundary Element Method (BEM) and the Finite Element Method (FEM). Comparable to the BEM, only the boundary, or in some cases even only parts of the boundary, need to be discretized. At the same time, the problem of strongly singular integrands, present in the BEM-approach, does not exist in the SBFEM. This is because the SBFEM is based on a variational principle and does not need any fundamental solutions. The so-called geometric scalability is a fundamental requirement of the SBFEM. It requires that the connection of any point on the boundary with the scaling center with a straight line must be possible without

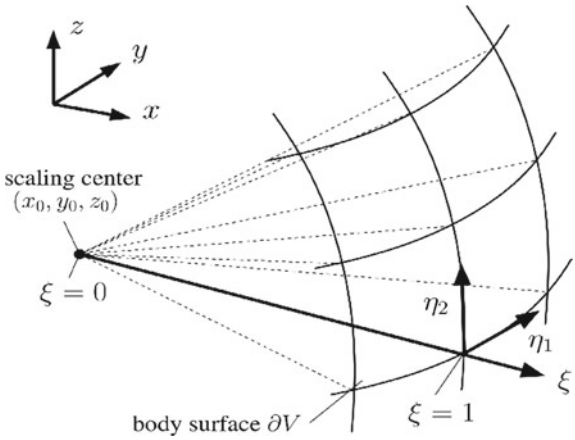

Fig. 19.2 Scaling coordinate system of the SBFEM

any intersections. Accordingly, a scaled boundary coordinate system is defined with its origin at the scaling center in a Cartesian coordinate system. The scaling coordinate ξ runs from the scaling center $\xi = 0$ to the boundary $\xi = 1$. In case of a 2D problem, a boundary coordinate η runs along the boundary. In the 3D case, two boundary coordinates η_1 and η_2 describe the surface of the body. Figure 19.2 illustrates this situation.

For an analysis of the whole domain only the boundary is discretized using isoparametric finite elements and shape functions $\boldsymbol{N}(\eta_1, \eta_2)$. The problem is still considered analytically in the scaling coordinate ξ. Thus, vector functions $\boldsymbol{u}(\xi)$ are introduced for the displacements on rays pointing from the scaling center to the finite element nodes on the boundary and the following kind of product ansatz or separation of variables ansatz is chosen:

$$\boldsymbol{u}(\xi, \eta_1, \eta_2) = \boldsymbol{N}(\eta_1, \eta_2)\boldsymbol{u}(\xi) \tag{19.1}$$

If this displacement representation is used within the principle of minimum total potential and the variations and integrations are performed finally a homogeneous differential equation system of Cauchy-Euler type is obtained:

$$\xi^2 \boldsymbol{E}_0 \boldsymbol{u}(\xi)_{,\xi\xi} + \xi\left[2\boldsymbol{E}_0 - \boldsymbol{E}_1 + \boldsymbol{E}_1^T\right]\boldsymbol{u}(\xi)_{,\xi} + \left[\boldsymbol{E}_1^T - \boldsymbol{E}_2\right]\boldsymbol{u}(\xi) = 0. \tag{19.2}$$

Here the quantities $\boldsymbol{E}_0, \boldsymbol{E}_1, \boldsymbol{E}_2$ are a kind of appropriately defined non-symmetric "stiffness matrices". This equation system can be solved by transformation to a quadratic eigenvalue problem and eventually leads to the following kind of solution

$$\boldsymbol{u}(\xi) = \sum_{i=1}^{n_\lambda} c_{pi} \xi^{\lambda_{pi}} \phi_{pi} + c_{ni} \xi^{\lambda_{ni}} \phi_{ni} \tag{19.3}$$

where the positive and negative exponents λ_{pi}, λ_{ni} are the eigenvalues of the eigenvalue problem, the quantities ϕ_{pi}, ϕ_{ni} are the corresponding eigenvectors and the constants $c_{pi,}$ c_{ni} can be identified from the given boundary conditions. So far, this kind of method is standard and is described for instance in [6].

In order to make the scaled boundary finite element method more efficient for the case of three-dimensional crack problems where there are meeting straight crack fronts an enriched separation of variables approach has been chosen and implemented [4]. It is of the following kind:

$$u_i(\xi, \eta_1, \eta_2) = \sum_{k \in N} N_k(\eta_1, \eta_2) u_{ik}(\xi) + \sum_{l \in P} N_l(\eta_1, \eta_2) \ldots \left[\sum_{s=1}^{n_s} \sum_{m=1}^{n_F} \left(F_{ism}(r, \varphi) - \sum_{k \in N} N_k(\eta_1, \eta_2) F_{ism}(r_k, \varphi_k) a_{sm}(\xi) \right) \right] \tag{19.4}$$

where the functions F_{ism} come from an appropriate 2D crack solution (e.g. also from a scaled boundary finite element analysis). The details of the implementation can be found in [4].

19.3 Analysis of Two Perpendicularly Meeting Inter-Fiber Cracks

As a representative 3D crack problem the situation of two perpendicularly meeting inter-fiber cracks in a [0°/90°]-laminate is considered. The local configuration and the employed SBFEM-surface mesh are shown in the left part of Fig. 19.3.

The SBFEM eigenvalue problem yields 6 independent crack deformation modes. Two of them are shown in the right part of Fig. 19.3. These deformation modes are characterized by singularity exponents that are different from the standard stress singularity exponent −0.5 for plane 2D cracks. The singularity exponents may be of a smaller absolute value than 0.5, but they may also be stronger (so-called "supersingularities"). It is a remarkable advantage of the SBFEM that it gives these singularity orders with high precision without the need of any post-processing. The effect of the enrichment of the SBFEM on the convergence properties has been studied thoroughly and it has been confirmed that in general the convergence rate at refining the mesh is significantly better when an enrichment is employed. For the two opening deformation modes of Fig. 19.3 this can be seen in Fig. 19.4.

The singular stress concentration at the location of two perpendicularly meeting inter-fiber cracks makes this location very prone for the initiation of a "secondary" crack in the interface plane, see Fig. 19.5.

For the assessment of the respective "post-cracked" problem the scaled boundary finite element method has to be employed in such a manner that it takes into account a post crack in the interface. To keep things as simple as possible only a quarter-model

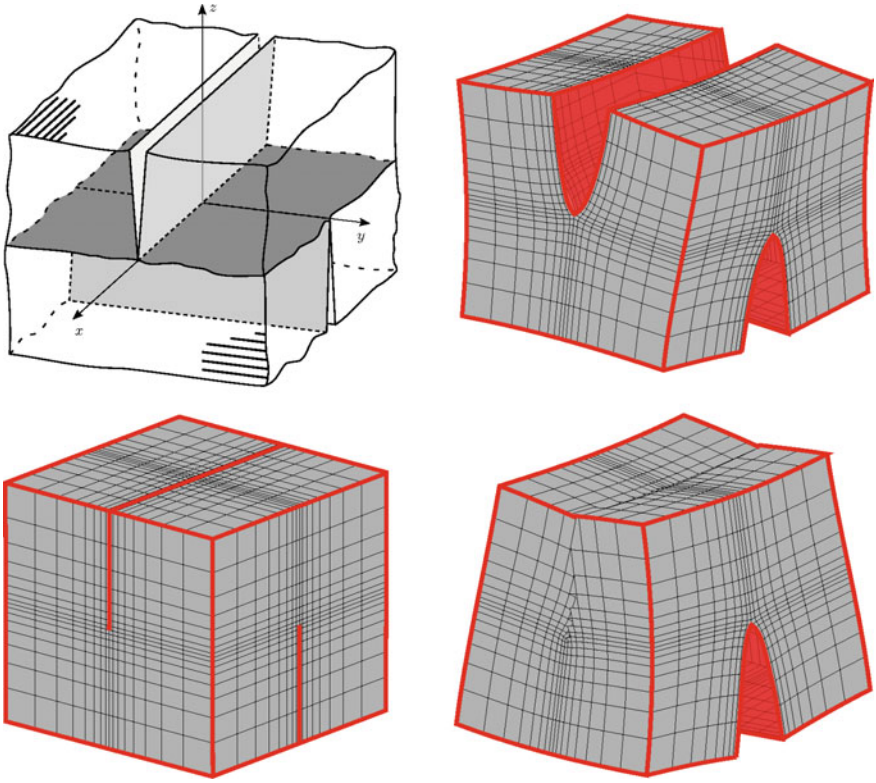

Fig. 19.3 Crack configuration, SBFEM surface mesh and crack opening modes

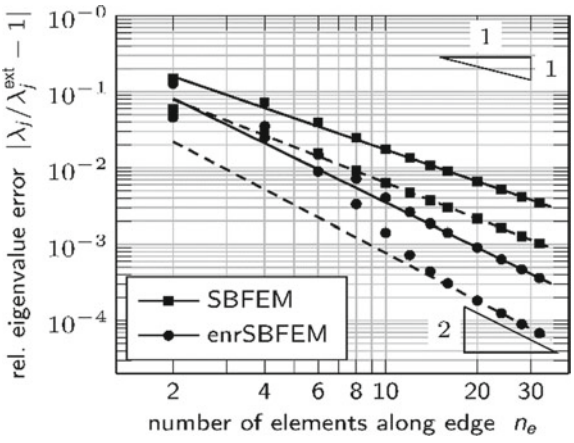

Fig. 19.4 Convergence of the standard SBFEM and the enriched SBFEM with mesh refinement for the considered two crack opening modes

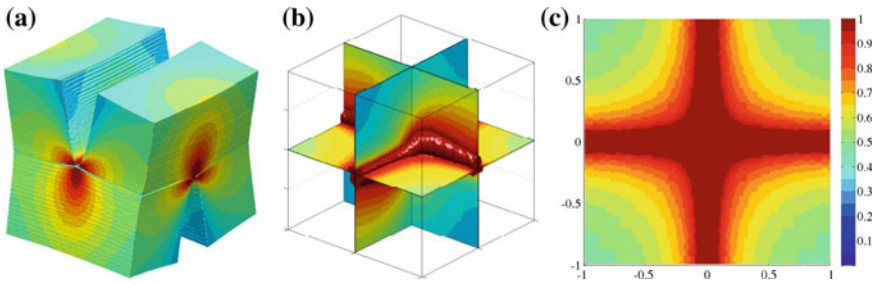

Fig. 19.5 Exemplary plot of stress effort for deformation mode with $\mathrm{Re}(\lambda_{3D} - 1) = 0.4554$. **a**, **b** Failure mode concept by Cuntze [7]. **c** Stress effort derived from Puck's action plane concept [8]

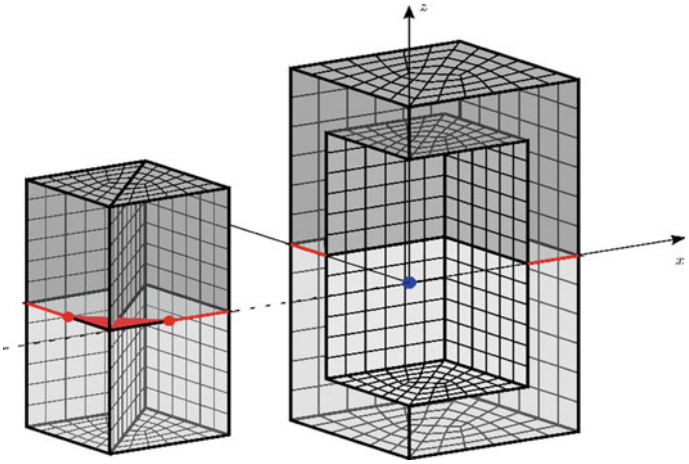

Fig. 19.6 SBFEM modeling of scalable triangular crack as a two-boundaries problem

is considered and a triangular shape has been assumed for the initiated crack. To simulate the crack initiation and propagation the SBFEM model has been modified in such a manner as it is sketched in Fig. 19.6. There is an inner SBFEM model with the triangular crack and two scaling centers at the ends of the crack front and there is an outer SBFEM model with the scaling center at the location of the originally meeting two inter-fiber cracks. By simply scaling the inner model different sizes of the secondary triangular crack can be simulated. The inner and outer models are combined to a so-called two-boundaries problem. As a result all required field quantities are efficiently available for any kind of cracking state.

19.4 Finite Fracture Mechanics Assessment

The initiation of a delamination cannot be predicted solely on the basis of the stress distribution for the non-delaminated situation since the presence of the stress singularity would always predict failure, even for arbitrarily small loads. On the other hand, the consideration of the energy release rate for a starting crack would not either allow to predict crack initiation since the energy release rate starts with the value zero. The way out of this unclear situation is challenging. From a very fundamental point-of-view such problems can be tackled by a variational approach free from a pre-existing crack as it has been suggested by Francfort and Marigo [9]. The corresponding computational effort however is very significant.

An easier way in this situation is possible in the framework of Finite Fracture Mechanics using a coupled stress and energy criterion, as it has originally been suggested by Leguillon [3]. The respective concept is to assume an instantaneous initiation of a crack of finite size when an appropriate strength criterion is fulfilled over the whole area ΔA of the generated crack and when at the same time the so-called incremental or averaged energy release rate $\bar{G}$ is sufficiently large to overcome the fracture toughness G_c of the material:

$$f\left(\sigma_{ij}\right) \geq \sigma_c \bigwedge \bar{G} \geq G_c. \tag{19.5}$$

In this connection the incremental energy release rate can be calculated from the change of the total potential as $\bar{G} = -\Delta \Pi / \Delta A$. The effective strength of a structure can be assessed by determining the smallest load for which the coupled criterion (19.5) is fulfilled for the first time. Mathematically this leads to an optimization problem which has to be solved by standard optimization calculus. In most cases this optimization problem can also be solved by an iterative procedure where the applied load and the generated crack size are modified stepwise until both subcriteria of condition (19.5) are fulfilled in a sufficiently precise manner. The solution of the optimization problem then consists in the critical load (or effective strength) and the size of the instantaneously generated crack.

In the case of the present two perpendicularly meeting inter-fiber cracks in a standard CFRP cross-ply laminate made of T800/epoxy material (with a transverse tensile strength of 55 N/mm^2 and a fracture toughness of 0.14 N/mm) the initiation of a secondary delamination crack happens under a biaxial tensile load of about 0.4% elongation. The generated secondary crack size is predicted to be of the order of 10^{-3} mm^2. Of course, this is a very small crack size, but nevertheless an interesting outcome.

19.5 Summary and Conclusion

The semi-analytical Scaled Boundary Finite Element Method turns out to be an appropriate method for the analysis of three-dimensional crack configurations where the requirement of scalability is fulfilled. The advantage of this method is that only the boundary of the considered solid body needs to be discretized. When there are stress singularities in the underlying configuration and the scaling center is placed directly at the location of the singularity, all singularity orders can be identified with little effort and high precision, even when they include super-singularities. The SBFEM has been enhanced by the implementation of a well-adjusted enrichment around meeting straight crack fronts. This implementation is working well and the enrichment leads to a significantly enhanced convergence behavior.

By means of the enriched SBFEM the situation of two perpendicularly meeting inter-fiber cracks has been analyzed more thoroughly. The initiation and growth of a triangular interface delamination crack has been taken into account by a corresponding scalable two boundaries model. By means of a coupled stress and energy criterion in the framework of Finite Fracture Mechanics the effective strength or critical load can be assessed with the implemented approach.

The implemented kind of approach and analysis has been tested so far only for two perpendicularly meeting inter-fiber cracks. It should, however, also work for other crack orientations, for the interaction of a delamination with an inter-fiber crack and also for the interaction of an inter-fiber crack with a free edge. This is left for future work.

References

1. Wang, A.S.D., Kishore, N.N., Li, C.A.: Crack development in graphite-epoxy cross-ply laminates under uniaxial tension. Compos. Sci. Technol. **24**, 1–31 (1985)
2. Hell, S., Becker, W.: The scaled boundary finite element method for the analysis of 3D crack interaction. J. Comput. Sci. **9**, 76–81 (2015)
3. Leguillon, D.: Strength or toughness? A criterion for crack onset at a notch. Eur. J. Mech. A Solids **21**, 61–72 (2002)
4. Hell, S., Becker, W.: The use of enriched base functions in the three-dimensional scaled boundary finite element method. In: Proceedings of the 7th European Congress on Computational Methods in Applied Sciences and Engineering, ID 5324, Crete (2016)
5. Hell, S., Becker, W.: Energy release rates at two perpendicularly meeting cracks by use of the Scaled boundary finite element method. Procedia Struct. Integr. **2**, 2471–2478 (2014)
6. Wolf, J.P.: The Scaled Boundary Finite Element Method. Wiley, Chichester (2003)
7. Cuntze, R.G.: Efficient 3D and 2D failure conditions for UD laminae and their application within the verification of the laminate design. Compos. Sci. Technol. **66**, 1081–1096 (2006)
8. Puck, A.: Festigkeitsanalyse von Faser-Matrix-Laminaten. Carl Hanser Verlag, Munich (1996)
9. Francfort, G.A., Marigo, J.-J.: Revisiting brittle fracture as an energy minimization problem. J. Mech. Phys. Solids **46**, 1319–1342 (1998)

Chapter 20
Analysis of Dynamic Variable Mass and Variable Parameter Systems Applying Semi-analytic Time-Integration

Helmut J. Holl

Abstract For open dynamic systems with moving boundaries the derivation of the equations of motion and the computation of the solution for the vibrations is discussed. The mechanical model has to consider the variable mass by the flow of mass through the boundary of the applied control volume and the variable parameter of the system in the derivation of the equations of motion. An efficient semi-analytic time-integration algorithm is introduced, analysed with respect to the numerical behaviour and applied to compute the solution of the non-symmetric and non-linear equations of motion. As an example a defined winding process in a Steckel mill is considered and the computed results of some characteristic forces and displacements are shown for given operation conditions.

Keywords Open system · Non-symmetric · Variable mass · Variable parameter · Time-integration · Semi-analytic

20.1 Introduction

The accurate computation of the vibrations in open dynamic systems with moving boundaries is important. Open systems considered within this context are winding processes, increase of load of a carrier, rockets and transportation of mass in a production system. There are two main items which have to be analysed. At first the effect of variable mass has to be considered which leads to the extended equations of Lagrange. These equations have to be used for the derivation of the equations of motion for such a system. The second item is the time-integration for such dynamic systems which has to consider efficiently the variable parameters and the variable mass terms as well as the non-linearity in the system and additionally has to guar-

H. J. Holl (✉)
Institute of Technical Mechanics, Johannes Kepler University of Linz,
Altenbergerstraße 69, 4040 Linz, Austria
e-mail: helmut.holl@jku.at
URL: http://www.jku.at/tmech/holl

S. Gutschmidt et al. (eds.), *IUTAM Symposium on Recent Advances in Moving Boundary Problems in Mechanics*, IUTAM Bookseries 34,
https://doi.org/10.1007/978-3-030-13720-5_20

antee a converged solution. A long time scale has to be computed as the production process usually is a long term procedure, where frequently also non-steady operation conditions occur. Therefore the numerical behavior of the algorithm has to be analysed carefully to give an efficient computation of the results. In this contribution a new approximation is used for the integration of the coordinate dependent force which are considered on the right hand side of the equation of motion. The applied approximation results in an unconditionally stable algorithm also for the variable mass terms and a high accuracy of the results.

The formulation of the extended equations of Lagrange has been derived by Irschik and Holl [1] for the use of Euler coordinates. The well known equations of Lagrange are restricted to constant mass systems only, see Ziegler [2], and the use of the extended equation of Lagrange is necessary to consider the flow of mass and energy through the boundary of the control volume of the system. Frequently non-linearities are present in the system and the parameters vary with time as the stiffness and some system parameters change. In Irschik and Holl [3] some contributions to dynamic systems with variable mass are discussed with respect to the balance of mass and linear momentum. From the cited literature it can be stated that dynamic variable mass systems are of permanent interest. The formulation of Meshchersky's reactive force is used by Cveticanin in [4] within various examples for variable mass open systems in production systems and manipulators. The Lagrange equations for a special variable mass system are discussed by Pesce in [5] for a system of particles and are applied to the deploying of a heavy cable from a reel and the impact of a rigid body to the free surface of a fluid. A generalized formulation of the Hamilton principle for non-material volumes is derived by Pesce and Casetta in [6]. In finding a constant of motion Casetta et al. [7] derived a formulation using Noether's theorem and applied it to the uncoiling of a strip from a drum. Casetta [8] introduced a new conservation law for dynamic systems for position dependent mass particles. A principle of generalized velocities is derived by Cveticanin in [9] and is applied to the separation of a rigid body. The symmetric and conserved quantities are discussed by Jiang and Xia in [10] and applied to a strip coiling drum.

A time integration scheme for dynamic systems described by a differential equation of second order is given by Newmark in [11] and this scheme has frequently been expanded and improved with different assumptions and applications. Some representative work is given in Chung and Hulbert in [12] and in Hilber et al. in [13] with emphasis to improve the numerical behaviour of the method. Fung [14] introduced an algorithm using polynomial approximations and collocation points, gives a comparison with Runge–Kutta methods and showed the spectral radius of the derived method in [15]. From the results it can be seen that the parameters of the method determine the stability of the algorithm. A half-explicit timestepping scheme is discussed by Schindler et al. [16] for the solution of contact problems in dynamic systems and is applied to a rotordynamic system to show the efficiency of the method. Soares [17] used an adaptive parameter depending on the critical frequency in order to get an unconditional stable algorithm. For a system with few coordinates a transformation to a system of differential equations of first order can be used and the solution is computed by a suitable Runge–Kutta method. Hairer [18] shows some numerical

solution methods and their behaviour and discusses the suitable application of different methods. The derivation and application of a semi-analytic time-integration algorithm is shown for rotordynamic systems by Holl in [19] and has been applied to non-symmetric and non-linear cases [20], where the numerical behaviour and efficiency for non-symmetric and non-linear systems is demonstrated. Exact solutions are known for special kinds of variable mass systems, which have been used by Holl et al. in [21] to evaluate a first approach for the semi-analytic time-integration.

20.2 Semi-Analytic Time-Integration Algorithm

20.2.1 Derivation of the Algorithm

With the extended equations of Lagrange for open systems the differential equation of motion for the mechanical system can be derived in the general form

$$\mathbf{M}\,\ddot{\mathbf{X}} + \left(\mathbf{D} + \mathbf{G} + \dot{\mathbf{M}}\right)\dot{\mathbf{X}} + (\mathbf{K} + \mathbf{N})\,\mathbf{X} + \mathbf{F}_N = \mathbf{F}(t) \tag{20.1}$$

where $\mathbf{M}$ is the mass matrix, $\dot{\mathbf{M}}$ its time-derivative, $\mathbf{D}$ is the damping matrix, $\mathbf{G}$ represents the gyroskopic matrix, $\mathbf{K}$ is the stiffness matrix, $\mathbf{N}$ is the matrix of the circulatory forces, $\mathbf{F}_N$ is the vector of non-linear restoring forces, $\mathbf{F}(t)$ is the vector of the excitation forces, $\mathbf{X}(t)$ is the vector of coordinates or degrees of freedom and n is the total number of degrees of freedom. $\mathbf{D} = \mathbf{D}_M + \mathbf{D}_N$ is subdivided into the part $\mathbf{D}_M$ which is diagonalized with a modal transformation and the residual (usually non-classic or non-symmetric) damping matrix $\mathbf{D}_N$. The algorithm starts with a separation of the solution into a quasi-static and a dynamic part

$$\mathbf{X} = \mathbf{X}_S + \mathbf{X}_D, \tag{20.2}$$

where the quasi-static part is computed by

$$\mathbf{K}\,\mathbf{X}_S = \mathbf{F}(t) \tag{20.3}$$

and the differential equation for the dynamic part is rewritten suitable for the application of the modal analysis in the form

$$\begin{aligned}\mathbf{M}\,\ddot{\mathbf{X}}_D + \mathbf{D}_M\,\dot{\mathbf{X}}_D + \mathbf{K}\,\mathbf{X}_D = &-\mathbf{F}_N - (\mathbf{K} + \mathbf{N})\;\mathbf{X}_S - \left(\mathbf{D} + \mathbf{G} + \dot{\mathbf{M}}\right)\;\dot{\mathbf{X}}_S \\ &-\mathbf{M}\,\ddot{\mathbf{X}}_S - \left(\mathbf{D}_N + \mathbf{G} + \dot{\mathbf{M}}\right)\;\dot{\mathbf{X}}_D - \mathbf{N}\,\mathbf{X}_D.\end{aligned} \tag{20.4}$$

The application of modal analysis with the modal transformation

$$\mathbf{X}_D = \boldsymbol{\Phi}\,\mathbf{q}_D \tag{20.5}$$

and the identities $\mathbf{\Phi}^T\mathbf{M}\mathbf{\Phi} = \mathbf{I}$, $\mathbf{\Phi}^T\mathbf{D}_M\mathbf{\Phi} = \Gamma = \text{diag}(2\zeta_i\omega_i)$ and $\mathbf{\Phi}^T\mathbf{K}\mathbf{\Phi} = \Omega = \text{diag}(\omega_i^2)$ gives the ith modal equation for the dynamic part

$$\ddot{q}_{Di} + 2\zeta_i\omega_i\,\dot{q}_{Di} + \omega_i^2\,q_{Di} = -\mathbf{\Phi}_i^T\mathbf{F}_N - \mathbf{\Phi}_i^T\,(\mathbf{K}+\mathbf{N})\,\mathbf{X}_S - \mathbf{\Phi}_i^T\left(\mathbf{D}+\mathbf{G}+\dot{\mathbf{M}}\right)\dot{\mathbf{X}}_S$$
$$-\mathbf{\Phi}_i^T\mathbf{M}\,\ddot{\mathbf{X}}_S - \mathbf{\Phi}_i^T\left(\mathbf{D}_N+\mathbf{G}+\dot{\mathbf{M}}\right)\,\mathbf{\Phi}\,\dot{\mathbf{q}}_D - \mathbf{\Phi}_i^T\mathbf{N}\,\mathbf{\Phi}\,\mathbf{q}_D = \mathbf{\Phi}_i^T\mathbf{P}. \tag{20.6}$$

Due to the non-symmetric matrices on the right hand side of the equations, the solution is not decoupled and a certain coupling between the modal coordinates is present. A time-stepping procedure has to consider the time evolution of the dynamic part of the solution. If the right hand side in (20.6) is summarized by an excitation force vector $\mathbf{P}$ and due to the modal transformation $P_i(\tau) = \mathbf{\Phi}_i^T\mathbf{P}$ the exact formulation for a linear system for the ith degree of freedom with $\omega_{id} = \omega_i\sqrt{1-\zeta_i^2}$ and for a discrete time step Δt instead of the time t is

$$\begin{Bmatrix} q_{Di} \\ \dot{q}_{Di} \end{Bmatrix}_{\Delta t} = \begin{bmatrix} A_{i11} & A_{i12} \\ A_{i21} & A_{i22} \end{bmatrix}_{\Delta t} \begin{Bmatrix} q_{Di0} \\ \dot{q}_{Di0} \end{Bmatrix} + \frac{1}{m}\int_0^{\Delta t} e^{-\zeta_i\omega_i(\Delta t-\tau)} \begin{Bmatrix} g_{i1}(\Delta t-\tau) \\ g_{i2}(\Delta t-\tau) \end{Bmatrix} P_i(\tau)d\tau \tag{20.7}$$

with the abbreviations

$$A_{i11} = e^{-\zeta_i\omega_i\Delta t}\left[\cos(\omega_{id}\Delta t) + \frac{\zeta_i}{\sqrt{1-\zeta_i^2}}\sin(\omega_{id}\Delta t)\right], \tag{20.8a}$$

$$A_{i12} = e^{-\zeta_i\omega_i\Delta t}\frac{1}{\omega_{id}}\sin(\omega_{id}\Delta t), \tag{20.8b}$$

$$A_{i21} = -e^{-\zeta_i\omega_i\Delta t}\frac{\omega_i}{\sqrt{1-\zeta_i^2}}\sin(\omega_{id}\Delta t), \tag{20.8c}$$

$$A_{i22} = e^{-\zeta_i\omega_i\Delta t}\left[\cos(\omega_{id}\Delta t) - \frac{\zeta_i}{\sqrt{1-\zeta_i^2}}\sin(\omega_{id}\Delta t)\right], \tag{20.8d}$$

$$g_{i1}(\Delta t-\tau) = \frac{1}{\omega_{id}}\sin\left[\omega_{id}\,(\Delta t-\tau)\right], \tag{20.8e}$$

$$g_{i2}(\Delta t-\tau) = \cos\left[\omega_{id}\,(\Delta t-\tau)\right] - \frac{\zeta_i}{\sqrt{1-\zeta_i^2}}\sin\left[\omega_{id}\,(\Delta t-\tau)\right]. \tag{20.8f}$$

In this semi-analytic time-integration procedure the approximation of the excitation force in (20.6) has to be defined within the mth time step $\Delta t = t_{m+1} - t_m$

$$P_i(\tau) = P_{im} + \Delta P_{im} \frac{\tau}{t_{m+1} - t_m} + \frac{4\ \Delta\Delta P_{im}}{(t_{m+1} - t_m)^2}\ \tau\ (t_{m+1} - t_m - \tau)\,, \tag{20.9}$$

where P_{im} is the ith force at the begin of the time step t_m, ΔP_{im} is the increment within the considered time step and with the force in the middle of the time step $P_{im+\frac{1}{2}}$ it follows for the parameter of the quadratic interpolation

$$\Delta\Delta P_{im} = P_{im+\frac{1}{2}} - P_{im} - \frac{\Delta P_{im}}{2}. \tag{20.10}$$

After integration for one time step it results

$$\begin{Bmatrix} q_{Di} \\ \dot{q}_{Di} \end{Bmatrix}_{\Delta t} = \begin{bmatrix} A_{i11} & A_{i12} \\ A_{i21} & A_{i22} \end{bmatrix}_{\Delta t} \begin{Bmatrix} q_{Di0} \\ \dot{q}_{Di0} \end{Bmatrix} + \begin{bmatrix} L_{i11} & L_{i12} & L_{i13} \\ L_{i21} & L_{i22} & L_{i23} \end{bmatrix}_{\Delta t} \begin{Bmatrix} P_{im} \\ \Delta P_{im} \\ \Delta\Delta P_{im} \end{Bmatrix} \tag{20.11}$$

with the elements of the load transfer matrices

$$L_{i11} = \frac{1}{\omega_i^2} \left[1 - e^{-\zeta_i \omega_i \Delta t} \left(\cos(\omega_{id} \Delta t) + \frac{\zeta_i}{\sqrt{1 - \zeta_i^2}} \sin(\omega_{id} \Delta t) \right) \right], \tag{20.12a}$$

$$L_{i12} = \frac{\omega_i \Delta t - 2\zeta_i}{\omega_i^3 \Delta t} + \frac{e^{-\zeta_i \omega_i \Delta t}}{\omega_i^3 \Delta t} \left(2\zeta_i \cos(\omega_{id} \Delta t) - \frac{1 - 2\zeta_i^2}{\sqrt{1 - \zeta_i^2}} \sin(\omega_{id} \Delta t) \right), \tag{20.12b}$$

$$L_{i13} = \frac{8\left(1 + \zeta_i \omega_i \Delta t - 4\zeta_i^2\right)}{\omega_i^4 \Delta t^2} - \frac{4\ e^{-\zeta_i \omega_i \Delta t}}{\omega_i^4 \Delta t^2} \left[2\left(1 - 4\zeta_i^2 - \zeta_i \omega_i \Delta t\right) \cos(\omega_{id} \Delta t) + \frac{\left(1 - 2\zeta_i^2\right) \omega_i \Delta t + 2\zeta_i \left(3 - 4\zeta_i^2\right)}{\sqrt{1 - \zeta_i^2}} \sin(\omega_{id} \Delta t) \right], \tag{20.12c}$$

$$L_{i21} = e^{-\zeta_i \omega_i \Delta t} \frac{1}{\omega_{id}} \sin(\omega_{id} \Delta t)\,, \tag{20.12d}$$

$$L_{i22} = \frac{1}{\omega_i^2 \Delta t} \left[1 - e^{-\zeta_i \omega_i \Delta t} \left(\cos(\omega_{id} \Delta t) + \frac{\zeta_i}{\sqrt{1 - \zeta_i^2}} \sin(\omega_{id} \Delta t) \right) \right], \tag{20.12e}$$

$$L_{i23} = \frac{4}{\omega_i^3 \Delta t^2}\Bigg[4\zeta_i - \omega_i \Delta t + e^{-\zeta_i \omega_i \Delta t}\left(\frac{2\left(1-2\zeta_i^2\right) - \zeta_i \omega_i \Delta t}{\sqrt{1-\zeta_i^2}} \sin\left(\omega_{id} \Delta t\right)\right.$$
$$\left. - \left(\omega_i \Delta t + 4\zeta_i\right) \cos\left(\omega_{id} \Delta t\right)\right)\Bigg]. \qquad (20.12f)$$

With the formulation (20.11) the solution at the end of the time step can be computed. However in the load vector parameters P_{im}, ΔP_{im} and $\Delta\Delta P_{im}$ in (20.6) the unknown coordinates are involved. Among different possible approximations of the time evolution of the unknown coordinates within the time step, for this analysis a linear variation is used for the displacement and the velocity and a constant value is taken for the acceleration of the coordinates:

$$q_{Di}(\tau) = q_{Di0} + \frac{q_{Di} - q_{Di0}}{\Delta t}\tau;\ \dot{q}_{Di}(\tau) = \dot{q}_{Di0} + \frac{\dot{q}_{Di} - \dot{q}_{Di0}}{\Delta t}\tau;\ \ddot{q}_{Di}(\tau) = \frac{\dot{q}_{Di} - \dot{q}_{Di0}}{\Delta t}. \qquad (20.13)$$

These approximations result in a very efficient algorithm and involves the unknown solution at the end of the time step q_{Di} and $\dot{q}_{Di}$. Inserting these approximations (20.13) in (20.11) and solving for the solution of the coordinates at the end of the time step after some algebraic manipulations it results for the incremental form with $\Delta q_{Di} = q_{Di} - q_{Di0}$ and $\Delta \dot{q}_{Di} = \dot{q}_{Di} - \dot{q}_{Di0}$

$$\begin{Bmatrix} \Delta q_{Di} \\ \Delta \dot{q}_{Di} \end{Bmatrix} = \mathbf{A}_{iSA} \begin{Bmatrix} q_{Di0} \\ \dot{q}_{Di0} \end{Bmatrix} + \mathbf{L}_{iSA}\ \Delta \mathbf{P}_{iN} \qquad (20.14)$$

The transfer matrix $\mathbf{A}_{iSA}$ and the load transfer matrix $\mathbf{L}_{iSA}$ for the implicit semi-analytic procedure depend on the used approximation (20.13), where $\Delta \mathbf{P}_{iN}$ is the increment of the non-linear force for the ith modal coordinate. Due to the non-linearity in (20.6) an incremental form and an iteration procedure is necessary. Finally the total solution is computed from the quasi-static and the dynamic part of the solution. There are different possible assumptions about the time evolution of the kinematic solution so that a family of algorithms with different transfer matrices can be derived. The present assumptions (20.13) lead to an efficient algorithm and some further improvements are under current research.

20.2.2 Error and Stability Analysis of the Algorithm

The analysis of the numerical behavior of the algorithm is performed by evaluating the accuracy in the form of the local and global error and the stability by evaluating the spectral radius of the algorithm which is shown by Hilber in [13] and Fung in [15]. This analysis is performed in the literature for linear and symmetric systems which are suitable for modal analysis as an exact reference solution is advantageous to compute the error. As the above presented semi-analytic method is exact in this case the error for such dynamic system vanish. So an enhanced error analysis has to

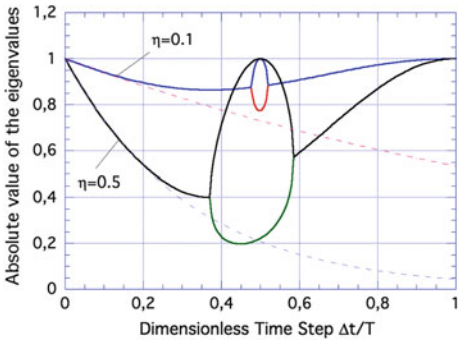

Fig. 20.1 Analysis of the spectral radius for damping force excitation

be performed. Analogous to the reformulations of (20.6) used in the derivations of the semi-analytic method for a single degree of freedom oscillator as a representative example portions of the system parameters are considered on the right hand side of the linear system

$$\ddot{q} + 2\zeta\omega\dot{q} + \omega^2 q = f - \alpha q - 2\eta\omega\dot{q} - \chi\ddot{q}. \tag{20.15}$$

For this dynamic SDOF-system a portion of the damping η, a part of the mass χ and a part of the stiffness α is considered as an excitation force to the dynamic system. This has the advantage that the numerical behavior can be analysed for each part separately and an exact solution is known for this designed test case. In computing the transfer matrix $\mathbf{A}_{SA}$ for the system (20.15) the approximations (20.13) are used in (20.11) and manipulated as explained in the above section. The accuracy is computed based on the truncation error which for the present algorithm is of second order. The stability is computed considering the maximum of the absolute values of the eigenvalues of the resulting transfer matrix $\mathbf{A}_{SA}$. Furthermore it can be shown for some non-symmetric coupled matrices these results are also valid and similar.

In a first step the undampled oscillator ($\zeta = 0$) is considered which is excited only by the damping force $2\eta\omega\dot{q}$ on the right hand side. With the assumption for the kinematic variables of (20.13) some computations are performed in order to get the formulation (20.14). When analysing the spectral radius of the transfer matrix for different dimensionless time steps the result is shown in Fig. 20.1 for two damping values, where the exact solution and the results for the algorithm is given. It can be stated that this algorithm is unconditionally stable as the spectral radius is less than one for all time steps. In a second step the portion of the stiffness parameter α is considered, which would represent a non-linearity in the system by the term αq in (20.15). The same procedure is performed again and in Fig. 20.2 the result is shown for a damped oscillator $\zeta = 0.1$ and a value for the non-linearity of $\alpha = 0.3$ for the present method. Additionally the results for the Newmark method and the exact values are shown. It can be seen, that the eigenvalues of the present method are very close to the exact solution. In a third step the excitation force is assumed to depend on a portion χ of the mass. Again for a damped oscillator ($\zeta = 0.02$) and different

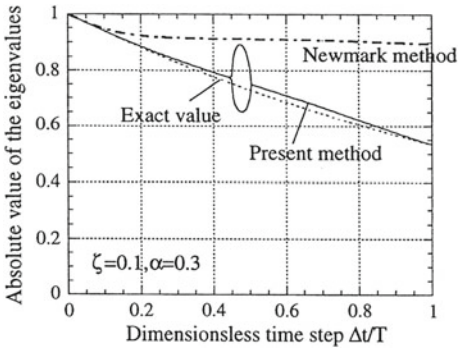

Fig. 20.2 Analysis of the spectral radius for stiffness proportional force excitation

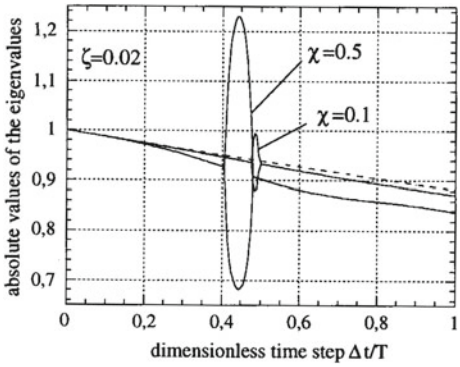

Fig. 20.3 Analysis of the spectral radius for splitted mass force excitation

values of the portion of the mass χ it can be seen in Fig. 20.3 an unconditionally stable method however there are also parameters for higher values of χ where the resulting algorithm is only conditionally stable and hence for these parameters cannot be used to solve a problem with many degrees of freedom which can be shown when applying modal transformation to such a system.

20.3 Mechanical Model of a Winding Process in a Steckel Mill

In a Steckel mill usually steel sheets are reversibly rolled and coiled in a storage unit situated on both sides where the temperature of the steel strip is homogenized. The strip passes the roller stand alternating in both directions where the thickness is reduced in a rolling mill stand situated between the two coiling units. A mechanical model of such a coiling unit is shown in Fig. 20.4, where the shown surface of the control volume on the left side defines the exit of the rolling mill stand where the steel strip moves with an axial speed $\dot{s}_B$. With the strip thickness h and the strip width b the flow of mass is defined by $\dot{m} = \rho\, b\, h\, \dot{s}_B$.

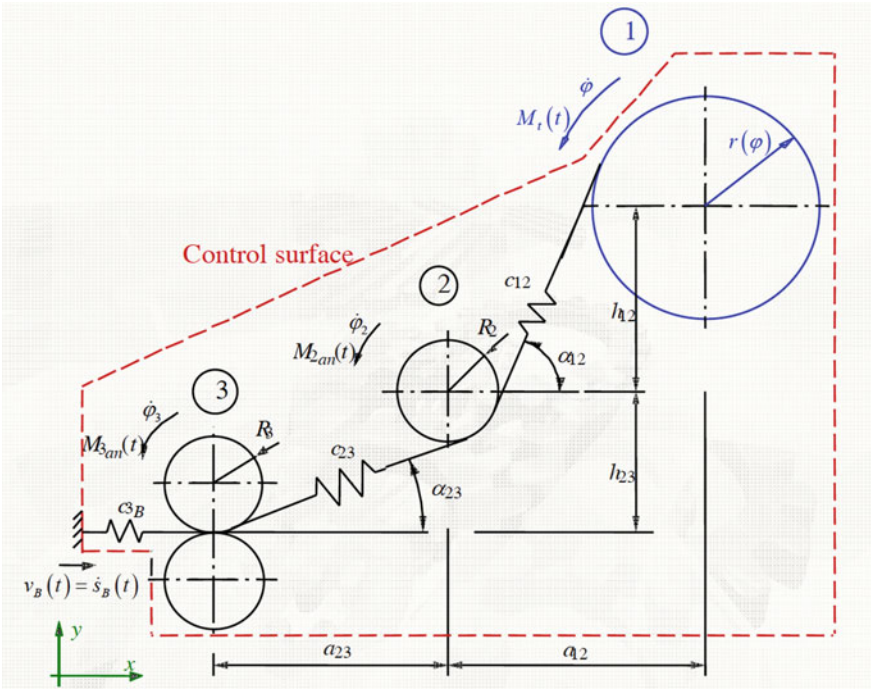

Fig. 20.4 Mechanical model of the Steckel mill

The rolled steel sheet with a defined thickness leaves the rolling mill stand and passes a pair of pitch rolls, which have the number ③ in Fig. 20.4, where the applied torque maintains a certain strip tension force. The strip passes the deflector roll ② before it is coiled on the coiling drum ①, where the outer radius changes with the number of layers of the sheet. At the three rotating units a torque is applied to get a good process and performance for a high quality of the product. The accurate simulation of the coiling process of the strip on the coiling drum would be very complicated but for sake of simplicity it is assumed that there is no relative motion between the coiled sheet and the layers are fixed on the drum when they touch the coiling drum. The rotating drum is modeled as a Laval-rotor and the elastic shaft involves a global Ritz' approximation where a variable stiffness results as the coiled sheets contribute to the stiffness. Due to the coiled strip the mass of the coiling drum changes with $\dot{m}_C = \rho\, b\, h\, \dot{\varphi}\, r$. No thermal deformation of the coiling drum is considered which corresponds to a homogeneous temperature distribution. The shown rigid bearings in Fig. 20.4 for the rolls are mounted on both ends of the elastic shaft so that a deflection coordinate is introduced considering the bending with a stiffness according to a Ritz approximation with one coordinate. When considering the variable outer radius of the coiling drum an Archimedian spiral $r = r_0 + \frac{h}{2\,\pi}\varphi$ is used, where h is the sheet thickness. The axially moving steel strip is modeled

considering longitudinal and transversal deformations in the regions between the rotating units using Ritz approximations, Ziegler [2]. For the longitudinal motion of the strip a linear Ritz approximation $u^*(\xi,t) = u_L + (1 - \frac{\xi}{L_0})u_R$ is applied, where ξ is the longitudinal coordinate, u_L is the strip length on the left side of the considered region with the length L_0 and u_R is the strip length on the right side, which are defined by the rotation angles of the rolls. For the transversal deflection of the strip the Ritz approximation $w^*(\xi,t) = w_B^*(\xi,t) + g_L\left(1 - \frac{\xi}{L_0}\right) + g_R\frac{\xi}{L_0}$ with $w_B^*(\xi,t) = \sin^2\left(\frac{\xi\pi}{L_0}\right)q_T(t)$ is used, where $g_L = 0$ at the left and $g_R = y_W - r$ at the right side of the region. The absolute transversal velocity of the moving strip is $\dot{w}^*(\xi,t) = \dot{w}_B^*(\xi,t) + \frac{dw_B^*(\xi,t)}{d\xi}\dot{u}^*(\xi,t) + (\dot{y}_W - \dot{r})\frac{\xi}{L_0}$. With the kinetic energy of the moving strip $T_S = \frac{1}{2}\int_0^{L_0}\rho A\dot{u}^*(\xi,t)^2 d\xi + \frac{1}{2}\int_0^{L_0}\rho A\dot{w}^*(\xi,t)^2 d\xi$, where the Rayleigh–Ritz approximation is inserted and integrated. The potential energy using the strain in the strip $\varepsilon_S = \varepsilon_{xx} - zw'' + \frac{1}{2}w'^2$ gives

$$V_S = \frac{1}{2}\int_0^{L_0}\left[EA\left(\frac{\partial u^*}{\partial\xi}\right)^2 + EI_S\left(\frac{\partial^2 w^*}{\partial\xi^2}\right)^2\right]d\xi + \int_0^{L_0}\frac{F_B}{2}\left(\frac{\partial w_B^*}{\partial\xi}\right)^2 d\xi \quad (20.16)$$

and with the above given Rayleigh–Ritz approximation after the integration results in $V_S = \frac{c_S}{2}(s_R - s_L)^2 + \frac{EJ_S\pi^4}{L_0^3}q^2 + \frac{F_B\pi^2}{4L_0}q_T^2$, which involves a coupling between the bending of the coiling drum and the axial motion of the strip. The steel strip enters the control volume with the speed $\dot{s}_B$ and the speed when attaching the coiling drum can be computed from the time derivative of the coiled strip length. For the Archimedian spiral $s_R = r_0\varphi + \frac{h\varphi^2}{4\pi} + x_W - \frac{\pi^2 q_T^2}{4L_0}$ is the coiled strip length with homogeneous initial condition, φ the rotation angle and x_W is the horizontal coordinate of the center of the shaft of the coiling drum.

With the actual momentum of inertia the kinetic energy of the coiling drum is given by $T_C = m_C\frac{\dot{x}_S^2 + \dot{y}_S^2}{2} + J_C\frac{\dot{\varphi}^2}{2}$, where the momentum of inertia $J_C = \frac{m_C}{2}\left(r^2 + \bar{r}_0^2\right)$ increases with the outer radius. The potential energy considers the deflection of the coiled drum $V_C = \frac{c_C}{2}\left[(x_W - x_{W0})^2 + (y_W - y_{W0})^2\right] - m_C g y_S$, where c_C is the computed bending stiffness of the coiling drum. The generalized forces for the extended Lagrange equations consider a damping at the rotating units. The resulting 10° of freedom of the system are the vertical and horizontal motion of the center of the coiling drum and the deflector roll, the rotation angles, the vertical motion of the pitch roll, the longitudinal and transversal sheet deformations in both regions between the rotating units. No gaps are allowed in the driving units and the controlled torques are applied at the rollers and the coiling drum. The resulting equations of motion after performing the described derivation cannot be given here as for all coordinates lengthy equations result.

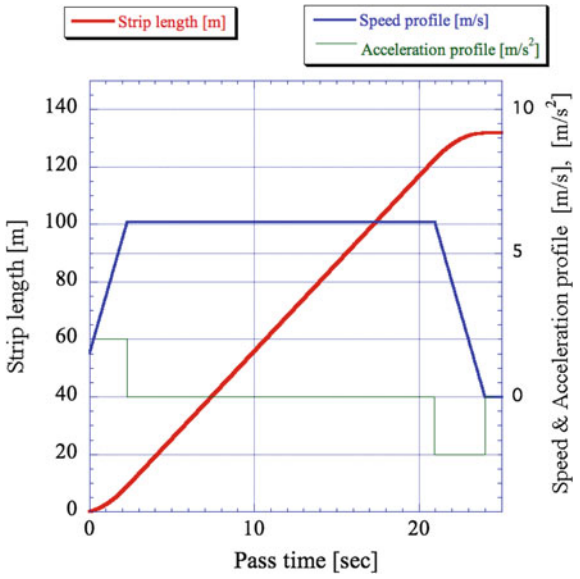

Fig. 20.5 Defined data of the strip length, speed and acceleration

20.4 Computed Results

The computation of the solution of the derived equations of motion for the open system with variable mass and variable parameter inserting proper system parameters ($a_{12} = 1.8\,\text{m}$, $a_{23} = 1.05\,\text{m}$, $l_{12} = 1.12\,\text{m}$, $l_{23} = 0.83\,\text{m}$, $m_C = 5000\,\text{kg}$, $I_C = 2350\,\text{kgm}^2$, $r = 0.7\,\text{m}$, $M_1 = -150\,\text{kNm}$, $M_2 = 0\,\text{Nm}$, $M_3 = 20.6\,\text{kNm}$, $b = 0.9\,\text{m}$, $h = 15\,\text{mm}$, $\rho = 7800\,\text{kg/m}^3$) is performed. As an example a given production process of a Steckel mill is considered with a defined speed profile, the corresponding axially moving strip length and the acceleration profile are shown in Fig. 20.5. The corresponding rotation angles are given in Fig. 20.6 and the resulting strip tension forces are shown in Fig. 20.7. The driving moments at the rotating units are kept constant in this representative example, so it can be seen that the strip tension forces are decreasing during the pass time as the radius of the coiling drum is increasing. Due to the speed profile some small vibrations are excited which can be observed in the strip tension forces. The components of the displacements of the center of gravity of each rotating units are shown in Fig. 20.8 and the displacement of the coiling drum in an orthogonal plane to the rotation axis is shown in Fig. 20.9. The oscillations are small as a save operation procedure is based to the simulations and an Archimedian spiral is used for the variable outer radius of the coiling drum. Also the transversal oscillations of the strip in Fig. 20.10 are small and decrease after a disturbance. The shown converged solution has been computed with different algorithms.

As a conclusion it can be stated that due to the performed simulations a comparison of the computation time shows that the Newmark procedure and the HHT-α-method described in [13] need about 80% higher computation time, whereas with a Runge

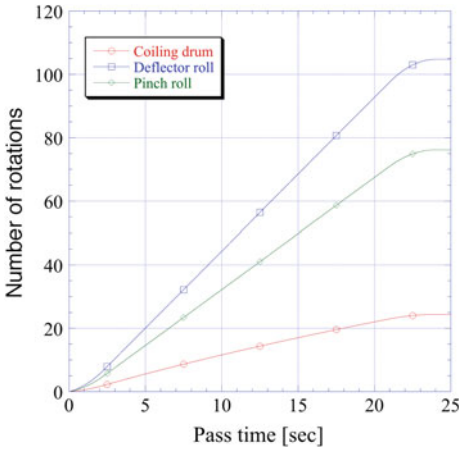

Fig. 20.6 Results for the rotation of the pitch roll, deflector roll and coiling drum

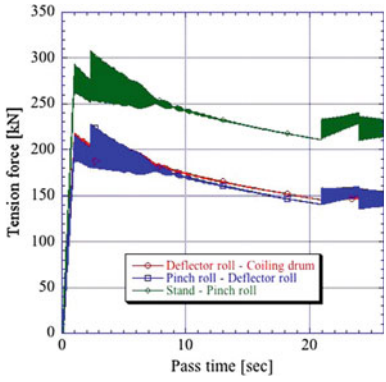

Fig. 20.7 Results of the strip tension forces in the three regions

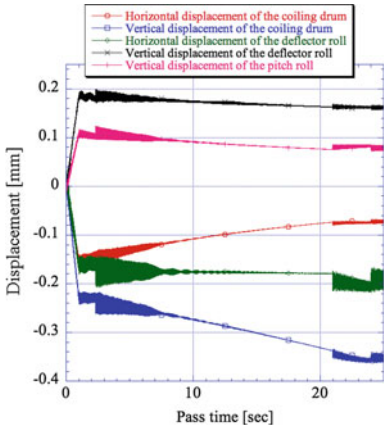

Fig. 20.8 Results for the motion of the center of mass of rolls and drum

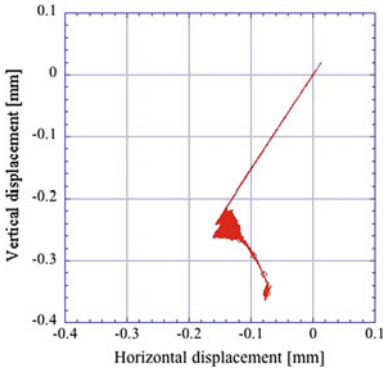

Fig. 20.9 Results of the position of the center of the coiling drum

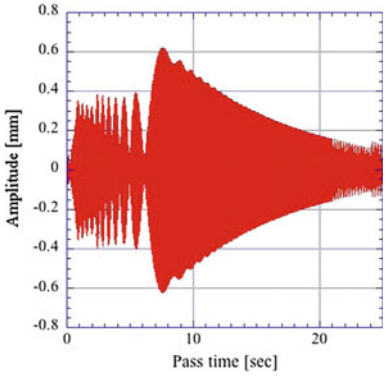

Fig. 20.10 Transversal vibrations of the strip between deflector roll and pitch roll

Kutta method the used computation time is 1,5 times higher. A more general approach for the approximation of the load function is in ongoing research an order to find an even better semi-analytic algorithm for non-linear systems with variable mass and parameters.

Acknowledgements This work has been supported by the LCM - K2 Center within the framework of the Austrian COMET-K2 program.

References

1. Irschik, H., Holl, H.J.: The equations of Lagrange written for a non-material volume. Acta Mech. **153**(3–4), 231–248 (2002)
2. Ziegler, F.: Mechanics of Solids and Fluids. Springer, New York (1991)
3. Irschik, H., Holl, H.J.: Mechanics of variable-mass systems - Part 1: balance of mass and linear momentum. Appl. Mech. Rev. **57**(2), 145–160 (2004)
4. Cveticanin, L.: Dynamics of Bodies with Time-Variable Mass. Springer, Berlin (2016)
5. Pesce, C.P.: The application of Lagrange equations to mechanical systems with mass explicitly dependent on position. J. Appl. Mech. **70**, 751–756 (2003)

6. Casetta, L., Pesce, C.P.: The generalized Hamiltons principle for a non-material volume. Acta Mech. **224**(4), 919–924 (2013)
7. Casetta, L., Irschik, H., Pesce, C.P.: A generalization of Noether's theorem for a non-material volume. Z. Angew. Math. Mech. **96**(6), 696–706 (2016)
8. Casetta, L.: Theorem on a new conservation law for the dynamics of a position-dependent mass particle. Acta Mech. **228**(1), 351–355 (2017)
9. Cveticanin, L.: Principle of generalized velocities in dynamics of planar separation of a rigid body. Acta Mech. **226**, 2511–2525 (2015)
10. Jiang, W.-A., Xia, L.-L.: Symmetry and conserved quantities for non-material volumes. Acta Mech. **229**, 1773–1781 (2018)
11. Newmark, N.M.: A method of computation for structural dynamics. J. Eng. Mech. Div. **85**, 67–94 (1959)
12. Chung, J., Hulbert, G.M.: A time integration algorithms for structural dynamics with improved numerical dissipations: the generalized-method. J. Appl. Mech. **60**, 371–375 (1993)
13. Hilber, H.M., Hughes, T.J.R., Taylor, R.L.: Improved numerical dissipation for time integration algorithms in structural dynamics. Earthq. Eng. Struct. Dyn. **5**, 283–292 (1977)
14. Fung, T.C.: Higher-order accurate time-step-integration algorithms by post-integration techniques. Int. J. Numer. Methods Eng. **53**, 1175–1193 (2002)
15. Fung, T.C.: Stability and accuracy of differential quadrature method in solving dynamic problems. Comput. Methods Appl. Mech. Eng. **191**, 1311–1331 (2002)
16. Schindler, T., Rezaei, S., Kursawe, J., Acary, V.: Half-explicit timestepping schemes on velocity level based on time-discontinuous Galerkin methods. Comput. Methods Appl. Mech. Eng. **290**, 250–276 (2015)
17. Soares, D.: A simple and effective single-step time marching technique based on adaptive time integrators. Comput. Methods Appl. Mech. Eng. **283**, 1138–1166 (2017)
18. Hairer, E., Wanner, G.: Solving Ordinary Differential Equations I: Nonstiff Problems. Springer Series in Computational Mathematics, vol. 8, 2nd edn. Springer, Berlin (2009)
19. Holl, H.J.: An efficient semi-analytic time-integration method with application to non-linear rotordynamic systems. Comput. Mech. **26**(4), 362–375 (2000)
20. Holl, H.J.: A time-integration algorithm for time-varying systems with non-classical damping based on modal methods. In: Wicks, A.L. (ed.) Proceedings of the 15th IMAC Society for Experimental Mechanics, pp. 1558–1564. Springer (1997)
21. Holl, H.J., Belyaev, A.K., Irschik, H.: Simulation of the duffing-oscillator with time-varying mass by a BEM in time. Comput. Struct. **73**, 177–186 (1999)

Chapter 21
Equipartition of Modal Energy in a Stiff Vibrating String Due to a Finite Curved Boundary Obstacle

Ashok K. Mandal and Pankaj Wahi

Abstract We study the characteristics of stiff strings vibrating against a curved boundary obstacle which is a situation encountered in stringed musical instruments like sitar, veena and tanpura. The wrapping and unwrapping of the string over the curved obstacle introduces a moving boundary which upon appropriate spatial scaling reveals the resulting nonlinearity. We find dominant quadratic nonlinearities which facilitate modal interactions leading to mode-locked solutions in the absence of damping. The analytical results for the phase-locked solutions are obtained using the method of multiple scales (MMS). We have further found a mode-locked state which tends to an equipartition of energy among the various vibrational modes with an increase in the number of modes considered for the analysis. . . .

Keywords Stiff strings · Modal interactions · Mode locking · Equipartition of energy

21.1 Introduction

Sitar, veena, tanpura (or tambura) etc. are plucked stringed musical instruments used in Indian classical music [1]. They are known to have attractive tonal quality of sound in terms of harmonicity, modulations in frequency and amplitude, and presence of a large number of overtones. These instruments have a finite-sized curved bridge at one end instead of a sharp bridge which is commonly used in western stringed instruments [2]. In this paper, we study the vibrational characteristics of a real sitar string with bending stiffness which is smoothly wrapping/unwrapping around a curved obstacle.

A. K. Mandal
Department of Mechanical Engineering, National Institute of Technology Jamshedpur, Jamshedpur 831014, Jharkhand, India
e-mail: ashok.mndl@gmail.com; ashok.me@nitjsr.ac.in

P. Wahi (✉)
Mechanical Engineering Department, Indian Institute of Technology Kanpur, Kanpur 208016, Uttar Pradesh, India
e-mail: pankajwahi@gmail.com; wahi@iitk.ac.in

S. Gutschmidt et al. (eds.), *IUTAM Symposium on Recent Advances in Moving Boundary Problems in Mechanics*, IUTAM Bookseries 34,
https://doi.org/10.1007/978-3-030-13720-5_21

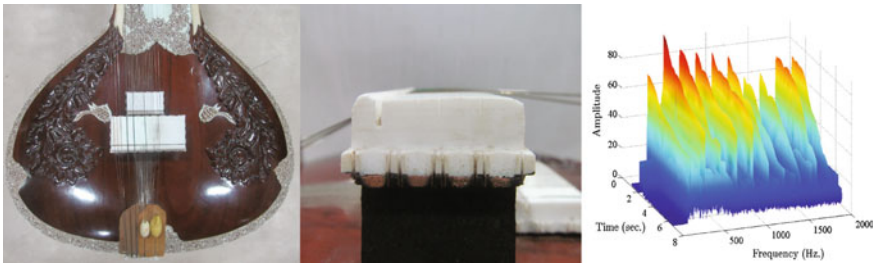

Fig. 21.1 Top and side view of a sitar bridge with a typical spectrogram obtained by plucking a string

Even though there have been several studies on a string vibrating against a curved obstacle [3–6], the vibration characteristics of the string in the presence of the obstacle has been reported only recently in [7–9]. The current paper extends the results in [7, 8] for ideal strings to strings with bending stiffness and shows the existence of a vibrating state with an equipartition of energy among all the modes even for a stiff string.

The top and side view of a sitar bridge is shown in Fig. 21.1. There are slots on the left elevated portion (as shown in the side view) of the bridge through which the strings pass so as to retain their position along the widthwise direction while the strings wrap and unwrap around the right portion which is a smooth curved surface. A typical spectrogram obtained when one of the strings of the sitar is plucked is shown in this figure as well. It can be seen that several overtones are present and each overtone has a modulated decay which signifies the amplitude modulations. Frequency modulations has not been well captured in the spectrogram shown in Fig. 21.1. However, experimental investigations of Raman [2] on sitar showed that several overtones were present in the sound while the experiments of Benade and Messenger [10] reported a complex variation in the sitar sound spectrum with the presence of modulation in frequency and amplitude of the various modes. We note that the strings in these musical instruments have non-planar vibrations involving motions both parallel and perpendicular to the bridge geometry. As will be seen later, our simplified model of a real string vibrating only perpendicularly to a curved boundary obstacle, however, is able to explain all these observed features of the sound of sitar.

Harmonic overtones (integral multiples of the fundamental) are desirable in sound to make it musical and soothing. Hence, there is a lot of emphasis in the design of musical instruments to make its sound have harmonic overtones. Stringed musical instruments have the vibration of strings as the source of sound which can produce harmonic overtones. However, these harmonic overtones are possible under highly idealized situation like no bending rigidity, fixed supports and no damping. In contrast, the strings used in almost all musical instruments have small but finite bending rigidity, sources of dissipation of energy and nonrigid end conditions which make the overtones inharmonic [11, 12]. It has already been shown in [9] that the presence

of a finite curved obstacle as in sitar and veena introduces a quadratic nonlinearity which enhances modal interactions and can lead to mode locking among the various vibrational modes. We extend the results of [9] to higher number of modes and find that there exists a mode-locked state which tends to the state of equipartition of energy among the various modes even for the stiff string as was observed for the case of an ideal string in [8].

21.2 Mathematical Model

A schematic diagram of the string vibrating against an obstacle is shown in Fig. 21.2 where all the quantities are nondimensionalized as in [7, 8]. The axial coordinate $\bar{x}$ is nondimensionalized by the length L of the string so that $l = 1$ and time is non-dimensionalized by $\sqrt{\frac{T}{\rho L^2}}$, where T is the uniform tension in the string and ρ is the uniform density per unit length. We assume that the string perfectly wraps/unwraps around the obstacle with a continuous contact patch and a unique point of separation at $\bar{x} = \gamma$. This implies that the wrapped length of the string is γ whereas the free length is $1 - \gamma$. For an ideal string, i.e., in the absence of any bending rigidity, the transverse displacement $\bar{y}(\bar{x}, \bar{\tau})$ (nondimensionalized by the height of the bridge) of the free portion of the string is given by the non-dimensional wave equation

$$\frac{\partial^2 \bar{y}(\bar{x}, \bar{\tau})}{\partial \bar{x}^2} - \frac{\partial^2 \bar{y}(\bar{x}, \bar{\tau})}{\partial \bar{\tau}^2} = 0\,, \quad \gamma \leq \bar{x} \leq 1 \tag{21.1}$$

with the standard displacement/geometric boundary conditions at the two ends

$$\bar{y}(\gamma, \bar{\tau}) = \bar{y}_b(\gamma, \bar{\tau}), \qquad \bar{y}(1, \bar{\tau}) = 0\,, \tag{21.2}$$

where $\bar{y}_b(\bar{x}, \bar{\tau})$ represents the profile of the boundary obstacle in the domain $0 \leq \bar{x} \leq b$ with b as the length of the obstacle. For simplicity of analysis, we will be approximating the shape of the obstacle with a parabola, i.e., $y_b(\bar{x}) = \alpha\, \bar{x}(b - \bar{x})$, where α is a constant representing its curvature. We note that the exact functional form for the obstacle does not alter the various conclusions drawn in the current paper on the effect of the wrapping nonlinearity on the modal interactions. The assumption of a parabola just simplifies the algebra.

Note that the point of separation or the wrapped length γ is another state variable along with the transverse displacement $\bar{y}(\bar{x}, \bar{\tau})$ and hence, an extra equation is required to determine it. This extra equation comes in the form of an additional boundary condition at the left end of the string, i.e., $\bar{x} = \gamma$ which can be obtained from the transversality condition, see [8] for details. However, we can simply make an assumption that the string remains tangent to the bridge surface at $\bar{x} = \gamma$ which leads to

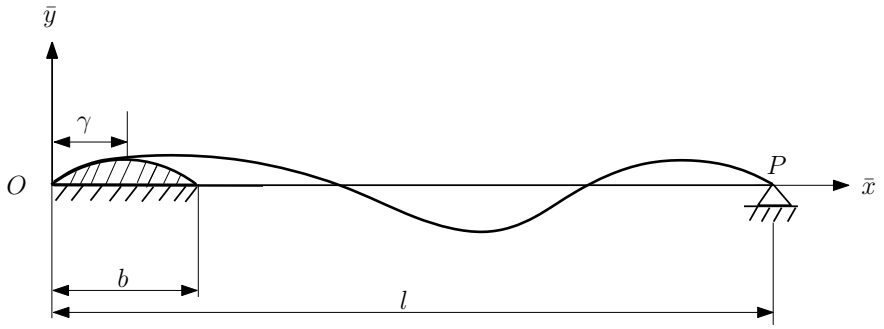

Fig. 21.2 Schematic diagram of vibration of string against boundary obstacle

$$\frac{\partial \bar{y}(\gamma, \bar{\tau})}{\partial \bar{x}} = \alpha(b - 2\gamma)\,. \tag{21.3}$$

Equation (21.1) along with Eqs. (21.2) and (21.3) uniquely determines the transverse displacement $\bar{y}(\bar{x}, \bar{\tau})$ of the free portion of the string and the wrapped length γ for an ideal string. In the presence of a nondimensional bending rigidity K for the string, the equation of motion for the free portion is modified to

$$\frac{\partial^2 \bar{y}(\bar{x}, \bar{\tau})}{\partial \bar{x}^2} - \frac{\partial^2 \bar{y}(\bar{x}, \bar{\tau})}{\partial \bar{\tau}^2} - K\frac{\partial^4 \bar{y}(\bar{x}, \bar{\tau})}{\partial \bar{x}^4} = 0\,, \quad \gamma \le \bar{x} \le 1\,. \tag{21.4}$$

We note that (21.4) is a fourth order PDE for $K \neq 0$ while it is a second order PDE for $K = 0$. Hence, two extra boundary conditions are required to completely define the problem for the case when $K \neq 0$. The extra boundary condition at the fixed end ($\bar{x} = 1$) can be easily identified as a pinned or a clamped support. However, the extra condition at the moving end (i.e., at $\bar{x} = \gamma$) is not completely clear. Continuity of string and slope continuity at $\bar{x} = \gamma$ have already been taken into account even for $K = 0$. However, for a beam in variable contact with a flat surface in the absence of adhesion, it has been shown that no point moment can exist at the point of separation. This in turn will imply curvature continuity at the point of separation for our case. Accordingly, the complete set of boundary conditions to determine $\bar{y}(\bar{x}, \bar{\tau})$ and γ for PDE (21.4) are:

$$\bar{y}(\gamma, \bar{\tau}) = \alpha\gamma(b - \gamma), \qquad \frac{\partial \bar{y}(\gamma, \bar{\tau})}{\partial \bar{x}} = \alpha(b - 2\gamma), \qquad \frac{\partial^2 \bar{y}(\gamma, \bar{\tau})}{\partial \bar{x}^2} = -2\alpha, \tag{21.5}$$

$$\bar{y}(1, \bar{\tau}) = 0, \qquad \frac{\partial^2 \bar{y}(1, \bar{\tau})}{\partial \bar{x}^2} = 0\,. \tag{21.6}$$

We note further that for typical parameters of the string used in the musical instruments, $K \ll 1$ and accordingly, it is a singular perturbation problem. The two new boundary conditions associated with the curvatures at the two ends affect the solution

for $K \neq 0$ in a very close neighborhood of the boundary and the solution in large part of the domain remains unchanged from the solution for $K = 0$. In fact, in the multiple scales analysis to be used in this work, the unperturbed equation turns out to be a second order PDE with the effect of the bending stiffness only appearing as a perturbation at the next order. Accordingly, for all practical purposes in this work, we will ignore the curvature boundary conditions and use the boundary conditions relevant to the ideal string only, i.e.,

$$\bar{y}(\gamma, \bar{\tau}) = \alpha\gamma(b - \gamma), \qquad \frac{\partial \bar{y}(\gamma, \bar{\tau})}{\partial \bar{x}} = \alpha(b - 2\gamma)\,, \quad \bar{y}(1, \bar{\tau}) = 0\,. \tag{21.7}$$

Note that, all the above quantities are nondimensional and γ is a function of time ($\bar{\tau}$) which makes the spatial domain dynamic. We use a scaling $x = \dfrac{\bar{x} - \gamma}{1 - \gamma}$ which makes the spatial domain from moving to fixed ($x \in [0, 1]$). We use $\bar{y}(\bar{x}, \bar{\tau}) = y(x, \tau)$, $\bar{\tau} = \tau$ and rewrite the above Eqs. (21.4) and (21.7) in the scaled domain to obtain

$$\frac{K}{(1-\gamma)^4}\frac{\partial^4 y}{\partial x^4} + \left[\frac{(x-1)^2\dot{\gamma}^2 - 1}{(1-\gamma)^2}\right]\frac{\partial^2 y}{\partial x^2} + \left[\frac{(x-1)}{(1-\gamma)}\left(\frac{2\dot{\gamma}^2}{(1-\gamma)} + \ddot{\gamma}\right)\right]\frac{\partial y}{\partial x} + \left[\frac{2(x-1)\dot{\gamma}}{(1-\gamma)}\right]\frac{\partial^2 y}{\partial x \partial \tau} + \frac{\partial^2 y}{\partial \tau^2} = 0, \tag{21.8}$$

$$\bar{y}(0, \bar{\tau}) = \alpha\gamma(b - \gamma), \qquad \frac{\partial \bar{y}(0, \bar{\tau})}{\partial \bar{x}} = \alpha(b - 2\gamma)(1 - \gamma)\,, \quad \bar{y}(1, \bar{\tau}) = 0, \tag{21.9}$$

where we drop all the explicit dependency of dependent variables for brevity.

21.3 Nonlinear Analysis Using Method of Multiple Scales

Equation (21.8) is a nonlinear equation where K is a small parameter. In order to analyze the system, we replace K by ϵk, where $0 < \epsilon \ll 1$ and introduce two time scales as $T_0 = t$ and $T_1 = \epsilon t$. We further assume

$$\gamma(t) = \gamma_{st} + \epsilon\gamma_1(T_0, T_1) + \epsilon^2\gamma_2(T_0, T_1) + O(\epsilon^3), \tag{21.10}$$

and

$$y(x, t) = y_{st}(x) + \epsilon y_1(x, T_0, T_1) + \epsilon^2 y_2(x, T_0, T_1) + O(\epsilon^3). \tag{21.11}$$

Substituting (21.10) and (21.11) along with $K = \epsilon k$ into (21.8) and applying the chain rule for differentiation, we get the following equations at different orders of ϵ:

$$O(1): \frac{d^2 y_{st}(x)}{dx^2} = 0, \tag{21.12}$$

$$O(\epsilon): \frac{k}{(1-\gamma_{st})^4}\frac{d^4 y_{st}(x)}{dx^4} + \frac{\partial^2 y_1(x,T_0,T_1)}{\partial T_0^2} - \frac{1}{(1-\gamma_{st})^2}\frac{\partial^2 y_1(x,T_0,T_1)}{\partial x^2} - \frac{(1-x)}{(1-\gamma_{st})}\frac{dy_{st}(x)}{dx}\frac{\partial \gamma_1(T_0,T_1)}{\partial T_0} - \frac{2\gamma_1}{(1-\gamma_{st})^3}\frac{d^2 y_{st}(x)}{dx^2} = 0, \tag{21.13}$$

$$\begin{aligned} O(\epsilon^2): \; & \frac{\partial^2 y_2(x,T_0,T_1)}{\partial T_0^2} - \frac{1}{(1-\gamma_{st})^2}\frac{\partial^2 y_2(x,T_0,T_1)}{\partial x^2} + \frac{k}{(1-\gamma_{st})^4}\frac{\partial^4 y_1(x,T_0,T_1)}{\partial x^4} \\ & - \frac{2\gamma_1(T_0,T_1)}{(1-\gamma_{st})^3}\frac{\partial^2 y_1(x,T_0,T_1)}{\partial x^2} - \frac{(1-x)}{(1-\gamma_{st})}\frac{\partial^2 \gamma_1(T_0,T_1)}{\partial T_0^2}\frac{\partial y_1(x,T_0,T_1)}{\partial x} \\ & - \frac{2(1-x)}{(1-\gamma_{st})}\frac{\partial \gamma_1(T_0,T_1)}{\partial T_0}\frac{\partial^2 y_1(x,T_0,T_1)}{\partial T_0 \partial x} + 2\frac{\partial^2 y_1(x,T_0,T_1)}{\partial T_0 \partial T_1} \\ & - \frac{\left(3\gamma_1^2(T_0,T_1) - 2\gamma_{st}\gamma_2(T_0,T_1) + 2\gamma_2(T_0,T_1)\right)}{(1-\gamma_{st})^4}\frac{\partial^2 y_{st}(x)}{\partial x^2} \\ & + \left[\frac{(1-x)^2}{(1-\gamma_{st})^2}\frac{\partial^2 y_{st}(x)}{\partial x^2} - \frac{2(1-x)}{(1-\gamma_{st})^2}\frac{\partial y_{st}(x)}{\partial x}\right]\left(\frac{\partial \gamma_1(T_0,T_1)}{\partial T_0}\right)^2 \\ & - \left[\frac{(1-x)\gamma_1(T_0,T_1)}{(1-\gamma_{st})^2}\frac{\partial y_{st}(x)}{\partial x} + \frac{2(1-x)}{(1-\gamma_{st})}\frac{\partial y_{st}(x)}{\partial x}\right]\frac{\partial^2 \gamma_1(T_0,T_1)}{\partial T_0 \partial T_1} \\ & - \frac{(1-x)}{(1-\gamma_{st})}\frac{\partial y_{st}(x)}{\partial x}\frac{\partial^2 \gamma_2(T_0,T_1)}{\partial T_0^2} + \frac{4k\gamma_1(T_0,T_1)}{(1-\gamma_{st})^5}\frac{d^4 y_{st}(x)}{dx^4} = 0. \end{aligned} \tag{21.14}$$

Similarly, from the boundary conditions (21.9), we obtain

$$y_{st}(0) = \alpha\gamma_{st}(b-\gamma_{st}), \tag{21.15}$$

$$y_1(0,T_0,T_1) = \alpha\gamma_1(T_0,T_1)(b-2\gamma_{st}), \tag{21.16}$$

$$y_2(0,T_0,T_1) = \alpha\gamma_2(T_0,T_1)(b-2\gamma_{st}) - \alpha\gamma_1^2(T_0,T_1), \tag{21.17}$$

$$\frac{dy_{st}(0)}{dx} = \alpha(b-2\gamma_{st})(1-\gamma_{st}), \tag{21.18}$$

$$\frac{\partial y_1(0,T_0,T_1)}{\partial x} = -\alpha\gamma_1(T_0,T_1)(2+b-4\gamma_{st}), \tag{21.19}$$

$$\frac{\partial y_2(0,T_0,T_1)}{\partial x} = 2\alpha\gamma_1^2(T_0,T_1) - \alpha\gamma_2(T_0,T_1)(2+b-4\gamma_{st}), \tag{21.20}$$

$$y_{st}(1) = 0, \quad y_1(1, T_0, T_1) = 0, \quad y_2(1, T_0, T_1) = 0\,. \tag{21.21}$$

The static solution for (21.13) satisfying the boundary conditions (21.15), (21.18) and (21.21) is obtained as

$$y_{st}(x) = \alpha\gamma_{st}(b - \gamma_{st})(1 - x)\,, \qquad \text{with} \quad \gamma_{st} = 1 - \sqrt{1 - b}\,. \tag{21.22}$$

We assume

$$y_1(x, T_0, T_1) = \alpha\gamma_1(T_0, T_1)(b - 2\gamma_{st})(1 - x) + f_1(x, T_0, T_1), \tag{21.23}$$

$$\text{and} \quad y_2(x, T_0, T_1) = \left(\alpha\gamma_2(T_0, T_1)(b - 2\gamma_{st}) - \alpha\gamma_1^2(T_0, T_1)\right)(1 - x) + f_2(x, T_0, T_1) \tag{21.24}$$

which satisfy boundary conditions (21.16), (21.17), and (21.21) with

$$f_i(0, T_0, T_1) = 0, \quad f_i(1, T_0, T_1) = 0\,, \quad \text{where} \quad i = 1, 2\,. \tag{21.25}$$

Now substituting (21.23) and (21.24) into (21.19) and (21.20), respectively, we obtain

$$\gamma_1(T_0, T_1) = -\frac{1}{2\alpha(1 - \gamma_{st})}\frac{\partial f_1(0, T_0, T_1)}{\partial x}, \tag{21.26}$$

$$\gamma_2(T_0, T_1) = -\frac{1}{2\alpha(1 - \gamma_{st})}\left(-\alpha\gamma_1^2(T_0, T_1) + \frac{\partial f_2(0, T_0, T_1)}{\partial x}\right). \tag{21.27}$$

Substituting (21.22), (21.23) and (21.26) into (21.13) and simplifying we get

$$\frac{\partial^2 f_1(x, T_0, T_1)}{\partial T_0^2} - \frac{1}{1 - b}\frac{\partial^2 f_1(x, T_0, T_1)}{\partial x^2} = 0. \tag{21.28}$$

Solution of (21.28) can be written as

$$f_1(x, T_0, T_1) = \sum_{m=1}^{N} f_{1m}(T_0, T_1)\sin(m\pi x), \tag{21.29}$$

where $f_{1m}(T_0, T_1) = A_m(T_1)\sin\left(\frac{n\pi T_0}{\sqrt{1-b}}\right) + B_m(T_1)\cos\left(\frac{n\pi T_0}{\sqrt{1-b}}\right)$ which satisfies (21.25). Substituting (21.22), (21.23), and (21.24) into (21.14) and following the procedure outlined in [8], we obtain the slow flow equations governing the evolution of $A_m(T_1)$ and $B_m(T_1)$ as

$$\frac{\partial A_m}{\partial T_1} = -\frac{m^3\pi^3 k B_m}{2(1-b)^{3/2}} + \frac{m\pi^2}{4\alpha(1-b)^{3/2}}\sum_{p=1}^{N} p(A_pA_m + B_pB_m)\delta_{p,2m}$$
$$+ \frac{\pi^3}{4m\alpha(1-b)^{3/2}}\sum_{n=1}^{N}\sum_{p=1}^{N} np^3(K_{4nm} - K_{3m})\left[(B_nB_p - A_nA_p)\delta_{n+p,m}\right.$$
$$\left. + (A_nA_p + B_nB_p)(\delta_{n-p,m} + \delta_{p-n,m})\right]$$
$$- \frac{\pi^3}{4m\alpha(1-b)^{3/2}}\sum_{n=1}^{N}\sum_{p=1}^{N} n^2p^2(2K_{4nm} - K_{3m})\left[(A_nA_p - B_nB_p)\delta_{n+p,m}\right.$$
$$\left. + (A_nA_p + B_nB_p)(\delta_{n-p,m} + \delta_{p-n,m})\right], \tag{21.30}$$

$$\frac{\partial B_m}{\partial T_1} = \frac{m^3\pi^3 k A_m}{2(1-b)^{3/2}} + \frac{m\pi^2}{4\alpha(1-b)^{3/2}}\sum_{p=1}^{N} p(A_mB_p - A_pB_m)\delta_{p,2m}$$
$$- \frac{\pi^3}{4m\alpha(1-b)^{3/2}}\sum_{n=1}^{N}\sum_{p=1}^{N} np^3(K_{4nm} - K_{3m})\left[(A_pB_n + A_nB_p)\delta_{n+p,m}\right.$$
$$\left. + (A_nB_p - B_nA_p)(\delta_{n-p,m} - \delta_{p-n,m})\right]$$
$$- \frac{\pi^3}{4m\alpha(1-b)^{3/2}}\sum_{n=1}^{N}\sum_{p=1}^{N} n^2p^2(2K_{4nm} - K_{3m})\left[(A_pB_n + A_nB_p)\delta_{n+p,m}\right.$$
$$\left. + (A_pB_n - A_nB_p)(\delta_{n-p,m} - \delta_{p-n,m})\right], \tag{21.31}$$

where $\delta_{n,m} = 1$ if $m = n$ and 0 otherwise, and K_{3m} and K_{4nm} are defined as

$$K_{3m} = \int_0^1 (1-x)\sin(m\pi x)dx = \frac{1}{m\pi},$$
$$K_{4nm} = \int_0^1 (1-x)\cos(n\pi x)\sin(m\pi x)dx = \begin{cases} \dfrac{1}{4m\pi} & \text{if } n = m, \\ \dfrac{m}{(m^2-n^2)\pi} & \text{if } n \neq m. \end{cases}$$

For convenience of further development, we write $A_m(T_1)$ and $B_m(T_1)$ in polar coordinates as

$$A_m(T_1) = R_m(T_1)\cos\left(\phi_m(T_1)\right), \quad \text{and} \quad B_m(T_1) = R_m(T_1)\sin\left(\phi_m(T_1)\right). \tag{21.32}$$

Also noting that our system is autonomous and hence, the relative phases are more important than the individual phases, we introduce the relative phases $\theta_q = (q+1)\phi_1 - \phi_{q+1}$ and obtain slow flow equations in terms of R_m and θ_q. These slow flow equations are

$$\begin{aligned}\frac{\partial R_m}{\partial T_1} &= \frac{m\pi^2}{4\alpha(1-b)^{3/2}}\sum_{p=1}^{N} pR_mR_p\cos(\theta_{2m-1}-2\theta_{m-1})\delta_{p,2m}\\ &-\frac{\pi^3}{4m\alpha(1-b)^{3/2}}\sum_{n=1}^{N}\sum_{p=1}^{N} np^3(K_{4nm}-K_{3m})R_nR_p\left[\cos(\theta_{m-1}-\theta_{p-1}-\theta_{n-1})\delta_{n+p,m}\right.\\ &\left.-\cos(\theta_{m-1}-\theta_{p-1}+\theta_{n-1})\delta_{n-p,m}-\cos(\theta_{p-1}-\theta_{n-1}-\theta_{m-1})\delta_{p-n,m}\right]\\ &-\frac{\pi^3}{4m\alpha(1-b)^{3/2}}\sum_{n=1}^{N}\sum_{p=1}^{N} n^2p^2(2K_{4nm}-K_{3m})R_nR_p\left[\cos(\theta_{m-1}-\theta_{p-1}-\theta_{n-1})\delta_{n+p,m}\right.\\ &\left.+\cos(\theta_{m-1}-\theta_{p-1}+\theta_{n-1})\delta_{n-p,m}+\cos(\theta_{p-1}-\theta_{n-1}-\theta_{m-1})\delta_{p-n,m}\right], \qquad (21.33)\end{aligned}$$

$$\begin{aligned}\frac{\partial\theta_q}{\partial T_1} &= -\frac{q(q+1)(q+2)\pi^3k}{2(1-b)^{3/2}}-\frac{(q+1)\pi^2}{4\alpha(1-b)^{3/2}}\left[2R_2\sin(\theta_1)-\sum_{p=1}^{N}pR_p\sin(\theta_{2q+1}-2\theta_q)\delta_{p,2(q+1)}\right]\\ &-\sum_{n=1}^{N}\sum_{p=1}^{N}\frac{(q+1)\pi^3np^3(K_{4n1}-K_{31})R_nR_p}{4\alpha(1-b)^{3/2}R_1}\left[\sin(\theta_{p-1}-\theta_{n-1})\delta_{p-n,1}-\sin(\theta_{p-1}-\theta_{n-1})\delta_{n-p,1}\right]\\ &-\sum_{n=1}^{N}\sum_{p=1}^{N}\frac{(q+1)\pi^3n^2p^2(2K_{4n1}-K_{31})R_nR_p}{4\alpha(1-b)^{3/2}R_1}\left[\sin(\theta_{p-1}-\theta_{n-1})\delta_{n-p,1}-\sin(\theta_{p-1}-\theta_{n-1})\delta_{p-n,1}\right]\\ &+\sum_{n=1}^{N}\sum_{p=1}^{N}\frac{\pi^3np^3(K_{4n(q+1)}-K_{3(q+1)})R_nR_p}{4(q+1)\alpha(1-b)^{3/2}R_{(q+1)}}\left[\sin(\theta_q-\theta_{p-1}-\theta_{n-1})\delta_{n+p,q+1}\right.\\ &\left.-\sin(\theta_q-\theta_{n-1}+\theta_{p-1})\delta_{n-p,q+1}+\sin(\theta_{p-1}-\theta_{n-1}-\theta_q)\delta_{p-n,q+1}\right]\\ &+\sum_{n=1}^{N}\sum_{p=1}^{N}\frac{\pi^3n^2p^2(2K_{4n(q+1)}-K_{3(q+1)})R_nR_p}{4(q+1)\alpha(1-b)^{3/2}R_{(q+1)}}\left[\sin(\theta_q-\theta_{p-1}-\theta_{n-1})\delta_{n+p,q+1}\right.\\ &\left.+\sin(\theta_q-\theta_{n-1}+\theta_{p-1})\delta_{n-p,q+1}-\sin(\theta_{p-1}-\theta_{n-1}-\theta_q)\delta_{p-n,q+1}\right], \qquad (21.34)\end{aligned}$$

where $m = 1, 2, \ldots, N$, $q = 1, 2, \ldots, N-1$ and $\theta_0 = 0$.

Equation (21.33) governs the evolution of the amplitudes of the various modes while Eq. (21.34) represents the dynamic departure of the higher mode frequencies from the integral multiple of the fundamental frequency. The first term in Eq. (21.34) is the inharmonicity introduced due to the bending stiffness whereas the remaining terms represent the inharmonicity introduced due to the quadratic modal interactions facilitated by the wrapping nonlinearity. The fixed points of Eqs. (21.33) and (21.34) represent periodic solutions of the system where the various modal frequencies are exact harmonics of the fundamental frequency. Such periodic solutions are referred as 'mode-locked periodic solutions'. There are infinitely many of these solutions each with a different overall energy content depending on the initial energy supplied to the system. However, if we fix the modal amplitude of one of the modes, say the first mode, there are finitely many of these periodic solutions that can exist. It is these finitely many mode-locked solutions and their characteristics that we discuss in the next section.

21.4 Mode Locked Periodic Solutions

The slow flow equations for 2 modes ($N = 2$) are:

$$\frac{\partial R_1}{\partial T_1} = \frac{\pi^2 R_1 R_2 \cos\theta_1}{2\alpha(1-b)^{3/2}}, \tag{21.35}$$

$$\frac{\partial R_2}{\partial T_1} = -\frac{\pi^2 R_1^2 \cos\theta_1}{8\alpha(1-b)^{3/2}}, \tag{21.36}$$

$$\frac{\partial \theta_1}{\partial T_1} = \frac{\pi^2}{\alpha(1-b)^{3/2}}\left[\pi k - R_2 \sin\theta_1 + \frac{R_1^2 \sin\theta_1}{8R_2}\right], \tag{21.37}$$

The condition for periodic solution turns out to be $\cos\theta_1 = 0$ which implies $\theta_1 = \frac{(2n+1)\pi}{2}$. Accordingly, there are two possibilities for the relationship between R_1 and R_2 corresponding to the mode-locked solution. The number of such possible solutions increases with an increase in the number of modes and the relationship becomes non-trivial. Accordingly, we will only report numerical results with the parameters $b = 0.05$, $\alpha = \frac{4}{b^2}$ and $k = 0.5 \times 10^{-6}$, and the first modal amplitude fixed to $R_1 = 0.1$. In Tables 21.1 and 21.2, we present the modal amplitudes and their stability properties for the various possible mode-locked periodic solutions for $N = 2$ and $N = 3$ modes, respectively. It can be seen from Table 21.1 that there are two neutrally stable mode-locked periodic solutions. Accordingly any arbitrary initial condition will result in a modulated response around this mode-locked state which accounts for the amplitude and frequency modulations. It can be seen from Table 21.2 that the number of possible mode-locked states increases to 5 with 3 of them being neutrally stable while 2 are unstable. The number of purely imaginary eigenvalues associated with a mode-locked state increases with an increase in the number of modes. We have verified that there is convergence in the amplitudes corresponding to the mode-locked solution with increasing N. There is also some convergence in the smallest purely imaginary eigenvalue associated with this mode-locked state. However, since an extra purely imaginary eigenvalue gets added with an increase in the considered mode by 1, convergence cannot be strictly established for the eigenvalues associated with these mode-locked states. A significant number

Table 21.1 Fixed points and corresponding eigenvalues for $k = 0.5 \times 10^{-6}$, $N = 2$

S. No.	Fixed points		Eigenvalues
	R_1	R_2	
1.	0.1	0.039325	0, $\pm i$ 0.000394
2.	0.1	0.031785	0, $\pm i$ 0.000423

Table 21.2 Fixed points and corresponding eigenvalues for $k = 0.5 \times 10^{-6}$, $N = 3$

S. No.	Fixed points			Eigenvalues
	R_1	R_2	R_3	
1.	0.1	0.008229	0.017052	$0, \pm i\ 0.000560, \pm i\ 0.000362$
2.	0.1	0.038348	0.016505	$0, \pm i\ 0.000478, \pm i\ 0.001044$
3.	0.1	0.044511	0.025425	$0, \pm i\ 0.000509, \pm i\ 0.000927$
4.	0.1	0.065971	0.046877	$0, \pm i\ 0.000971, \pm 0.000444$
5.	0.1	0.067798	0.061334	$0, \pm i\ 0.000954, \pm 0.000554$

Table 21.3 A neutrally stable fixed point with an increasing number of modes

N	Fixed points
	$R_1,\ R_2,\ \ldots,\ R_N$
2	0.1, 0.039325
3	0.1, 0.044511, 0.025425
4	0.1, 0.046417, 0.028602, 0.019603
5	0.1, 0.047235, 0.029965, 0.021505, 0.016508
6	0.1, 0.047601, 0.030577, 0.022353, 0.017630, 0.014652
7	0.1, 0.047748, 0.030832, 0.022711, 0.018100, 0.015258, 0.013465
8	0.1, 0.047773, 0.030898, 0.022819, 0.018249, 0.015450, 0.013701, 0.012685

of purely imaginary eigenvalues for the mode-locked state explains the complex modulations observed both in the modal amplitudes and frequencies in the nominally harmonic sound of these musical instruments.

The total number of possible solutions increases exponentially with an increase in N. However, there is always a neutrally stable solution around the original solutions given in Table 21.1 and the evolution of one of them with an increase in the number of modes is presented in Table 21.3 and represented graphically in Fig. 21.3 wherein we have plotted the amplitude ratios of the modal coordinates $\left(\frac{R_n}{R_1}\right)$ for $n = 2, 3, 4, 5, 6$. It can be seen from Fig. 21.3 that the relative amplitudes $\left(\frac{R_n}{R_1}\right)$ are converging to $\frac{1}{n}$ (shown with the dashed line) with an increase in the number of modes N. A comparison of Table 21.3 with a similar table for $k = 0$ reported in [8] reveals that this neutrally stable solution is converging faster to the limiting value of $\frac{R_n}{R_1} = \frac{1}{n}$ with a non-zero bending stiffness k. As discussed in [8], this mode-locked solution corresponds to the state of equipartition of energy among the various vibrational modes of the string. Since there are other neutrally stable solutions possible for our system, we finally numerically verify that a general plucked initial condition which is given while playing these musical instruments in fact results in modulated

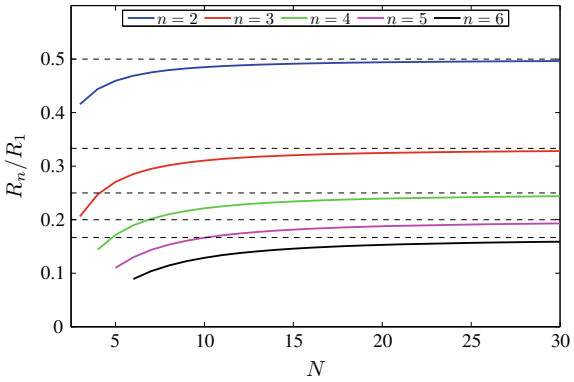

Fig. 21.3 Convergence of the relative amplitudes. The dotted lines correspond to $\frac{1}{n}$

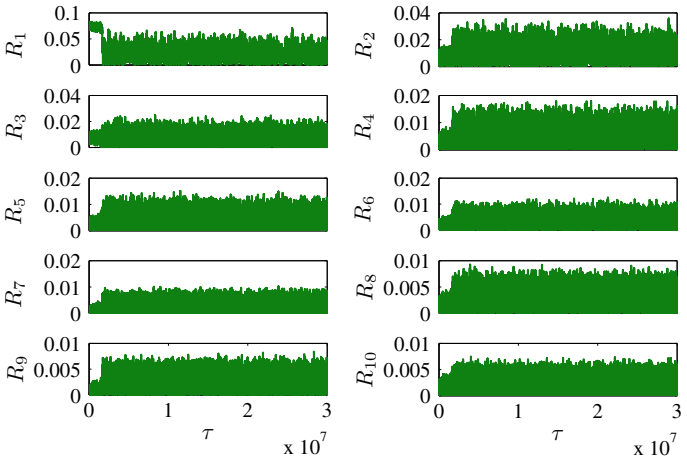

Fig. 21.4 Amplitude plot corresponding to the plucking of the string at half the length. For the exact initial condition, kindly refer to [8]

response around this equipartition state. This is shown in Fig. 21.4 for plucking at the center of the string and it can be seen that the initial characteristics of the solution differ from the final one and the mean value of the solution from the final phase indeed satisfies the condition of equipartition of energy.

21.5 Conclusion

In this work, we have investigated the possibility of phase locked solutions for stiff strings vibrating against obstacles. Method of multiple scales is used to obtain the slowly varying amplitude and relative phase equations. We observe that the system has finitely many mode-locked periodic solutions with a fixed amplitude of the first mode, some of which are neutrally stable. Neutral stability of these solutions explains the amplitude and frequency modulations observed in the musical instruments with finite curved bridge at one end. One such neutrally stable solution tends to a state of equipartition of energy among the various modes with an increase in the number of modes. Numerical simulations with initial conditions corresponding to plucking the string shows that the equipartition energy state is preferred at steady state. Hence, higher modes of the string also become prominent in the sound of musical instruments with a finite curved bridge like sitar and veena.

References

1. Deva, B.C.: Musical Instruments of India: Their History and Development, 2nd edn. Munshiram Manoharlal, New Delhi (1987)
2. Raman, C.V.: On some Indian stringed instruments. Proc. Indian Assoc. Cultiv. Sci. **7**, 29–33 (1921)
3. Burridge, R., Kappraff, J., Morshedi, C.: The sitar string, a vibrating string with a one sided inelastic constraint. SIAM J. Appl. Math. **42**(6), 1231–1251 (1982)
4. Taguti, T.: Dynamics of simple string subject to unilateral constraint: a model analysis of sawari mechanism: acous. Sci. Tech. **29**(3), 203–214 (2008)
5. Vyasarayani, C.P., Birkett, S., McPhee, J.: Modeling the dynamics of a vibrating string with finite distributed unilateral constraint: application to the sitar. J. Acous. Soc. Am. **125**(6), 3673–3682 (2009)
6. Alsahlani, A., Mukherjee, R.: Vibration of a string wrapping and unwrapping around an obstacle. J. Sound Vib. **329**, 2707–2715 (2010)
7. Mandal, A.K., Wahi, P.: Natural frequencies, mode shapes and modal interactions for strings vibrating against an obstacle: relevance to sitar and veena. J. Sound Vib. **338**, 42–59 (2015)
8. Mandal A.K.: Vibration characteristics of strings in the presence of a smooth curved boundary obstacle: relevance to stringed musical instruments. Ph.D. thesis, IIT Kanpur (2016)
9. Mandal, A.K., Wahi, P.: Mode-locking and improved harmonicity for real strings vibrating in the presence of a curved obstacle. Nonlinear Dyn. **88**(3), 2203–2224 (2017)
10. Benade A.H., Messenger W.G.: Sitar spectrum properties. In: The 103rd Meeting of Acoustical Society of America, Chicago, Illinois; Abstract available at J. Acous. Soc. Am. **71**(S1), S83–S83 (1982)
11. Donkin, W.F.: Acoustics. Clarendon Press, Oxford (1870)
12. Rayleigh, J.W.S.: The Theory of Sound. Macmillan and Co. London (1877)

Chapter 22
FEM with Floquet Theory for Non-slender Elastic Columns Subject to Harmonic Applied Axial Force Using 2D and 3D Solid Elements

Eoin Clerkin and Markus Rieken

Abstract The Rayleigh–Ritz formulation of finite element method using solid elements is implemented for a 2D and 3D clamped-clamped column which is subject to a periodically applied axial force. Non-linear strain is considered. A mass element matrix and two stiffness matrices are obtained. After assembly by elements, the calculated natural frequencies and buckling loads are compared to Euler–Bernoulli beam theory predictions. For 2D triangular and 3D cuboid elements, a large number of degrees of freedom are required for sufficient convergence which adds particular computational costs to applying Floquet theory to determine stability of the harmonically forced column. A method popularised by Hsu et al. is used to reduce the computational load and obtain the full monodromy matrix. The Floquet multipliers are discussed in relation to their bifurcations. The versatile 2D and 3D elements used allows for the discussion of non-slender columns. In addition, the stability of a 3D steel column comprised of impure materials or with changed aspect ratio are investigated.

Keywords Column · Time periodic · Finite element method · Rayleigh–Ritz · Floquet theory · Hsu method

22.1 Introduction

The finite element method (FEM) is an ubiquitous and versatile tool developed by engineers to solve partial differential equations for complex composite materials across varied geometries and boundary conditions [32]. Modelling of elastostatic structures is important throughout structural engineering as a first step in the design and optimisation of a new bridge, automobile, skyscraper, aircraft, or

E. Clerkin (✉) · M. Rieken
Dynamics and Vibration Group, FNB, Faculty of Mechanical Engineering,
Technische Universität Darmstadt, Dolivostraße 15, 64293 Darmstadt, Germany
e-mail: eoin@clerkin.biz
URL: http://www.eoin.clerkin.biz

S. Gutschmidt et al. (eds.), *IUTAM Symposium on Recent Advances in Moving Boundary Problems in Mechanics*, IUTAM Bookseries 34,
https://doi.org/10.1007/978-3-030-13720-5_22

ship. Determining stability of the structure, i.e. renitent to minute perturbation of its material, is achieved using the well-known complex eigenvalue analysis (CEA) which is efficiently implemented in commercially-available FEM software suites. However, for some problems in engineering, e.g. involving asymmetric rotors with anisotropic support in a fixed-frame coordinate system [21, 22] or structures subject to periodic loads [9, 37] as is studied in this manuscript, time-periodicity must arise in the equations of motion (EQM) making the CEA as a method of stability-determination mathematically invalid. Misleadingly, some instabilities are still correctly detected by CEA while others in the plane of oscillation are missed. Stability of time-periodic linear differential equations may be reliably determined using Floquet theory (FT) [10, 36]. However, significant computational and numerical difficulties occur as the degrees of freedom (DOF) of the problem grows. Implications of periodic dynamics on node definition and meshing in elastodynamic structures, as well as possible incompatibility with several time-saving approaches adopted in FEM software means that commercial solutions are not currently available.

A column subjected to harmonically applied axial force is a paradigmatic example of an elastostatic structure with time-periodic parameter excitation [5, 8]. Under minor simplifications, particularly slenderness for this study, the long established Euler–Bernoulli beam theory (EBBT) provides useful analytical benchmarks. For a constant applied force P_0, an expression for the critical load at which buckling in the column occurs, known as the *Euler buckling load*, may be easily obtained from EBBT. Barsoum et al. [2] studied the buckling problem under various boundary conditions using a FEM. For a column harmonically forced with frequency Ω and amplitude P_1, perturbation methods [15, 38] have yielded stability boundaries. Iwatsubo et al. [19] studied vibrations and stability of columns under periodic load, while later in Ref. [18], they used a finite difference method to theoretically predict stability boundaries validated by experiment. They categorised four types of resonances and studied their stability behaviour by discretization of the EBBT under four different boundary condition scenarios in [20]. Hsu et al. [17] outlined a method to numerically calculate stability more efficiently which is used extensively in this manuscript. Friedman et al. [11] built upon this method to study a clamped-clamped column under periodic axial load (cf. Fig. 22.1a) using the FEM with 1D beam elements. Beam elements are the 1D finite element schematically drawn in Fig. 22.1b, which have two nodes each with a single translational and bending moment. Due to the well developed EBBT and the small computational cost when using beam elements, many authors [5, 7, 11, 26–28, 33] have studied the harmonically forced column (cf. Fig. 22.1a) as a paradigmatic example of the FEM with FT. Using only a handful ($<<10$) of beam elements, the critical stability boundaries and the first three eigenfrequencies all show a remarkable agreement with analytic results obtained from theory and experiment [7, 18]. However, to make a genuine use of the power of the FEM, the technique must be able to efficiently determine stability using a versatile non-germane finite element as the degrees of freedom (DOF) of the system significantly increases. In this work, the stability of non-slender columns (cf. Fig. 22.1c) are investigated using the Rayleigh–Ritz formulation of the FEM using 2D triangular (cf. Fig. 22.1d) and 3D cuboid (cf. Fig. 22.1e) linear elements. The nonlinear phenomenon of buckling therefore requires

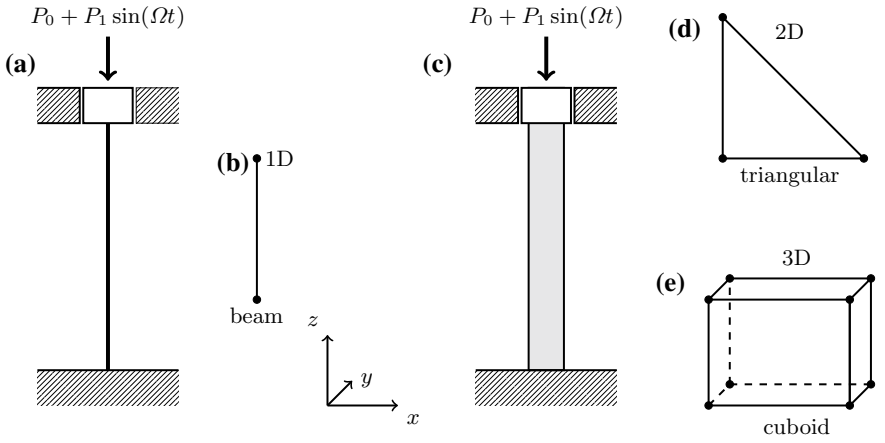

Fig. 22.1 Column under constant and periodic axial load; **a** slender, and **c** non-slender. A classical 1D beam element is shown in **b**, 2D and 3D solid elements are shown in **d** and **e**

a nonlinear strain approach. Thousands of DOF are needed for sufficient convergence which introduces significant computational cost which needs to be overcome. The added versatility of using these solid elements allows the investigation of alternative column configurations.

In Sect. 22.3, implementation of the Rayleigh–Ritz formulation of the FEM using 2D triangular elements for an elastic column under load is outlined. Steps to adapt the method for the 3D cuboid elements are discussed subsequently in Sect. 22.3.1. Equations of motion in the form of a system of second order ordinary differential equations with time-periodic coefficients are obtained. In Sect. 22.4, Floquet theory for stability determination is briefly introduced along with the numerical algorithm for obtaining the monodromy matrix in this work. The computation load needed for modelling an elastic column with the FEM using solid elements is addressed in Sect. 22.5. In particular, the number of elements for sufficient convergence and a timing test using different methods for calculation of Floquet multipliers is discussed. But first, in Sect. 22.2, the results of the stability determination of a 2D and 3D non-slender elastic column in various material configuration under periodic applied load is presented.

22.2 Stability of a Non-slender Harmonically-forced Column

The use of versatile 2D and 3D solid elements used in this manuscript allows the investigation of stability of non-slender columns with more complex configurations than permissible using 1D beam elements. In order to study the stability of a generic elastic

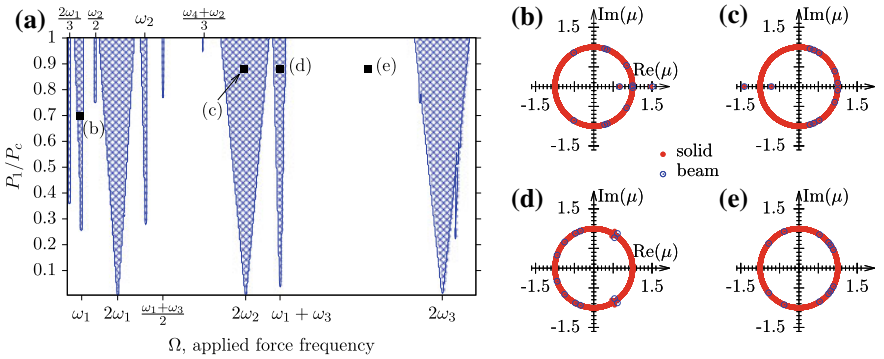

Fig. 22.2 **a** Stability map for $P_0 = 0$ as P_1 and Ω are varied. Regions of instability of the zero solution are shown in blue. "ω_i" denotes the ith natural frequency. Diagrams **b–e** show the Floquet multipliers μ at various points of Fig. 22.2 a calculated for beam and solid 2D triangular elements. Due to a large number of degrees of freedom, the red points join together to form a solid unit circle

industrially-relevant material, the following parameter values consistent with a steel column (Young's modulus $E = 2.1 \times 10^{11}$ Pa, density $\rho = 7850\,\text{kg m}^{-3}$, Poisson's ratio $\nu = 0.3$) of length $l = 1\,\text{m}$ of width $l_x = 0.05\,\text{m}$ and of breadth $l_y = 0.05\,\text{m}$, which equates to a cross-sectional area $A = 0.0025\ \text{m}^2$ and a moment of inertia $I = \left(l_y l_x^3/12\right) = 5.208 \times 10^{-7}\ \text{m}^4$, were chosen. These values were used to generate all graphs and diagrams of this section unless otherwise stated in its caption. EBBT (see e.g. Ref. [14]) was used to estimate the first $\omega_1 = 1670$ Hz, second $\omega_2 = 4604$ Hz, third $\omega_3 = 9026$ Hz and fourth $\omega_4 = 1492$ Hz natural frequency. These natural frequency values are labelled as an interpretive reference throughout the figures of this section. However, some caution needs to be attached as the approximation of EBBT is not very accurate to the true natural frequencies for a non-slender column calculated by experiment or here by elastic theory.

In Fig. 22.2a, a stability diagram for a harmonically forced steel column is obtained for different forcing amplitude and frequency. The forcing strength, shown on the vertical axes is normalised over the EBBT calculated static Euler buckling load P_c, whilst frequencies denoting the EBBT calculated first, second and third harmonics, their doubles and combinations are shown at the top and bottom horizontal axes. Areas in white have stable combinations of forcing strength and frequency. The subplot, Fig. 22.2e, shows the Floquet multipliers, μ calculated at the position marked with a solid black square and labelled (e). It shows the Floquet multipliers as calculated via beam elements in open black circles and 2D solid triangular elements as closed red circles. The red circles, due to their large quantity, have merged together to form a solid red line. As may be seen, all multipliers lie on the unit circle in the complex plane and therefore the system is determined to be marginally stable according to FT [36]. The areas of Fig. 22.2a in blue with a fishnet pattern denote unstable parameter combinations (P_1, Ω). Each area has a similar "V" shape, which is wider at the top and extends down and ends in a tip. Although in this figure, only the instabilities

regions with the widest frequency range at the static critical load ($P_1 = P_c$) extend all the way to zero forcing strength, this is a sampling error anomaly in the diagram. All blue regions irrespective of thickness would extend to zero forcing strength if the diagram could be made with high enough resolution. Although this could mean that a steel column would be highly susceptible to instabilities from the slightest external force applied at these discrete frequencies [4], in reality, if damping were considered for the production of this figure, each unstable frequency would be tapered off at a finite non-zero level, thus making the column robust to "small" periodic loads.

One class of instability region extends to the natural harmonics $\omega_1, \omega_2, \omega_3$ of the column. The point labelled (b) is contained in the ω_1 instability region and is a characteristic example. As may be seen in Fig. 22.2b, a pair of Floquet multipliers has left the unit circle and is positioned on the real axis $\mathrm{Im}(\mu) = 0$. As one of the Floquet multipliers has an absolute value greater than "1", the system is determined to be unstable via FT [36]. Although in a generic sense, the loss of stability would be consistent with a fold bifurcation of limit cycles, due to presence of the left/right symmetry in the column, we may deduce that this is a pitchfork of limit cycles bifurcation [35]. The pitchfork bifurcation is synonymous with buckling. The widest of the blue instabilities are labelled at double the natural frequencies. As an example, the point labelled (c) is contained in the $2\omega_2$ instability region. Fig. 22.2c shows its Floquet multipliers. Similar to the point discussed before, a pair of Floquet multipliers are no longer on the unit circle and are on the real axis, $\mathrm{Im}(\mu) = 0$. However, this time the bifurcation which caused a loss of stability has occurred near "-1" which is consistent with with a period-doubling bifurcation. We may deduce that the cyclic states must be of fixed type with respect to the symmetry [23, 31]. In the blue instability region, the solution with the column oscillating vertically at the driving frequency is not stable. For unstable parameter values near the period-doubling bifurcation line, new periodic solutions exist and are stable whereby the column would oscillate at twice or half the supplied frequency [13]. The last blue instability region which we will discuss occurs at the linear combinations of the natural frequencies. The point label (d) is contained in the $\omega_1 + \omega_3$ instability region. In this case a double pair of Floquet multipliers (four) has left the unit circle with non-zero imaginary part ($\mathrm{Im}(\mu) \neq 0$) with two of the Floquet multipliers having an absolute value greater than "1". If these frequencies were incommensurate with the driving frequency, a torus bifurcation and resultant quasi-periodic motion would be expected [13]. However, as they instead occur at discrete multiples, periodic behaviour is maintained and these are well known in the applied mechanics literature as combination resonances [1, 9, 34].

In Fig. 22.3, the maximal Floquet multiplier, which is the eigenvalue of the monodromy matrix of largest absolute value, for a 3D column calculated with cuboid elements for a range of forcing frequency is plotted. Using Floquet theory, a system is determined to be unstable when one of the eigenvalues of its monodromy matrix is greater than one [36]. The force amplitude is fixed at $P_1 = 0.5P_c$ and the force frequency is varied. These diagrams may be compared with the centre line of Fig. 22.2a. For large intervals of the frequency Ω in Fig. 22.3a–c, the maximal Floquet multiplier is exactly one and therefore the system is considered to be marginally stable

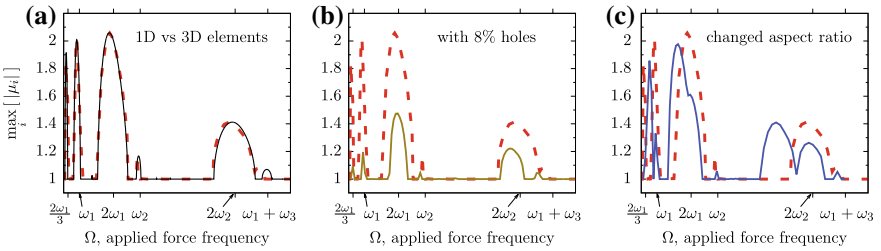

Fig. 22.3 For $P_1 = 0.5P_c$, the maximal Floquet multiplier is plotted against the frequency of the applied force for 3D elements under different scenarios. **a** Black solid line is Floquet multipliers for 1D beam elements and red dashed line are for 3D cuboid elements. **b** 8% of the elements are random removed for the brown solid line. **c** Aspect ratio is changed so that the width and breadth of the 3D column differs, i.e. $l_y = 0.04$ m for the blue solid line

meaning that a small perturbation does not grow as the system evolves through one complete cycle. However, several humps of larger than one values are seen around discrete frequency values. As a Floquet multiplier is greater than one, the 3D column is unstable at these forcing frequencies. Fig. 22.3a compares the maximal Floquet multipliers calculated using beam elements for a 1D column (thin solid black line) and cuboid elements for a 3D column (thick red dashed line). The two curves match almost identically, except at the $\omega_1 + \omega_3$ combination resonance instability where the unstable interval occurs at a slightly lower frequency for 3D elements than the 1D elements. The extra dimension in the case of the 3D column allows us to investigate how the stability of the column is affected by alternate column configurations. In Fig. 22.3b, a column with an impure steel material is modelled via randomly removing 8% of the 3D elements (brown solid line). The frequency of instability is slightly shifted to a lower frequency which would be consistent with the stiffness of the column being reduced. Furthermore, the magnitude and interval length of the instability for each of the unstable frequency intervals are diminished. It may be therefore argued that the robustness of the column against frequency-induced instabilities has been increased by reducing the purity of the material. In Fig. 22.3c, the aspect ratio of the 3D column has been changed to 5 : 4 meaning its breadth is 20% less than its width. As may be seen, the instability intervals have been split into one matching the harmonically induced buckling in the breadth direction and one in the width direction. However, the interval of instabilities has been greatly increased and so it may be inferred that a column of unequal aspect ratio is considerably less stable. This concludes our discussion on the stability of a non-slender, an impure and with a non-symmetric aspect ratio 3D steel column.

22.3 Rayleigh–Ritz Formulation of the FEM for a Column under load

For the sake of brevity of notation, the main steps for obtaining the EQM is outlined in this section for a harmonically loaded column using 2D triangular elements. Relatively straight forward adaption for the 3D hexahedral element will be discussed subsequently. In order to apply the Rayleigh–Ritz formalisation of the FEM, expressions for energies of the system must be obtained. A standard kinetic energy $\mathcal{T}(t)$ over an element, written in integral form is

$$\mathcal{T}^{(e)}(t) = \frac{1}{2}\int\int_{V^{(e)}} \rho \left[\dot{u}(x,y,t),\ \dot{v}(x,y,t)\right] \begin{bmatrix}\dot{u}(x,y,t)\\ \dot{v}(x,y,t)\end{bmatrix} \mathrm{d}x\,\mathrm{d}y \tag{22.1}$$

where ρ is the mass per unit area, and $V^{(e)}$ is the area of an element. $u(x,y,t)$ and $v(x,y,t)$ are the spatial- and time-varying components of the displacement vector field in the x and y direction respectively. The overscript dot represents differentiation with respect to time, t. Using a Ritz representation, spatial and temporal contributions may be separated

$$[u(x,y,t), v(x,y,t)]^{\mathrm{T}} = \mathbf{N}(x,y)\,\vec{q}(t) \tag{22.2}$$

where $\vec{q}(t)$ is a vector of nodal temporal displacements and $\mathbf{N}(x,y)$ is a matrix of shape functions. As schematically drawn in Fig. 22.1d, the 2D triangular element has a node at each of its three vertices. The simple linear shape function used in this work is

$$N_i(x,y) = \alpha_i + \beta_i x + \gamma_i y \quad \text{for} \quad i = 1,2,3$$

which means that $\mathbf{N}$ is a 6×2 matrix and $\vec{q}$ is a vector of size 6 for the temporal displacements, one for each spatial direction for each node in an element. Useful integration formulas available in Ref. [39] reduce the need to integrate the integral of Eq. (22.1) computationally for 2D elements. We may write the kinetic energy in matrix form as

$$\mathcal{T}^{(e)}(t) = \dot{\vec{q}}^{\mathrm{T}}(t) \int\int_{V^{(e)}} \rho\,\mathbf{N}^{\mathrm{T}}\mathbf{N}\ \mathrm{d}x\,\mathrm{d}y\ \dot{\vec{q}}(t) = \dot{\vec{q}}^{\mathrm{T}}(t) \underbrace{\frac{\rho A h}{12}\begin{pmatrix} 2&0&1&0&1&0\\ 0&2&0&1&0&1\\ 1&0&2&0&1&0\\ 0&1&0&2&0&1\\ 1&0&1&0&2&0\\ 0&1&0&1&0&2 \end{pmatrix}}_{\mathbf{M}^{(e)}} \dot{\vec{q}}(t) \tag{22.3}$$

Using elastic theory [25], the internal potential energy within the material of the column due to stresses and strains may be written as

$$\mathcal{V}^{(e)} = \frac{1}{2}\int\int_{V^{(e)}} \boldsymbol{\epsilon}^{\mathrm{T}}\boldsymbol{\sigma}\ \mathrm{d}x\,\mathrm{d}y \tag{22.4}$$

as an integral of the product of the strain $\boldsymbol{\epsilon}$ and stress $\boldsymbol{\sigma}$ tensors over the area of the element. Stresses within the column due to the innate material $\boldsymbol{\sigma}_0$ and the external force $\boldsymbol{\sigma}_1$ are treated separately.

$$\boldsymbol{\sigma} = \boldsymbol{\sigma}_0 + \boldsymbol{\sigma}_1 \tag{22.5}$$

Assuming plane stress, stresses are related to the corresponding strains within the material by the matrix $\mathbf{C}$ via

$$\boldsymbol{\sigma}_0 = \mathbf{C}\,\boldsymbol{\epsilon} \quad \text{with} \quad \mathbf{C} = \frac{E}{1-\nu^2}\begin{pmatrix} 1 & \nu & 0 \\ \nu & 1 & 0 \\ 0 & 0 & \frac{1-\nu}{2} \end{pmatrix} \tag{22.6}$$

where E is Young's modulus of elasticity and ν is Poisson's ratio. For more information on the material matrix, one may consult Ref. [25]. In order to apply an external force in as simple a fashion as possible, uniaxial stress is assumed, i.e. the strain in the vertical y direction is modulated with the harmonic function $p(t)$ across its cross-sectional area.

$$\boldsymbol{\sigma}_1 = \begin{bmatrix} 0 \\ \frac{p(t)}{A} \\ 0 \end{bmatrix} \tag{22.7}$$

It should be noted that this simplification suffices as our aim is to determine the stability of the undeformed column. However if one wished to model the stability of a buckled state, which exists in the instability regions of Fig. 22.2, the stress would at least need to vary over its cross sectional area to account for the inner and outer side of the bend being under compression and tensile stress respectively. To incorporate the nonlinear phenomenon of buckling using linear shape functions, a nonlinear strain approach is warranted. Reference [29] is followed

$$\boldsymbol{\epsilon} = \overbrace{\begin{bmatrix} \left[\frac{\partial u}{\partial x}\right] \\ \left[\frac{\partial v}{\partial y}\right] \\ \left[\frac{\partial u}{\partial y} + \frac{\partial v}{\partial x}\right] \end{bmatrix}}^{\text{Cauchy strain}} + \overbrace{\begin{bmatrix} \left[\frac{1}{2}\left[\left(\frac{\partial u}{\partial x}\right)^2 + \left(\frac{\partial v}{\partial x}\right)^2\right]\right] \\ \left[\frac{1}{2}\left[\left(\frac{\partial u}{\partial y}\right)^2 + \left(\frac{\partial v}{\partial y}\right)^2\right]\right] \\ \left[\frac{1}{2}\left[\frac{\partial u}{\partial x}\frac{\partial u}{\partial y} + \frac{\partial v}{\partial x}\frac{\partial v}{\partial y}\right]\right] \end{bmatrix}}^{\text{Green-Lagrangian}} \tag{22.8}$$

Combining these for the integral Eq. (22.4) yields the potential energy in matrix form

$$\mathcal{V}^{(e)}(t) = \frac{1}{2}\vec{q}^{\mathrm{T}}(t)V^{(e)}\left[\frac{E}{1-\nu^2}\begin{pmatrix} \beta_1^2 & 0 & \beta_1\beta_2 & 0 & \beta_1\beta_3 & 0 \\ 0 & \gamma_1^2 & 0 & \gamma_1\gamma_2 & 0 & \gamma_1\gamma_3 \\ \beta_1\beta_2 & 0 & \beta_2^2 & 0 & \beta_2\beta_3 & 0 \\ 0 & \gamma_1\gamma_2 & 0 & \gamma_2^2 & 0 & \gamma_2\gamma_3 \\ \beta_1\beta_3 & 0 & \beta_2\beta_3 & 0 & \beta_3^2 & 0 \\ 0 & \gamma_1\gamma_3 & 0 & \gamma_2\gamma_3 & 0 & \gamma_3^2 \end{pmatrix} + \frac{\nu E}{1-\nu^2}\begin{pmatrix} 0 & \beta_1\gamma_1 & 0 & \beta_1\gamma_2 & 0 & \beta_1\gamma_3 \\ \beta_1\gamma_1 & 0 & \beta_2\gamma_1 & 0 & \beta_3\gamma_1 & 0 \\ 0 & \beta_2\gamma_1 & 0 & \beta_2\gamma_2 & 0 & \beta_2\gamma_3 \\ \beta_1\gamma_2 & 0 & \beta_2\gamma_2 & 0 & \beta_3\gamma_2 & 0 \\ 0 & \beta_3\gamma_1 & 0 & \beta_3\gamma_2 & 0 & \beta_3\gamma_3 \\ \beta_1\gamma_3 & 0 & \beta_2\gamma_3 & 0 & \beta_3\gamma_3 & 0 \end{pmatrix} + \frac{E(1-\nu)}{2(1-\nu^2)}\begin{pmatrix} \gamma_1^2 & \beta_1\gamma_1 & \gamma_1\gamma_2 & \beta_2\gamma_1 & \gamma_1\gamma_3 & \beta_3\gamma_1 \\ \beta_1\gamma_1 & \beta_1^2 & \beta_1\gamma_2 & \beta_1\beta_2 & \beta_1\gamma_3 & \beta_1\beta_3 \\ \gamma_1\gamma_2 & \beta_1\gamma_2 & \gamma_2^2 & \beta_2\gamma_2 & \gamma_2\gamma_3 & \beta_3\gamma_2 \\ \beta_2\gamma_1 & \beta_1\beta_2 & \beta_2\gamma_2 & \beta_2^2 & \beta_2\gamma_3 & \beta_2\beta_3 \\ \gamma_1\gamma_3 & \beta_1\gamma_3 & \gamma_2\gamma_3 & \beta_2\gamma_3 & \gamma_3^2 & \beta_3\gamma_3 \\ \beta_3\gamma_1 & \beta_1\beta_3 & \beta_3\gamma_2 & \beta_2\beta_3 & \beta_3\gamma_3 & \beta_3^2 \end{pmatrix} + \frac{p(t)}{A}\begin{pmatrix} \gamma_1^2 & 0 & \gamma_1\gamma_2 & 0 & \gamma_1\gamma_3 & 0 \\ 0 & \gamma_1^2 & 0 & \gamma_1\gamma_2 & 0 & \gamma_1\gamma_3 \\ \gamma_1\gamma_2 & 0 & \gamma_2^2 & 0 & \gamma_2\gamma_3 & 0 \\ 0 & \gamma_1\gamma_2 & 0 & \gamma_2^2 & 0 & \gamma_2\gamma_3 \\ \gamma_1\gamma_3 & 0 & \gamma_2\gamma_3 & 0 & \gamma_3^2 & 0 \\ 0 & \gamma_1\gamma_3 & 0 & \gamma_2\gamma_3 & 0 & \gamma_3^2 \end{pmatrix}\right]\vec{q}(t) \tag{22.9}$$

Each of the four 6×6 matrices could be regarded as four different stiffness matrices for a study which requires material parameters to be varied independently. As Poisson's ratio ν and Young's modulus E will not vary in this study, the first three matrices are combined to define $\mathbf{K}_0^{(e)}$. The fourth matrix is used to define $\mathbf{K}_1^{(e)}$ which is due to the additional stress introduced by the vertical load. Each β_i and γ_i may be simply resolved to their numerical values by considering the geometry, namely cathetus and area, of the right-angle triangular element. For a fixed length, width and number of elements in the mesh, the triangular elements come in a up or down orientation and therefore resolve to just two different numerical stiffness matrices. These are compiled by assembly of elements as outlined in Ref. [39] to generate a global mass $\mathbf{M}$ and two global stiffness matrices $\mathbf{K}_0$ and $\mathbf{K}_1$. Once the kinetic and potential energies are written in global matrix form similar to Eqs. (22.3) and (22.9), Hamilton's principle of stationary action and integration by parts provides the basis to combine them correctly.

$$\delta \int_{t_1}^{t_2} \left(\mathcal{T}(t) \; - \; \mathcal{V}(t) \right) \mathrm{d}t = 0 \tag{22.10}$$

where t_1 and t_2 are arbitrary start and end time t. EQM are obtained as the vanishing condition inside the integral, shown by combining the terms in the square brackets of the following two expressions

$$\int \delta\mathcal{T}\,\mathrm{d}t = \frac{1}{2}\int \delta\left(\dot{\vec{q}}^{\mathrm{T}}\mathbf{M}\dot{\vec{q}}\right)\mathrm{d}t = -\int (\delta\vec{q})^{\mathrm{T}}\left[\mathbf{M}\ddot{\vec{q}}_e\right]\mathrm{d}t \tag{22.11}$$

$$\int \delta\mathcal{V}\,\mathrm{d}t = \frac{1}{2}\int \delta\left(\vec{q}^{\mathrm{T}}\left(\mathbf{K}_0 + p(t)\mathbf{K}_1\right)\vec{q}\right)\mathrm{d}t = \int (\delta\vec{q})^{\mathrm{T}}\left[\left(\mathbf{K}_0 + p(t)\mathbf{K}_1\right)\vec{q}\right]\mathrm{d}t \tag{22.12}$$

One term in the integration by parts method will disappear as the variational method does not vary the initial and final states of the system. Reference [14] discusses vanishing terms in the integration of parts technique due to boundary conditions in some detail. In our case boundary conditions are satisfied by removing all clamped degrees of freedom for the top and base of the column. The following system of 2nd order linear differential equations are obtained.

$$\mathbf{M}\ddot{\vec{x}} + \mathbf{D}\dot{\vec{x}} + \left(\mathbf{K}_0 + p(t)\mathbf{K}_1\right)\vec{x} = \vec{0} \tag{22.13}$$

where a Rayleigh damping matrix $\mathbf{D}$ proportional to a linear combination of the mass and stiffness equation, i.e. $\mathbf{D} = \mu\mathbf{M} + \lambda\mathbf{K}$, may be added subsequently. $\vec{x}$ is the total time-varying displacement for each spatial direction at each node of the column mesh. The mass matrix $\mathbf{M}$ and first stiffness matrix $\mathbf{K}_0$ is validated by looking at convergence to the natural frequencies of the column. Subsequently $\mathbf{K}_1$ is verified in relation to the constant load Euler buckling problem. Validation is further discussed in Sect. 22.5. When $p(t)$ is a time-periodic harmonic function such as $\cos(\Omega t)$, the above equation is a sparse version of the coupled Mathieu equation and stability diagrams Fig. 22.2 match those in the literature [16]. In the next sections, the method to determine the stability of the system Eq. (22.13) as used in figures of Sect. 22.2 will be outlined.

22.3.1 *Interlude: Adaptation for the 3D Column*

In order to adapt the technique for the 3D hexahedral elements as schematically drawn in Fig. 22.1e, the z spatial coordinate and its component of the displacement vector $w(x, y, z, t)$ must be considered. The vector of temporal nodal displacements $q(t)$ is of size 24, 3 displacement vectors for each of its 8 nodes. For example the kinetic energy is over all three spatial coordinates, and ρ is the standard volumetric density. As shape functions Lagrange polynomials were used

$$N_i = \frac{1}{8}(1 + \xi\xi_i)(1 + \eta\eta_i)(1 + \zeta\zeta_i) \tag{22.14}$$

where ξ, η and ζ are natural coordinates inside the element ranging from -1 to 1. If a cuboid is delimited by $[x_{min}, x_{max}] \times [y_{min}, y_{max}] \times [z_{min}, z_{max}]$, then the natural coordinates may be resolved as [40]

$$\xi = \frac{2(x - x_{min})}{x_{max} - x_{min}} - 1, \qquad \eta = \frac{2(y - y_{min})}{y_{max} - y_{min}} - 1, \qquad \zeta = \frac{2(z - z_{min})}{z_{max} - z_{min}} - 1. \tag{22.15}$$

Thus, for the Ritz representation Eq. (22.2), the matrix $\mathbf{N}$ has size 3×9. and the resultant mass matrix element is of size 24×24. The strains (22.8) will be needed to take into account one extra translation and two extra shear strain directions. See Refs. [29, 40]. As in the 2D case, two stiffness matrices are obtained but of a considerably larger 24×24 size. The method follows almost precisely Sect. 22.3.

22.4 Floquet Theory—Determining Stability for Time-Periodic Mechanical Systems

A fundamental solution matrix $\Phi(t)$ of a differential equation consists of a complete set of linearly independent solutions, one per each column of the matrix. It specifies all solutions as for each initial starting vector $\vec{c}$, $\vec{x}(t) = \Phi(t)\vec{c}$ defines a unique solution. Floquet's theorem [10] states the form of *all* fundamental solution matrices for linear ordinary equations with time-periodic coefficients as

$$\Phi(t) = \mathbf{Q}(t) \exp(t\mathbf{B}) . \tag{22.16}$$

which consists of the time-periodic matrix $\mathbf{Q}(t)$ and an exponential matrix, with matrix of constant coefficients $\mathbf{B}$. The matrix $\exp(\tau\mathbf{B}) = \left[\Phi(\tau)\Phi^{-1}(0)\right]$, where τ is the period, is called the monodromy matrix. The system is spectrally unstable if any of its eigenvalues have an absolute value greater than one as after one complete revolution of the cycle a perturbation in the direction of the associated eigenvector would have grown. For a textbook which defines the concepts rigorously, we direct the reader to Ref. [36]. It will be the aim of the rest of this section to elaborate on a computational approach to obtain the monodromy matrix. In order to apply Floquet theory, the second order system Eq. (22.13) is transformed using $\vec{y} = \left[\vec{x},\ \dot{\vec{x}}\right]^{\mathrm{T}}$ into a first order system

$$\dot{\vec{y}} = \mathbf{A}(t)\vec{y} \tag{22.17}$$

where matrix $\mathbf{A}(t)$ is time-periodic with period τ and has the following block matrix form

$$\mathbf{A}(t) = \begin{bmatrix} \mathbf{0} & \mathbf{I} \\ \mathbf{M}^{-1}\mathbf{K}_0 + p(t)\mathbf{M}^{-1}\mathbf{K}_1 & \mathbf{M}^{-1}\mathbf{D} \end{bmatrix} \tag{22.18}$$

To determine stability of Eq. (22.17), one must check the stability for each degrees of freedom. For small systems, a direct approximation method may be implemented by integrating over a single period for each degree of freedom, thus checking if the magnitude of a small perturbation grows or contracts. Success of this technique will be a discussion in Sect. 22.5

22.4.1 Hsu Method [17]

An alternative approach which shows considerable computational saving is to follow the method in Ref. [11, 17]. The essential part of the Hsu method is to split up a single period into N parts in order to approximate the time periodic $\mathbf{A}(t)$ by a large enough number of constant matrices at discrete times. It is an attractive method as stiffness and mass matrices may be obtained at "frozen" times using standard meshing packages of commercially-available FEM software provided nodal positions and

its elements are not redefined. For the general case

$$\mathbf{A}(t) \approx \begin{cases} \mathbf{A}\,(\tau/2N) & \text{for } 0 \le t < (\tau/N) \\ \mathbf{A}\,(3\tau/2N) & \text{for } (\tau/N) \le t < (2\tau/N) \\ \mathbf{A}\,(5\tau/2N) & \text{for } (2\tau/N) \le t < (3\tau/N) \\ \vdots & \vdots \\ \mathbf{A}\,((2j+1)\tau/2N) & \text{for } ((j-1)\tau/N) \le t < ((j+1)\tau/N) \\ \vdots & \vdots \\ \mathbf{A}\,((2N-3)\tau/2N) & \text{for } ((N-2)\tau/N) \le t < ((N-1)\tau/N) \\ \mathbf{A}\,((2N-1)\tau/2N) & \text{for } ((N-1)\tau/N) \le t < \tau \end{cases} \tag{22.19}$$

In order to integrate around a single period, the first step in the integration would be approximated by

$$\vec{y}(\tau/N) = \exp\left[\int_0^{(\tau/N)} \mathbf{A}\,(s)\;\mathrm{d}s\right]\vec{y}(0) \approx \exp\left[\,(\tau/N)\,\mathbf{A}\,(\tau/2N)\,\right]\vec{y}(0) \tag{22.20}$$

whilst the subsequent second step would be

$$\vec{y}(2\tau/N) = \exp\left[\int_{(\tau/N)}^{2(\tau/N)} \mathbf{A}\,(s)\;\mathrm{d}s\right]\vec{y}\,(\tau/N) \approx \exp\left[\,(\tau/N)\,\mathbf{A}\,(3\tau/2N)\,\right]\vec{y}\,(\tau/N) \tag{22.21}$$

The general condition for an unspecific integration step is

$$\vec{y}(j\tau/N) = \exp\left[\int_{((j-1)\tau/N)}^{(j\tau/N)} \mathbf{A}(s)\,\mathrm{d}s\right]\vec{y}((j-1)\tau/N) \approx \exp\left[\,(\tau/N)\,\mathbf{A}((2j+1)\tau/2N)\,\right]\vec{y}((j-1)\tau/N) \tag{22.22}$$

Clearly Eqs. (22.20)–(22.22) may be combined by substituting in the previous approximation step to integrate round a complete orbit which results in the recurrence relation

$$\vec{y}(\tau) = \prod_{j=1}^{N} \exp\left[\int_{(N-j)(\tau/N)}^{(N-j+1)(\tau/N)} \mathbf{A}(s)\mathrm{d}s\right]\vec{y}(0) \approx \prod_{j=1}^{N} \exp\left[\left(\tfrac{\tau}{N}\right)\mathbf{A}\left((\tau/N)\left(\tfrac{(N-j)}{N}+\tfrac{1}{2}\right)\right)\right]\vec{y}(0) \tag{22.23}$$

As the vector $\vec{y}(0)$ is general and a full set of linearly independent vectors produces the monodromy matrix, the identity matrix is chosen $\Phi^{-1}(0) = \mathbf{I}$. Equation (22.23) may be regarded as similar to a direct integration method using a symplectic Euler integrator. The growth matrix or monodromy matrix simplifies to

$$\exp\left[\tau\mathbf{B}\right] = \Phi(\tau) \approx \prod_{j=1}^{N} \exp\left[\left(\frac{\tau}{N}\right)\mathbf{A}\left((\tau/N)\left(\frac{(N-j)}{N}+\frac{1}{2}\right)\right)\right] \tag{22.24}$$

The absolute values of the eigenvalues of this matrix Eq. (22.24) are used to predict stability of the harmonically forced column as discussed in Sect. 22.2. The main numerical cost of Hsu method is repeated calculation of the matrix exponential which is known to be computationally expensive [30] and is addressed in the next section.

22.5 Computational Details

Using the FEM with 2D and 3D solid elements to model a harmonically forced column requires a large number of elements to achieve an adequate accuracy. In Fig. 22.4a the relative difference for the first three eigenfrequencies for the unforced column as compared to EBBT versus the number of elements is plotted. The numerical values for EBBT is contained in Sect. 22.2. As may be seen from Fig. 22.4a, all three frequencies converge as the number of elements increases. Shear locking due to use of linear solid elements is expected to overestimate the stiffness within the column, yet all three eigenfrequencies, especially visible for the third eigenfrequency, converge to values below those calculated by EBBT. This is consistent with EBBT slightly overstating the true natural frequencies (see results in Ref. [24]) for non-slender columns. As only the mass matrix $\mathbf{M}$ and a single stiffness matrix $\mathbf{K}_0$ of Eq. (22.13) was used for an unforced column, Fig. 22.4a was appropriate in this work to validate these two matrices. Figure 22.4b shows the relative difference of the buckling calculated by the FEM and the theoretical Euler buckling load versus the number of elements. Similarly, as observed by other authors [28], the buckling load calculated via the FEM is slightly less than that estimated via EBBT. Fig. 22.4b is used to validate the second stiffness matrix $\mathbf{K}_1$ of Eq. (22.13). It should be noted, that a significant increase in the number of 2D and 3D solid elements over 1D beam

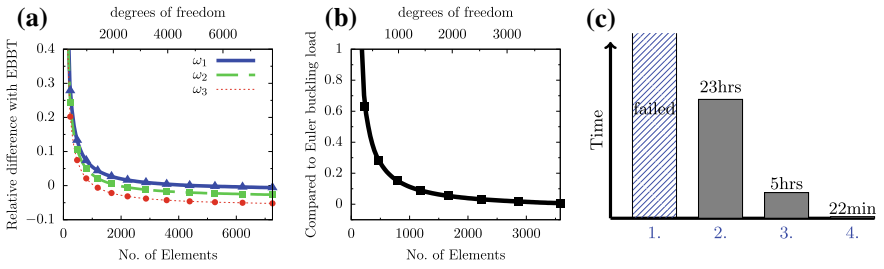

Fig. 22.4 **a** First 3 eigenfrequencies of unloaded column compared to EBBT as number of triangular elements is varied. Validation for mass $\mathbf{M}$ and stiffness matrix $\mathbf{K}_0$. **b** Critical buckling load compared to Euler buckling load as number of triangular elements changes. Validation for second stiffness matrix $\mathbf{K}_1$. **c** Histogram plot of time taken by various methods: 1: Euler and Trapezoidal methods failed to converge, 2: Dormand–Prince method, 3: Hsu method using 2nd order approximation matrix exponential method, and 4: Hsu method with scaling and squaring method

elements were needed for convergence of the frequencies (cf. Fig. 22.4a) and the buckling load (cf. Fig. 22.4b). In order to control for numerical errors in the determination of stability with the 2D and 3D elements, a large enough number of elements to allow convergence to within approximately 1% was sought using diagrams such as Figs. 22.4a, b. For results in Sect. 22.2, it was found that 2528 DOF and 2832 DOF to achieve this for the triangular element and for the cuboid element respectively.

Lastly, we discuss a few techniques to calculate the Floquet multipliers and their computational load. Figure 22.4c shows a histogram diagram with the total time taken for several trial methods. The comparison was conducted for a 348 DOF test case using a single thread of an Intel(R) Core i7 CPU 960 @ 3.20 GHz with 8 GB RAM with ASCII C code compiled with GNU C compilers. In order to calculate the Floquet multipliers, the standard direct integration technique was first implemented. Using either a simple Euler step or trapezoidal integration method, the time traces blew up for arbitrary small stepsize. Failure of these techniques was probably due to the EQM Eq. (22.13) being stiff. In order to alleviate this, a special integrator for stiff equations was utilised, namely the Prince-Dormand method [6] which is an 8th order Runge–Kutta method. The total time taken (23 h) may be seen in the second column of the histogram diagram Fig. 22.4c. Next Hsu method (Sect. 22.4.1) was implemented in order to calculate monodromy matrix. By far the most computationally expensive part of the technique is repeated calculations of a matrix exponential. For this reason, Hsu et al. suggested to take only the first few terms in its Taylor expansion. It was found that although each matrix exponential estimation was substantially quicker, a much larger number of matrix exponential steps were required (cf. Eq. (22.24)) to comply with our error tolerance. The total time for this trial was 5 h. Lastly Hsu method using the "scaling and squaring" Moler and van Loan method 3 recommended in Ref. [30] for matrix exponential determination implemented in the GNU scientific library (GSL) yielded significant faster computations (22 min) as the total number matrix exponential needed to be calculated could be reduced. Although the simple timing comparison conducted here needs to be treated with care as substantial improvements could be possible via tweaking of algorithms, a clear improvement may be seen in Fig. 22.4c in the amount of time taken by each method run on a single thread of the processor. Additionally Hsu method [17] with scaling and squaring method may be easily parallelized as each matrix exponential computation may be treated independently. Parallelization was achieved using Open Multi-Processing [3] allowing a possible 8-fold speedup for the Intel i7 with 4 cores and 2 threads per core. Diagrams and figures of Sect. 22.2 were produced on a 32 symmetric node cluster each with 64 GB RAM, 4 AMD Opteron CPU run at 2.6 GHz and 48 threads.

22.6 Conclusion

In this work, time-periodic equations of motion for a non-slender 2D and 3D column under periodically-applied axial load is obtained by a Rayleigh–Ritz formulation of the FEM. Versatile solid elements such as linear triangular or linear cuboid elements are used meaning a non-linear strain approach is required to obtain buckling instabilities. Unlike for beam elements, a large number of these germane elements are required for sufficient convergence of the natural frequencies and Euler buckling load. The resultant growth of the DOF required leads to significant numerical and computational difficulties in determining stability via Floquet theory [10]. Numerical schemes of the direct integration method and Hsu method is compared. The significant computational load is handled via purposely written C-code using the GSL [12] with OpenMP [3] parallelization. The use of versatile solid elements allows one to determine stability of elastodynamic structures of non-simple geometry. As two examples of the flexibility of the technique, two configurations of a 3D steel column under harmonically-applied force is discussed. In the results section of this manuscript, it is concluded that a column with non-symmetric aspect ratio is less stable whilst a column made of nonhomogeneous, in this case with holes, material is more stable.

Notes and Comments. This work was supported by DFG (HA 1060/56-1). We thank the graduate school of computational engineering for use of its "icluster" and Prof. Peter Hagedorn for general encouragement.

References

1. Anilkumar, A., Kartik, V.: In-plane parametric instability of a rigid body with a dual-rotor system. In: ASME 2015 International Mechanical Engineering Congress and Exposition. American Society of Mechanical Engineers (2015)
2. Barsoum, R.S., Gallagher, R.H.: Finite element analysis of torsional and torsional-flexural stability problems. Int. J. Numer. Methods Eng. **2**(3), 335–352 (1970)
3. Board, O.A.R.: OpenMP Application Programming Interface (2015). http://openmp.org/
4. Chen, C.-C., Yeh, M.-K.: Parametric instability of a beam under electromagnetic excitation. J. Sound Vib. **240**(4), 747–764 (2001)
5. Dohnal, F.: A Contribution to the Mitigation of Transient Vibrations: Parametric Anti-resonance; Theory, Experiment and Interpretation (2012)
6. Dormand, J.R., Prince, P.J.: A family of embedded Runge–Kutta formulae. J. Comput. Appl. Math. **6**(1), 19–26 (1980)
7. Dufour, R., Berlioz, A.: Parametric instability of a beam due to axial excitations and to boundary conditions. J. Vib. Acoust. **120**(2), 461–467 (1998)
8. Evan-Iwanowski, R.M.: On the parametric response of structures(parametric response of structures with periodic loads). Appl. Mech. Rev. **18**, 699–702 (1965)
9. Evan-Iwanowski, R.: Resonance Oscillations in Mechanical Systems. North-Holland (1976)
10. Floquet, G.: Sur les équations différentielles linéaires à coefficients périodiques. Annales scientifiques de l'École normale supérieure **12**, 47–88 (1883)
11. Friedmann, P., Hammond, C., Woo, T.-H.: Efficient numerical treatment of periodic systems with application to stability problems. Int. J. Numer. Methods Eng. **11**(7), 1117–1136 (1977)

12. Gough, B.: GNU Scientific Library Reference Manual. Network Theory Ltd. (2009)
13. Guckenheimer, J., Holmes, P.: Nonlinear Oscillations, Dynamical Systems, and Bifurcations of Vector Fields, vol. 42. Springer Science & Business Media, Berlin (2013)
14. Hagedorn, P., DasGupta, A.: Vibrations and Waves in Continuous Mechanical Systems. Wiley, New York (2007)
15. Hagedorn, P., Koval, L.R.: On the parametric stability of a Timoshenko beam subjected to a periodic axial load. Arch. Appl. Mech. **40**(3), 211–220 (1971)
16. Hansen, J.: Stability diagrams for coupled Mathieu-equations. Ing.-Arch. **55**(6), 463–473 (1985)
17. Hsu, C.: On approximating a general linear periodic system. J. Math. Anal. Appl. **45**(1), 234–251 (1974)
18. Iwatsubo, T., Saigo, M., Sugiyama, Y.: Parametric instability of clamped-clamped and clamped-simply supported columns under periodic axial load. J. Sound Vib. **30**1, 65–IN2 (1973)
19. Iwatsubo, T., Sugiyama, Y., Ishihara, K.: Stability and non-stationary vibration of columns under periodic loads. J. Sound Vib. **23**(2), 245–257 (1972)
20. Iwatsubo, T., Sugiyama, Y., Ogino, S.: Simple and combination resonances of columns under periodic axial loads. J. Sound Vib. **33**, 211–221 (1974)
21. Kang, J.: Moving mode shape function approach for spinning disk and asymmetric disc brake squeal. J. Sound Vib. **424**, 48–63 (2018)
22. Kirchgäßner, B.: Finite Elements in Rotordynamics. Procedia Eng. **144**, 736–750 (2016)
23. Klíč, A.: Period doubling bifurcations in a two-box model of the brusselator. Apl. Mat. **28**(5), 335–343 (1983)
24. Labuschagne, A., van Rensburg, N.F.J., Van der Merwe, A.J.: Comparison of linear beam theories. Math. Comput. Model. **49**(1), 20–30 (2009)
25. Landau, L.D., Lifshitz, E.M.: Course of Theoretical Physics Vol 7: Theory of Elasticity. Pergamon Press, Oxford (1970)
26. Lee, H.: Dynamic stability of a moving column subject to axial acceleration and force perturbations. Eng. Comput. **12**(7), 609–618 (1995)
27. Lee, H.: Dynamic stability of spinning pre-twisted beams subject to axial pulsating loads. Comput. Methods Appl. Mech. Eng. **127**(1–4), 115–126 (1995)
28. Li, S.-R., Batra, R.C.: Relations between buckling loads of functionally graded Timoshenko and homogeneous Euler–Bernoulli beams. Compos. Struct. **95**, 5–9 (2013)
29. Martin, H.C.: On the derivation of stiffness matrices for the analysis of large deflection and stability problems. Matrix Methods Struct. Mech. **80**, 697–716 (1966)
30. Moler, C., Van Loan, C.: Nineteen dubious ways to compute the exponential of a matrix, twenty-five years later. SIAM Rev. **45**(1), 3–49 (2003)
31. Nikolaev, E.V.: Bifurcations of limit cycles of differential equations admitting an involutive symmetry. Sbornik: Math. **186**(4), 611 (1995)
32. Oden, J.T., Reddy, J.N.: An Introduction to the Mathematical Theory of Finite Elements. Dover Publications, Mineola (2012)
33. Rao, S., Gupta, R.: Finite element vibration analysis of rotating Timoshenko beams. J. Sound Vib. **242**(1), 103–124 (2001)
34. Talimian, A., Beda, P.: Dynamic stability of a thin plate subjected to bi-axial edged loads. Acta Polytech. Hung. **15**(2), 125–139 (2018)
35. Vanderbauwhede, A.: Local Bifurcation and Symmetry, vol. 75. Pitman Advanced Publishing Program, Boston (1982)
36. Walter, W.: Ordinary Differential Equations. Graduate Texts in Mathematics, vol. 182. Springer, Berlin (1998)
37. Weichert, D., Maier, G.: Inelastic Behaviour of Structures Under Variable Repeated Loads: Direct Analysis Methods, vol. 432. Springer, Berlin (2014)
38. Weidenhammer, F.: Der eingespannte, achsial pulsierend belastete Stab als Stabilitätsproblem. Arch. Appl. Mech. **19**(3), 162–191 (1951)
39. White, R.E.: An Introduction to the Finite Element Method with Applications to Nonlinear Problems. Wiley, New York (1985)
40. Zienkiewicz, O.C., Taylor, R.L., Zhu, J.Z.: The Finite Element Method: Its Basis and Fundamentals. The Finite Element Method. Elsevier Science, New York (2013)

Chapter 23
Effects of Non-neighbouring Members in an Array of Beams Vibrating in Fluids

Arun Kumar Manickavasagam, Stefanie Gutschmidt and Mathieu Sellier

Abstract Broadband, multi-functional and parallel-processing devices are often built on coupled oscillators or arrays of resonators. Different length scales and applications determine the dominating coupling mechanism of the device. In this work we investigate the effects of fluid coupling between members of a one-dimensional cantilever array. We are specifically interested in studying the influence of non-neighbouring members in view of trying to distinguish between local and global (array) effects. Our analysis is based on the Navier-Stokes equation for incompressible flow which is solved using a boundary-integral technique resulting in the hydrodynamic coupling matrix through which added mass and hydrodynamic dissipation effects are inferred. Results clearly suggest that non-neighbouring members play a significant role with an increase in size of the array and at gap widths less than half the width of the cantilever.

Keywords Fluid coupling · Array effects · Non-neighbouring members · Added mass · Hydrodynamic dissipation

23.1 Introduction

With recent improvements and increased performance specifications of MEMS (micro-electromechanical systems) based technologies such as e.g. scanning probe microscopy [1] or biosensors [2], but also larger scale applications like piezoelectric fans [3] and flapping wings for propulsion [4], there has been a growing interest to understand the collective dynamics of coupled oscillators, especially when immersed in a fluid. Other examples of coupled nonlinear oscillators include networks of pacemaker cells in the heart, congregations of synchronously flashing fireflies and crickets

A. K. Manickavasagam (✉) · S. Gutschmidt · M. Sellier
University of Canterbury, 8041 Christchurch, New Zealand
e-mail: arun.manickavasagam@pg.canterbury.ac.nz

S. Gutschmidt et al. (eds.), *IUTAM Symposium on Recent Advances in Moving Boundary Problems in Mechanics*, IUTAM Bookseries 34,
https://doi.org/10.1007/978-3-030-13720-5_23

chirping in unison. While dominating coupling effects can be of different origin (fluid, mechanical, thermal, etc.) and size, in this work we focus purely on hydrodynamic interactions between members of the array and the ways in which these influence the collective dynamics of the array. More specifically, we investigate the hydrodynamic influences of non-neighbouring members on the overall array dynamics. The aim of this work is to be able to distinguish between parameter domains at which coupling effects of non-neighbouring members significantly influence or even determine the overall performance of the system and for which these can be neglected.

Basak and Raman [5] studied the hydrodynamic coupling effects between nearest neighbour members of an array of M micro-mechanical beams. The array under investigation was an edge-to-edge configuration and the authors studied the effects of hydrodynamic forces for a range of gap widths, amplitude ratios and relative phases analytically and computationally. They concluded that the dynamics of microbeams in an array can be tuned to either maximize or minimize the hydrodynamic resistance on individual microbeams. Intartaglia et al. [6] investigated the hydrodynamic coupling effects of a pair of cantilevers in a face-to-face configuration. Their work sheds light on mutual influences of the two beams, manifested in added mass and dissipation effects. They showed that the added mass effect is magnified for decreasing gaps and hydrodynamic damping decreases as the gap increases. Their proposed theoretical approach was also validated experimentally in water on centimeter sized compliant beams subject to base excitation. Cellini et al. [7] investigated hydrodynamic coupling effects in a parallel array (face-to-face configuration) of five identical ionic polymer metal composites (IPMCs) subjected to low frequency base excitation limiting the interactions only to nearest neighbours. Their analysis suggests that closely spaced IPMCs result in higher harvested powers, which is also validated experimentally. While these works have studied the nearest neighbour interactions, they have ignored the effects of non-neighbouring members.

In this paper we focus on small sized arrays with three and five beams in an edge-to-edge configuration (considering motion in transverse direction only), see Fig. 23.1 for the cross-sectional view of cantilevers in fluid. The beams are long, slender cantilever structures immersed in an incompressible, viscous fluid. While the hydrodynamic coupling effects of a pair and local neighbours of cantilevers in an array have been studied in detail [5], we will focus on the theoretical analysis of hydrodynamic coupling on the effects stemming from non-neighbouring members and/or global array properties.

The paper is organized as follows. In Sect. 23.2, we present the boundary-integral theory resulting in matrix-vector equations to compute the added mass and hydrodynamic dissipation effects over the width of the beam. In Sect. 23.3, we extend the theoretical model introduced by Basak and Raman [5] incorporating the effects of non-neighbouring members in a three and a five-beam array. Results are discussed and conclusions are drawn in Sect. 23.4.

23.2 General Formulation of the Array Model

23.2.1 Streamfunction Formulation

In this section we extend the boundary-integral formulation [5] for an array of M beams in general matrix form. The final expression determines the hydrodynamic forces along the width of each beam. We consider small amplitude oscillations of infinitely thin cantilever beams of rectangular cross section, each of width $2b$ and spaced $2g$ apart, see Fig. 23.1. The derivations are based on previous work by Tuck [8], Tung [9] and Raman [5]. We, however, highlight new and additional terms of non-neighbouring members and compare and validate our results against theirs.

We base the derivations of mathematical expressions on the following assumptions:

1. Each microbeam can be of arbitrary cross section as long as the cross section remains uniform along its length.
2. The fluid motion along the axial direction $\mathbf{E_x}$ can be neglected for lower flexural modes.
3. Only transverse vibrations of the beam along $\mathbf{E_z}$ are considered and any lateral motion along $\mathbf{E_y}$ is ignored.
4. Only hydrodynamic coupling effects are considered, ignoring any effects arising from structural coupling.
5. The fluid is incompressible as the acoustic wavelength in both liquids and gases typically exceeds the characteristic length scale of the microbeam.
6. Furthermore, all beams are assumed to oscillate with the same frequency and with small amplitudes and possibly different phases.

Since the nonlinear convective effects are negligible due to the small amplitude assumption, the fluid flow is governed by the linearized Stokes and the continuity equation. The Fourier transformed unsteady Stokes and continuity equation for the fluid is given by [9]

$$i\omega\rho\mathbf{u} = -\nabla p + \mu\nabla^2\mathbf{u}, \ \nabla.\mathbf{u} = 0, \tag{23.1}$$

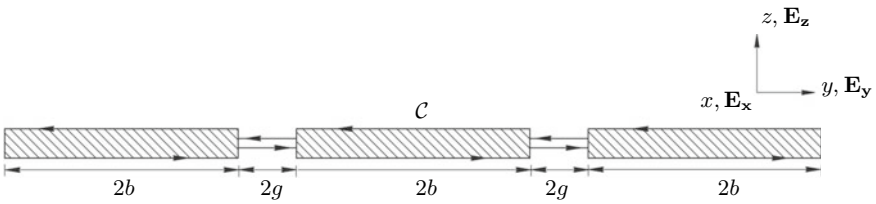

Fig. 23.1 Sketch of the boundary value problem for three oscillating rectangular cross-sectional beams. $\mathbf{E_x}$, $\mathbf{E_y}$, $\mathbf{E_z}$ is the vector basis corresponding to the x, y and z coordinate system

where ω is the driving frequency, $\mathbf{u}(y, z|\omega)$ is the fluid velocity vector given by $\mathbf{u} = v(y, z|\omega)\mathbf{j} + w(y, z|\omega)\mathbf{k}$, where v and w are magnitudes of velocities in the lateral and transverse directions respectively, $p(y, z|\omega)$ is the pressure field in the fluid, and ρ and μ are the density and dynamic viscosity of the fluid respectively. The beam cross sections in the $y - z$ plane are separated from the fluid domain by a closed contour $\mathcal{C}$.

The far-field boundary condition is that $\mathbf{u} \to 0$ as $y, z \to \pm\infty$ and the velocity at the solid-fluid interface is given by:

$$v = 0, \ w = W_m, \tag{23.2}$$

at z = 0 (beam), where v and w are flow velocities along $\mathbf{E_y}$ and $\mathbf{E_z}$ respectively and W_m is the transverse velocity amplitude of the beam cross section.

Following Tuck's work [8], we introduce a stream function $\psi(y, z)$ to satisfy the continuity equation in (23.1)

$$v = \psi_z, \ w = -\psi_y. \tag{23.3}$$

Thus, the boundary conditions at the solid-fluid interface in terms of the streamfunction are

$$\psi_z = 0, \ -\psi_y = W_m. \tag{23.4}$$

Reformulating Eq. (23.1) in terms of the streamfunction and application of Green's theorem yields the following expression for the streamfunction: [5]

$$\begin{aligned}\psi(y, z|\omega) = \int_{\mathcal{C}} (&\Psi(y', z'|\omega) G_n(y, z|y', z') \\ &- \Psi_n(y', z'|\omega)\Omega(y, z, |y', z') - \zeta(y', z'|\omega)\Psi_n(y, z|y', z') \\ &+ \frac{1}{\eta} P(y', z'|\omega)\Psi_l(y, z|y', z'))dl,\end{aligned} \tag{23.5}$$

where (y, z) is a point in the fluid domain, (y', z') is a point on the contour $\mathcal{C}$, ζ is the fluid vorticity, and G, Ω and Ψ are the Green's functions for the Laplace operator, the Helmholtz operator and for the operator $\nabla^4(.) - iRe\nabla^2(.)$ respectively. The subscripts n and l define derivatives in normal (transverse) and parallel (lateral) directions to the contour $\mathcal{C}$, respectively.

The problem then involves differentiating the above equation with respect to z and y in turn to obtain the velocity components v and w resulting in coupled integral equations. A numerical scheme is then used to convert the system of integral equations into a corresponding system of matrix equations using quadrature. A nonuniform discretization technique is employed to discretize the beam into N unequal segments, to avoid square root singularities. Also, the equations are allowed to hold at the midpoint of each segment to avoid logarithmic singularity [8]. Once all the matrix

entries are computed, linear system is solved in MATLAB to obtain the unknown pressure jumps. A more detailed procedure on computing the pressure jumps can be found in [5].

23.3 Hydrodynamic Coupling of Arrays in Fluids

We focus in this section on the hydrodynamic coupling effects between members in an array. We provide a generalized matrix formulation for an array of M beams incorporating coupling contributions of all members and study the influence of non-neighbouring members in a three-and a five-beam array.

Derivations of the hydrodynamic coupling matrix are based on existing work by Basak and Raman [5] whereas the new contribution in this paper is the consideration, analysis and discussion of coupling contributions of all members. We consider identical beams equally spaced apart. The width of each beam is $2b$ and the gap between each is $2g$. The unsteady streamfunction is computed for transverse vibrations and the velocity matching conditions are formulated for M beams. The transverse velocity of the mth beam in the array is given by $W_m(z) = \hat{W}_m e^{i(\omega t+\theta_m)}$, where $\hat{W}_m$ is the velocity amplitude and θ_m is the phase of vibration of the mth beam. Also velocity matching conditions for each beam is formulated following a similar procedure as that by Basak and Raman [5]. We nondimensionalise gaps, pressure jumps, velocity amplitudes and unsteady Reynolds number to make comparisons meaningful. The uncoupled integral equations are then solved using a numerical procedure similar to the one used by Tuck [8] and Basak and Raman [5]. The hydrodynamic matrix elements for an array of M beams incorporating interactions between all members in the array are given by

$$G_{m,n} = \left[A_{kj}\right]_{m,n},$$

where $m, n \in 1...M$ and A_{kj} is given by

$$\begin{aligned} A_{kj} &= \int_{\xi_j}^{\xi_{j+1}} L(\sqrt{iRe}|\xi' - \xi|)d\xi', \\ &= \frac{1}{2\pi}[f(Re, \xi'_{j+1}, \xi_k) - f(Re, \xi'_j, \xi_k)], \end{aligned} \tag{23.6}$$

and

$$\begin{aligned} f(Re, \xi_j{}', \xi_k) = \frac{i}{Re}\Bigg(&\frac{1}{\xi'_j - \xi_k} + sgn(\xi'_j - \xi_k)i\sqrt{iRe}K_1 \\ &\times (-i|\xi'_j - \xi_k|\sqrt{iRe})\Bigg). \end{aligned} \tag{23.7}$$

Each diagonal entry contains hydrodynamic influence coefficients due to the segments of the same microbeam whereas each off diagonal entry comprises of elements

representing the hydrodynamic coupling generated by the neighbouring ($(m+1)$th and $(m-1)$th) and non-neighbouring members on the mth beam. For example, G_{11} contains hydrodynamic influence coefficients on the first microbeam due to the segments of the same microbeam whereas G_{12} contains hydrodynamic influence coefficients on the first microbeam due to the segments of the second microbeam, and so on. The logarithmic and square-root singularities are circumvented by allowing the equations to hold at the middle point of each segment and by dividing each beam into unequal number of segments N respectively. For instance, elements of sub-matrix G_{11} are computed by running a loop over the number of nodes j $(0, \ldots, N)$ for each k $(0, \ldots, N-1)$ which is the midpoint of each segment on the first beam [8].

The velocity matching equations for any beam other than the first beam can be written in matrix notation as follows

$$r_{m1} e^{i\theta_{m1}} [1\,1 \ldots 1]^T = \hat{\boldsymbol{G}} [P_m]^T \tag{23.8}$$

where r_{m1} and θ_{m1} are the relative amplitude and phase of the mth beam with respect to beam 1. We consider beam 1 (left-most beam) as our reference and hence $r_{11} = 1$ and $\theta_{11} = 0$.

The coupling matrix $\hat{\boldsymbol{G}}$ incorporating all member interactions for a three and a five-beam array are given by:

$$\hat{\boldsymbol{G}}_{\boldsymbol{III}} = \begin{bmatrix} G_{11} & G_{12} & G_{13} \\ G_{21} & G_{22} & G_{13} \\ G_{31} & G_{32} & G_{33} \end{bmatrix},$$

$$\hat{\boldsymbol{G}}_{\boldsymbol{V}} = \begin{bmatrix} G_{11} & G_{12} & G_{13} & G_{14} & G_{15} \\ G_{21} & G_{22} & G_{23} & G_{24} & G_{25} \\ G_{31} & G_{32} & G_{33} & G_{34} & G_{35} \\ G_{41} & G_{42} & G_{43} & G_{44} & G_{45} \\ G_{51} & G_{52} & G_{53} & G_{54} & G_{55} \end{bmatrix},$$

where the elements in red represent the coupling contributions of non-neighboring members and are set to zero as in previous work [5, 6, 9] when only nearest neighbour interactions are considered. The solutions for the nondimensional pressure jump are found simply by inverting the coupling matrix and multiplying it by the velocity vector.

23.4 Beam Array Analysis

Non-dimensional parameters that influence the coupled hydrodynamics are the gap $\bar{g} = g/b$, the amplitude ratio r_{m1}, the relative phase θ_{m1}, the unsteady Reynolds number Re and the non-neighbouring members. The effect of the first four parameters have been studied for nearest neighbour interactions and the focus in this paper is on

the influence of non-neighbouring members for different gap widths and two different configurations, namely in-phase vibrations and out-of-phase vibrations (where alternating beams vibrate in opposite directions).

In-phase Vibration Analysis

We consider all beams to oscillate in-phase with identical vibration amplitudes incorporating nearest neighbour interactions initially. The imaginary (ΔP_i^*) and real (ΔP_r^*) parts of the pressure across the middle beam in a three and a five-beam array are analysed for varying gap sizes between members at $Re = 1$.

The imaginary part (ΔP_i^*) of the pressure drop across the beam is 90° out-of-phase with its transverse velocity and contributes to the added mass whereas the real part (ΔP_r^*) of the pressure drop is in-phase with its transverse velocity and contributes to the hydrodynamic dissipation. We notice from Fig. 23.2 that at gaps greater than twice the width of the beam (i.e. $g/b > 2$), each beam behaves independently without interactions with its neighbours. The pressure distribution in such cases is similar to that of a single beam vibrating in an unbounded fluid [8]. However, as the gap width is reduced the imaginary and real parts of pressure behave in non-intuitive ways. The critical gaps at which they switch trends is different as also observed by Basak and

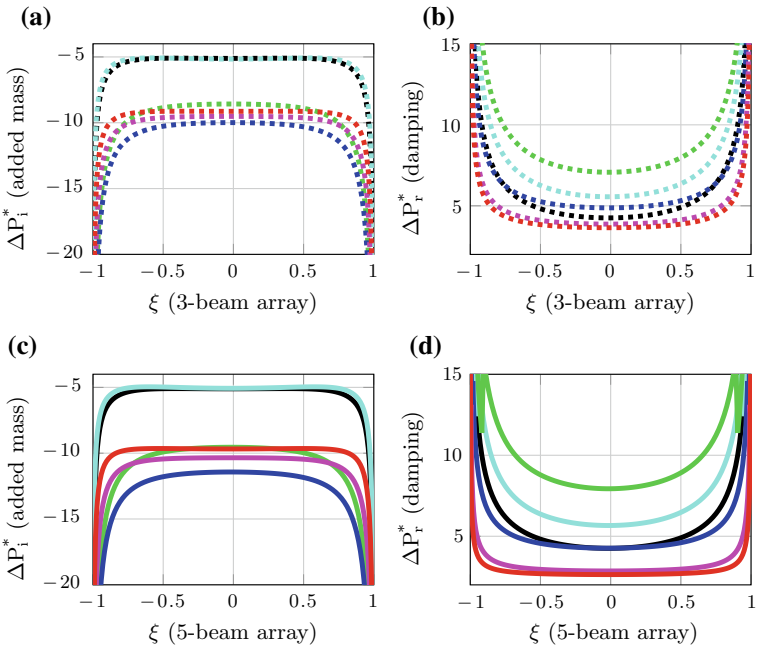

Fig. 23.2 Variation of imaginary and real parts of pressure across the middle beam subject to in-phase vibration mode; a), b) in a three-beam array (dotted line) and c), d) in a five-beam array (solid line). Plots for $\bar{g} = 8$ [black], $\bar{g} = 2$ [cyan], $\bar{g} = 0.8$ [green], $\bar{g} = 0.4$ [blue], $\bar{g} = 0.2$ [magenta] and $\bar{g} = 0.1$ [red] are shown

Raman [5]. For instance, added mass and damping initially increase in magnitude as the beams are brought close to each other but the added mass effect starts to decrease for $g/b < 0.4$ whereas damping starts to decrease for $g/b < 0.8$ both in a three and a five-beam array.

Non-neighbouring members are then incorporated in the array to predict their effects on the added mass and damping of the whole array. Fig. 23.3 presents the differences in pressure parts over the middle beam with all members included as compared to only nearest neighbours for a three-beam array represented by dotted lines and a five-beam array represented by solid lines respectively. We restrict our attention to three gap widths: $g/b = 8$ ——, 0.4 —— and 0.1 —— only.

There is no significant effect of neighbouring members in a three and a five-beam array when the beams are far apart as can be seen in Fig. 23.3. The dotted line overlaps the solid line for a gap width of $g/b = 8$, suggesting that each beam in the array behaves independently. However, as the beams are brought in close proximity to each other, the added mass effect increases more in the five-beam array. This implies that the effect of non-neighbouring members becomes significant as the array size increases due to increasing contribution to additional "global effects".

In Fig. 23.3 we have also plotted the differences in real part (proportional to hydrodynamic dissipation effects) of pressure when all members are incorporated and the case where only nearest neighbours are incorporated, both for a three and a five-beam array. Again, as expected there is no difference for gap widths $g/b > 8$ as the dotted line overlaps the solid line implying that each beam behaves independently. The damping effects in a three-beam array alternates between negative and positive values as we reduce the gap width. In a five-beam array the trend is positive with the damping effect increasing initially until $g/b = 0.4$ but decreasing as the gap width is reduced beyond 0.4.

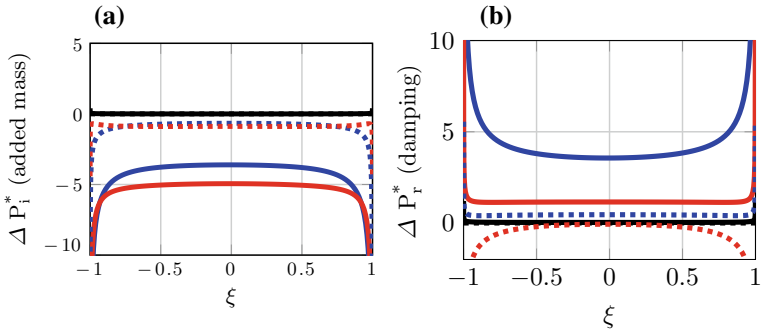

Fig. 23.3 Differences in imaginary and real parts of pressure with all members incorporated and only nearest members incorporated in a three (dotted line) and a five (solid line) beam array with all members vibrating in-phase at maximum amplitudes. Plots for $\bar{g} = 8$ ——, $\bar{g} = 0.4$ —— and $\bar{g} = 0.1$ —— are shown

Hence, both added mass and damping effects are significantly impacted by the global non-neighbouring members dynamics and the increase in size of the array. The significance of non-neighbouring members increases as the array size increases.

Out-of-phase Vibration Analysis

Initially, we consider beams oscillating in an out-of-phase mode with identical vibration amplitudes incorporating nearest neighbour interactions only. The imaginary (ΔP_i^*) and real (ΔP_r^*) parts of the pressure across the middle beam in a three and a five-beam array are plotted in Fig. 23.4, for varying gaps.

We notice that when the beams are far apart there is no change in the imaginary and real parts of pressure in a three and a five-beam array [8]. In this case each beam behaves like a single separate beam in an unbounded fluid. As the gap between beams decreases, the added mass effect decreases in magnitude as can be seen in Fig. 23.4a, c. Also, the magnitude of the added mass in a five-beam array is more than that of the three-beam array for $g/b < 0.8$. The damping behaves in a non-intuitive manner for a three-beam array whereas for a five-beam array it decreases as the gap width is reduced which leads us to the conjecture that array effects are enhanced as the size of the array increases.

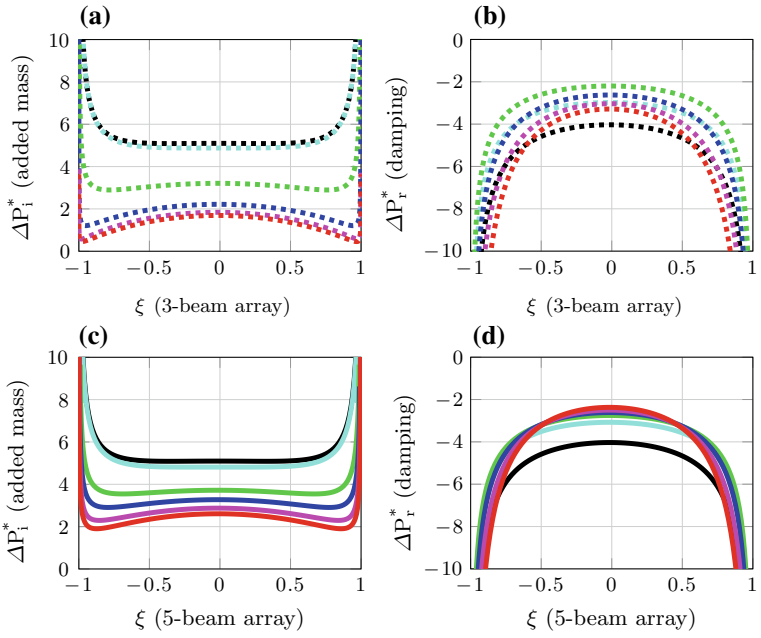

Fig. 23.4 Variation of imaginary and real parts of pressure across the middle beam subject to out-of-phase vibration mode; **a**, **b** a three-beam array (dotted line) and **c**, **d** a five-beam array (solid line). Plots for $\bar{g} = 8$ [—], $\bar{g} = 2$ [—], $\bar{g} = 0.8$ [—], $\bar{g} = 0.4$ [—], $\bar{g} = 0.2$ [—] and $\bar{g} = 0.1$ [—] are shown

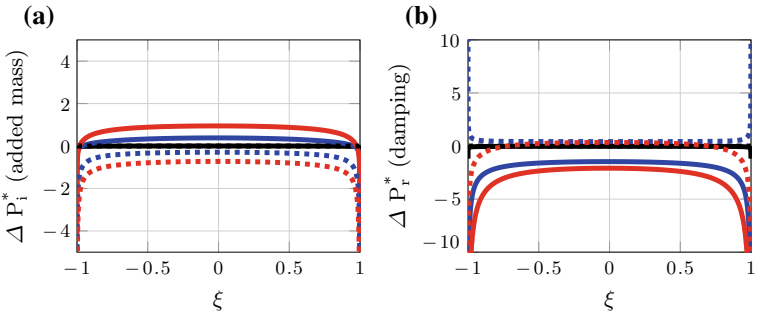

Fig. 23.5 Differences in imaginary and real parts of pressure with **a** all members incorporated and **b** only nearest members incorporated in a three (dotted line) and a five-beam array (solid line) with all members vibrating in an out-of-phase manner at maximum amplitudes. Plots for $\bar{g} = 8$ ——, $\bar{g} = 0.4$ —— and $\bar{g} = 0.1$ —— are shown

Now, we incorporate the non-neighbouring members in addition to the nearest neighbours to predict their effects on the added mass and damping matrices of the array.

Similar to the in-phase case, Fig. 23.5 depicts that the members of the array behave independently when they are far apart i.e. $g/b = 8$. With the addition of non-neighbouring members the added mass effect shows a similar trend magnitude-wise to that of a five-beam array and a three-beam array. The real part of pressure (hydrodynamic dissipation effects) on the other hand reaches a maximum value near $g/b = 0.4$ in a three-beam array and decreases as the members are brought closer whereas in a five-beam array, it shows a monotonic trend i.e. the hydrodynamic dissipation effects decrease with decreasing gap widths.

23.5 Conclusion

The underlying physics of the hydrodynamic interactions between multiple members in a three and five-beam array have been systematically analysed for two different modes, namely in-phase and out-of-phase, with and without the incorporation of non-neighbouring members at a particular Reynolds number $Re = 1$. Based on the boundary element technique given by Tuck [8] and the generalized coupling matrix given by Basak et al. [5], we incorporated the additional coupling contributions due to non-neighbouring members to investigate their effects on the added mass and the damping of the whole array. In this paper we focused only on the sensitiveness of the hydrodynamic effects (added mass and damping) due to different gap widths, relative phases and the effects of non-neighbouring members.

For the in-phase mode, the magnitude of the added mass effect increases as the array size increases. Hydrodynamic dissipation effects on the other hand reach an

optimum value for a critical gap width near $g/b = 0.4$ and drop further as the gap width is reduced. The drop in the dissipation effects is much more enhanced in a five-beam array compared to that of a three-beam array.

For the out-of-phase mode, added mass effect shows a similar trend both in a three-and a five-beam array with increase in magnitude as the gap widths are reduced. However, the hydrodynamic dissipation effects on the other hand show a monotonic trend in a five-beam array with increase in magnitude as the gap widths are reduced whereas in a three-beam array the effect can be neglected.

A key conclusion is that non-neighbouring members play a significant role as the array size increases irrespective of the phase and cannot be ignored for arrays having more than three members. In particular, the effect is enhanced for nondimensional gap widths g/b less than 0.4.

References

1. Michels, T., Rangelow, I.W.: Review of scanning probe micromachining and its applications within nanoscience. Microelectron. Eng. 191–203 (2014). https://doi.org/10.1016/j.mee.2014.02.011
2. Gupta, A.K., Nair, P.R., Akin, D., Ladisch, M.R., Broyles, S., Alam, M.A., Bashir, R.: Anomalous resonance in a nanomechanical biosensor. Proc. Natl. Acad. Sci. U. S. A. **103**(36), 13362–13367 (2006). https://doi.org/10.1073/pnas.0602022103
3. Kimber, M., Lonergan, R., Garimella, S.V.: Experimental study of aerodynamic damping in arrays of vibrating cantilevers. J. Fluids Struct. **25**(8), 1334–1347 (2009). https://doi.org/10.1016/j.jfluidstructs.2009.07.003
4. Shyy, W., Berg, M., Ljungqvist, D.: Flapping and flexible wings for biological and micro air vehicles. Prog. Aerosp. Sci. **35**(5), 455–505 (1999)
5. Basak, S., Raman, A.: Hydrodynamic coupling between micromechanical beams oscillating in viscous fluids. Phys. Fluids **19**(1), 1–13 (2007). https://doi.org/10.1063/1.2423254
6. Intartaglia, C., Soria, L., Porfiri, M., A, P.R.S.: Hydrodynamic coupling of two sharp-edged beams vibrating in a viscous fluid. Proc. R. Soc. **470**(2162), 1–25 (2013)
7. Cellini, F., Intartaglia, C., Soria, L., Porfiri, M.: Effect of hydrodynamic interaction on energy harvesting in arrays of ionic polymer metal composites vibrating in a viscous fluid. Smart Mater. Struct. **23**(4), 1–15 (2014). https://doi.org/10.1088/0964-1726/23/4/045015
8. Tuck, E.O.: Calculation of unsteady flows due to small motions of cylinders in a viscous fluid. J. Eng. Math. **3**(1), 29–44 (1969)
9. Tung, R.C., Jana, A., Raman, A.: Hydrodynamic loading of microcantilevers oscillating near rigid walls. J. Appl. Phys. **104**(11), 1–8 (2008). https://doi.org/10.1063/1.3033499

Author Index

S. Gutschmidt et al. (eds.), *IUTAM Symposium on Recent Advances in Moving Boundary Problems in Mechanics*, IUTAM Bookseries 34,
https://doi.org/10.1007/978-3-030-13720-5